University College London

Monitoring the spin environment of coupled quantum dots: towards the deterministic generation of photonic cluster states

Author:
Oliver William Seton Tedder

Supervisor:
Dr. Jeroen Elzerman

A thesis submitted in partial fulfilment of the requirements for the degree of Doctor of Philosophy

in the

Department of Electronic & Electrical Engineering

and the

London Centre for Nanotechnology

May 2018

I, Oliver William Seton Tedder, confirm that the work presented in this thesis is my own. Where information has been derived from other sources, I confirm that this has been indicated in the thesis

Abstract

Indium gallium arsenide self-assembled quantum dots have attracted a lot of attention due to their ability to trap single electrons and holes whose spin can be manipulated optically. This makes them attractive as qubits and light sources in various quantum computing and communication schemes. However, the spin of electrons and holes rapidly decoheres due to hyper-fine interaction with the atomic nuclei of the dot. The theme of this thesis is to find ways of overcoming this decoherence, in particular to allow generation of photonic cluster states from quantum dots. This was first approached by designing theoretical schemes to measure and compensate for the source of the decoherence, which were experimentally tested. Two new systems were then theoretically designed where the effects of decoherence could be mitigated.

It is shown theoretically that exciting a quantum dot with a laser of well-defined polarisation and monitoring the polarisation of emitted photons, it is possible to determine the vector polarisation of the nuclear spin ensemble. It is shown through simulation that this measurement can be performed on and possibly faster than the time-scale of nuclear fluctuations. The fundamental concept behind the measurement procedure is proved in an experiment using coupled quantum dots. Through the course of the experiment anomalous behaviour of the dots was discovered. A second theoretical proposal is made for a system allowing the fast application of an effective field to compensate for the decoherence mechanism.

It is then shown by simulation that a coupled dot system with a prepared in-plane nuclear spin polarisation, can allow optical spin rotation and entanglement generation. A different system is then theoretically proposed where the electron spin in quantum dot can be replaced with another qubit, such as embedded manganese atoms. It is shown through simulation that this system also allows the generation of photonic cluster states.

Acknowledgements

First and foremost, I acknowledge the help and guidance of my supervisor Dr Jeroen Elzerman. I am grateful to have been given the freedom to wander between projects and spend time working on different ideas. I am thankful to Jeroen and Professor Steven Bramwell for arranging an extension to my funding, allowing me to perform additional experimental work for this thesis. My thanks go to Professor Ataç İmamoğlu and Dr Javier Miguel-Sanchez for providing the samples used in this thesis. I thank Dr Guy Matmon for access to his seemingly bottomless treasure trove of optical elements. Similarly, I thank Dr Richard Thorogate and Dr Sanjeev Kumar for lending equipment and advice regarding the cryogenics. I thank the whole of Professor John Morton's Quantum Spin Dynamics group for welcoming me as a pseudo-member, and in particular, Salahuddin Nur and Dr Hee-Jin Lim for breaking the silence of the optics lab. Salahuddin's sense of humour and optimism served as an important reminder that the world wasn't going to end if the experiment didn't go to plan. Lastly, I thank my family for their constant love and support throughout the PhD. Without their continual encouragement this thesis may never have materialised.

Contents

List of Figures

List of Tables

Chapter 1

Introduction

1.1 Quantum computing

Computers have revolutionised the way information is processed. Since the invention of the transistor in 1947 and construction of the first transistorised computer some years after, they have become orders of magnitude smaller and more powerful. Yet even with the number of transistors and processing power following Moore's law, some problems remain computationally intractable for these classical machines. Problems such as prime factoring of large numbers and simulating quantum systems become essentially impossible as the computation increases in size.

In a classical computer the smallest denomination of information is a logical bit which exists in one of two states, 0 or 1. This could be represented as the switching state of a transistor, or the polarity of a magnetic domain on a hard disk. These bits can be manipulated using logic gates to perform useful transformations of further discrete logical bits. They can be easily initialised and measurements can be trivially performed with virtually no back action on the rest of the system.

Quantum computers proposed by Richard Feynman in 1982 [1] use a very different unit of information storage, and an equally unusual method of processing it. In these machines information is stored in quantum bits, or qubits. Like bits, qubits have two orthogonal states abstractly 0 and 1 which might be the spin of a spin-1/2 particle, but unlike their classical counterparts qubits can exist in a coherent mixture or complex superposition of

these two states. Mathematically the qubit's orthogonal, or basis, states are represented by kets $|0\rangle$ and $|1\rangle$ which are vectors that live in a 2D complex vector space. A general state can be then be written as $|\psi\rangle = a|0\rangle + b|1\rangle$ where the *amplitudes* a and b are complex numbers that describe how much the qubit is in each of the orthogonal states. It might be tempting to think of $|\psi\rangle$ as simply a probability distribution that determines the probability of either outcome, however the fact that the amplitudes can be complex implies that some phase also exists between the two outcomes. The superposition allows, in some sense, a quantum computer to perform many computations in parallel, since the input to the computation can be a superposition of several problem configurations. It is this behaviour which allows under some circumstances quantum computers to solve problems faster than their classical counterparts.

1.1.1 Circuit model of quantum computing

Classical information is processed in a computer by complex electrical circuits along which information flows in the form of an electrical current or a propagating change in potential. The circuit model of quantum computing looks on the surface very similar. Lines in a quantum circuit represent qubits and like their electrical analogue, the computation progresses as qubits (or rather the information they encode) move from start to finish. Figure 1.1 shows an example of a quantum circuit.

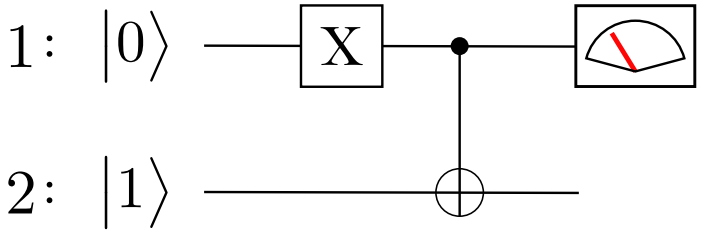

FIGURE 1.1: An example of a quantum circuit showing two qubits labelled 1 (top) and 2 (bottom). From left to right: qubits 1 and 2 qubits are initialised in the states $|0\rangle$ and $|1\rangle$ states respectively, a Pauli-X gate is applied to qubit 1 which changes its state to $|1\rangle$, a controlled-NOT gate is applied between both qubits which changes the state of qubit 2 to $|1\rangle$, qubit 1 is measured in the computational basis.

In this model qubits are initialised into a known state, often the 'computational basis' elements $|0\rangle$ or $|1\rangle$. They are manipulated by gates to change their amplitudes a and

b, and finally their state is read out. With qubits represented by vectors it is a natural extension that gates should be represented by matrices. In this sense, a quantum computer simply multiplies a very large matrix.

Experimentally implementing an arbitrary gate may seem a very difficult challenge, however it has be shown that in the same way that the NAND gate is universal for classical computation (all classical circuits can be decomposed into an arrangement of NAND gates), single qubit rotations and controlled-NOT (CNOT) gates between pairs of qubits are universal for quantum computation [2]. If a quantum computer implementation can perform rotations and two qubit CNOT gates then in principle it can implement any quantum computation (provided that there are sufficient numbers of qubits). This reduces the demand on experimental implementations significantly.

One additional quirk of quantum information is that the state of a system, or result of a quantum computation, cannot be measured in the same way as a classical system. On attempting to measure $\left|\psi\right\rangle$ it will 'collapse' randomly into the state $\left|0\right\rangle$ or $\left|1\right\rangle$. Not all is lost however, as the moduli of the amplitudes determine with what probability it will collapse into $\left|0\right\rangle$ or $\left|1\right\rangle$. The implication is that not all of the information stored in the state can be accessed by a single measurement, so many measurements must be taken in different directions (bases) and the results compiled together. This is generally the area of quantum state tomography, which is touched upon in this thesis.

Even with this limitation quantum computers can solve some problems significantly faster than classical computers. One of the most well known is the factoring algorithm of Peter Shor [3] which runs in polynomial time on a quantum computer (i.e. the amount of time taken for the algorithm to factor a number N is a polynomial function $\log N$). This is faster than the best known classical algorithm which runs in sub-exponential time [4] (the run time is exponential in $\log N$).

Even with the restriction to only a select few operations this model of quantum computation has large experimental demands. Initially isolated qubits must be entangled together, and rotated individually to high fidelity. The phase evolution of parts of the system must be tracked with high accuracy and accounted for, requiring precision electronics and tight control over the environment. Whilst small demonstration units have

had great success, scaling these to the point of universal or even just useful computational systems is a grand challenge [5]. A different model of quantum computation discussed next could hold the key to substantial reduction in the hardware requirements.

1.1.2 Measurement based quantum computing

The circuit model of quantum computation feels somewhat familiar with some experience of electronics, and even with the odd behaviour of the information carriers, the notion of computation by continued manipulation of those carriers is not so far removed from everyday experience.

A radically different way of performing quantum computation is that of measurement based quantum computing (MBQC) proposed by Raussendorf and Briegel in 2001 [6]. This model bears little resemblance to any classical model of information processing. In this model the qubits are initialised into a highly entangled cluster state, a state in which qubit measurements display non-classical correlations [7]. These states can be visualised as a graph where vertices represent qubits, and edges between two qubits mean a CNOT gate has been applied between them. Hence these states are also known as graph states. An example of such a state is shown in Figure 1.2.

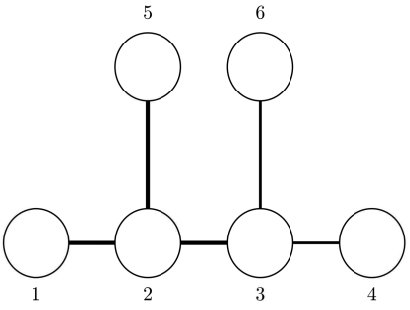

FIGURE 1.2: An example of a graph or cluster state. The circles represent physical qubits and lines between then represent a controlled-NOT gate having been applied between then.

The computation then proceeds by simply measuring the qubits. Which qubits are measured, and in what basis, will depend on the computation at hand, and the results of previous measurements. The result of the computation is given by the results of the final qubit measurements.

Remarkably this process can efficiently simulate any quantum circuit, that is the two models are computationally equivalent [8]. Each element in the equivalent circuit requires a particular pattern of measurements on the graph state and so the graph must be large enough to 'hold' the computation [9, 10]. This approach to quantum computation holds several advantages over the traditional circuit model. Preparation of the resource state, and the computation itself, are two separate processes. Thus the preparation step can performed prior to the start of the computation, allowing the resource state to be repeatedly generated and purified to increase its Fidelity [11] (e.g. when the resource state is generated via fusion of smaller cluster states, the success of the fusion operation is heralded by measurement outcomes [12]). The computation itself only requires single qubit measurements which are experimentally easier to perform than multi-qubit (non-local) measurements (in the case of photonic polarisation qubits, two-qubit measurements require interference on a beam splitter in a phase stable setup [13], whereas single qubit measurements require only a single photon detector preceded by a polariser).

Up until recently these cluster states have almost always been created using probabilistic sources, namely spontaneous parametric down-conversion [14, 15] or four wave mixing [16]. Whilst successful production can be heralded the probabilistic nature is an inherent limit to the generation rate [17]. Quantum dots may be able to address this problem.

1.2 Quantum dots, photons and cluster states

To build a quantum computer in either architecture, a physical manifestation of a qubit is required. One promising implementation is the spin of electrons and holes trapped in nano-structures. The spin is sufficiently isolated to survive for some time (longer than the typical timescale of quantum opterations [18]) against environmental noise [19–21], yet couples strongly enough to external fields and probes such that its state can be manipulated and interrogated [18, 22–24]. Carriers can be trapped in a number of ways [21, 25, 26] but this thesis focusses on the use of semiconductor quantum dots [19]. These are small regions of one semiconductor surrounded by another of a different band-gap. They exhibit quantum confinement due to their small size (10s of nanometres) [27]. The confinement potential gives rise to narrow energy levels, from which quantum dots get their name 'artificial atoms'. Electrons and holes can be introduced into the dot

from highly doped layers nearby, either relying on inherent quantum tunnelling, or by applying external potentials, or through optical excitation of carriers. Once trapped, a single electron or hole can act as a spin qubit with relatively long coherence time. If the semiconductors used have direct band gaps, the dots also act as centres of radiative recombination since photo generated excitons are localised to the dot by quantum confinement. Quantum dots are very attractive photon sources featuring narrow linewidths and high indistinguishability [28–31]. This feature has been exploited for control of the spin qubit and also quantum communication proposals [32].

The dots used in this thesis were grown from gallium arsenide and indium arsenide by the self assembly method. Dots grown by this method routinely outperform those grown more directly through droplet epitaxy, in terms of their photon linewidths [33–35]. However they suffer from unpredictable growth location and size which affects their energy structure. This poses severe problems for using their confined spins as qubits in a gate like processor since finding two that are close enough in energy to be entangled is rare [36], let alone physically close enough to allow direct coupling.

MBQC could again come to the rescue by utilising the aforementioned optical properties of quantum dots. A proposal by Lindner and Rudolph in 2009 showed that it was possible to generate photonic linear cluster states (that is, cluster states where the qubits are photons) from quantum dots [37]. A selling point of their proposal was that it only required primitive operations on the spin qubit. In their proposal the spin of a trapped electron acted as a solid state 'seed' qubit from which the rest of the photonic cluster state was grown. Whilst these linear cluster states are not sufficient for anything more than single (logical) qubit rotations, protocols exist for the fusing together of smaller cluster states into larger ones, large enough for more complex computations [12, 38]. The proposal was extended later by Economou, Lindner and Rudolph [39] to generate two dimensional cluster states.

Nevertheless, performing these quantum control primitives to high enough fidelity and in a way that is amenable to experiment is still a daunting challenge. Significant progress was made very recently by Schwartz *et al.* who were able to demonstrate the creation of a linear cluster state with entanglement extending to 5 photons [40]. In their experiment, the spin of a dark exciton in the dot was used in place of the electron spin. This

metastable state was used because of its longer coherence time [41] as well as its built in rotation mechanism. In addition, a higher excited state afforded them a way of separating the cluster state photons from stray photons from the control mechanisms. Whilst a remarkable proof of concept, the use of a metastable is non-ideal for a scalable system since it sets a limit on the possible length of cluster state. An electron qubit would ideally be used but this is susceptible to decoherence from the nuclear spin ensemble.

A contribution of this thesis is the theoretical design of a system using coupled quantum dots where photonic cluster states could be generated using only optical manipulation. A second related contribution is the theoretical development of a scheme where the electron spin could be replaced in the Lindner and Rudolph scheme by a different two level system whilst still benefiting from the optical properties of quantum dots. The replacement spin considered is the spin of Manganese atoms implanted into quantum dots, though the scheme is sufficiently general that the idea and results could be applied to other systems. Nonetheless the issue of decoherence is still a major issue for many quantum control schemes involving quantum dots.

1.3 Decoherence

One measure of the 'quality' of a qubit is its coherence time. Quantified by the time T_2, this is the time taken for a qubit prepared in a superposition state to loose its phase information and 'decohere' into a (classically) statistical mixture. Inhomogeneous dephasing causes further apparent decoherence in ensemble measurements, characterised by a coherence time T_2^*. Early measurements of the electron spin revealed short coherence times on the order of a few nanoseconds [42, 43] (short in comparison to the radiative lifetime of the excited states, and corresponding times in atomic systems [44]). It was later understood that the coupling of the electron spin to the nuclei of the host material played a dominant role in the decoherence. The net effect of the nuclei is to present an effective magnetic field, known as the Overhauser field, which couples to the electron spin just as an external field would. The Overhauser field varies in strength and direction randomly over the course of an experiment, resulting in an inhomogeneous dephasing time T_2^* of several nanoseconds. The field can be decoupled from the electron spin by refocussing pulses or dynamic decoupling to reveal a homogeneous dephasing

time T_2 around 3 μs [43]. Under normal experimental conditions the nuclei assume a thermal distribution, however their interaction with the electron spin can be exploited to polarise them. Various polarisation schemes can generate huge effective fields of several Tesla, which are themselves a useful feature [45]. In addition the nuclei can be polarised to reduce fluctuations and decrease the inhomogeneous electron spin dephasing rate [46]. This has very recently been demonstrated by Éthier-Majcher *et al.* who were able to increase T_2^* by over an order of magnitude to 39 ns [47].

A contribution of this thesis is the theoretical development and experimental demonstration of an *active* mechanism for sensing the state of the Overhauser field and a means of compensating for it. The field sensing mechanism exploits the optical properties of a quantum dot, and in particular the link between the exciton spin state and photon polarisation. The essence is that by exciting the dot with a laser of known polarisation, and analysing the polarisation of spontaneously emitted photons, the total field in the dot can be reconstructed. Whilst this is in principle possible in single quantum dots, using vertically stacked tunnel coupled dots allows for greater freedom in designing the protocol and in particular for separating the spontaneously emitted photons from the laser background. In fact the use of coupled quantum dots is crucial for the field compensation scheme. The latter uses the large nuclear field that can be established though polarisation, along with fast electrical control to apply an effective magnetic field to an electron spin sitting in one of the dots.

1.4 Outline

The basic physics of the quantum dots and devices are described in detail in Chapter 2. The bulk and confined states are described, and from these the optical selection rules are derived. These allow discussion of standard methods for manipulation of spin qubits. The role of the nuclear spin ensemble is explained, and coupled quantum dots are introduced.

The states in a coupled quantum dot are modelled in Chapter 3. The methodology used here is also employed elsewhere so the model is described with some rigour. The model

is applied to experimentally collected data in order to extract important parameters of coupled quantum dots.

Chapter 4 describes the construction of the confocal microscope setup and supporting apparatus used for all experimental investigations in this thesis. Construction and operation of the equipment is described in detail. Characterisation procedures are described as well as standard measurement techniques. The spectral suppression stage is built and characterised, which is used later in the experimental demonstration of the field sensing mechanism.

The schemes for sensing and compensating for the Overhauser field are theoretically designed in Chapter 5. A simulation is built for the sensing mechanism and is used to estimate the performance of the scheme. An experiment is performed using coupled quantum dots to prove the concept. Whilst performing the experiment, anomalous behaviour of the coupled quantum dots was discovered. Possible explanations for the anomalous behaviour are discussed. The scheme to compensate for the Overhauser field is designed theoretically and is demonstrated in simulation.

In Chapter 6 the Lindner and Rudolph proposal is described and ways of verifying it are simulated. The model of the coupled quantum dots states is used to theoretically design the new system allowing for all-optical spin manipulation and entanglement generation. The theoretical proposal allowing for the replacement of the electron spin in the Lindner and Rudolph proposal is discussed, and it is simulated to investigate how it would perform in practise.

Finally in Chapter 7 the state of this research and possible directions for the future are discussed.

Chapter 2

Self-assembled quantum dots

In this chapter the basic physics of quantum dots and devices is recapped. In Section 2.1 the growth of the quantum dots is described as well as the device structure which allows the transition energies to be tuned in-situ. The fundamental electronic states in the semi-conductor materials and quantum dots are described in Section 2.2. These are then used to derive the optical selection rules in Section 2.3. Neutral and charged excitons that can be generated by the selection rules are described in Section 2.4. The ground state of the charged exciton can be used as a spin qubit and Section 2.5 describes some of the methods employed to control it. Spin decoherence mechanisms are covered and this leads on to discussion of the nuclear spin ensemble and polarisation in Section 2.6. Coupled quantum dots are described in Section 2.7.

2.1 Growth and fabrication

2.1.1 Growth of self-assembled quantum dots

The quantum dots used in this thesis are grown by molecular beam epitaxy (MBE). Indium arsenide (InAs) is grown on gallium arsenide (GaAs) and the lattice mismatch (0.57nm and 0.61nm for GaAs and InAs respectively) causes strain in the structure. This InGaAs wetting layer grows in thickness and after ~ 1.7 monolayers [48] it relaxes to form islands [27]. This is the so-called Stanski-Krastanow (SK) growth mode. The islands nucleate randomly along the wetting layer although long range order can be

established by processing the sample prior to growing the quantum dots [49]. They have a height of the order 10nm and lateral dimensions of 10s of nanometres. They can be overgrown with GaAs which blue-shifts the quantum dot optical transitions due to increased strain [50].

2.1.2 Schottky diode structure

For quantum dots to be useful in a larger system (where for example they will be coupled together) the optical transition energies should be identical or at least well defined. The energy structure of the quantum dots depends on their size, morphology and chemical composition. These parameters are fixed during the growth procedure but cannot be controlled precisely. In order to compensate for this an external in-situ method of tuning the energy level structure is required.

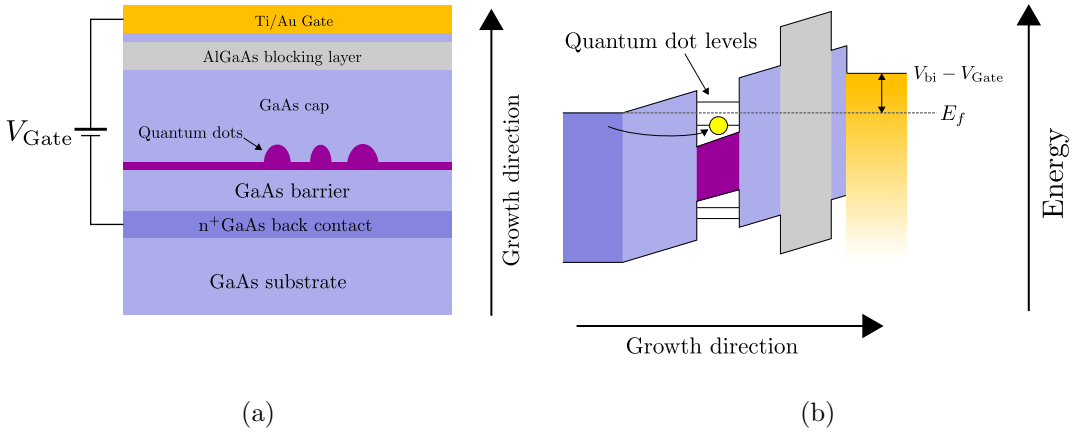

FIGURE 2.1: (a) The sample structure that allows application of an electric field along the growth direction. (b) The resulting band structure that allows deterministic charging and tuning of the quantum dots. Changing the gate voltage V_{Gate} alters the quantum dot energy levels with respect to the Fermi energy of the heavily doped n$^+$GaAs back contact. When an empty level of the quantum dot is tuned below the Fermi energy E_f of the back contact, an electron (yellow circle) can tunnel into it. V_{bi} is the built-in voltage of the junction.

By growing the quantum dot layer inside a Schottky diode structure as in Figure 2.1a an electric field can be applied along the growth axis. Changing the voltage applied between the gate and back contact tilts the bands and shifts the quantum dot energy levels [51] as shown in Figure 2.1b. By tuning the first quantum dot level beneath the Fermi energy of the highly doped back contact E_f, an electron can tunnel from the back contact into the quantum dot [28]. The energy required for a second electron to enter

the dot is higher because of the Coulomb repulsion between the electrons and so it is blocked from entering the dot [21, 22, 52]. This is known as Coulomb blockade and it allows control over the number of carriers in the quantum dot ground state. In addition to deterministic charging, the exciton recombination energy can be tuned via the DC Stark effect [53]. The exciton stark shift is given by

$$\Delta E_{\text{stark}} = -\beta \left|\mathbf{E}\right|^2 - e\mathbf{d_0} \cdot \mathbf{E} \tag{2.1}$$

where β is a constant, e is the electronic charge, $\mathbf{E}$ is the electric field and $\mathbf{d_0}$ is the separation of the electron and hole at zero field due to the dot's chemical composition [54]. At the electric field strengths used in this thesis the second term dominates, so the Stark shift is linear. In typical device structures, the DC Stark shift facilitates tuning of a given transition on the order of 200 μeV[28, 53], assuming a typical Startk shift of 2 μeV/mV and a charge stability region of 100 mV (equivalent to a change in wavelength of only 150 pm at 960 nm). The transition energy can be tuned further by applying strain which can allow shifts of up to 0.45 nm [55] which is important when trying to tune several dots into resonance.

2.2 Electronic states

In order to understand and engineer the behaviour of the quantum dots the electronic states of the material must be fully understood.

2.2.1 Bulk states

Both GaAs and InAs are semiconductors with zincblende crystal structure. They have direct band gaps so optical transitions are efficient. In equilibrium the valence band states are all occupied and the conduction band states are empty. The valence electrons of the two atomic species in each semi-conductor are in p and s-type orbitals which hybridise to form tetrahedral sp^3 bonds in the crystal. Near the band edges the conduction band Bloch states $\left|s\right\rangle$ have the symmetry of the s-type orbitals and angular momentum

$l = 0$. Including spin the conduction band eigenstates can be written as [56]

$$|c^{1/2}_{+1/2}\rangle = |s\rangle|\uparrow\rangle \tag{2.2}$$

$$|c^{1/2}_{-1/2}\rangle = |s\rangle|\downarrow\rangle \tag{2.3}$$

where the superscript is the angular momentum j and subscript is the z projection j_z. The valence band Bloch states can be written as linear combinations of three states $|x\rangle$, $|y\rangle$ and $|z\rangle$ which posses the symmetry of the each of the p-type orbitals. These have angular momentum $l = 1$. By coupling together the spin and angular momentum states the 6 eigenstates can be written as [56, 57]

$$|v^{3/2}_{+3/2}\rangle = -\frac{1}{\sqrt{2}}|x+iy\rangle|\uparrow\rangle \qquad \text{Heavy hole } \Uparrow \tag{2.4}$$

$$|v^{3/2}_{-3/2}\rangle = +\frac{1}{\sqrt{2}}|x-iy\rangle|\downarrow\rangle \qquad \text{Heavy hole } \Downarrow \tag{2.5}$$

$$|v^{3/2}_{+1/2}\rangle = -\frac{1}{\sqrt{6}}\left[|x+iy\rangle|\downarrow\rangle + 2|z\rangle|\uparrow\rangle\right] \qquad \text{Light hole } \Uparrow \tag{2.6}$$

$$|v^{3/2}_{-1/2}\rangle = +\frac{1}{\sqrt{6}}\left[|x-iy\rangle|\uparrow\rangle + 2|z\rangle|\downarrow\rangle\right] \qquad \text{Light hole } \Downarrow \tag{2.7}$$

$$|v^{1/2}_{+1/2}\rangle = -\frac{1}{\sqrt{3}}\left[|x+iy\rangle|\downarrow\rangle + |z\rangle|\uparrow\rangle\right] \qquad \text{SO hole } \Uparrow \tag{2.8}$$

$$|v^{1/2}_{-1/2}\rangle = +\frac{1}{\sqrt{3}}\left[|x-iy\rangle|\downarrow\rangle - |z\rangle|\uparrow\rangle\right] \qquad \text{SO hole } \Downarrow \tag{2.9}$$

Of the $j = 3/2$ states the two with $j_z = \pm 3/2$ are the heavy hole (hh) states, and those with $j_z = \pm 1/2$ are the light hole (lh) states. The two states with $j = 1/2$ are the spin orbit split-off band (so). These eigenstates are found from diagonalising the spin orbit interaction Hamiltonian which raises the energy of the hh and lh states, whilst lowering the energy of the so states, splitting them by Δ_{so} (see Section 2.3 of [58]). In GaAs $\Delta_{so} = 340$ meV and in InAs $\Delta_{so} = 380$ meV and so the so bands can be neglected as transitions to them will be far detuned from those involving the the hh and lh states (which are the states of interrest). The two hh and lh manifolds are split by Δ_{hh-lh} due to strain and/or quantum confinement. Uniaxial compression raises the energy of the lh states above the hh states, whilst stretching causes the opposite effect [56].

2.2.2 Confined states

In order to repeatedly probe the spin of an electron or hole it should first be trapped in all three dimensions. This can be done by engineering a region of the semiconductor to have a smaller band-gap than the surrounding material. Electrons and holes see this as a 3D potential energy well which localises their wavefunctions in space. The SK growth method forms small mesas of InAs (with a bandgap of 0.42 eV at 4 K [59]) surrounded by GaAs (with a bandgap of 1.52 eV at 4 K). As a result of the confinement in each direction, the density of states in the quantum dot are almost discrete [60]. The potential in the growth direction (z) can be approximated as a square well which quantises the momentum in this direction (p_z). This confinement shifts the energy of the *lh* and *hh* states differently due to their different effective masses[1]. The effects of strain overcompensate for this confinement shift and so the *hh* states remain higher in energy than the *lh* states by $\Delta_{hh-lh} \approx 10$ meV [56]. As a result mixing between the two hole types is suppressed and so the *lh* valence states can be, for the most part, entirely neglected. The heavy hole states can therefore be treated as a pseudo spin-1/2 system. The overall band-structure is shown in Figure 2.2.

The z direction confinement energies are sufficiently large that only the first confined state need be considered. In the x-y plane the confinement is roughly parabolic. As such the confined states in the plane are the eigenstates of the 2D quantum harmonic oscillator (QHO) which can be described by two quantum numbers l and m with energy

$$E_{l,m} = \hbar\omega\,(l + m + 1) \tag{2.10}$$

It can be shown that the z component of angular momentum of the 2D QHO eigenstates is

$$L_z^{l,m} = \pm\,(l - m) \tag{2.11}$$

and the levels with $l + m = 0$, 1, 2 ... are labelled the s, p, d ... shells. This discrete level structure is shown in Figure 2.3.

[1]The kinetic energy contribution is $\langle p_z^2 \rangle \frac{1}{2m^*}$. Both *lh* and *hh* will have the same p_z since this is governed by the geometry, but the effective mass m^* of the *lh* states is smaller so the contribution is larger.

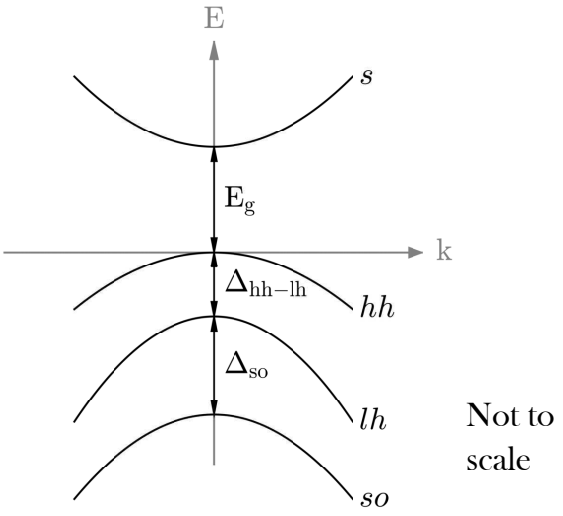

FIGURE 2.2: Band structure of the doubly degenerate energy bands in GaAs. Energy is plotted against the k-vector perpendicular to the strain axis. *s*, *hh*, *lh* and *so* are the conduction, heavy-hole, light-hole and spin-orbit split off bands respectively. E_g, Δ_{hh-lh} and Δ_{so} are the energy gap, light-hole-heavy-hole and spin-orbit splitting respectively. Adapted from [56].

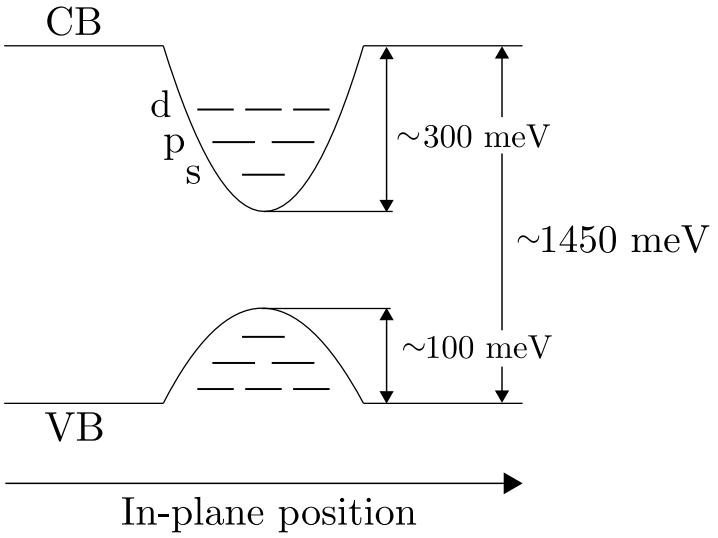

FIGURE 2.3: The discrete level structure in a quantum dot due to the in plane 2D harmonic confinement. CB and VB are the conduction band and valence band of the semiconductor material. Adapted from [56].

Using the envelope function approximation the wavefunction of an electron in the quantum dot can be written as the underlying Bloch wavefunction modulated by a function which describes the effect of the confining potential. The total electron wavefunction

can be described in the position representation by

$$\Psi\left(\underline{r}\right) = \langle \underline{r}|u\rangle \, \phi_{l,m}\left(\underline{r}\right) \tag{2.12}$$

where $\phi_{l,m}\left(\underline{r}\right)$ is the 2D QHO position eigenstate with quantum numbers l and m. Since the *lh* and *so* states can be ignored $\left|u\right\rangle$ is one of (2.2), (2.3), (2.4) or (2.5). The point to take away from this is that the electron (or hole) states pick up the symmetry and spin nature of the underlying Bloch states and the confined states. This will have implications for the allowed optical transitions between confined states.

2.3 Optical transitions

The fundamental transitions involve raising an electron from one of the valence band confined states to one of the conduction band confined states. Neglecting other dynamic interactions such as tunnelling, the states (2.12) are stationary. Transitions between them can be driven by coupling to optical fields. The allowed transitions between the confined states are derived in this section following [56].

The non-relativistic Hamiltonian in the Heisenberg picture for a charged particle in a field ([56] Section 5.1.2, [61] Section 5.1.1) can be expanded in the Coulomb gauge to

$$H_{\text{tot}} = H_0 - \frac{q}{m_0}\mathbf{A}\left(\mathbf{r},t\right)\cdot\mathbf{p} + H_f \tag{2.13}$$

where q, m_0 and $\mathbf{p}$ are the charge, mass and momentum of the particle respectively, and $\mathbf{A}\left(\mathbf{r},t\right)$ is the vector potential of the field. The first term describes the stationary states of the system, the second term is the coupling between the particle and the quantised field, and the third is the Hamiltonian of the free field. The second term generates interactions between the stationary states of H_0 and the photon field, and so is termed the interaction Hamiltonian. Written in the Schrödinger picture and using the dipole approximation, it can be expanded as

$$H_{\text{int}} \approx -\frac{q}{m_0}\sum_{\mathbf{k},s} A_{\mathbf{k}}\left(a_{\mathbf{k},s}\mathbf{e}_{\mathbf{k}s}\cdot\mathbf{p} + a^{\dagger}_{\mathbf{k},s}\mathbf{e}^{*}_{\mathbf{k}s}\cdot\mathbf{p}\right) \tag{2.14}$$

where $A_{\mathbf{k}}$, $a_{\mathbf{k},s}$ and $\mathbf{e}_{\mathbf{k}s}$ are the amplitude, annihilation operator and polarisation vector of the photon with momentum $\mathbf{k}$ and polarisation s. The mathematics are simplified by considering a single photon mode, so the $\mathbf{k}$ and s labels can be discarded. The transition rate between two states $\left|1\right\rangle$ and $\left|2\right\rangle$ can be evaluated by calculating the matrix element $\left\langle 2\right| H_{\text{int}} \left|1\right\rangle$. In the quantum dot case, the states $\left|1\right\rangle$ and $\left|2\right\rangle$ are tensor products of the quantum dot states (2.12) with the radiation field with n photons in the state $\left|n\right\rangle$. Equation (2.14) can now be used to derive the common Faraday and Voigt selection rules.

2.3.1 Symmetry

First a quick note about the symmetry of the states. The momentum operator $\mathbf{p}$ in (2.14) operates directly on the underlying Bloch states of (2.12), and $a_{\mathbf{k},s}$ operates on the photon field. The envelope functions are unchanged and so the matrix element will contain an overlap of these functions, something like

$$\int \phi^*_{l',m'} \phi_{l,m} \, \mathrm{d}\mathbf{r} \tag{2.15}$$

which will be zero for functions of different parity. This for example only allows transitions from s to s states, and so in the following the s envelope function is implicit.

2.3.2 Selection rules in the Faraday geometry

In this context the Faraday geometry means that there is a magnetic field which is aligned with the growth direction; however, the field itself is not important here. The system eigenstates are those in (2.2), (2.3), (2.4) and (2.5). The fundamental transitions that raise an electron from the valence band to the conduction band states are then

$$\left|v^{3/2}_{+3/2}\right\rangle \rightarrow \left|c^{1/2}_{+1/2}\right\rangle \tag{2.16}$$

$$\left|v^{3/2}_{+3/2}\right\rangle \rightarrow \left|c^{1/2}_{-1/2}\right\rangle \tag{2.17}$$

$$\left|v^{3/2}_{-3/2}\right\rangle \rightarrow \left|c^{1/2}_{+1/2}\right\rangle \tag{2.18}$$

$$\left|v^{3/2}_{-3/2}\right\rangle \rightarrow \left|c^{1/2}_{-1/2}\right\rangle \tag{2.19}$$

First consider the transition (2.16). The angular momentum decreases by 1 so this transition is expected to be allowed and mediated by a left-hand circularly polarised (L)

photon. The initial state is

$$\left|1\right\rangle = \left|v^{3/2}_{+3/2}\right\rangle \left|n+1\right\rangle \tag{2.20}$$

and the final state is

$$\left|2\right\rangle = \left|c^{1/2}_{+1/2}\right\rangle \left|n\right\rangle \tag{2.21}$$

where the number of photons has reduced by one since one has taken part in the transition. The transition matrix element then becomes

$$\left\langle 2\right| H_{\text{int}} \left|1\right\rangle = -\frac{q}{m_0} A \left(\left\langle n\right| a \left|n+1\right\rangle \mathbf{e} + \left\langle n\right| a^{\dagger} \left|n+1\right\rangle \mathbf{e}^{*} \right) \cdot \left\langle c^{1/2}_{+1/2} \right| \mathbf{p} \left| v^{3/2}_{+3/2} \right\rangle \tag{2.22}$$

The second term in the brackets goes to zero and the first goes to $\sqrt{n+1}$ (see for example equation (4.4.1) in [62]) leaving

$$\left\langle 2\right| H_{\text{int}} \left|1\right\rangle = -\frac{q}{m_0} A\sqrt{n+1}\mathbf{e} \cdot \left\langle c^{1/2}_{+1/2} \right| \mathbf{p} \left| v^{3/2}_{+3/2} \right\rangle \tag{2.23}$$

The momentum matrix elements $\left\langle s\right| p_{\alpha} \left|\alpha\right\rangle = p_{cv}$ are the same for $\alpha \in \{x, y, z\}$ [56]. Note that $\left\langle s\right| p_{\beta} \left|\alpha\right\rangle = 0$ when $\beta \neq \alpha$ since $\left|s\right\rangle$ and $\left|\alpha\right\rangle$ have even and odd parity respectively, so p_{β} must be an odd function (of α) to give a non-zero result. This means

$$\left\langle c^{1/2}_{+1/2} \right| \mathbf{p} \left| v^{3/2}_{+3/2} \right\rangle = \left(\left\langle s\right| \left\langle \uparrow \right| \right) \mathbf{p} \left(-\frac{1}{\sqrt{2}} \left| x+iy \right\rangle \left| \uparrow \right\rangle \right) \tag{2.24}$$

$$= -\frac{1}{\sqrt{2}} \left(\left\langle s\right| \mathbf{p} \left|x\right\rangle + i \left\langle s\right| \mathbf{p} \left|y\right\rangle \right) \left\langle \uparrow \right| \left. \uparrow \right\rangle \tag{2.25}$$

$$= -\frac{1}{\sqrt{2}} p_{cv} \left(\hat{\mathbf{x}} + i\hat{\mathbf{y}} \right) \tag{2.26}$$

and putting these together

$$\left\langle 2\right| H_{\text{int}} \left|1\right\rangle = \frac{q}{m_0\sqrt{2}} A\sqrt{n+1}\, p_{cv} \mathbf{e} \cdot \left(\hat{\mathbf{x}} + i\hat{\mathbf{y}} \right) \tag{2.27}$$

$$\equiv C\mathbf{e} \cdot \left(\hat{\mathbf{x}} + i\hat{\mathbf{y}} \right) \tag{2.28}$$

where C is a constant. Two (essentially equivalent) things can be said about this. Firstly, in order to maximise the transition rate from $\left|1\right\rangle$ to $\left|2\right\rangle$ which is $\propto \left|\left\langle 2\right| H_{\text{int}} \left|1\right\rangle\right|$, the polarisation vector should be set to $\mathbf{e} = \hat{\mathbf{x}} - i\hat{\mathbf{y}}$ so this transition is driven strongest

by L polarised light as expected. Secondly the hermitian conjugate of (2.28) (the reverse process) says that the decay from $|2\rangle$ to $|1\rangle$ is accompanied by excitations of the photon field with the same polarisation, emission of an L polarised photon. The same calculation using states in (2.19) gives the matrix element

$$-C\mathbf{e}\cdot(\hat{\mathbf{x}}-i\hat{\mathbf{y}}) \tag{2.29}$$

showing that a polarisation vector of $\mathbf{e}=\hat{\mathbf{x}}+i\hat{\mathbf{y}}$ maximises the transition rate. This means that this transition is right-hand circularly polarised (R) as expected from the change in angular momentum.

Finally by observing that the spin component of the Bloch functions are unchanged by H_{int}, the transitions (2.18) and (2.17) give zero matrix element as the orthogonal spin components integrate to zero. An intuitive argument for this is that since there is nothing that acts on the spin part, there is no way to flip the spin as is necessary for the transition. Equivalently a single photon transition cannot provide the ± 2 units of angular momentum required. These selection rules are summarised in Figure 2.4.

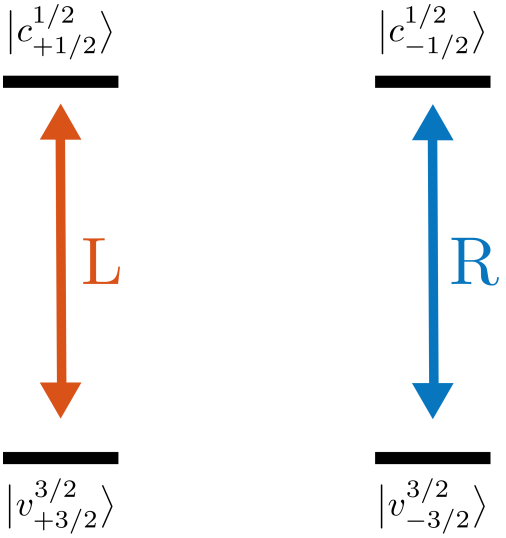

FIGURE 2.4: The allowed transitions between fundamental carrier states. The blue and red arrows denote transitions mediated by right (R) and left-hand (L) circularly polarised photons respectively.

2.3.3 Selection rules in the Voigt geometry

The Voigt geometry means that there is a magnetic field perpendicular to the growth direction. In this case the eigenstates of the system change to be linear superpositions of those above

$$\left|c^{1/2}_{+1/2}\right\rangle_x = \frac{1}{\sqrt{2}}\left(\left|c^{1/2}_{+1/2}\right\rangle + \left|c^{1/2}_{-1/2}\right\rangle\right) \tag{2.30}$$

$$\left|c^{1/2}_{-1/2}\right\rangle_x = \frac{1}{\sqrt{2}}\left(\left|c^{1/2}_{+1/2}\right\rangle - \left|c^{1/2}_{-1/2}\right\rangle\right) \tag{2.31}$$

$$\left|v^{3/2}_{+3/2}\right\rangle_x = \frac{1}{\sqrt{2}}\left(\left|v^{3/2}_{+3/2}\right\rangle + \left|v^{3/2}_{-3/2}\right\rangle\right) \tag{2.32}$$

$$\left|v^{3/2}_{-3/2}\right\rangle_x = \frac{1}{\sqrt{2}}\left(\left|v^{3/2}_{+3/2}\right\rangle - \left|v^{3/2}_{-3/2}\right\rangle\right) \tag{2.33}$$

and so the transitions of interest are

$$\left|v^{3/2}_{+3/2}\right\rangle_x \rightarrow \left|c^{1/2}_{+1/2}\right\rangle_x \tag{2.34}$$

$$\left|v^{3/2}_{+3/2}\right\rangle_x \rightarrow \left|c^{1/2}_{-1/2}\right\rangle_x \tag{2.35}$$

$$\left|v^{3/2}_{-3/2}\right\rangle_x \rightarrow \left|c^{1/2}_{+1/2}\right\rangle_x \tag{2.36}$$

$$\left|v^{3/2}_{-3/2}\right\rangle_x \rightarrow \left|c^{1/2}_{-1/2}\right\rangle_x \tag{2.37}$$

The matrix elements and polarisations can be calculated by applying the same machinery. Note that unlike the Faraday case, each of the new eigenstates has both $\left|\uparrow\right\rangle$ and $\left|\downarrow\right\rangle$ and it is expected that all four transitions are allowed. This is indeed the case and the matrix elements for transitions (2.34)-(2.37) (with a global phase removed) with their corresponding polarisations are

$$C\mathbf{e}_{\mathbf{k}s}\cdot\hat{\mathbf{y}} \qquad \text{H polarised} \tag{2.38}$$

$$iC\mathbf{e}_{\mathbf{k}s}\cdot\hat{\mathbf{x}} \qquad \text{V polarised} \tag{2.39}$$

$$iC\mathbf{e}_{\mathbf{k}s}\cdot\hat{\mathbf{x}} \qquad \text{V polarised} \tag{2.40}$$

$$C\mathbf{e}_{\mathbf{k}s}\cdot\hat{\mathbf{y}} \qquad \text{H polarised} \tag{2.41}$$

which are summarised in Figure 2.5. These transitions are mediated by horizontally (H) and vertically (V) polarised photons. The presence of a magnetic field is again not important, only to define a quantisation axis. In other words, the selection rules in

the Voigt system are identical to the Faraday system, only here they are inspected in a different basis.

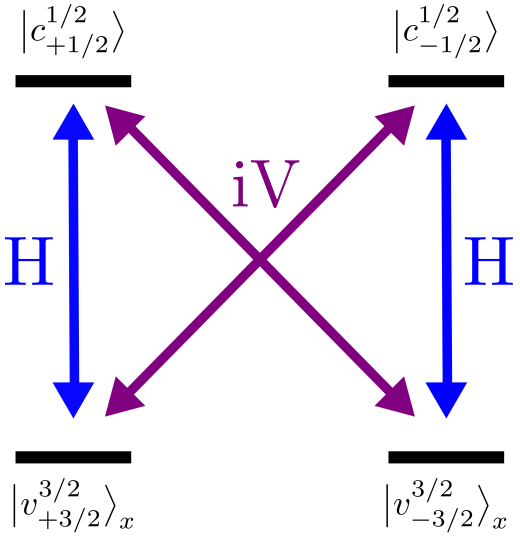

FIGURE 2.5: The allowed transitions between fundamental carrier states in the Voigt geometry. The blue and purple arrows denote transitions mediated by H and V polarised photons respectively. The presence of the imaginary unit implies that the V transitions are out of phase with the H ones.

2.4 Excitons

The selection rules derived the previous section allow an electron to be raised from the valence band states to the conduction band states. The vacant state in the valence band is referred to as a hole. Together the hole and electron form an exciton. The excitons are grouped by the charge of the ground and excited state.

2.4.1 Neutral excitons

Starting from an empty dot where all of the valence states are full, an optical excitation can excite an electron from the valence level to a conduction level. An R polarised photon can excite an electron from the bound state $|v^{3/2}_{-3/2}\rangle$ to the state $|c^{1/2}_{-1/2}\rangle$. This picture is simplified by considering the ground state to be empty ($|0\rangle$), and the excited state to contain a spin down electron in the conduction state ($|\downarrow\rangle$) and a spin up hole in the valence state ($|\Uparrow\rangle$). Hence the excited state is written as $|\downarrow\Uparrow\rangle$. Since the conduction levels are initially empty there is no restriction on the spin of the electron

that takes part. In this case the allowed transitions form a V system as shown in Figure 2.6.

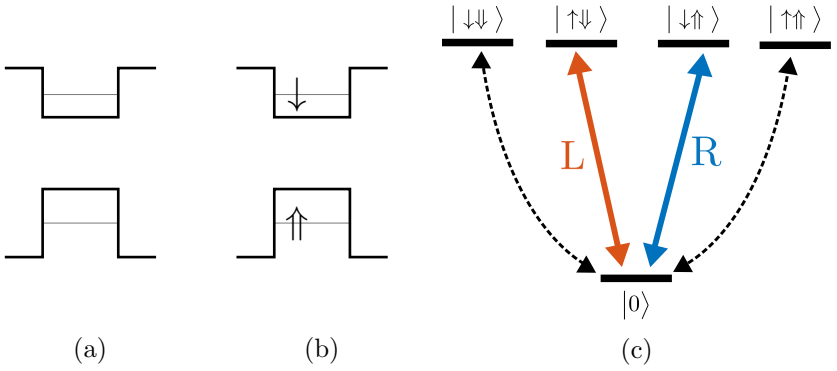

FIGURE 2.6: The (a) initial and (b) one of the final states in the X_0 system. (c) The transitions between the empty ground state and the allowed excited states are shown by the coloured arrows with polarisations R (blue arrow) and L (red arrow). Transitions which are forbidden by the selection rules are shown by the black dashed arrows.

The states $|\uparrow\Downarrow\rangle$ and $|\downarrow\Uparrow\rangle$ can be generated by L and R polarised photons as shown by the arrows. These are called the bright excitons. They correspond to processes (2.16) and (2.19). The states $|\uparrow\Uparrow\rangle$ and $|\downarrow\Downarrow\rangle$ are called dark excitons because they cannot be created by optical excitation according to the selection rules. They correspond to processes (2.18) and (2.17) which were the transitions whose interaction matrix element was zero. In reality the dark exciton can be created through processes that flip the spin of the electron or hole however transitions to them are very weak.

Due to the asymmetric shape of real quantum dots the electron and hole interact via an anisotropic exchange interaction. This has been thoroughly reviewed by Bayer *et al.* [63]. This exchange interaction couples the bright excitons together giving rise to two new bright exciton states $|X\rangle$ and $|Y\rangle$ which are split by an energy δ_1. The new states are superpositions of the old ones and so the optical transitions to them are linearly polarised at zero field. The dark excitons are also coupled together to give new eigenstates $|X_D\rangle$ and $|Y_D\rangle$ which are split by an energy δ_2. The bright and dark manifolds are further split from each other by the energy δ_0. These new states are shown in Figure 2.7.

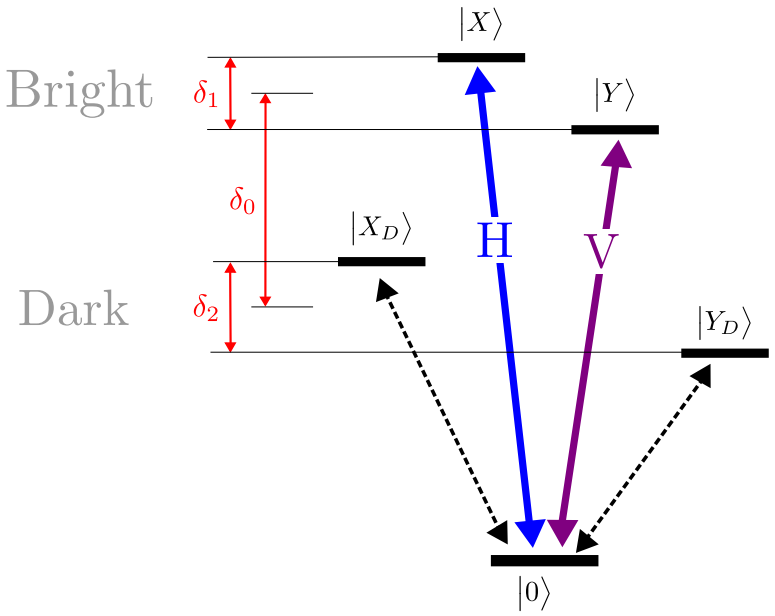

FIGURE 2.7: The transitions in the X_0 system in the presence of anisotropic electron-hole exchange. The heavy-hole bright and dark excitons are coupled together to form new bright ($|X\rangle$, $|Y\rangle$) and dark states ($|X_D\rangle$, $|Y_D\rangle$). Optical transitions to new bright states are linearly polarised (H and V) at zero magnetic field and are split by an energy δ_1. The new dark states are split by δ_2 and the bright and dark manifolds are split by δ_0.

In both of the above cases the ground state and excited had zero net charge so these are called the neutral excitons or X_0 . The splitting between the new eigenstates (e.g. between $|X\rangle$ and $|Y\rangle$) is known as the fine structure splitting (FSS). This causes problems in some schemes, such as when using biexcitons to generate entangled Bell states. In this case the energy splitting inhibits entanglement generation between the H and V polarised photon generated by a biexciton cascade [32]. By applying additional strain to the structure, the FSS can be reduced [64].

2.4.2 Charged excitons

If the dot already contains some electrons in the conduction band, or holes in the valence band, then then some of the transitions are blocked by the Pauli exclusion principle. For example the ground state shown in Figure 2.8a contains one electron. Since only the s-shell is considered, to add an additional electron to the conduction state its spin must be anti-parallel to the existing electron. As a result only one excited state can be reached whose configuration is shown in Figure 2.8b. This system is called the negatively charged trion or X_{1-} reflecting the total charge of the ground and excited state. There is a similar

transition involving a $|\downarrow\rangle$ resident electron. Symmetry requires that the electrons form a spin singlet which has zero net spin. As a result there is no electron-hole exchange interaction for trions. The physics is the same for a resident hole, in which case the system is called the X_{1+} .

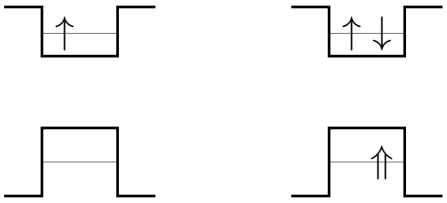

(a) (b)

FIGURE 2.8: The (a) initial and (b) one of the final states in the X_{1-} system.

The transitions in this system in the Faraday geometry are shown in Figure 2.9. In the figure, and the rest of this thesis $|\uparrow\downarrow\rangle$ is to be interpreted as the spin singlet $(|\uparrow\downarrow\rangle - |\downarrow\uparrow\rangle)/\sqrt{2}$.

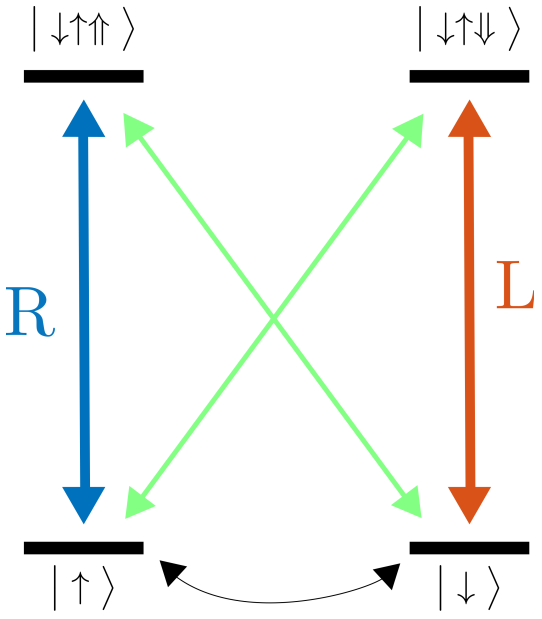

FIGURE 2.9: The transitions between the two ground state and the allowed excited states in the Faraday geometry. Allowed transitions are shown by the coloured arrows labelled by the polarisation of the photon that mediates them. Transitions which are forbidden by the selection rules are shown by the green arrows. The thin black arrows show the presence of ground state mixing due to coupling with the solid state environment.

The blue and red arrows show the optical transitions allowed by the selection rules. The green arrows show transitions which are forbidden by the selection rules. They can take place due to a magnetic field misaligned with the growth axis, mixing of the light and heavy hole states, or interaction with nuclear spins of the lattice. The black arrow shows mixing of the ground state which can occur due to several processes described later.

In the Voigt geometry the ground and excited states change to be linear super-positions of the states in the Faraday geometry. The selection rules change to those shown in Figure 2.10.

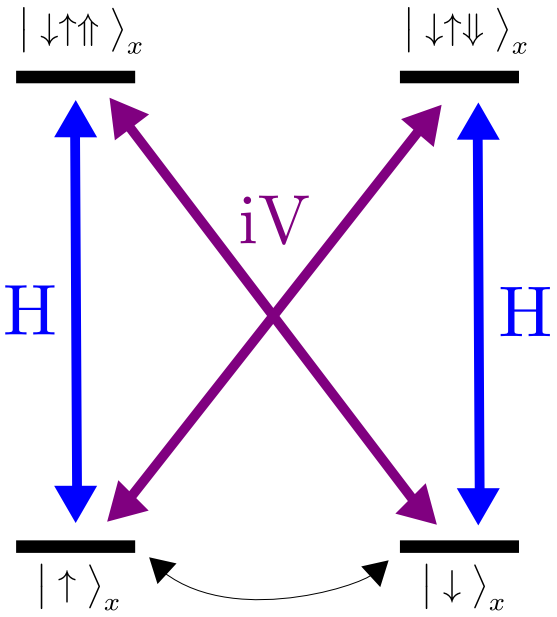

FIGURE 2.10: The transitions between the two ground state and the allowed excited states in the Voigt geometry. Allowed transitions are shown by the coloured arrows labelled by the polarisation of the photon that mediates them. The thin black arrows show the presence of ground state mixing due to coupling with the solid state environment.

The blue and purple arrows show the transitions which are allowed by the selection rules for the new spin eigenstates. The black arrow indicates that the ground states can again be mixed. In addition to the spin-selective absorption [60, 65] there are additional Coulomb energies in a charged exciton system due to there being a greater number of charged particles. These red-shift the X_{1-} transitions and blue shift the X_{1+} transitions [66].

2.5 Electron spin qubits

Fundamental material properties combined with clever device structures have enabled isolation of individual carriers. For the spin to be used as a qubit, methods are required to initialise, manipulate and readout its state. The optical transitions derived previously enable several different methods of doing so. Some of the most commonly used are described below.

2.5.1 Initialisation

The spin of an electron tunnelling into an empty dot from a dopant or the back contact will not in general be polarised. Spin-pumping is a fast way of initialising the electron into a spin eigenstate. In the following, electrons are referred to though many of the schemes also apply to holes.

Spin pumping in the Faraday geometry

The ground state of the X_{1-} system contains a single electron. A magnetic field in the Faraday geometry splits the ground states by an energy Δ_g. The excited states contain a pair of electrons which form a spin zero singlet so the Zeeman splitting Δ_e is only due to the hole. This spin state of the ground state electron can be prepared by spin pumping as shown in Figure 2.11.

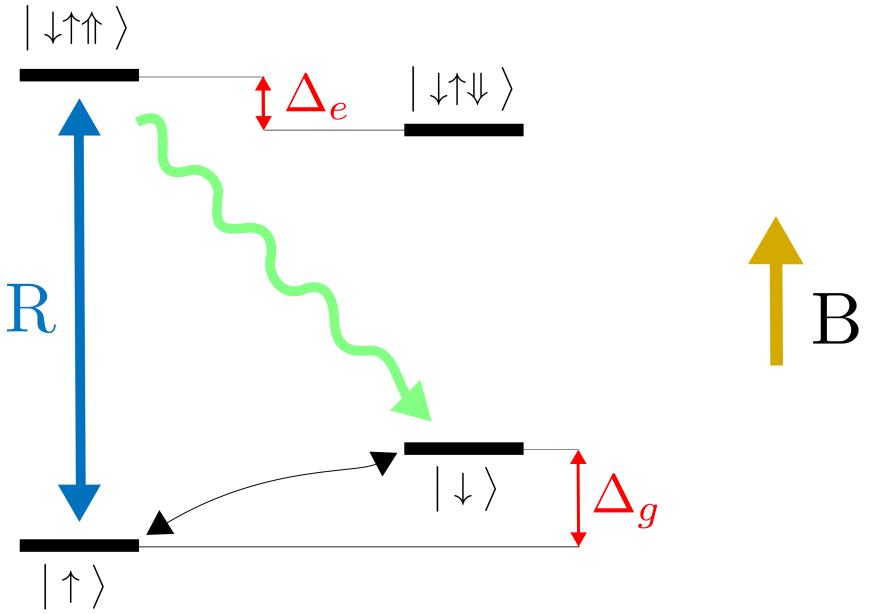

FIGURE 2.11: Spin pumping in the Faraday geometry. A magnetic field (yellow arrow) splits the energy of the ground and excited states by Δ_g and Δ_e respectively. When driving the transition from $|\uparrow\rangle$ (blue arrow) the system can relax via a forbidden diagonal transition (green arrow) to the $|\downarrow\rangle$ state where it is decoupled from the laser and shelved. Interaction with the environment can relax the spin from $|\downarrow\rangle$ to $|\uparrow\rangle$ (small black arrows).

In this process the ground state $|\uparrow\rangle$ is excited to $|\downarrow\uparrow\Uparrow\rangle$ by an R polarised laser (blue arrow). The most likely next step is for the exciton to recombine and the system to decay back down to the state $|\uparrow\rangle$. However there is a chance that the system will decay via the forbidden transition (green arrow). The rate of this forbidden transition is around 3 orders of magnitude less than the allowed transition, but it will occur eventually if the electron is continually excited. When it does the electron will end up in the state $|\downarrow\rangle$ and is then decoupled from the driving laser. If there is no, or a very weak magnetic field, the electron spin can be flipped from $|\uparrow\rangle \leftrightarrow |\downarrow\rangle$ by interaction with nuclear spins or by flipping its spin with an electron in the back contact. When a magnetic field is applied, both the electron and nuclear energy levels are split by the Zeeman effect. The nuclear Zeeman splitting is on the order of 2000 times smaller than the electron splitting and this detuning suppresses the nuclear spin flip (in the same way that an optical transition is driven less strongly when the driving laser is detuned) [67]. The electron spin has been initialised into the state $|\downarrow\rangle$. Atatüre *et al.* were able to achieve 99.8% initialisation fidelity using this method at a field of 300 mT, with a initialisation rate of 300 kHz or equivalent time-scale of around 3.3 μs [28, 68].

Spin pumping in the Voigt geometry

The same principle can be employed in the Voigt geometry [69]. In this case the allowed transitions are different since the spin eigenstates are not those that the optical field couples to. The spin pumping process is shown in Figure 2.12.

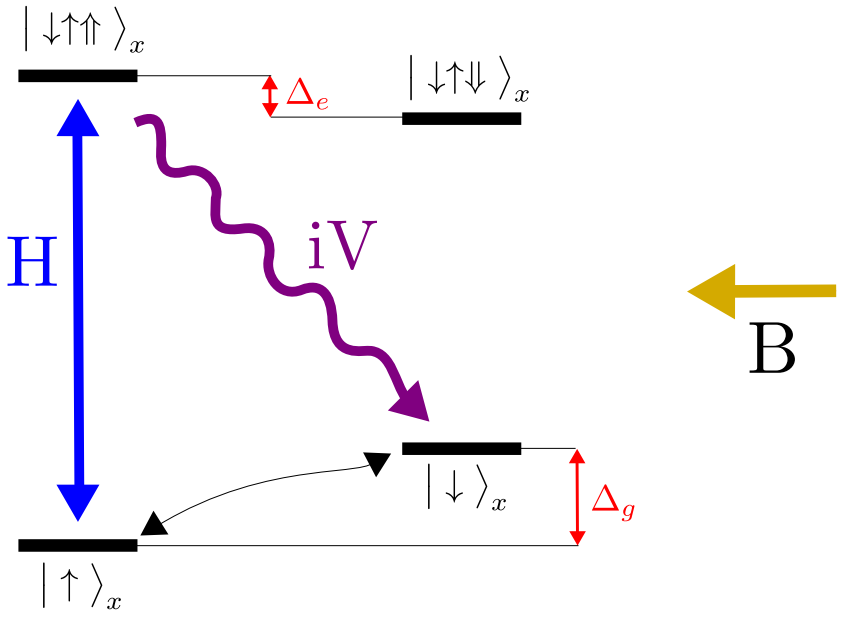

FIGURE 2.12: Spin pumping in the Voigt geometry. A magnetic field (yellow arrow) splits the energy of the ground and excited states by Δ_g and Δ_e respectively. When driving the transition from $|\uparrow\rangle_x$ (blue arrow) the system can relax via the allowed diagonal transition (purple arrow) to the $|\downarrow\rangle_x$ where it is decoupled from the laser and shelved. Interaction with the environment can relax the spin from $|\downarrow\rangle_x$ to $|\uparrow\rangle_x$ (small black arrows).

In this process the ground state $|\uparrow\rangle_x$ is excited to $|\downarrow\uparrow\Uparrow\rangle_x$ by an H polarised laser (blue arrow). The system can now decay back down the blue arrow to the $|\uparrow\rangle_x$ state or down the purple arrow to the $|\downarrow\rangle_x$ state. If the system relaxes down the purple arrow to $|\downarrow\rangle_x$ then it becomes decoupled from the laser and so the spin remains shelved in the $|\downarrow\rangle_x$ state. The spin has been pumped into the $|\downarrow\rangle_x$ state. Interaction with nuclear spins can again cause the spin to mix between $|\uparrow\rangle_x \leftrightarrow |\downarrow\rangle_x$. Since this scheme relies on only optically allowed transitions it is expected to operate a lot faster. Indeed Xu *et al.* achieved spin initialisation with a fidelity of $98.9 \pm 0.4\%$ at a field of 880 mT, with an initialisation rate of 500 MHz or equivalent time-scale of 2 ns [68]. The field strength used here is larger than in the experiment by Atatüre *et al.*, likely to overcome

an observed gate voltage dependent g-factor, and allow separate addressing of the two Λ schemes in the Voigt system.

2.5.2 Manipulation

Single qubit gates or rotations are one of the necessary components for universal quantum computing. Once an electron has been trapped and initialised, several methods are available to achieve rotations of the spin.

Precession in a field

Just as a gyroscope precesses around its weight vector due to gravity, a magnetic moment will precess around an external magnetic field, the well known Larmour precession. This can be used in a quantum dot to cause precession of the electron spin. The Hamiltonian for the interaction of a spin-1/2 particle and a magnetic field is in general given by $H = -\mu_B g \mathbf{S} \cdot \mathbf{B}$, where μ_B is the Bohr magneton, $\mathbf{S}$ is the spin matrix and $\mathbf{B}$ is the magnetic field. g is the g-factor of the spin which is a dimensionless constant which governs the strength of the interaction of the spin with the magnetic field. If this is the only energy contribution then the time evolution in the Schrödinger picture is given by the operator

$$U = \exp\left(-\frac{it}{\hbar}\mu_B g \mathbf{S} \cdot \mathbf{B}\right) \tag{2.42}$$

For an electron with isotropic g-factor, this rotates the spin around the $\mathbf{B}$ axis by an angle that depends on the field strength, g-factor, and the time that the field is switched on for.

Electron spin resonance

A static field will split the $\left|\uparrow\right\rangle$ and $\left|\downarrow\right\rangle$ states by the Zeeman interaction. Since the $\left|\uparrow\right\rangle$ and $\left|\downarrow\right\rangle$ states have a different magnetic spin, transitions between them can be driven by a magnetic field perpendicular to the spin axis. To drive this transition strongly, the perpendicular field is modulated at the precession frequency (is resonant with the precession). Such a time-varying field can be generated by a current in a nearby nearby low impedance coil [70], or coplanar strip line fabricated above the sample [71, 72]. At

typically achievable magnetic fields the energy difference between these levels (due to the static field) is in the microwave range. The perpendicular field couples the $|\uparrow\rangle$ and $|\downarrow\rangle$ levels in the same way as the Pauli x or y matrices depending on the phase, and so generates rotations of the qubit. By initialising the electron spin and rotating it by different angles the rotation of the electron can be directly observed in electron spin resonance experiments [70].

Raman transitions and coherent population trapping

Both precession around a magnetic field and electron spin resonance allow rotations on the order of a μs. This is rather slow in the context of the radiative lifetime of excitons in the quantum dot and the electron coherence time. A much faster method uses Raman transitions to perform rotations. A Raman transition can occur in a Λ type system of three levels as shown in Figure 2.13.

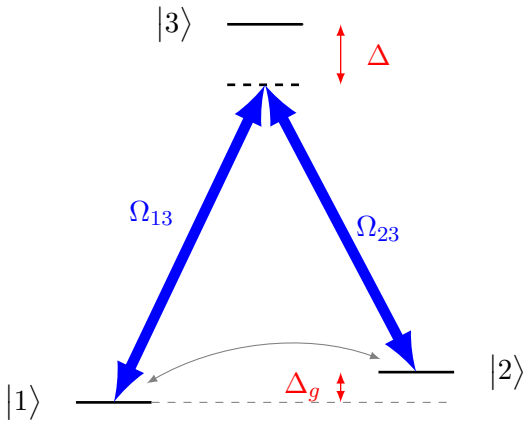

FIGURE 2.13: A level scheme allowing a Raman transition between the ground states $|1\rangle$ and $|2\rangle$ via the shared excited state $|3\rangle$. Two lasers drive transitions with Rabi frequencies Ω_{13} and Ω_{23} but are detuned from the excited state by Δ. The ground states are split by energy Δ_g.

States $|1\rangle$ and $|2\rangle$ represent the ground states to rotate between, and $|3\rangle$ is a shared excited state that can be reached by both ground states. The blue arrows show the energy two lasers which are tuned to a virtual energy state Δ below $|3\rangle$. Consider this system with zero detuning ($\Delta = 0$). If only transition Ω_{13} is driven, population is moved from level $|1\rangle$ to level $|3\rangle$ which can then decay back to $|1\rangle$ or to $|2\rangle$. A similar process occurs when transition Ω_{23} is driven. With both lasers on and detuned from the transition energy by $\Delta > 0$ the two interaction terms now interfere [73] and

with sufficiently large Δ, population is transferred between the ground states without populating the excited state. In this situation the shared excited state $|3\rangle$ can be ignored, and the two ground states $|1\rangle$ and $|2\rangle$ are coupled by an effective field with effective Rabi frequency $\Omega_{\text{eff}} = |\Omega_{13}|\,|\Omega_{23}|\,/2\,|\Delta|$ [74].

A related phenomenon is coherent population trapping (CPT) which also occurs in a 3-level system. In this case strong laser fields re-diagonalise the system Hamiltonian to give new eigenstates which are mixtures of the ground and excited states[2]. When the two lasers are exactly resonant with the transitions, two of the new eigenstates are combinations of the ground states only [75]. Of these two states only one couples to the laser fields. The other, again due to quantum interference, is not coupled and so is a *dark* state. This dark state is

$$|\psi_{\text{dark}}\rangle = \frac{1}{\sqrt{|\Omega_{13}|^2 + |\Omega_{23}|^2}}\Big[\Omega_{13}|1\rangle - \Omega_{23}|2\rangle\Big] \tag{2.43}$$

where Ω_{13} and Ω_{23} are the (complex) Rabi frequencies of those transitions. The system will spontaneously decay from the excited state to the dark state. Since the laser field does not couple to $|\psi_{\text{dark}}\rangle$ and there is no excited state component to decay, the system will be shelved in the dark state. Notice that the $|\psi_{\text{dark}}\rangle$ can be externally controlled by varying the relative amplitude and phase of the lasers driving the transitions.

This is exploited in the control method of Economu and Reinecke [76] where one Λ scheme is selected from the Voigt system of Figure 2.10. Two phase locked laser pulses briefly re-diagonalise the system into the dark and light CPT states and the excitation gives the bright state a phase relative to the dark state. The effect after rotating back to the ground state system is that of a rotation about an axis which depends on the relative amplitude and phase of the Rabi frequencies, by an angle which depends on the pulse detuning, power and bandwidth. A similar approach was taken by Hansom *et al.* in InGaAs quantum dots where they used the small transverse component of the fluctuating Overhauser field to enable the Λ system of the Voigt geometry [45].

[2]The laser Rabi frequencies are large enough that the off-diagonal elements of the Hamiltonian dominate over the diagonal terms, causing the new eigenstates to be mixtures of the bare system eigenstates.

Fast optical pulses

Several methods have been described for rotating an optically active qubit. A strong magnetic field would suffice, but this is slow to control and a single field can only produce rotations around one axis. Directly driving transitions between the two states is also possible but again only allows rotations around one axis, and is relatively slow for electrons in quantum dots. Raman transitions are quite a lot faster but in the method above require laser fields at two frequencies to operate. Another related protocol has been implemented by Press *et al.* which again uses the two Λ systems of the Voigt geometry [77]. All 4 transitions are coupled to by a short broadband circularly polarised laser pulse which results in rotations of the spin around an equatorial axis. By combining spin pumping with the rotations induced by a magnetic field and fast optical pulses, they were able to demonstrate arbitrary single qubit rotations in under 40 ps. This has become the standard method of spin qubit control in these systems.

2.5.3 Readout

The initialisation procedures can double as readout schemes. Optical spin-pumping as described in Section 2.5.1 relies on the electron spin being driven into a 'dark' state (that does not couple to the driving laser) either due to polarisation, energy or both. Once shelved the system will no longer absorb light and so this loss of contrast can be interpreted as a measurement of the spin state [68, 78]. More generally, spin dependent resonance fluorescence allows the spin state to be probed [65, 77]. In this scheme, a laser is tuned and polarised such that it would excite a transition from one spin state in a quantum dot. After application of the pulse, if any spontaneous emission is observed the spin state has been projected into the ground state corresponding to that transition.

The initialisation and readout stages can be separated by using a tunnel coupled quantum dot system. One dot hosts the spin qubit, and the other is used to read out the spin's state. The scheme relies on having optical transitions in the readout dot that depend on the spin state of the electron in the qubit dot. This was demonstrated by Vamivakas *et al.* and used to show quantum jumps in the system [23]. The same system was used by Kim *et al.* but in addition a shared excited state provided a Λ scheme for qubit manipulation [79].

2.5.4 Decoherence

Using the methods above, the spin of an electron in a quantum dot can be prepared in the general state $\cos(\theta/2)\,|\uparrow\rangle + \sin(\theta/2)\,e^{i\phi}|\downarrow\rangle$, however it will not remain in that state indefinitely. There are many processes in the solid state system that will cause the state to change undesirably. The time scale on which the state changes is described by parameters T_1 and T_2 which describe the decay of an individual system. The time before θ is randomised to the equilibrium state is characterised by the longitudinal relaxation time T_1. The time before ϕ is randomised and any relative phase information in the system is lost is characterised by the transverse decoherence time T_2. Further apparent transverse decoherence is observed by the ensemble and/or non-stationary nature of measurements. This gives rise to a third characteristic time T_2^* over which the system appears to lose coherence. The reader is referred to the excellent analogy involving athletes and racetracks in Section 4.2 of [80] for an intuitive explanation of these times.

Co-tunnelling

In samples where the quantum dot layer is close to a highly doped back contact, carriers can tunnel from the Fermi sea of the back contact to the dot [22]. In addition a carrier in a dot can swap places with another carrier in the back contact in a co-tunnelling event [81]. These events are suppressed away from the edges of charging plateaus, but near the edge can be responsible for a decrease in T_1 times which can inhibit spin pumping [82, 83]. These events can change a bright exciton into a dark exciton through a flip of the electron spin [81]. This rate depends on the distance between the quantum dot and the back contact as well as the position of the quantum dot levels with respect to the Fermi level of the back contact [84]. In a sample with a 30 nm GaAs tunnel barrier between the reservoir and the dots showed a spin-flip co-tunnelling time of 1 ns [83].

Phonons

Electron spin relaxation due to direct coupling with phonons is reduced in quantum dots (compared to in bulk) due to the reduced dimensionality caused by quantum confinement [19, 20]. Phonons can induce local electric field fluctuations (through expansion and contraction of the lattice) which cannot on their own induce relaxation. The spin-orbit

interaction has a weak effect due to the large mismatch between the typical size of a quantum dot (10s of nanometres) with the spin-orbit length in GaAs ($l_{SO} \sim 1 - 10$ μm), however it does mix different spin states. The result is that phonons can now weakly couple different spin states leading to relaxation [21, 85]. For small magnetic fields single phonon process are weakened [86] and two-phonon relaxation processes become more important [87]. The T_1 time scales as B^{-5} from 170 ms at 1.75 T, to 120 μs at 14 T [21, 67]. At low temperatures if spin-phonon coupling were the only relaxation mechanism then T_2 would be equal to $2T_1$ [88]. However experiments have demonstrated that T_2 is orders of magnitude less than T_1 and so another mechanism must be at play. This mechanism is the hyperfine coupling with the nuclear spin ensemble which is discussed next.

2.6 Nuclear spins

In recent years it has been shown that the dominant decoherence mechanism for electrons in quantum dots is interaction with the lattice nuclei [89]. Nuclei couple to the electron spin through the hyperfine interaction. The dominant interaction between a nuclear spin I^j and electron spin S is the Fermi contact part of the interaction which can be written as

$$H_{hf}^j = \frac{\nu_0}{2} A^j \left|\psi\left(\mathbf{r}_j\right)\right|^2 \left(2I_z^j S_z + \left[I_+^j S_- + I_-^j S_+\right]\right) \tag{2.44}$$

where ν_0 is the volume of the unit cell, A^j is the hyperfine coupling constant, and $\psi\left(\mathbf{r}_j\right)$ is the electron envelope function at the position of the nucleus ($\mathbf{r}_j$). The quantum dot is made from $\sim 10^5$ atoms, each of which has a non-zero nuclear spin. The electron wavefunction extends over the whole quantum dot and so it interacts with all of them. The effect is that the electron feels an effective magnetic field called the Overhauser field

$$\mathbf{B}_N = \frac{\nu_0}{g_e \mu_B} \sum_j A^j \left|\psi\left(\mathbf{r}_j\right)\right|^2 \left\langle \mathbf{I}_j \right\rangle \tag{2.45}$$

In thermal equilibrium there is no net polarisation of the nuclear spins and so $\mathbf{B}_N$ fluctuates around 0 with an RMS noise value of $\delta\mathbf{B}_N \sim 20 - 40$ mT [90–92].

The Hyperfine interaction of the electron spin with each nuclear spin has a two-fold effect. The raising and lowering operators in (2.44) allow the electron spin to flip with a nuclear spin. This process limits the T_1 time to under 1 ns at zero field [93]. Application of a magnetic field along $\hat{\mathbf{z}}$ suppresses these flip-flops due to the difference in electron and nuclear Zeeman splitting, leading to an increase of T_1 above around 100 mT.

The $\hat{\mathbf{z}}$ component of the Overhauser field cannot be suppressed in this way since it still contributes to the precession of the electron. The total field along $\hat{\mathbf{z}}$ is a sum of the external field and the Overhauser field component which fluctuates randomly. In an ensemble measurement this means the electron spin in each quantum dot instantaneously feels a slightly different total field strength. Thus the Larmour frequencies are slightly different, yielding a T_2^* of several nano-seconds [18, 42]. Equally, in a repeated measurement, the Larmour frequencies will be slightly different for each experimental run [80]. The effect of low frequency Larmour noise can be rejected through the use of a Hahn echo pulse sequence [94]. Electron spin T_2 times of around 3 μs have been demonstrated at large magnetic fields [43]. Narrowing the nuclear distribution is one approach to reduce fluctuations and thus reduce the decoherence rate, for example by polarising the nuclei [91]. Éthier-Majcher *et al.* used CPT to narrow the nuclear distribution and extend T_2^* from 3.2 ± 0.1 ns to 39 ± 2 ns [47]. Nevertheless inhomogeneous decoherence in the nuclear spins themselves still limits the electron coherence time.

The nuclei also couple to the spin of holes in the dot, though the dominant coupling mechanism is a dipolar interaction rather than the Fermi contact term shown in (2.44). The coupling strength to the hole spin is around 0.1 times that of the electron and in the opposite direction. In addition the interaction is strongly anisotropic and varies from dot to dot [91].

2.6.1 Polarisation

The flip-flop terms in (2.44) allow for the exchange of angular momentum between the electron and nuclear spin. By continually repolarising the spin of an electron in a quantum dot, angular momentum is transferred to the nuclear ensemble. This can be done optically thanks to the selection rules described in Section 2.3. Continual pumping in this way can generate Overhauser fields of several Tesla. Tartakovskii *et al.*

demonstrated generation of large polarisations by non-resonant excitation of excitons above the confined states [95]. Photogenerated electrons and holes could then tunnel into the quantum dot states during which time the hole spin could flip, leading to the formation of both light ($\left|\downarrow\Uparrow\right\rangle$, $\left|\uparrow\Downarrow\right\rangle$) and dark ($\left|\uparrow\Uparrow\right\rangle$, $\left|\downarrow\Downarrow\right\rangle$) excitons in the quantum dot. The former radiatively decay quickly. The dark excitons can decay via an intermediate state where the electron flips its spin with a nuclear spin, and it is these interactions which are responsible for the build-up of nuclear polarisation.

In general the electron-nuclear spin flip flop rate is reduced due to the large difference in Zeeman energies $g_e\mu_B/g_N\mu_N \approx 1000$ [91]. Flip-flops can still occur but the probability decreases quickly with increased field. Interaction of an electron in a quantum dot with electrons in the Fermi sea causes broadening of the energy levels. In the case of a small Zeeman splitting, this broadening increases the probability of a spin flip with a nucleus. So called co-tunnelling assisted spin-flips are important at low fields [96].

This energy barrier is overcome in a different way in an experiment by Chekhovich *et al.* in which a forbidden X^+ transition is driven in order to polarise the nuclear spins [97]. In a quantum dot confining holes, the transition $\left|\Downarrow\right\rangle \rightarrow \left|\Downarrow\Uparrow\uparrow\right\rangle$ is normally forbidden as it would involve the creation of a spin up electron and a spin up hole. It is allowed via a second order process involving a σ^+ photon where the electron spin is flipped with a nuclear spin to get to the allowed excited state. In this case the energy required by the flip is provided by the laser. They were able to generate Overhauser field of 1.5 T, corresponding to a nuclear ensemble polarisation of 65%.

Another method used to generate nuclear spin polarisation was demonstrated by Kloeffel *et al.* [98]. In this experiment an quantum dot is tuned so that its lowest level lies just above the Fermi-level of the Fermi sea of a heavily doped layer. Excitation with σ^+ light generates a neutral exciton $\left|\downarrow\Uparrow\right\rangle$. The Coulomb interaction of the electron and hole pushes the energy level below the Fermi sea which allows an $\left|\uparrow\right\rangle$ electron (with spin determined by the Pauli exclusion principle) to tunnel into the dot. The dot then contains an X_{1-} trion ($\left|\downarrow\uparrow\Uparrow\right\rangle$) whose electrons form a spin singlet which does not interact with the nuclear spins. After the radiative lifetime the X_{1-} recombines leaving the $\left|\uparrow\right\rangle$ electron behind. Without the hole's Coulomb attraction the electron is now higher in energy than the sea, and so tunnels out of the dot with time scale of around 10

ps. During that time it can flip its spin with a nuclear spin as the short lifetime relaxes energy conservation [91].

2.6.2 Line dragging

One of the most striking effects of nuclear polarisation is line dragging. The quantum dot transition energy depends on the microscopic state of the nuclear spins, and so a flip of one nuclear spin can shift the transition energy. A nuclear spin can flip through via non-collinear component of the Hyperfine interaction which arises due to quadrupolar fields (described later) [91]. As a result, when the laser is detuned slightly from the current transition energy, it becomes resonant with a transition from the ground state to an excited state with one nuclear spin flipped. Thus the system is excited to this new excited state, accompanied by a flip of a nuclear spin. Depending on the spin of the electron in the excited state, this feedback acts to either 'drag' the transition towards resonance with the laser, or 'push' it away from resonance [99–101]. The result is a strong departure from the typical Lorentzian line shape shown in Figure 2.14a, to a 'top-hat' profile shown in Figure 2.14b.

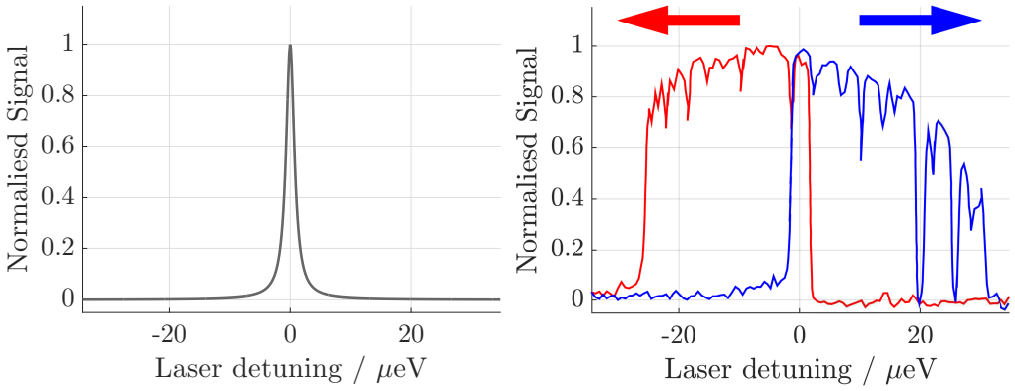

FIGURE 2.14: (a) the typical Lorentzian line-shape from a two level system (b) the observed line-shape when scanning a laser over the high energy Zeeman optical transition in a quantum dot at high magnetic field. The line is dragged by the laser when it is moved from low to high detuning (blue line) and from high to low detuning (red line). 'Normalised Signal' could be the photon count rate in a resonance fluorescence experiment, or the contrast in a differential transmission experiment. Adapted from [99]. The large dips in the blue line are not explained but could be caused by laser power fluctuations or mode-hops causing a sudden drop in then nuclear spin polarisation rate, causing the transition to become detuned.

The width of the top-hat profile is limited by the amount of nuclear spin polarisation that can be built up. This is determined by the rate of optical polarisation, versus the rate of depolarisation (either electron mediated spin diffusion within, and out of the dot, or electron mediated depolarisation due to co-tunnelling with the back contact) [102]. Dragging can be used to prepare Overhauser fields of up to 3 T [95, 100]. In general the movement of the quantum dot resonance caused by the Overhauser is known as the Overhauser shift.

2.6.3 Manipulation

The direction of the Overhauser field vector can be controlled as well as its strength. This was demonstrated by Makhonin *et al.* who used fast radio frequency pulses generated by a nearby coil, together with a strong static magnetic field to rotate an Overhauser field of 0.5 T [103]. They demonstrated that the field could be rotated to anywhere on the Bloch sphere. Through this method they extracted T_2^* and T_2 times of 16 ± 1 μs and 310 ± 30 μs respectively. These numbers conjure the idea of a long-lived qubit but note that the Overhauser field is a mesoscopic entity consisting of 10^4-10^5 nuclear spins (and so cannot be treated as a single two level system).

2.6.4 Quadrupolar effects

Strain and random positioning of the atomic species in the quantum dot give rise to local electric field gradients. The non-spherical charge distribution of the atomic nuclei with spin greater than one half generates an electric quadrupole which couples to the electric field gradients [91]. This causes the nuclear energy levels to split by an amount that depends on the nuclei's position in the dot [104]. Each nuclear spin feels therefore feels a different effective magnetic field, the quadrupolar field, which detunes them from one-another but also from the nuclei outside of the dot. This detuning allows nuclear polarisation to survive for up to 1 hour in empty quantum dots [102]. In the presence of a magnetic field this depolarisation time can rise to several hours [105] and even days [106]. The detuning also permits nuclear polarisation to exist at zero magnetic field [107, 108]. In the case of small external fields and a quantum dot filled with an odd number of electrons [102], the polarisation decays on a time scale of 10 ms [109]. The

depolarisation mechanism is spin flip-flops with unpaired resident electrons whose spin is randomised by co-tunnelling with the reservoir [91, 110].

Finally, the nuclei precess around the sum of any external magnetic field and the internal quadrupolar field. Since each nuclear spin feels a different quadrupolar field they precess at a different rate resulting in a broad noise spectrum of the Overhauser field. Because of the broad spectrum, the combined effects of the nuclei on the electron spin quickly become uncorrelated and can nolonger be reversed by, for example, refocussing pulses. This is the cause of the fast electron spin decoherence [111].

2.7 Coupled quantum dots

A single quantum dot can host a very promising spin qubit and provides mechanisms for interacting with it. Adding a second dot that is tunnel coupled to the first provides many more levels and transitions with which to design interesting schemes and experiments.

The strain effects that initially led to the self-assembly of quantum dots can be exploited to grow vertically aligned pairs of dots. When the first layer of dots is capped by a GaAs spacer layer, the strain field spreads through the spacer and dots growing in a wetting layer above will preferentially nucleate above those in the layer below [112]. This alignment is illustrated in Figure 2.15a. The same mechanism allows multiple layers of dots to be aligned as shown in the scanning electron microscope image in Figure 2.15b.

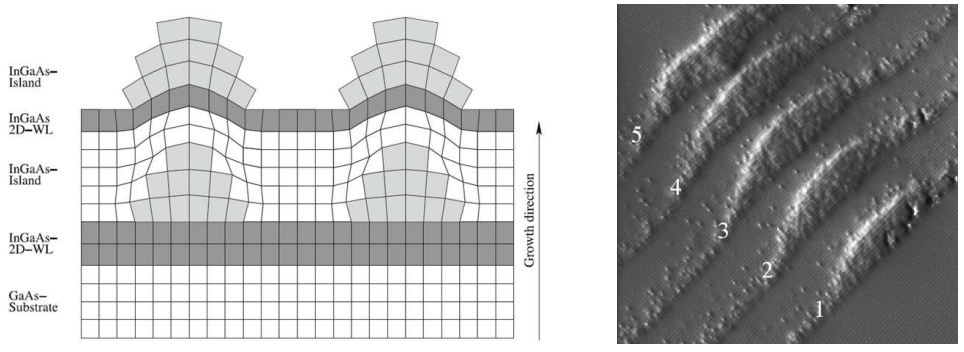

(a) (b)

FIGURE 2.15: (a) The strain field emanating from a quantum dot in one layer causes quantum dots in the layer above to align to it. Reproduced from [56] with permission. (b) Scanning electron microscope image of a sample cross-section containing 5 dots vertically aligned due to strain. Repoduced from [113] with permission.

If the barrier between two stacked dots is below around 20 nm [114], electrons [115] and holes [116] can coherently tunnel between them [114, 117]. The devices used in this thesis contain two layers of quantum dots, the majority of which are found in aligned pairs. They are grown inside a diode structure which allows tuning via the methods in Section 2.1.2. Because the upper and lower dots are at different distances from the contacts, the gate potential they feel is slightly different. In addition to the sequential charging and exciton Stark shift, changing the gate voltage shifts all of the levels in the bottom dot with respect to the top dot. The size and shape of each dot in the pair are random due to the growth process but dots in the layer above generally have lower emission energies than those in the first layer.

When each dot of a tunnel coupled pair contains a single electron the ground states hybridise into singlet and triplets when the single electron levels are tuned into resonance. The singlet and triplet form a qubit which at a particular gate voltage (known as the 'sweet-spot') is first order insensitive to magnetic and electric field noise, since the net spin is zero and energy dispersion with respect to gate voltage is zero. This qubit exhibits an enhanced T_2^* from 32 ns possibly up to 2 μs [115]. Since the ground and excited states have a net charge of $-2e$, this charging state is called the X_{2-} .

The flexibility of the coupled dots is used several times in this thesis to solve various problems with both theoretical and experimental validation. Therefore, in the next chapter a detailed model is built to investigate the energy structure of coupled quantum dots. The model is built using single particle basis states. The ground and excited states are calculated for typical coupled quantum dot parameters, and the simulation results are connected to experiment by calculation of the transition energies. The model is validated by comparison to experimental data collected during the course of one of the experiments in Chapter 5.

Chapter 3

Simulating coupled quantum dot states

Chapter 2 introduced the basic physics in quantum dots and the optical transitions which can occur in them. In the last section the concept of tunnel coupled dots was introduced. There are many geometrical and electrostatic parameters in these systems that complicate the transitions and energy level structure. Figure 3.1 shows data collected from a photoluminescence experiment on one dot of a coupled pair. The lines in the plot originate from transitions between the bound states. Without a detailed model of the system it is impossible to fully understand these data.

This chapter develops a model for calculating the states and energies in a system of coupled quantum dots. On the one hand, this is necessary so that the data like the above can be understood. On the other, having these models facilitates the design of new experiments and schemes. The model is built for all charge configurations, X_0 (where the quantum dot ground state is empty) to X_{3-} (where the ground state contains thee electrons) but only the X_{1-} (where the ground state contains one electron) is shown since it demonstrates all of the concepts involved and is explicitly used later on in this thesis. Section 3.1 walks through building the model to calculate the ground state energies, introducing some basic concepts. Section 3.2 then does the same for the excited states. In Section 3.3 the results of the previous two sections are combined to calculate the optical transitions available in the system. Finally in Section 3.4 the model is used

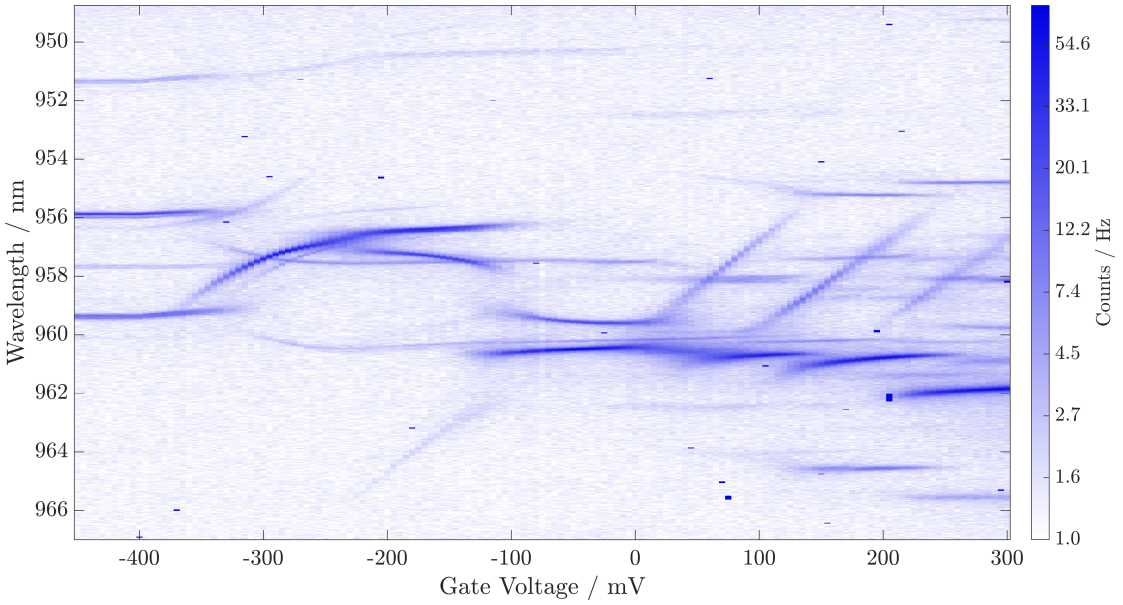

FIGURE 3.1: Data from a photoluminescence gate sweep experiment (described later in this thesis) which probes the optical transitions in quantum dots.

to predict and fit to some experimentally collected data to extract important physical parameters.

3.1 Ground states

The ground state of the X_{1-} charge state contains a single electron. In a classical picture the electron is confined to either in dot L or R of the coupled pair as shown in Figure 3.2. Since the dots are at different distances from the gate and back contact, an electron in dot L will feel a different potential to the one in dot R. The potential energy of an electron in dot L is $-eV_{\text{Gate}}t_L/t_{\text{tot}}$ where e is the electronic charge and V_{Gate} is the voltage applied to the gate. t_L and t_{tot} are the distances from the back contact to the dot and the separation of the back contact and the gate respectively. Similarly the potential energy of an electron in dot R is equal to $-eV_{\text{Gate}}t_R/t_{\text{tot}}$.

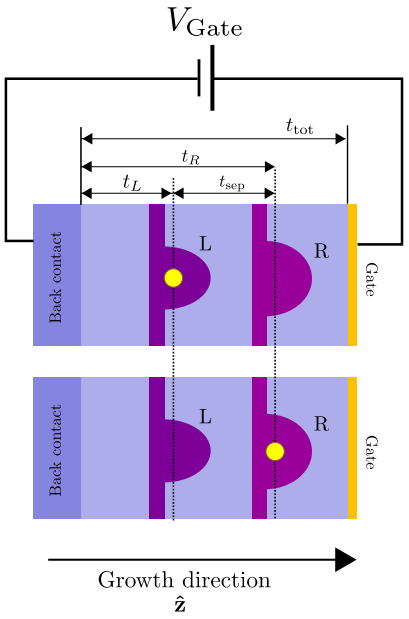

FIGURE 3.2: Schematic of a double quantum dot charged with a single electron (yellow circle) which can be either in dot L (top) or dot R (bottom). The device geometry that gives rise to the difference in potential energy for electrons in either dot is labelled.

In addition the confinement energies of the electron in either dot are E^L_{conf} and E^R_{conf} which are in general different. The total energy is a sum of the potential and confinement energies which is shown in Figure 3.3.

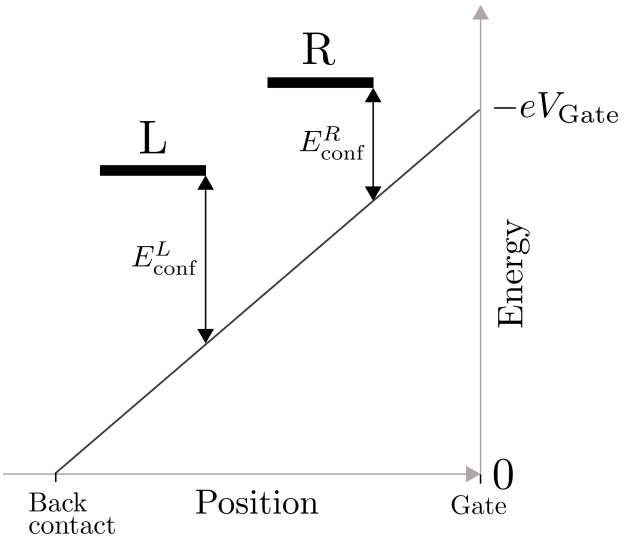

FIGURE 3.3: The single electron energy levels in dot L (L) and dot R (R) and their relation to the gate voltage V_{Gate}.

This picture can be simplified significantly by noting that the interesting behaviour and transitions in the system arise due to the differences in energy levels, not their absolute values. With this in mind the energy scale is shifted so that the energy at the position

of the electron in dot L is always zero[1]. In this case the new confinement energy of the electron in dot R is just equal to $-\,\mathrm{d}E = E^R_{\mathrm{conf}} - E^L_{\mathrm{conf}}$. The gate voltage dependence of the electron in dot R is then redefined as

$$\begin{aligned} E^R_{g,e} &= \left(-eV_{\mathrm{Gate}}\frac{t_R}{t_{\mathrm{tot}}}\right) - \left(-eV_{\mathrm{Gate}}\frac{t_L}{t_{\mathrm{tot}}}\right) \\ &= -eV_{\mathrm{Gate}}\frac{t_{\mathrm{sep}}}{t_{\mathrm{tot}}} \\ &= -eV_{\mathrm{Gate}}l \end{aligned} \tag{3.1}$$

where in the last line the lever arm $l = t_{\mathrm{sep}}/t_{\mathrm{tot}}$ has been introduced. By changing the gate voltage the detuning of the levels of dot L and R can be varied as shown in Figure 3.4.

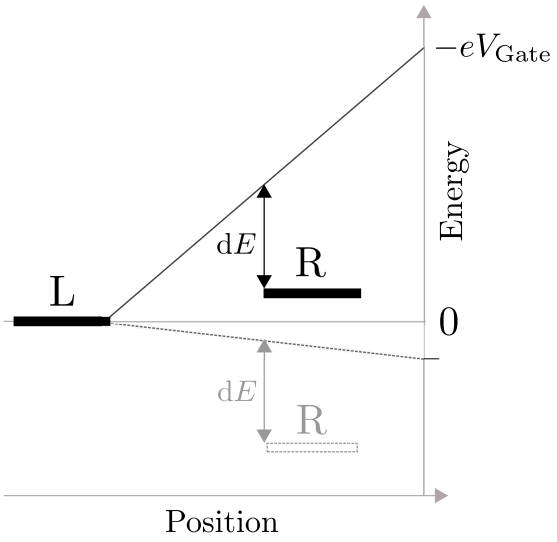

FIGURE 3.4: The single electron energy levels after renormalising the energy of dot L (L) to be zero. The energy level in dot R (R) is shown for two gate voltages V_{Gate} demonstrating how changing the voltage changes the detuning between the levels.

3.1.1 Building the model

Moving now to a quantum mechanical model, if the spin of the electron is included then the basis states of the system are

$$\left|\uparrow,0\right\rangle \quad , \quad \left|\downarrow,0\right\rangle \quad , \quad \left|0,\uparrow\right\rangle \quad \text{and} \quad \left|0,\downarrow\right\rangle \tag{3.2}$$

[1]This is just redefining where the zero of potential energy is. This is always allowed so long as it is applied consistently to all states of the system

where $\left|\uparrow,0\right\rangle$ for example means the electron is in dot L with spin up. The effects of confinement are included by a Hamiltonian which describes the energy of the eigenstates. This is given by

$$H_0 = -\,\mathrm{d}E\Big(\left|0,\uparrow\right\rangle\!\left\langle 0,\uparrow\right| + \left|0,\downarrow\right\rangle\!\left\langle 0,\downarrow\right|\Big) \tag{3.3}$$

which shifts the two states with the electron in dot R down by $\mathrm{d}E$. The change in energy with gate voltage is added through the Hamiltonian

$$H_V = E^R_{g,e}\Big(\left|0,\uparrow\right\rangle\!\left\langle 0,\uparrow\right| + \left|0,\downarrow\right\rangle\!\left\langle 0,\downarrow\right|\Big) \tag{3.4}$$

The coherent tunnelling of electrons between dots L and R is included through the Hamiltonian

$$H_t = t_e\Big(\left|0,\downarrow\right\rangle\!\left\langle\downarrow,0\right| + \left|0,\uparrow\right\rangle\!\left\langle\uparrow,0\right|\Big) + \text{H.c.} \tag{3.5}$$

where t_e is the electron tunnelling energy. Tunnelling becomes significant when t_{sep} is less than around 20 nm.

A magnetic field couples to the electron spin through the Zeeman Hamiltonian

$$H_B = \frac{1}{2}\mu_B\Big(g^L_e\sigma^L\cdot\mathbf{B}^L + g^R_e\sigma^R\cdot\mathbf{B}^R\Big) \tag{3.6}$$

where $\sigma^{L/R}$ are vectors of Pauli matrices acting on the spin in dots L/R, $g_e^{L/R}$ are the electron g-factors, and $\mathbf{B}^{L/R}$ is the magnetic field. This allows for any total magnetic field difference, due to for example, field inhomogeneities caused by the magnet used to apply an external field. Explicitly

$$\sigma_L = \begin{pmatrix} \left|\uparrow,0\right\rangle\!\left\langle\downarrow,0\right| + \left|\downarrow,0\right\rangle\!\left\langle\uparrow,0\right| \\ -i\left|\uparrow,0\right\rangle\!\left\langle\downarrow,0\right| + i\left|\downarrow,0\right\rangle\!\left\langle\uparrow,0\right| \\ \left|\uparrow,0\right\rangle\!\left\langle\uparrow,0\right| - \left|\downarrow,0\right\rangle\!\left\langle\downarrow,0\right| \end{pmatrix} \quad \sigma_R = \begin{pmatrix} \left|0,\uparrow\right\rangle\!\left\langle 0,\downarrow\right| + \left|0,\downarrow\right\rangle\!\left\langle 0,\uparrow\right| \\ -i\left|0,\uparrow\right\rangle\!\left\langle 0,\downarrow\right| + i\left|0,\downarrow\right\rangle\!\left\langle 0,\uparrow\right| \\ \left|0,\uparrow\right\rangle\!\left\langle 0,\uparrow\right| - \left|0,\downarrow\right\rangle\!\left\langle 0,\downarrow\right| \end{pmatrix} \tag{3.7}$$

The total Hamiltonian is the sum of all the previous parts

$$H_{\text{tot}} = H_0 + H_V + H_t + H_B \tag{3.8}$$

The energies and eigenstates of the system as a function of all of the above parameters can be found by diagonalising H_{tot}.

3.1.2 Gate sweep

Without tunnelling

To first demonstrate the behaviour of the system the tunnelling strength and magnetic field in each dot is set to zero. Figure 3.5 shows the energy levels of H_{tot} as a function of V_{Gate}. The parameters used to generate this, and subsequent plots are the ones extracted from the data set at the end of this chapter.

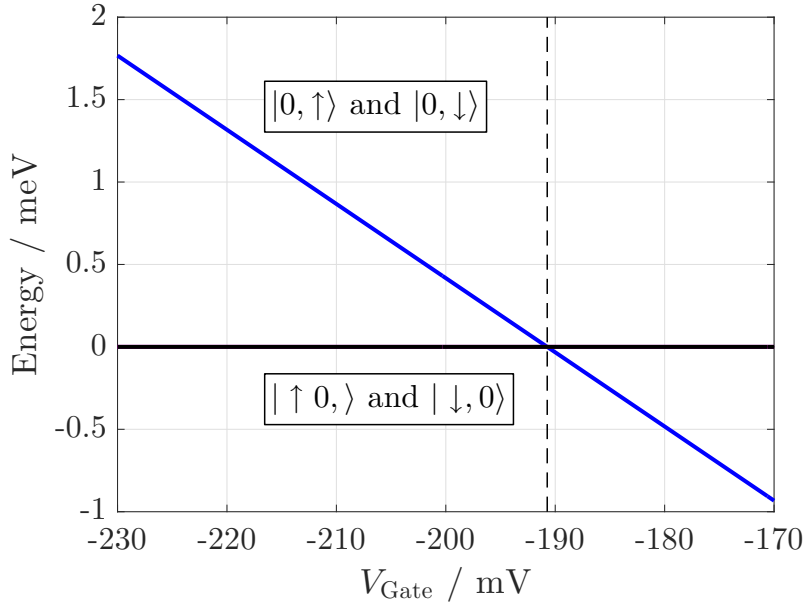

FIGURE 3.5: Ground state energy levels when sweeping the gate voltage, with no magnetic field or tunnelling.

Since there is no magnetic field both spin states in dot L and R are degenerate. The change potential energy due to the gate voltage causes the energy of the electron in dot R to shift. The electron energy levels in dot L and R become equal when the electric potential energy is equal to the difference in confinement energies. This happens when $V_{\text{Gate}} = -\,\mathrm{d}E/\,(el)$ which is shown by the dotted line in the figure. Since the two levels are not coupled they simply cross through each other and the states themselves are unaffected.

Adding a magnetic field in the Faraday geometry (along the growth direction) splits the spin states by different amounts as shown in Figure 3.6.

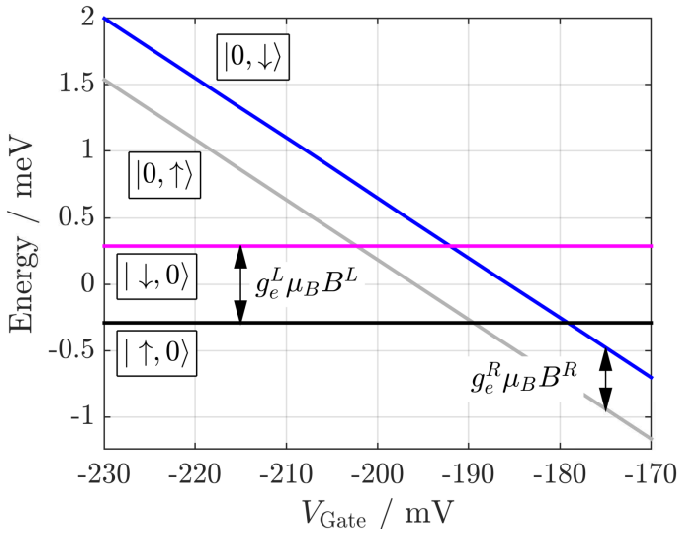

FIGURE 3.6: Energy levels in the presence of magnetic field in the Faraday geometry of strength B^R and B^L in dots R and L respectively.

A field in the growth direction ($\hat{\mathbf{z}}$) shifts the states but doesn't change them. Fields in the $\hat{\mathbf{x}}$ and $\hat{\mathbf{y}}$ direction mix the states as well as changing their energy. This isn't explored any further in this chapter but is used in Chapter 6.

With tunnelling

If electron tunnelling is now switched on by setting t_e to a non-zero value the energy levels anti-cross. An anti-crossing is the well known signature of a coupled system. The energy levels of the system are shown in Figure 3.7.

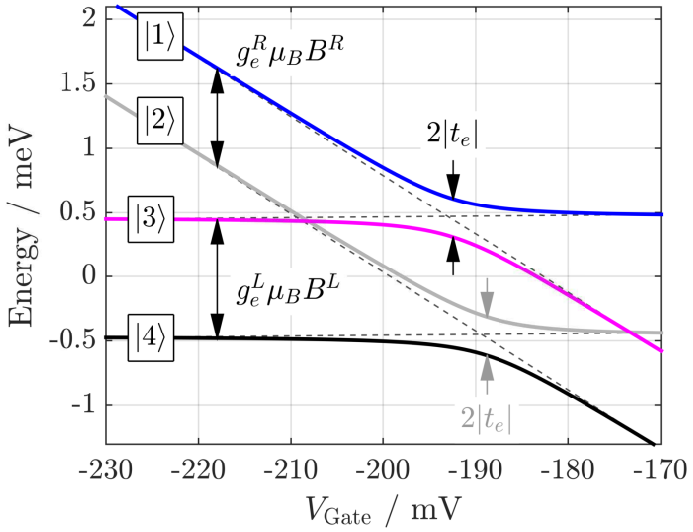

FIGURE 3.7: Energy levels in the the single electron coupled dot. A magnetic field is present in the Faraday geometry of strength B^R and B^L in dots R and L respectively. g_e^R and g_e^L are the electron g-factors in dots R and L. μ_B is the Bohr magneton. Electron tunnelling with strength t_e causes the levels to anti-cross.

At the anti-crossings the levels are separated by twice the magnitude of the tunnelling strength [118]. The coupling mixes the states so they can no longer be assigned labels like $|\uparrow,0\rangle$ and $|\downarrow,0\rangle$. Figure 3.8 shows the system's eigenstates at each voltage where the states are labelled $|1\rangle$ to $|4\rangle$.

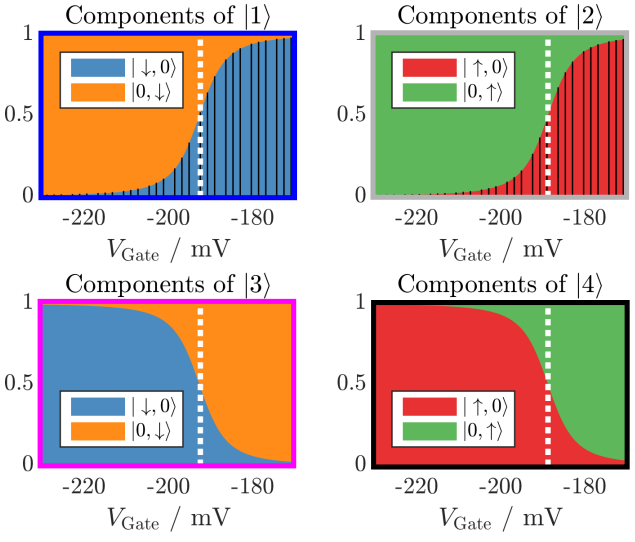

FIGURE 3.8: Eigenstates in the the single electron coupled dot. A magnetic field is present in the Faraday geometry. Electron tunnelling causes the states to mix. White lines show the position of the anti-crossings.

In this figure each coloured area represents a basis state of the system. At each gate

voltage, the size of each coloured area shows the magnitude of that basis component in the state. The black line shading on the state area plot indicates that that component has a sign of -1 with respect to the unshaded area. Far to the left, each eigenstate is a pure basis state. Moving to the right, the coupled basis state 'leaks' into the eigenstate, and far to the right the eigenstates have switched. At the positions of the anti-crossings the eigenstates are equal super-positions of each basis state so each state is half one colour and half another.

3.2 Excited states

An optical excitation will generate an additional electron and hole. The excited state of the X_{1-} is therefore a charged exciton containing two electrons and one hole. Now there are six possible arrangements of the charge. The first three configurations have the hole in dot R and are labelled $(0, eeh)$, (e, eh) and (ee, h). The next three have the hole in dot L and are labelled (h, ee), (eh, e) and $(eeh, 0)$. These configurations are shown in Figure 3.9.

The potential energies of the electrons due to the gate voltage are the same as in Section 3.1. The potential energies of the holes are different since they sit at different positions to the electron as shown in Figure 3.10.

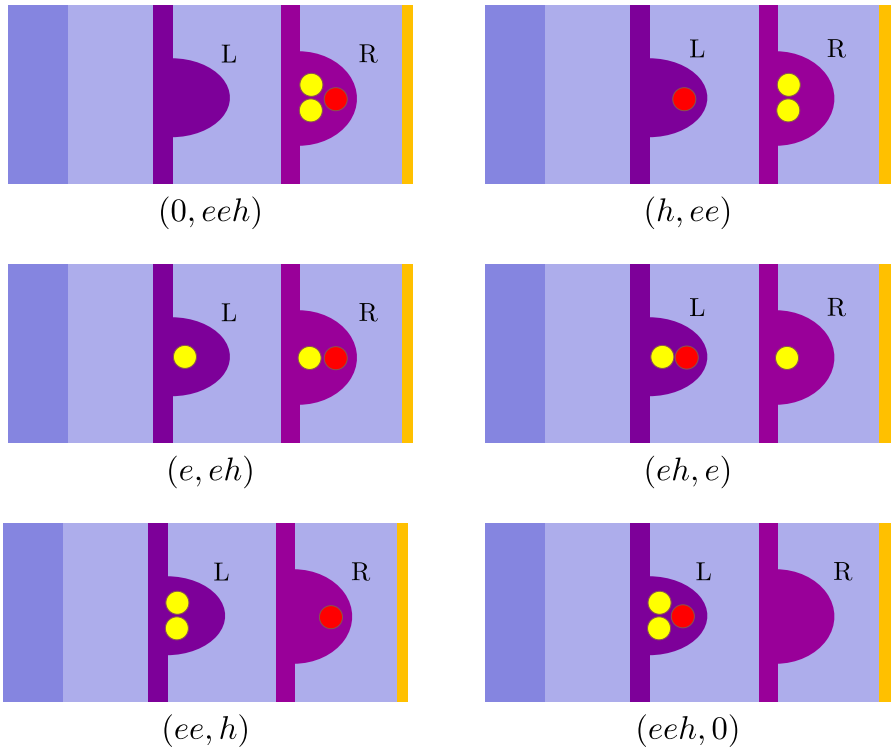

FIGURE 3.9: All possible configurations of the two electrons (yellow circles) and hole (red circle) in the X_{1-} system. The label given to each configuration is written underneath it.

From the diagram the electric potential energy of holes in dots L and R are $eV_{\text{Gate}}(t_L + d_L)/t_{\text{tot}}$ and $eV_{\text{Gate}}(t_R + d_R)/t_{\text{tot}}$ respectively where d_L and d_R are the separations that lead to the permanent exciton dipoles. Since the zero of potential energy was redefined to be at the position of the electron in dot L, the quantity $\left(eV_{\text{Gate}}\frac{t_L}{t_{\text{tot}}}\right)$ must be subtracted from the hole potential energies. The electrostatic energies of the holes in either dot are then

$$E^L_{g,h} = eV_{\text{Gate}}\delta^L \tag{3.9}$$

and

$$E^R_{g,h} = eV_{\text{Gate}}(l + \delta^R) \tag{3.10}$$

where l is the lever arm from before and $\delta^L = d_L/t_{\text{tot}}$ and $\delta^R = d_R/t_{\text{tot}}$ are parameters that control the exciton Stark shifts. The total gate dependence of the charge configurations in Figure 3.9 can then be found by simply summing the contributions from each electron and hole. For example the $(0, eeh)$ configuration contains two electrons and

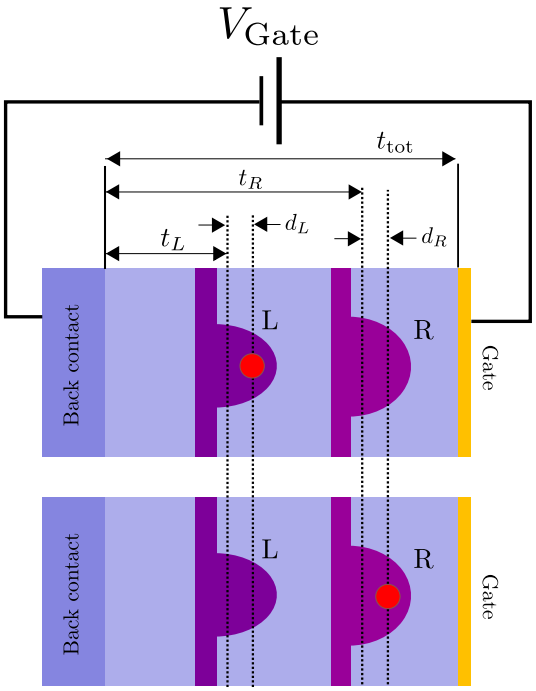

FIGURE 3.10: Schematic of a double quantum dot showing a single hole (red circle) which can be either in dot L (top) or dot R (bottom). The holes sit at different locations in the dot than the electrons (which sit at distances t_L and t_R from the back contact) due to differences in the dot chemistry.

one hole in dot R so the energy due to the gate potential is just $2E^R_{g,e} + E^R_{g,h}$. Similarly the (e, eh) configuration contains one electron in dot L, one electron in dot R and one hole in dot R so the total energy due to the gate potential is $E^R_{g,e} + E^R_{g,h}$. There is no contribution from the electron in L since the potential energy was defined to be zero.

The confinement energies of the electrons and holes in the excited system are not so easy to separate out since Coulomb interactions between the particles shift the electron and hole energies up and down. It is easiest to simply derive the energy of each charge configuration separately. To derive these energies it is easier to start from the simpler configurations of the neutral excitons which contain a single electron and single hole. The following demonstrates the process for deriving the energy of the $(0, eeh)$ configuration.

The neutral exciton in dot R has the configuration $(0, eh)$ shown in Figure 3.11. It is defined to have energy X^R_0 which includes contributions from quantum confinement, the material band-gap and the Coulomb interaction energy between the electron and hole. This energy can be directly measured through experiment and so is a fixed parameter of the model.

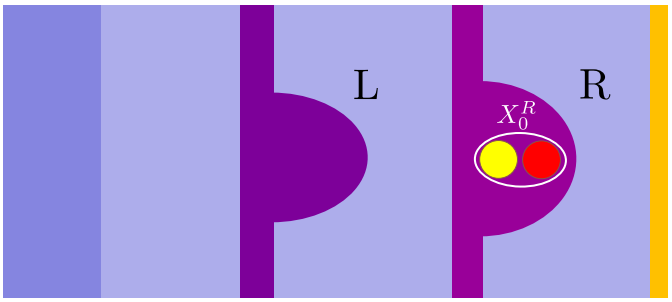

FIGURE 3.11: Charge configuration of the X_0 in dot R denoted $(0, eh)$. The electron and hole are shown as the yellow and red circle respectively. The energy of the configuration is shown in white.

To get from the $(0, eh)$ configuration to the $(0, eeh)$ configuration an electron is added in dot R. The system gains energy from the confinement of the new electron equal to $-\mathrm{d}E$, and the repulsion between the two electrons which is denoted by V_{ee}^{RR}. It also loses energy due to the attraction between the new electron and the hole which is denoted by V_{eh}^{RR}. The final energy of the $(0, eeh)$ configuration is thus

$$E_{(0,eeh)} = X_0^R + V_{ee}^{RR} - \mathrm{d}E - V_{eh}^{RR} \tag{3.11}$$

This new configuration is shown in Figure 3.12.

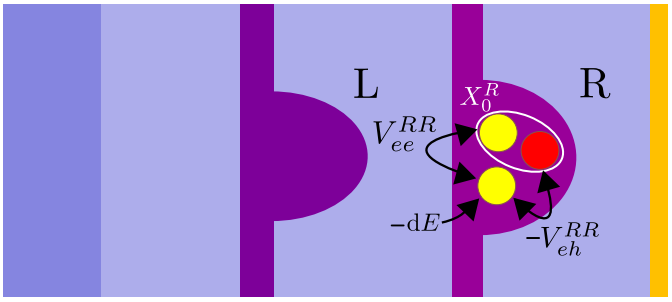

FIGURE 3.12: Charge configuration of the X_0 in dot R with an additional electron in dot R denoted (e, eh). The electrons and hole are shown as the yellow and red circles respectively. The additional energy contributions from the pair-wise Coulomb interactions with the new electron as well as the confinement energy are shown. The energy of the original X_0 configuration is shown in white.

Similar processes starting from the $(eh, 0)$ as well as the $(0, eh)$ configurations can be used to derive the energies for all six of the excited state configurations. Using these results a quantum mechanical description of the excited states can be built as it was for the ground states.

3.2.1 Building the model

In a quantum mechanical model including the spin of the electrons and holes, the system is described by 24 basis states. The first 12 are

$$\begin{array}{cccccc} |s\Uparrow,0\rangle & |\Uparrow,s\rangle & |\uparrow\Uparrow,\uparrow\rangle & |\uparrow\Uparrow,\downarrow\rangle & |\downarrow\Uparrow,\uparrow\rangle & |\downarrow\Uparrow,\downarrow\rangle \\ |s,\Uparrow\rangle & |0,s\Uparrow\rangle & |\uparrow,\uparrow\Uparrow\rangle & |\uparrow,\downarrow\Uparrow\rangle & |\downarrow,\uparrow\Uparrow\rangle & |\downarrow,\downarrow\Uparrow\rangle \end{array} \tag{3.12}$$

The other 12 states with hole spin down ($\Downarrow$) are not shown, but are also included in the calculation. Two electrons in the same quantum dot must have opposite spin since only the s-shell is considered, and thus must form a singlet state represented by the S (the triplet states involve a higher orbital level). The calculated energies of each charge configuration from confinement and Coulomb interaction between carriers is included through the Hamiltonian

$$\begin{aligned} H_0 = {} & E_{(e,eh)}\left(|\uparrow,\uparrow\Uparrow\rangle\langle\uparrow,\uparrow\Uparrow| + |\uparrow,\downarrow\Uparrow\rangle\langle\uparrow,\downarrow\Uparrow| + |\downarrow,\uparrow\Uparrow\rangle\langle\downarrow,\uparrow\Uparrow| + |\downarrow,\downarrow\Uparrow\rangle\langle\downarrow,\downarrow\Uparrow|\right) \\ & + E_{(eh,e)}\left(|\uparrow\Uparrow,\uparrow\rangle\langle\uparrow\Uparrow,\uparrow| + |\uparrow\Uparrow,\downarrow\rangle\langle\uparrow\Uparrow,\downarrow| + |\downarrow\Uparrow,\uparrow\rangle\langle\downarrow\Uparrow,\uparrow| + |\downarrow\Uparrow,\downarrow\rangle\langle\downarrow\Uparrow,\downarrow|\right) \\ & + E_{(0,eeh)}\left(|0,s\Uparrow\rangle\langle 0,s\Uparrow| + |0,s\Downarrow\rangle\langle 0,s\Downarrow|\right) \\ & + E_{(eeh,0)}\left(|s\Uparrow,0\rangle\langle s\Uparrow,0| + |s\Downarrow,0\rangle\langle s\Downarrow,0|\right) \\ & + E_{(ee,h)}\left(|s,\Uparrow\rangle\langle s,\Uparrow| + |s,\Downarrow\rangle\langle s,\Downarrow|\right) \\ & + E_{(h,ee)}\left(|\Uparrow,s\rangle\langle\Uparrow,s| + |\Downarrow,s\rangle\langle\Downarrow,s|\right) \end{aligned} \tag{3.13}$$

The electrostatic energy contribution from the gate voltage is included through the Hamiltonian

$$\begin{aligned} H_V = {} & E^R_{g,h}|s,\Uparrow\rangle\langle s,\Uparrow| \\ & + E^L_{g,h}|s\Uparrow,0\rangle\langle s\Uparrow,0| \\ & + \left(2E^R_{g,e} + E^R_{g,h}\right)|0,s\Uparrow\rangle\langle 0,s\Uparrow| \\ & + \left(2E^R_{g,e} + E^L_{g,h}\right)|\Uparrow,s\rangle\langle\Uparrow,s| \\ & + \left(E^R_{g,e} + E^R_{g,h}\right)|\alpha,\beta\Uparrow\rangle\langle\alpha,\beta\Uparrow| \\ & + \left(E^R_{g,e} + E^L_{g,h}\right)|\alpha\Uparrow,\beta\rangle\langle\alpha\Uparrow,\beta| \end{aligned} \tag{3.14}$$

where $\alpha, \beta = \{\uparrow, \downarrow\}$ represent all combinations of electron spin projection. There are an additional 6 terms where the hole is spin down ($\Downarrow$).

Tunnelling

Both the electrons and the holes can tunnel between dots L and R. Electron tunnelling is included through the Hamiltonian

$$H_{t_e} = t_e\Big(\big|s,\Uparrow \big\rangle\!\big\rangle \uparrow,\downarrow\Uparrow\big| - \big|s,\Uparrow \big\rangle\!\big\rangle \downarrow,\uparrow\Uparrow\big| + \big|0,s\Uparrow \big\rangle\!\big\rangle \uparrow,\downarrow\Uparrow\big| - \big|0,s\Uparrow \big\rangle\!\big\rangle \downarrow,\uparrow\Uparrow\big|\Big) + \text{H.c.} \tag{3.15}$$

$$+ \text{four similar terms for different hole configurations}$$

where the minus sign is due to the sign in the electron singlet. Hole tunnelling is represented by

$$\begin{aligned} H_{t_h} = t_h\Big(&\big|s,\Uparrow \big\rangle\!\big\rangle s\Uparrow,0\big| + \big|0,s\Uparrow \big\rangle\!\big\rangle \Uparrow,s\big| + \big|\uparrow,\uparrow\Uparrow \big\rangle\!\big\rangle \uparrow\Uparrow,\uparrow\big| + \\ &\big|\uparrow,\downarrow\Uparrow \big\rangle\!\big\rangle \uparrow\Uparrow,\downarrow\big| + \big|\downarrow,\uparrow\Uparrow \big\rangle\!\big\rangle \downarrow\Uparrow,\uparrow\big| + \big|\downarrow,\downarrow\Uparrow \big\rangle\!\big\rangle \downarrow\Uparrow,\downarrow\big|\Big) + \text{H.c.} \\ &+ \text{a similar term for hole spin down configurations} \end{aligned} \tag{3.16}$$

Magnetic field

A magnetic field is included through a Zeeman Hamiltonian similar to (3.7) but with one such term for each electron and hole. The Pauli matrices are built up in a similar way e.g. the Pauli X matrix for one electron is a sum of all outer product terms that would flip the spin of that electron. The electron g-factor is isotropic but the g-factor of the hole is not [119] and so the Zeeman Hamiltonian reads like

$$\begin{aligned} H_B = &\ 0.5\mu_B \sum_{i=1,2} \left(g^L_{e_i}\sigma^L_{e_i} \cdot \mathbf{B}^L + g^R_{e_i}\sigma^R_{e_i} \cdot \mathbf{B}^R\right) \\ &+ 0.5\mu_B \sum_{j=L,R} \left(g^j_{h,p}\left(\sigma^j_{h,X}B^j_x + \sigma^j_{h,Y}B^j_y\right) + g^j_{h,z}\sigma^j_{h,Z}B^j_z\right) \end{aligned} \tag{3.17}$$

where i runs over the two electrons, j runs over each quantum dot, $g_{h,p}$ is the in-plane g-factor of the hole (which is typically very small) and $g_{h,z}$ is the out-of-plane g-factor (treating the hole as a pseudo spin-1/2 particle).

Electron-hole exchange

The electron-hole exchange interaction outlined in Section 2.4.1 must also be included. The intra-dot electron-hole exchange (between electrons and holes in the same dot) is included through the Hamiltonian

$$
\begin{aligned}
H_{ex} =& \frac{1}{2}\delta_1^{RR}\Big(\left|\uparrow,\uparrow\Downarrow\right\rangle\!\!\left\langle\uparrow,\downarrow\Uparrow\right| \;+\; \left|\downarrow,\uparrow\Downarrow\right\rangle\!\!\left\langle\downarrow,\downarrow\Uparrow\right| \;+\text{H.c.}\Big) \\
&+ \frac{1}{2}\delta_2^{RR}\Big(\left|\uparrow,\downarrow\Downarrow\right\rangle\!\!\left\langle\uparrow,\uparrow\Uparrow\right| \;+\; \left|\downarrow,\downarrow\Downarrow\right\rangle\!\!\left\langle\downarrow,\uparrow\Uparrow\right| \;+\text{H.c.}\Big) \\
&+ \frac{1}{2}\delta_0^{RR}\Big(\left|\uparrow,\downarrow\Uparrow\right\rangle\!\!\left\langle\uparrow,\downarrow\Uparrow\right| \;+\; \left|\uparrow,\uparrow\Downarrow\right\rangle\!\!\left\langle\uparrow,\uparrow\Downarrow\right| \;+\; \left|\downarrow,\downarrow\Uparrow\right\rangle\!\!\left\langle\downarrow,\downarrow\Uparrow\right| \;+\; \left|\downarrow,\uparrow\Downarrow\right\rangle\!\!\left\langle\downarrow,\uparrow\Downarrow\right|\Big) \\
&- \frac{1}{2}\delta_0^{RR}\Big(\left|\uparrow,\uparrow\Uparrow\right\rangle\!\!\left\langle\uparrow,\uparrow\Uparrow\right| \;+\; \left|\uparrow,\downarrow\Downarrow\right\rangle\!\!\left\langle\uparrow,\downarrow\Downarrow\right| \;+\; \left|\downarrow,\uparrow\Uparrow\right\rangle\!\!\left\langle\downarrow,\uparrow\Uparrow\right| \;+\; \left|\downarrow,\downarrow\Downarrow\right\rangle\!\!\left\langle\downarrow,\downarrow\Downarrow\right|\Big) \\
&+ \;\text{four similar terms for the hole in the dot L with factors } \delta_1^{LL},\ \delta_2^{LL} \text{ and } \delta_0^{LL}
\end{aligned}
\tag{3.18}
$$

The terms proportional to δ_0^{RR} split the dark and bright exciton states, terms proportional to δ_1^{RR} mix the bright states, and terms proportional to δ_2^{RR} mix the dark states. Inter-dot exchange between electrons and holes in different dots is included with energies δ_0^{LR}, δ_1^{LR} δ_2^{LR} but the data show that this effect is negligible. There is also an exchange interaction between the two electrons but it is very small [116] and subsequent calculations match the data very well without it.

The total Hamiltonian is the sum of all of these terms

$$H_{\text{tot}} = H_0 + H_V + H_{t_e} + H_{t_h} + H_B + H_{ex} \tag{3.19}$$

3.2.2 Gate sweep

Without tunnelling

The Hamiltonian H_{tot} is again diagonalised to find its energy levels as a function of V_{Gate}. Figure 3.13 shows the energy levels when external fields, exchange splitting and tunnelling are all absent. Since nothing couples the states the eigenstates correspond exactly to the charge distributions.

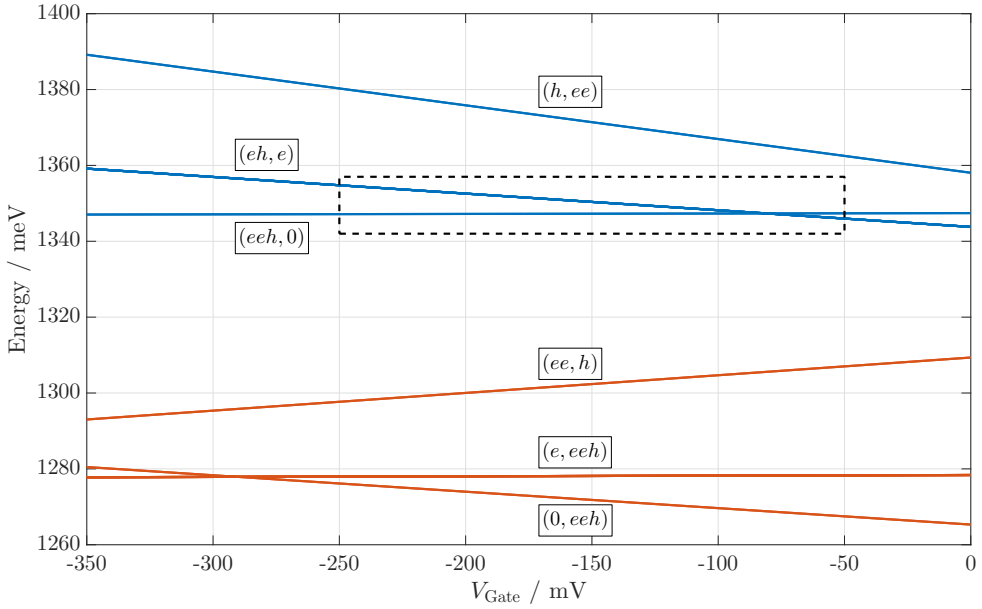

FIGURE 3.13: Excited state energy levels and states when sweeping the gate voltage, with no magnetic field or tunnelling. Because there is no tunnelling the states correspond exactly to different charge configurations.

The states are separated into two main bundles, those with the hole in dot L (blue lines) and those with the hole in dot R (red line). The bundles are split mainly by the difference in dot energy (the difference between X_0^L and X_0^R). Within each bundle there are 3 configurations where the two electrons are both in dot L, both in dot R, and one in each dot. The offset of each line is determined by the Coulomb interaction terms $E_{(ee,h)}$ etc. so these control where the crossings take place.

With tunnelling

Electron and hole tunnelling is now turned back on by setting t_e and t_h to non-zero values. This causes the levels to anti-cross as for the ground states. For example, the levels that crossed in the dashed box in Figure 3.13 now anti-cross as shown in Figure 3.14.

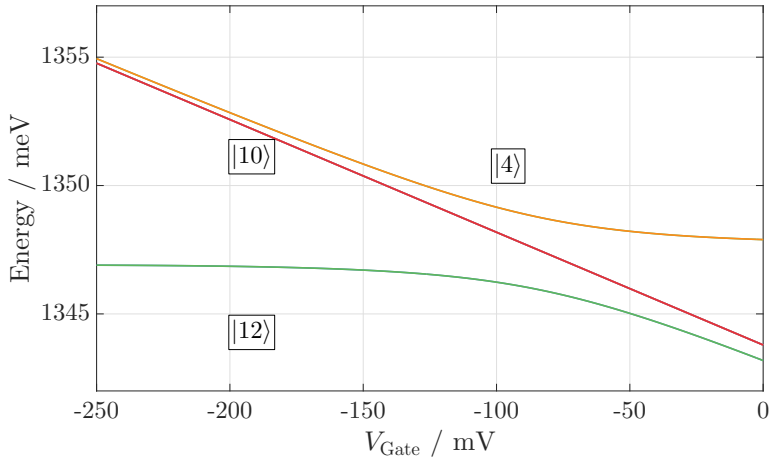

FIGURE 3.14: Excited state energy levels when sweeping the gate voltage with electron and hole tunnelling. The states that previously crossed in the dashed box in Figure 3.13 now anti-cross.

The reason for the anti-crossing can be seen by looking at the states themselves. States $|4\rangle$ and $|12\rangle$ are shown in Figure 3.15 where again the coloured areas show how much of each basis state is contained within each eigenstate.

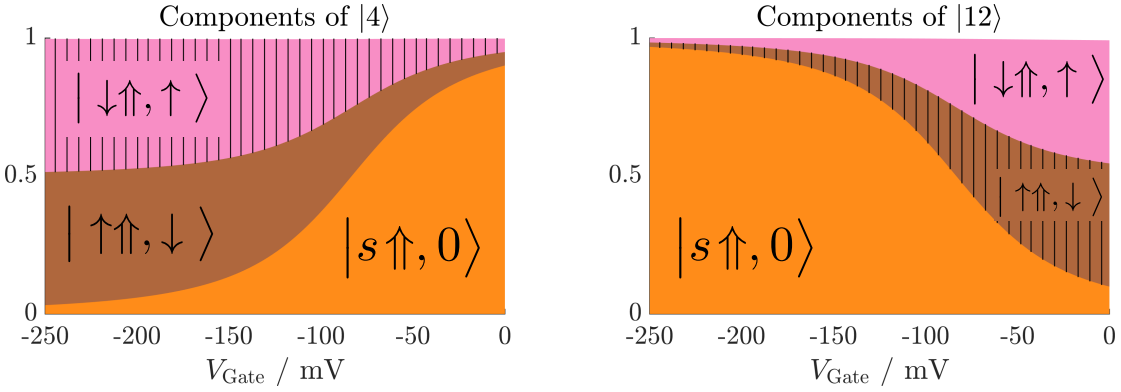

FIGURE 3.15: Excited state energy levels and states when sweeping the gate voltage, with no magnetic field or tunnelling.

It can be seen in the above figure that states $|4\rangle$ and $|12\rangle$ both contain the same basis vectors but the amount of each basis vector changes with gate voltage. All of the basis-vectors can be reached from each-other by electron tunnelling and so they become coupled together. This coupling is what causes the anti-crossing. Hole tunnelling also causes anti-crossings between states with the hole in dot L and R by the same mechanism. State $|10\rangle$ consists entirely of the basis state $|\downarrow\Uparrow,\downarrow\rangle$ which can't be reached by any of the basis states in $|4\rangle$ or $|12\rangle$ by tunnelling alone so it doesn't interact with the other eigenstates.

The exchange terms δ_1^{RR} cause anti crossings between states with bright excitons in dot R, such as between $\left|\uparrow,\downarrow\Uparrow\right\rangle$ and $\left|\uparrow,\uparrow\Downarrow\right\rangle$. The δ_1^{LL} exchange terms do the same for bright excitons in dot L. States with dark excitons in either dot also anti cross due to the δ_2^{RR} and δ_2^{LL} terms.

3.3 Transitions

3.3.1 Method of calculation

In an experiment where the quantum dot is optically excited, neither the ground nor excited energy levels are directly measured. Rather the difference between them is probed. The data shown in Figure 3.1 at the beginning of this chapter was generated by a photoluminescence (PL) gate sweep. This is typical characterisation experiment that involves photo-generating electrons and holes above the band gap which fall into the quantum dot and radiatively decay to the ground states. At each gate voltage a peak appears in the data at the difference in energy between the ground and excited states. The brightness of a point on the figure at wavelength λ and gate voltage V_g depends on two things: whether there is an excited state and ground state that differ in energy by $\hbar c/\lambda$ at the voltage V_g, and whether an optical transition between those states is allowed by the selection rules. The first can be easily calculated by diagonalising the ground and excited state Hamiltonians and calculating the energy difference between all pairs of ground and excited states. For the single electron system above there are $4 \times 24 = 96$ combinations so the possible transition energies in the system are

$$\Delta E_{i,j} = \sum_{\substack{i=1..24 \\ j=1..4}} E_{e,i} - E_{g,j} \tag{3.20}$$

where $E_{e/g,i}$ is the energy of the i^{th} excited/ground state.

If there exists a $\Delta E_{i,j} = \hbar c/\lambda$ the second constraint is met by looking at the corresponding excited and ground states $\left|i\right\rangle_e$ and $\left|j\right\rangle_g$. According to Section 2.3.2 an electric dipole transition is only possible if the momentum matrix element of the ground and excited state is non-zero. Using the same method as in Section 2.3 the strength and polarisation of the allowed transitions in the system can be derived. In general the ground and

excited states $\big|g\big\rangle$ and $\big|e\big\rangle$ are superpositions of all the basis states

$$\big|g\big\rangle = \alpha\big|0,\uparrow\big\rangle + \beta\big|0,\downarrow\big\rangle + \gamma\big|\uparrow,0\big\rangle + \delta\big|\downarrow,0\big\rangle \tag{3.21}$$

$$\begin{aligned}\big\langle e\big| = a^*\big\langle 0, s\Uparrow\big| + b^*\big\langle 0, s\Downarrow\big| + c^*\big\langle\uparrow,\uparrow\Downarrow\big| + d^*\big\langle\uparrow,\downarrow\Uparrow\big| + \\ e^*\big\langle\downarrow,\uparrow\Downarrow\big| + f^*\big\langle\downarrow,\downarrow\Uparrow\big| + g^*\big\langle s\Uparrow,0\big| + \dots\end{aligned} \tag{3.22}$$

where only some of the optically active excited states are included (those that could be reached by generation of a bright, direct exciton in one of the dots). The quantity of interest is

$$\begin{aligned}\langle e|\,\mathbf{p}\,|g\rangle =& a^*\alpha\,\langle 0, s\Uparrow|\,\mathbf{p}\,|0,\uparrow\rangle + b^*\beta\,\langle 0, s\Downarrow|\,\mathbf{p}\,|0,\downarrow\rangle + \\ & c^*\gamma\,\langle\uparrow,\uparrow\Downarrow|\,\mathbf{p}\,|\uparrow,0\rangle + d^*\gamma\,\langle\uparrow,\downarrow\Uparrow|\,\mathbf{p}\,|\uparrow,0\rangle + \\ & g^*\gamma\,\langle s\Uparrow,0|\,\mathbf{p}\,|\uparrow,0\rangle + \dots\end{aligned} \tag{3.23}$$

where those combinations that would evaluate to zero have been left out[2]. The orbital components of the hole wavefunctions give the matrix element vector different $\hat{\mathbf{x}}$ and $\hat{\mathbf{y}}$ components depending on the spin ((2.24)-(2.26)). This can be generalised for (3.23) by noting that all of the ground states have s character and all of the excited states involve raising a single valence electron to a conduction state. In this case each term contributes vector quantities like (2.26) depending on the spin involved. So (3.23) becomes

$$\begin{aligned}\langle e|\,\mathbf{p}\,|g\rangle =& \; a^*\alpha\,(-\hat{\mathbf{x}} + i\hat{\mathbf{y}}) + b^*\beta\,(\hat{\mathbf{x}} + i\hat{\mathbf{y}}) \\ & + c^*\gamma\,(\hat{\mathbf{x}} + i\hat{\mathbf{y}}) + d^*\gamma\,(-\hat{\mathbf{x}} + i\hat{\mathbf{y}}) \\ & + g^*\gamma\,(-\hat{\mathbf{x}} + i\hat{\mathbf{y}}) + \dots \\ =& \; (-a^*\alpha + b^*\beta + c^*\gamma - d^*\gamma - g^*\gamma + \dots)\,\hat{\mathbf{x}} \\ & + (a^*\alpha + b^*\beta + c^*\gamma + d^*\gamma + g^*\gamma + \dots)\,i\hat{\mathbf{y}}\end{aligned} \tag{3.24}$$

where a normalisation constant has been discarded which is the same for all states. By calculating (3.24) for all combinations of ground and excited states, the *relative* strength of the system's transitions can be found by taking the norm of the matrix element. The polarisation of the transitions can be determined from the vector quantity.

[2] i.e. ignore those transitions that include the generation of an exciton as well as tunnelling of the resident electron, for example from $\big|\uparrow,0\big\rangle$ to $\big|0,s\Uparrow\big\rangle$. The mixing of the ground and excited states ensures that transitions between eigenstates with these components are brightened appropriately.

Computationally this is done by building two rectangular matrices $\mathbf{M}_+$ and $\mathbf{M}_-$ which specify the allowed transitions between ground and excited states. The $\mathbf{M}_+$ matrix links ground basis states to excited basis states which contain a spin up hole ($\Uparrow$) and so describes the right-hand circularly polarised transitions. The $\mathbf{M}_-$ matrix does the same for those excited basis states that contain a spin down hole ($\Downarrow$) and so it describes the left-hand circularly polarised transitions. For example $\mathbf{M}_+$ is built of terms like $\left|s\Uparrow,0\right\rangle\!\!\left\langle \uparrow,0\right|$ such that when $\langle e|\,\mathbf{M}_+\,|g\rangle$ is calculated, terms like $\langle s\Uparrow,0|\,\mathbf{M}_+\,|\uparrow,0\rangle$ are non-zero. Similarly $\mathbf{M}_-$ is built of terms like $\left|s\Downarrow,0\right\rangle\!\!\left\langle \downarrow,0\right|$. All of the terms in (3.23) contribute a $+i\hat{\mathbf{y}}$ to the matrix element. Terms with a spin up hole contribute a $+\hat{\mathbf{x}}$ whilst terms with a spin down hole contribute a $-\hat{\mathbf{x}}$. The momentum matrix elements are then

$$\begin{aligned}\langle e|\,\mathbf{p}\,|p\rangle_x &= -\langle e|\,\mathbf{M}_+\,|g\rangle + \langle e|\,\mathbf{M}_-\,|g\rangle \\ \langle e|\,\mathbf{p}\,|p\rangle_y &= +i\,\langle e|\,\mathbf{M}_+\,|g\rangle + i\,\langle e|\,\mathbf{M}_-\,|g\rangle\end{aligned} \tag{3.25}$$

As in Section 2.3.2 these can be used to find the ideal polarisation for driving each transition, and equivalently the polarisation of the photon resulting from a radiative decay from $\left|e\right\rangle$ to $\left|g\right\rangle$.

To calculate the simulated PL gate sweep the above procedures are use to calculate the signal intensity at each position λ and V_g. The energy levels are convoluted with a Lorentzian of FWHM δ to take into account the fact that the transitions are not infinitely sharp but have some linewidth.

3.3.2 Gate sweep

Without tunnelling

The above method is used to calculate the transitions between the ground and excited states of the system. Figure 3.16a shows the energy of all the possible transitions in the system (all of the terms in (3.20)). Figure 3.16b shows a simulated photoluminescence (PL) gate sweep measurement using the same transitions with weights and broadening applied (20 pm broadening is applied to emulate the resolution of the spectrometer used for these measurements).

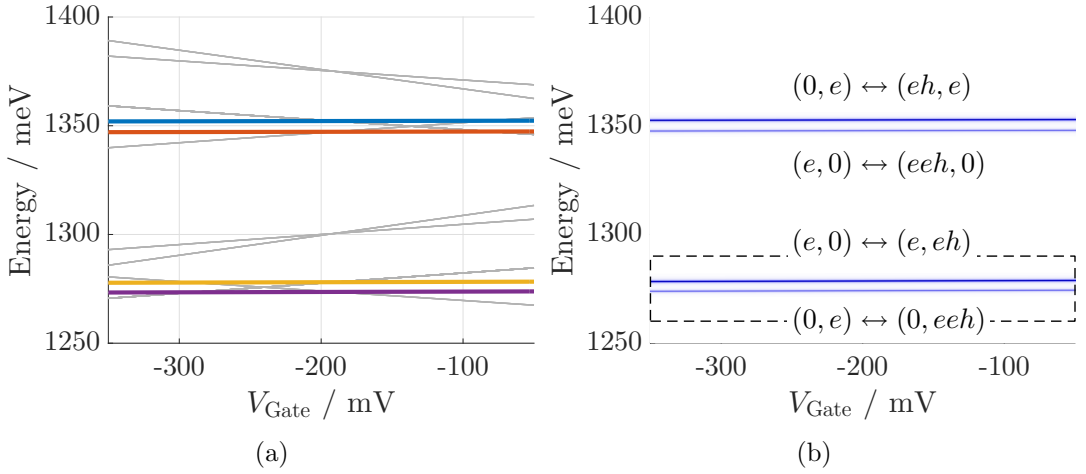

FIGURE 3.16: Transitions energies (a) between all ground and excited states in the 1 electron double dot when the dots are not tunnel coupled. Gray lines are forbidden by the selection rules and so only the coloured lines show up in the simulated photoluminescence data (b). Because there is no tunnelling the states correspond exactly to different charge configurations.

There are a total of 96 transition lines which again form two bunches corresponding to the hole residing in dot L or dot R. However the simulated data in Figure 3.16b shows that only some of these transitions are allowed. These are the ones in colour in Figure 3.16a. The gray lines show forbidden transitions which are either indirect (e.g. $\left|\downarrow,0\right\rangle \leftrightarrow \left|s,\Uparrow\right\rangle$) or involve a spin-flip of the electron or hole (e.g. $\left|\downarrow,0\right\rangle \leftrightarrow \left|s\Uparrow,0\right\rangle$). In a real system indirect transitions are allowed but have a low transition strength. The highest energy line in the spectrum comes from transitions from the $(0,e)$ ground states to the (eh,e) excited states of which four are allowed. Since both the ground and excited states have the same total charge distribution the line doesn't move with gate voltage (actually the line will move due to the exciton stark shift in dot L but this is too small to see in the figure). The next lowest line comes from transitions between ground states $(e,0)$ and excited states $(eeh,0)$. There are only two allowed transitions for these charge states and so the line is half the intensity.

The transitions from one of the ground states to the accessible excited states are shown in Figure 3.17. Because there is no tunnelling to mix the states, the system eigenstates are just the basis states. As a result each ground state is only coupled to three excited states and the transitions are circularly polarised.

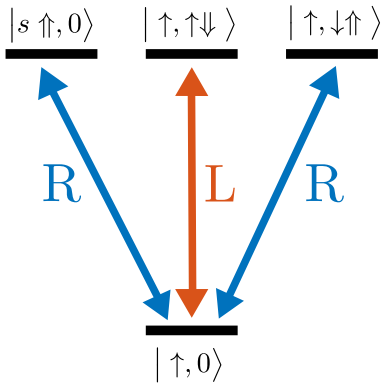

FIGURE 3.17: Transitions between one of the grounds and the optically accessible excited states in the one electron double dot with no tunnelling. The transitions are labelled by their polarisation (left (L) or right-hand (R) circularly polarised)

With tunnelling

Now the transitions are calculated again with the tunnelling turned on. The anti-crossings in the ground and excited states shown in the previous sections also cause anti-crossings at the same locations in the PL gate sweep. Figure 3.18 shows a simulated PL gate sweep in the region of the dashed rectangle in Figure 3.16b.

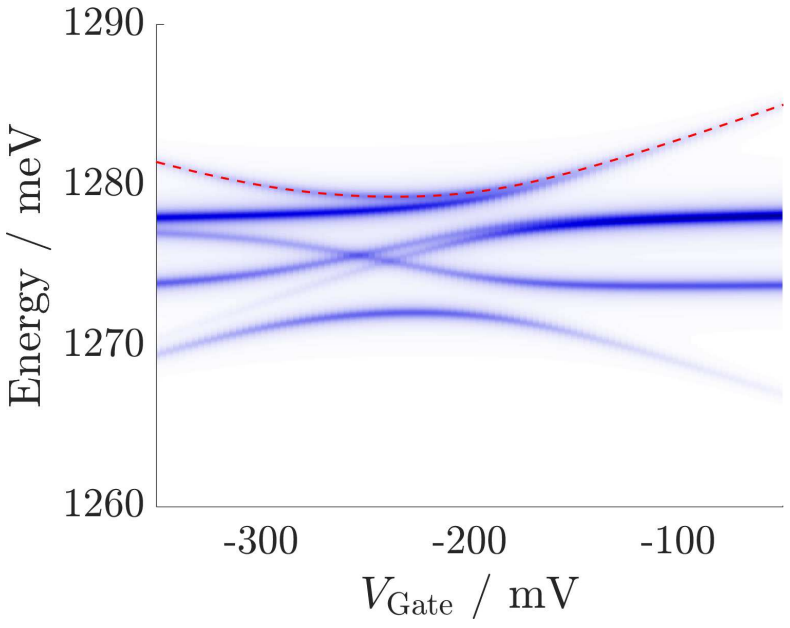

FIGURE 3.18: Simulated PL gate sweep in the 1 electron charged double dot in the presence of tunnel coupling. The mixing of states caused by the tunnelling lights up many previously forbidden transitions. The red line shows the energy of the transition between ground state $|2\rangle$ and excited state $|15\rangle$.

Now there are many more bright lines than just the two seen before. The reason for this is the mixing of the ground and excited states induced by the tunnel coupling. For example, Figure 3.19 shows the second ground state, and fifteenth excited state of the system, labelled $|2\rangle$ and $|15\rangle$ respectively. The energy of the transition between these two states is shown by the red line in Figure 3.18.

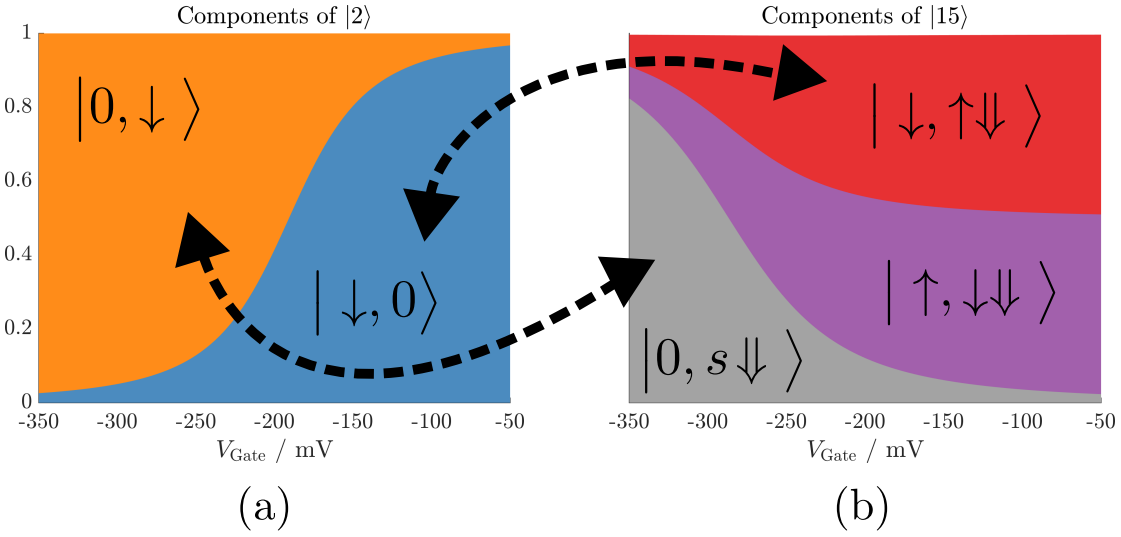

FIGURE 3.19: One of the ground states and excited states in the one electron charged coupled dot system. Tunnelling in the ground and excited states causes the basis states to mix together. The mixing causes previously forbidden transitions to become optically active. The black lines show basis states that can be reached from each other by optical excitations.

The excited state $|15\rangle$ contains components like $|\uparrow, \downarrow\Downarrow\rangle$ which are normally not accessible from the ground states via allowed transitions. However because this basis state is mixed in with other allowed states $|\downarrow, \uparrow\Downarrow\rangle$ and $|0, s\Downarrow\rangle$ which are accessible from the ground state components (as shown by the black arrows), optical transitions between states $|2\rangle$ and $|15\rangle$ are allowed.

3.4 Fitting to experimental data

A crucial first step in any experiment is to characterise the quantum dot by performing a PL gate sweep experiment. The model for the singly charged exciton system (X_{1-}) has been constructed above. In a PL experiment the gate is generally swept far enough that transitions involving the X_0 (where the ground state is empty), X_{2-} (where the ground state contains two electrons) and higher, will also be seen. Models for these charging

states and the transitions in them can be built and calculated in a similar way. A PL gate sweep of the dot used later in Chapter 5 with the transition energies calculated by the model is shown in Figure 3.20. Notice that many of the transition lines are not seen because they involved transitions that are forbidden.

The model contains many free parameters which must be carefully tuned so that the model fits the data. At first this seems a daunting task but some parameters can be extracted with ease and the remainder can be automatically optimised. The process used to derive the model parameters for the fit in Figure 3.20 is described below.

3.4.1 Parameter extraction

The process of fitting the PL gate sweep data begins by extracting some model parameters manually. These are described in the next sections.

Neutral exciton energies

The calculation of the excited state coulomb energies in Section 3.2.1 started from the neutral exciton energy X_0^R. The energies of the X_0 transitions are determined only by parameters X_0^R and X_0^L which can be read directly off of the PL date sweep data. The lines labelled 1. and 2. in 3.20 come from the X_0 transitions and lie at values X_0^R and X_0^L respectively. Values of 1352.61 meV and 1278.62 meV for X_0^L and X_0^R are found to give good agreement.

Electron tunnelling

In the data several anti-crossing are seen that arise from electron tunnelling between the dots. One of the most prominent is the one labelled 3. in the X_0 region of dot R which is due to electron tunnelling in the X_0 excited state. The separation of the lines at the anti-crossing is controlled by the tunnelling matrix element t_e and so its value can be estimated by comparing the experimental PL to rough plots of the simulated level scheme. In this case $t_e = 1.2$ meV is found to give good agreement.

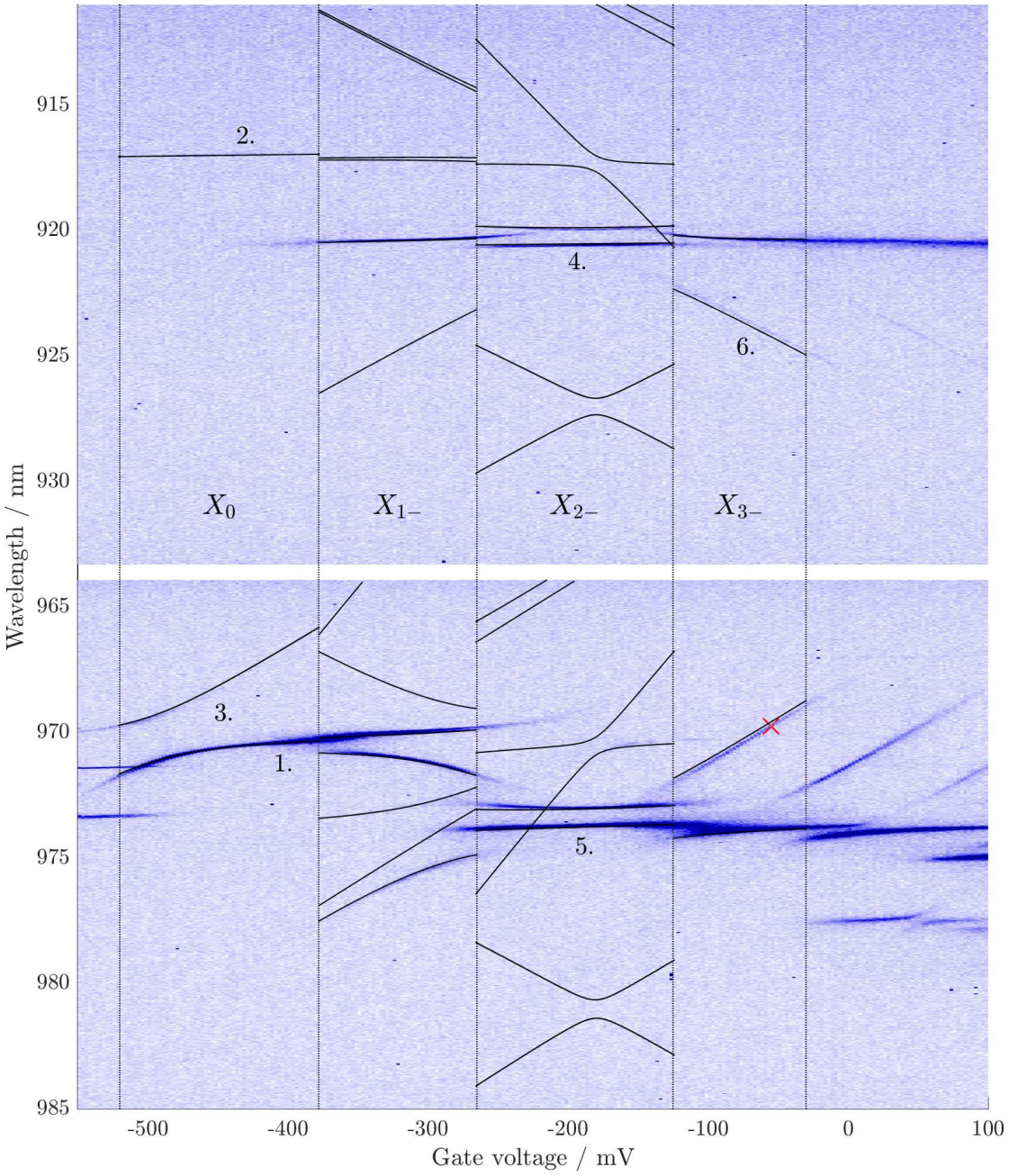

FIGURE 3.20: Photoluminescence gate sweep of the coupled quantum dot used in the experiments in Chapter 5. Black solid lines are the simulated energy levels that agree very well with the data. The regions that correspond to different charge states in the system are separated by dotted lines and each region is labelled according to its charge. Some transitions are numbered to be referred to in the main text. They correspond to: *1.* X_0 recombination in dot R. *2.* X_0 recombination in dot L. *3.* electron tunnelling in the X_0 excited state. *4.* X_{2-} recombination to the triplet state in dot L. *5.* X_{2-} recombination to the triplet state in dot R. *6.* indirect X_{3-} recombination in dot L. The red cross is a point used during the automatic optimisation procedure described in the text.

Stark shifts

The gate dependence of some of the transitions comes only from the parameters δ^L and δ^R. One example is the X_{2-} transitions from the triplet ground states with configuration (e, e) to the excited states with configuration (e, eeh). A quick calculation shows that the difference in electric potential energy between the excited state and the ground state is $e\delta_r V_{\text{Gate}}$ so the slope of this line in the PL gate sweep is just equal to $e\delta_r$. By looking closely at the lines labelled 4. and 5. the Stark shifts $e\delta_l \approx 1.1$ μeV/mV and $e\delta_r \approx 1.67$ μeV/mV can be extracted. The Stark shift is different for dots R and L because of the difference in size and chemical composition which gives rise to a different permanent dipole.

Lever arm

The lines with large slopes come from indirect transitions. The line labelled 6. for example comes from the X_{3-} transition between states with configuration (e,ee) and (ee,eeh) (inferred from the similarity between the model and the data). A quick calculation shows that gate dependence of this transition is $\left(l + \delta^R\right) eV_{\text{Gate}}$. Having already found δ_r, the lever arm can be estimated as $l \approx 0.045$. In this sample the intended growth parameters were $t_{\text{sep}} \approx 12$ nm and $t_{\text{tot}} = 334$ nm to give a predicted leverarm of ≈ 0.036 which is close to the measured value. Differences are likely due to imprecise layer thicknesses, or charging of other layers in the device which are not taken into account by this simple model [120].

3.4.2 Optimisation of remaining parameters

The remaining parameters of the model are the six Coulomb parameters V_{ee}^{LL}, V_{ee}^{RR}, V_{ee}^{LR}, V_{eh}^{LL}, V_{eh}^{RR}, V_{eh}^{LR} and the difference in single electron confinement energies $\mathrm{d}E$. These are found by an automatic routine that varies the parameters to minimise the quantity

$$L = \sum_i \left(\frac{y_i - x_i}{x_i} \right)^2 \tag{3.26}$$

which is a sum of the squared normalised differences between quantities identified above from the experimental data (x_i) and the corresponding quantities predicted given the model (y_i).

The x_i are values identified from the data far from any anti-crossings so that tunnelling can be neglected and their theoretical values can be easily calculated from the model parameters. The exact position is chosen on a case by case basis but generally so that the energy with and without tunnelling are within 5%. For example the first term in the sum for $i = 1$ is calculated by looking at the red cross in Figure 3.20. The cross is at a gate voltage of -55 mV and a wavelength of 969.755 nm and lies on the line that comes from a transition between charge configurations (e, ee) and (ee, eeh). By building a model similar to the one in this chapter for the X_{3-} system one finds that the energy of this transition far from the tunnelling anti-crossing is equal to

$$\begin{aligned} E(V) &= E_{(ee,eeh)} - E_{(e,ee)} + e(l + \delta^R)V \\ &= X_0^R + V_{ee}^{LL} + 2V_{ee}^{LR} - 2V_{eh}^{LR} - V_{eh}^{RR} + \mathrm{d}E + e(l + \delta^R)V \end{aligned} \tag{3.27}$$

At each iteration of the minimisation routine the difference between $x_1 = 969.775$ nm (the transition wavelength from the data) and $y_1 = hc/E(-55)$ (the transition wavelength predicted from the model) is calculated and used to construct the quantity L along with other points.

Since there are 7 parameters to fit there must be at-least 8 constraints x_i and y_i. One constraint that was found to be particularly necessary involved the X_{2-} system where there are two electrons in the coupled dot. The ground state has two anti-crossings, one when the $(ee, 0)$ and (e, e) configurations are degenerate, and another when the $(0, ee)$ and (e, e) configurations are degenerate. These anti-crossings are separated by a voltage

$$\Delta V = \left(V_{ee}^{LL} - 2V_{ee}^{LR} + V_{ee}^{RR}\right)/l \tag{3.28}$$

Sometimes the routine would find parameters that made $\Delta V < 0$ which put the anti-crossings on the wrong side of each other. This resulted in the singlet and triplet transitions in the simulated data being the wrong way around. To solve this was necessary

to add a term to L that was 0 if $\Delta V > 0$ and 10^4 if $\Delta V < 0$ (10^4 was chosen empirically). Although this addition made the problem discontinuous it successfully coaxed the routine into finding the correct parameters.

The minimisation routine arrives at a full set of parameters shown in Table 3.1. The parameters read directly off of the data are shown in the top half of the table. The remaining parameters found by the minimisation routine are shown in the bottom half. These parameters were used to generate the simulated transition energies which show excellent agreement with the data.

Parameter	**Value**
X_0^L	1352.61 meV
X_0^R	1278.62 meV
t_e	1.2 meV
δ^L	1.10 μeV/mV
δ^R	1.67 μeV/mV
l	0.045
dE	8.6 meV
V_{ee}^{LR}	22.3 meV
V_{ee}^{LL}	30.8 meV
V_{ee}^{RR}	31.8 meV
V_{eh}^{LR}	22.6 meV
V_{eh}^{LL}	36.0 meV
V_{eh}^{RR}	36.5 meV

TABLE 3.1: Model parameters used to fit the PL gate sweep data. Parameters in the top half of the table were determined directly from the data. Parameters in the bottom half of the table were found by the numerical fitting routine.

It is interesting to note some general properties of the Coulomb interaction energies. The direct interaction energies between charge carriers in the same dot (terms with LL and RR) are always higher than for carriers in different dots (terms with LR) which is to be expected since the Coulomb interaction falls off with separation. In addition the direct coulomb energies are both larger in dot R than dot L due to the size differences of the dot. The remaining discrepancies between the simulation and the data could be down to a break-down of the assumption that the Coulomb parameters don't change between charging regions. It is possible that the addition of extra charges and associated Coulomb interactions changes the shape of the electron and hole wavefunctions, altering their overlap and thus changing the energy of their Coulomb interactions.

The hole tunnelling strength, g-factors, and electron-hole exchange energies are missing from Table 3.1. In the data set shown there are no anti-crossings due to hole tunnelling so t_h cannot be estimated. The hole anti-crossings are not visible because they occur at gate voltages which are outside of the charge stability regions. The data was taken at zero magnetic field so the g-factors cannot be estimated from this measurement. The electron-hole exchange energies can not be fitted because the resolution the measurement is limited by the spectrometer and the dark excitons are not seen.

3.5 Conclusion

In this chapter the theoretical model used to describe and investigate coupled quantum dot states has been developed. It was shown that from a fairly simple starting point all of the states and transitions could be calculated. This allows a thorough understanding of the system states which is crucial for designing more complicated schemes. The framework described in this chapter is used extensively in the remainder of this thesis to design new systems and model existing ones.

In the next chapter the setup used for the experimental investigations in this thesis is described. The process of building and operating the equipment is described as well as routine characterisation measurement techniques.

Chapter 4

Building the experimental setup

In this chapter the construction of the experimental setup is described. At the beginning of this thesis work only the bath cryostat, sources, detectors and some optical components were present. Over the course of the PhD, the sample holder, microscope, control and analysis software were all designed and built. Initially the microscope was built using optical cages [101, 121], however due to the weight of the microscope head and length of the arm it was very susceptible to mechanical noise making more sensitive measurements difficult to perform. To solve this issue the microscope was rebuilt onto a breadboard above the cryostat which reduced the mechanical noise considerably. The experimental setup underwent many revisions to improve stability and performance, leading eventually to the form presented in this chapter.

There are a common set of requirements to any experiment involving quantum dots. The sample must be cooled by liquid helium to around 4K to minimise broadening of the quantum dot energy levels due to phonons (by reducing the phonon population). The sample must then be searched to find a quantum dot that is suitable for the experiment. Once a suitable dot has been found it must be characterised in more detail using resonant methods.

In this thesis the samples were cooled through the use of a helium bath cryostat. The sample was mounted on top of 3 nano-positioners which allowed movement of the sample in all 3 dimensions. A confocal microscope constructed on top of the cryostat allowed

imaging of the sample. The same microscope allowed up to two lasers to be independently polarised and focused to spot sizes of around 1 μm on the sample. The laser light reflected from the sample as well as fluorescence from the quantum dots could be collected into an optical fibre to be sent to various different detection and analysis stages.

In Section 4.1 the individual components of the experimental setup are described. Section 4.2 describes the steps involved in preparing the setup for experiments at low temperature. In Section 4.3 the various types of measurement used to characterise the quantum dots are described. In Section 4.4 the setup built for spectrally separating quantum dot light from laser light is described and characterised.

4.1 Experimental setup

4.1.1 Cryostat and cryogenic insert

The cryostat used is a helium bath cryostat from Oxford Instruments. It sits on top of a platform with active dampers to reduce mechanical vibrations. A schematic of the cryostat is shown in Figure 4.1. The cryostat is composed of 3 sections. The outermost section is the outer vacuum jacket (OVC) which serves to thermally insulate the inner sections from each other and the components at room temperature. The next section is a liquid nitrogen jacket which is filled with liquid nitrogen (LN). The innermost section is the main bath. This is filled with liquid helium (LH) and contains a superconducting magnet which can generate a field of up to 10 T along the vertical axis.

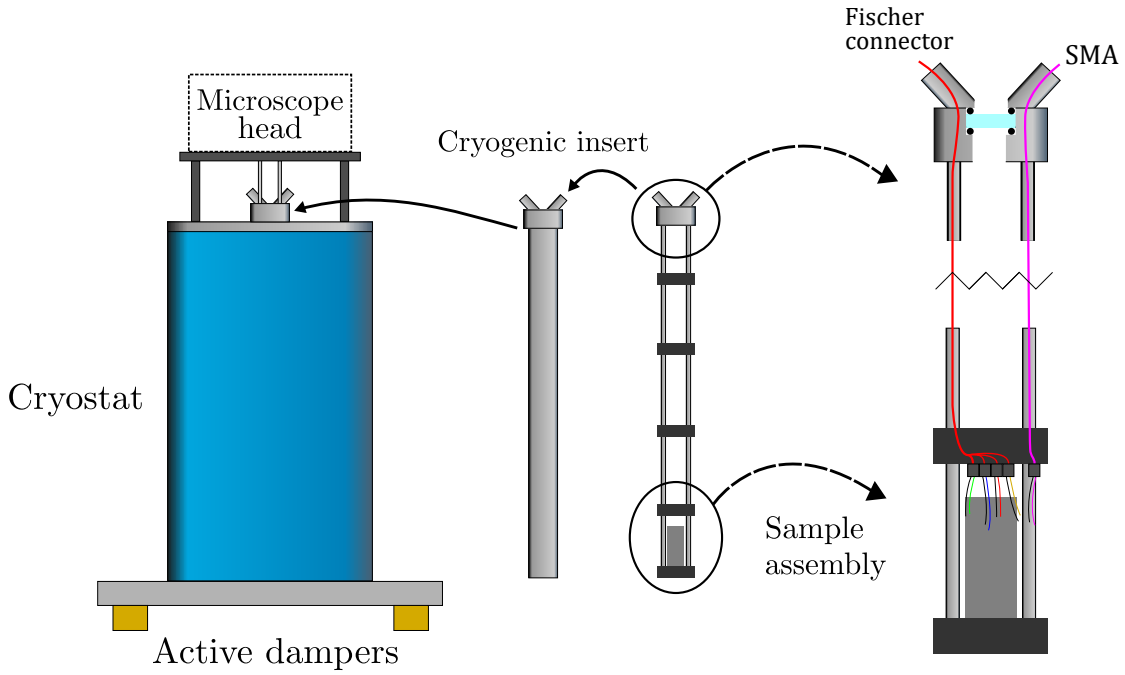

FIGURE 4.1: The bath cryostat (blue cylinder) rests on a platform which sits on a set of active vibration dampers (yellow boxes). A cryogenic insert (gray cylinder) can be inserted into the centre of the cryostat. The cryogenic insert contains a 30 mm cage system, sealed at the top by a wedged glass window (blue). Wires (shown in red and pink) run from the top, through the cage system, to break-out points at the bottom. The microscope head sits on a platform which rests on top of the cryostat.

A cryogenic insert can be inserted into the middle of the cryostat so that it sits in the bore of the magnet with the bottom section immersed in LH. The insert is a 2-inch diameter steel tube which is sealed at the bottom. The tube is sealed at the top by a wedged glass window (Thorlabs WW11050-C13) between two rubber O-rings which form a vacuum seal which holds at-least up to 5×10^{-4} mbar. It contains a standard 30 mm optical cage system which runs the full length of the tube. The bottom of the cage system has push connectors for 14 twisted wire pairs. The rods of the cage system are hollow and the wires run up the inside of them. The window holder assembly passes the wires through to the outside of the tube in a way which does not compromise the vacuum seal. Of these wires, 10 pairs go to two Fischer connectors and the remainder go to 4 SMA connectors on the window holder. Only some of these are shown in Figure 4.1 for clarity. A wedged window is used to prevent interference due to reflections. The sample assembly described next is attached to the bottom of the cage system.

4.1.2 Sample assembly and microscope lens

The samples containing the quantum dots are ~ 4 mm^2 pieces of GaAs. A layer of titanium and gold evaporated on the surface of the GaAs in a 'key-hole' shape acts as the metal gate of the Schottky diode structure. An Ohmic contact to the back highly doped layer is made by annealing metal into the sample. Each sample is attached to a sample plate by a small amount of GE varnish. The sample plate is a 0.5 mm thick 1 cm $\times$ 1 cm copper square with a 2 mm diameter hole in the centre. The sample is positioned in the centre of the sample plate so that the circular part of the gate lines up directly with the hole. Thin wires connect the metal gate and Ohmic contact to copper strips stuck onto (but electrically insulated from!) the sample plate. The wires are soldered onto the copper strips but connected by silver paste to the sample gate and contact. Thicker wires are then soldered onto the copper strips and connected to one of the twisted pairs of the cryogenic insert so that voltages can be applied to the sample. By attaching each sample to its own plate, samples can be moved around and attached to the rest of the assembly without directly touching them.

The sample plate is screwed onto a custom designed copper sample holder. A silicon photo-diode (Vishay BPW34) sits directly under the sample plate with its active area aligned with the hole. This photo-diode is used to measure light transmitted through the sample. Wires are soldered onto the two pins of the photo-diode and connected to another of the twisted pairs of the cryogenic insert.

The sample, sample plate, sample holder and photo-diode are shown in Figure 4.2a and exploded in Figure 4.2b.

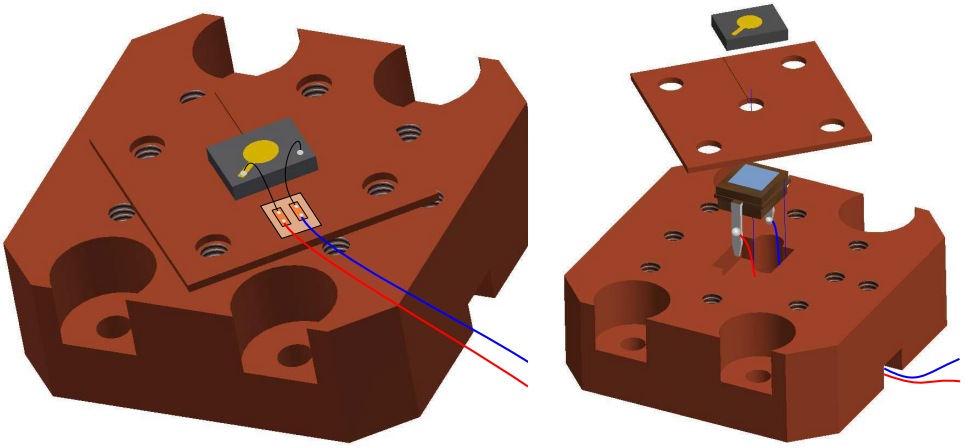

(a) (b)

FIGURE 4.2: (a) The sample assembly showing the sample with metallic gate in yellow. Wires from the sample gate (red) and back contact (blue) are shown. (b) Exploded view of the assembly. From the top down are the sample (showing the metallic gate in yellow), sample plate, photo-diode and sample holder. Red and blue wires from the photo-diode contacts are shown.

The above assembly is attached on top of a stack of 3 nano-positioners which are rigidly attached to the cage system of the cryogenic insert. Two lateral nano-positioners (Attocube ANPx100) allow the sample to be moved by up to 7.5 mm in the x-y plane in steps of around 100 nm. An additional nano-positioner (Attocube ANPz100) allows movement along the axis of the cage system by up to 6 mm in similar step sizes. The voltage pulses to drive the positioners are generated by an amplifier (Attocube ANC150) which can be controlled manually, but more often by the attached computer.

Finally, an aspheric lens of numerical aperture 0.68 (Thorlabs C330TME-B) is held in position in the cage system. The lens acts as the objective lens of the confocal microscope (described next) and so it fixes the sample plane. It must therefore be vertically positioned in the cage system so that the sample would side in the middle of the magnet. The entire sample assembly is shown in Figure 4.3.

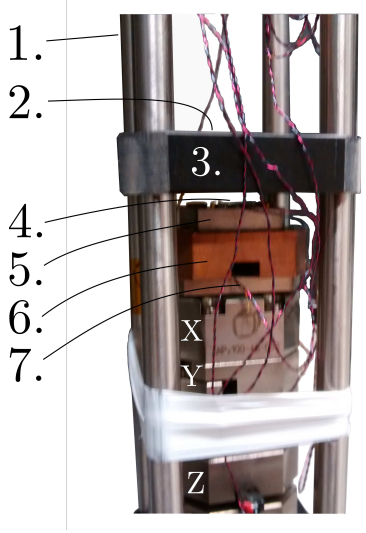

FIGURE 4.3: The full sample section. Labelled components are: (1) cage system; (2) lens (hidden), (3) lens holder, (4) sample, (5) sample plate (a thicker design), (6) sample holder,; (7) wires to photo-diode, (X,Y,Z) the X, Y and Z nano-positioners. All of this goes inside the cryogenic insert.

The wires in the image are the 2 pairs going to the sample gate and the photo-diode, and 3 pairs of control wires for the nano-positioners. White Teflon tape is used to keep the wires from straying outside of the cage system and getting trapped between the cage and the tube. Some measurements require application of oscillatory voltages to the sample which can couple into the sample holder and photo-diode. Because the ceramic in the nano-positioners is non-conducting, the sample holder and plate are floating. As a result the oscillatory voltages can couple into the photo-diode wires which then show up as crosstalk in the photo-diode signal. A wire is soldered onto the sample holder and connected to another of the twisted pairs of the cryogenic insert which lead to one of the SMA connectors. The sample holder and plate can then be grounded through the SMA connector which reduces the crosstalk. Crosstalk can also be reduced by making sure that the wires from the gate and the photo-diode are far apart from each other inside the tube.

4.1.3 Microscope head

The head of the confocal microscope is built on an optical breadboard that rests on four rubber feet on top of the cryostat as shown in Figure 4.1. To keep the microscope head aligned with the lens, the top of the cryogenic insert is rigidly connected to the bottom of the breadboard. The microscope allows for up to two excitation lasers to

be used at once. Each laser is independently collimated and polarised, then they are combined on a beam sampler (BS), (Thorlabs BSF10-B). Half of the combined beam is reflected via a 50:50 non-polarising beam splitter (NPBS), (Thorlabs CM1-BS014) downwards through the wedged window of the cryogenic insert to the lens. The same lens acts to focus emission from the quantum dots and reflected laser light back along the same path to the beam splitter. The transmitted part of the beam passes through another polariser (Thorlabs LPVIS050-MP2) and part of the beam (1% and 10% for P and S polarised light respectively) is picked off using a beam sampler and sent to a sensitive CCD (charge coupled device) camera (Brightstar Mammut Lyuba L429-M). This camera allows imaging of the sample but also monitoring of the laser reflections which is useful for alignment of the microscope. The magnification of the imaging system is around 50× with each camera pixel representing around 180 nm. The rest of the light is coupled into a polarisation-maintaining (PM) fibre, referred to as the collection fibre, to be taken elsewhere for analysis. For some measurements a quarter wave plate (QWP), (Thorlabs AQWP05M-980) is placed between the NPBS and wedged window. The QWP allows the transformation of the excitation light from linearly polarised to circularly polarised to match the quantum dot selection rules. It is also used to compensate for unwanted birefringence in the NPBS and BS which is especially important when trying to suppress reflected laser light as required by one of the later high-resolution characterisation measurements. A schematic of the full microscope is shown in 4.4.

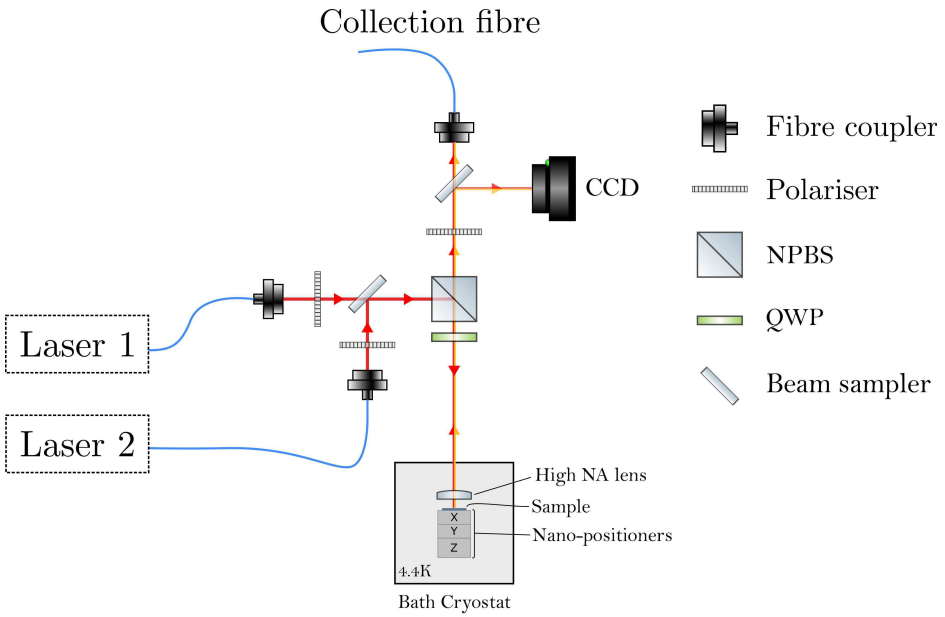

FIGURE 4.4: A schematic of the full microscope setup. The red line shows the path of the laser light, and the yellow line shows the path of light emitted from the sample (ignoring reflection at the NPBS). Polarisation-maintaining fibres are shown by blue lines. NPBS: non-polarising beam splitter, QWP: quarter-wave plate, CCD: charge-coupled device (camera).

Figure 4.5 shows a side view of the microscope head with the path of one excitation laser traced out in red. The path goes from the out-coupler (labelled Excitation 1) via a pair of mirrors for alignment, through the polariser, BS and NPBS down to the sample assembly in the cryostat. The reflected part (typically around 30%) goes back through the NPBS, is reflected off a mirror at 45°, through the second BS and to the collection fibre (hidden). The 1 or 10% reflected from the BS is directed around behind the 45° mirror toward the camera. Pairs of mirrors just after the two out-couplers and before the collection fibre coupler are used to independently control the tilt and position of the beam where necessary.

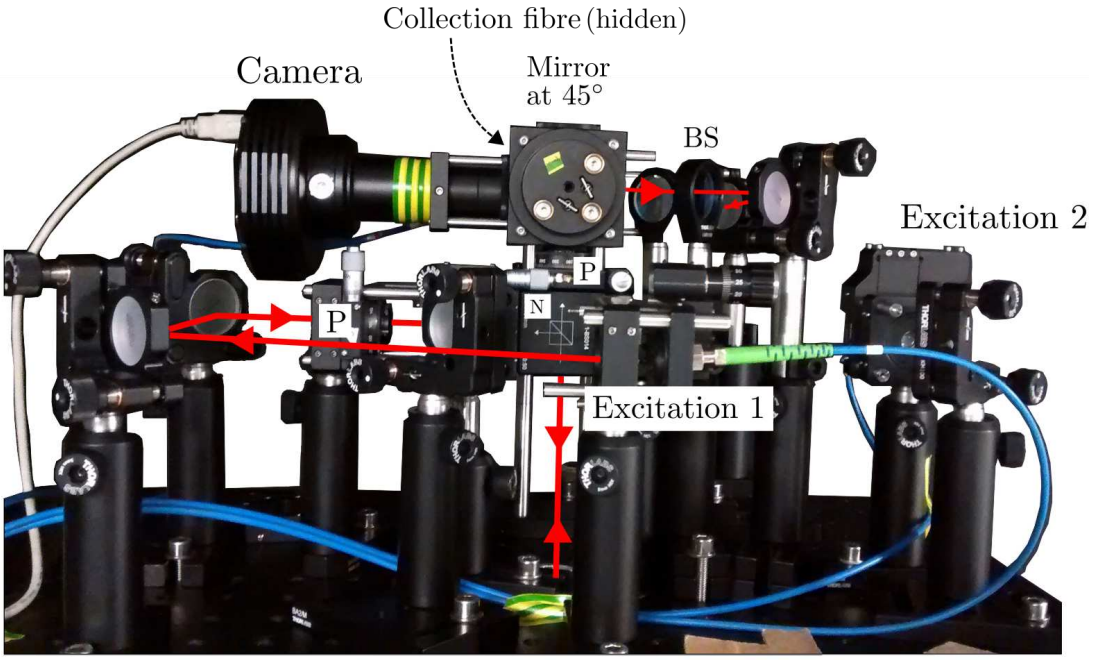

FIGURE 4.5: A photograph of the microscope head. Labelled components are: (N) non-polarising beam splitter, (P) polariser, (BS) beam sampler. The quarter wave plate is not present in this photograph. The collection fibre coupler is hidden behind the 45° mirror.

4.1.4 Sources

Laser for non-resonant excitation

Imaging and initial characterisation is performed by illuminating the sample with light above the band-gap which corresponds to around 816 nm for GaAs. For these experiments light from a Fabry-Perot laser (Thorlabs S1FC780) emitting at 780 nm is used. This laser can supply around 7 mW of power. The output power can be modulated manually or via a DC voltage which is useful for automating power dependence measurements. The linewidth of this laser is typically around 0.7 nm, however since this laser is used to generate carriers in the wetting layer a narrow linewidth is not required.

Laser for resonant excitation

High resolution measurements require the use of a laser with line-width much less than the quantum dot line-widths of several μeV. In addition since every quantum dot will have different transition energies a tunable laser must be used. For these measurements a tunable Littman/Metcalf external cavity diode laser (Sacher Lasertechnik LION) is

used. The laser current and temperature are stabilised by internal PID controllers. This laser has a linewidth of under 0.5 neV (< 100 kHz) and can be tuned by changing the position of a grating which forms part of the laser cavity [122]. The grating can be moved by an internal stepper motor resulting in large changes in wavelength. Using the motor, the wavelength can be scanned from around 920 nm to around 980 nm. These large changes are however, not reproducible due to hysteresis (corresponding to around 0.3 nm) and mechanical tolerances in the drive system.

Smaller reproducible changes can be made by applying a voltage to a piezo crystal behind the grating which changes the cavity lengths by smaller increments. A voltage of 0 to 10 V is generated by the auxiliary output of a lock-in amplifier (Stanford Research 830 DSP) which is then low pass filtered and amplified to 0 to 120 V (Attocube ANC200). The high voltage is filtered again and passed to the piezo crystal. The filters used are low pass RC type with a cut at 12 Hz to prevent electrical noise from reaching the laser. In this way the wavelength can be scanned by around 450 pm. By continuously monitoring the laser wavelength using a wavemeter and changing the voltage by small increments, the wavelength can be accurately and reproducibly controlled to within 0.1 pm.

Before amplification the voltage is also passed to the laser controller (Sacher Lasertechnik PilotPC) so the laser current can be set to change with the piezo voltage, a technique known as current coupling. Increasing the current to the laser diode shifts the laser's mode-hops to higher wavelengths. By increasing the current as the piezo voltage increases, the mode-hop free tuning range can be extended to up to 60 pm[1]. This setup is shown in Figure 4.6.

[1]This is very dependent on what optical power and wavelength range is required. The former will dictate by how much the laser current can be altered (whilst staying above the minimum required power) and the latter dictates at what current the mode-hops exist.

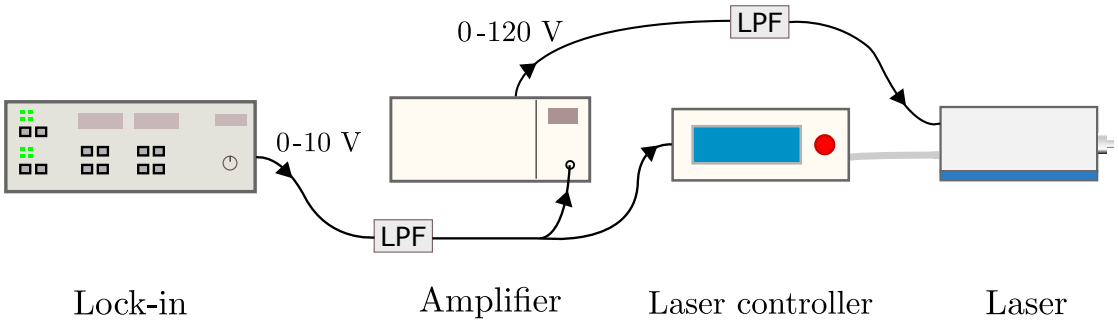

FIGURE 4.6: The configuration used to generate the voltages required for the laser piezo crystal. The lock-in generates a voltage of 0-10 V which is sent to the current-coupling input of the laser controller, and also amplified to 0-120V to drive the laser piezo crystal. Boxes labelled LPF are RC-type low pass filters with a cut at 12 Hz.

Controlling the laser power

The quantum dot response is power dependent and non-linear, so it is important to be able to finely control the optical power sent to the sample. The setup shown in Figure 4.7 enables this.

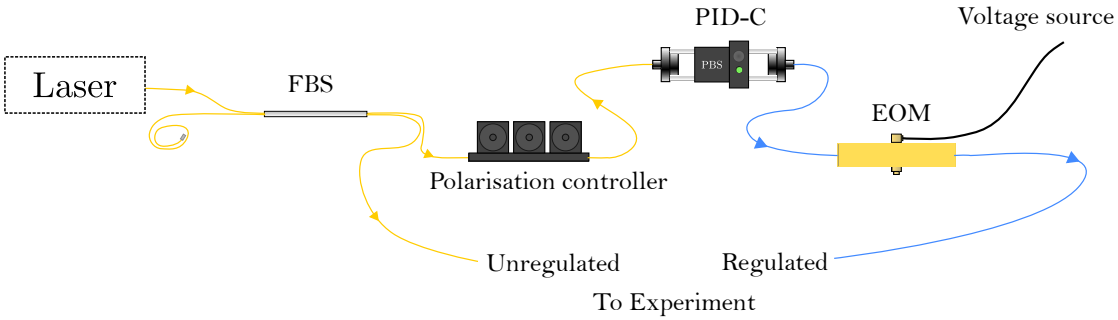

FIGURE 4.7: The setup used to control the optical power delivered to the experiment. Downstream from the laser are a 90:10 non-polarising fibre beam splitter (FBS), polarisation control paddles, the PID controller liquid crystal variable attenuator (PID-C) with preceding polarising beam splitter (PBS) required for operation, and an electro-optic modulator (EOM). Blue and yellow lines represent polarisation maintaining (PM) and non-PM maintaining fibres.

The laser appropriate for the experiment is sent into one arm of a fibre beam splitter. A small portion (10 or 1%) is picked off and sent to the unregulated output with uncontrolled polarisation, which typically goes to the wavemeter (HighFinesse WS-6) to allow wavelength stabilisation as described above. The rest is carried via fibre through a manual polarisation controller consisting of a set of three paddles. The paddles contain 1oops of fibre which act as two 1/4 and one 1/2 wave plates which together can be used to change from any polarisation to any other polarisation. The light is sent through a

polarising beam splitter (PBS) and the paddles are adjusted to maximise the amount of light that is transmitted. The light then passes through a PID controlled liquid crystal variable attenuator (Thorlabs NEL03) which acts to keep the output power stable. Finally the light is carried by PM fibre to an electro-optic modulator (EOM), (Jenoptik AM 830) which is a voltage controlled amplitude modulator. The light is then taken from the regulated output via PM fibre to wherever it is needed, typically to one of the excitation arms of the microscope.

The general mode of operation is to set the PID variable attenuator set point to the maximum required power and then either alter the EOM voltage to control the output power, or quickly ramp the EOM voltage to generate pulses from the regulated output. Using a fast electrical pulse generator, optical pulses of under 200 ps can be created though the on-off ratio is typically only around 30. Care must be taken to ensure that the laser power going into the variable attenuator will not drop to below the set point. The PID controlled attenuator is able to attenuate noise up to 100 Hz by a factor of 100, and up to 1 kHz by a factor of 10. Using this setup, the power could be stabilised to within 5%.

4.1.5 Detectors

Spectrometer

Very often it is necessary to analyse the different spectral components in the collected light. To do this, the light from the collection fibre is collimated, filtered by a long pass filter with a cut at 900 nm (Thorlabs FEL0900), and focussed by a doublet lens (Thorlabs AC254-050-B) onto the entrance slit of a grating spectrometer (Princeton Instruments SP-2750). The slit width is set to around 3-5 μm. Parabolic mirrors in the spectrometer direct the light onto the grating which spatially separates the different frequency components. The spectrometer contains 3 gratings with 300, 1200 and 1500 grooves per mm (gpmm) on a turret whose rotation can be controlled via software. Light reflected from the grating is then refocussed onto a CCD camera (Princeton Instruments PyLoN 100BR eXcelon) which is cooled by LN to $-120°$C (153 K). Cooling the sensor reduces the dark counts per pixel from over 65000 Hz to under 10 Hz and allows imaging of low intensity light. The filter blocks the strong reflection of the 780 nm laser used

during photoluminescence measurements (described later). Without it, scattered laser light reaches the camera even when the grating deflects the main laser spot far from the CCD. The spectrometer setup is shown in Figure 4.8. Using the 1500 gpmm grating the spectral resolution of the setup is around 10 pm.

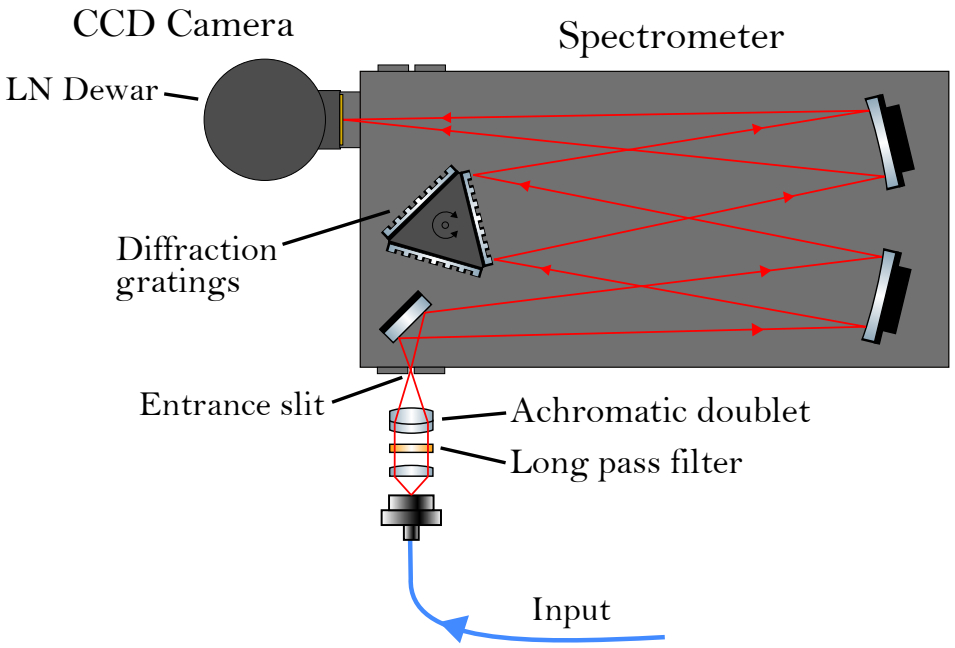

FIGURE 4.8: The spectrometer setup showing the fibre input coupling stage, internal computer controlled grating turret, and CCD camera with attached liquid nitrogen (LN) dewar. The path of one spectral component is shown in red.

Sample photo-diode

The photo-diode beneath the sample plate mentioned in Section 4.1.2 is used to record the amount of light transmitted through the sample during differential transmission experiments (described later). Since it is on the sample assembly, it is also cooled to around 4 K by the LH. The signal from the photo-diode is passed to the outside by an SMA terminated pair of wires inside the cryogenic insert. The signal from the SMA is taken to a low noise electrical amplifier (Femto DLPCA-200) which can amplify the signal by up to a factor of 10^{11} V/A. For most of the measurements in this thesis the amplification is set to 10^{8} V/A where the bandwidth is 50 kHz. The output which ranges from 0 to around 10 V is usually taken both to the input of the lock-in amplifier and to an analogue-to-digital converter (ADC) to allow the DC value to be recorded.

Amplified photo-diode

The intensity of light in the collection fibre can be measured by connecting the collection fibre directly to a low noise amplified Silicon photo-diode (Femto OE-200-SI). The signal from the internal photo-diode can again be amplified by a factor of up to 10^{11} V/A such that optical powers as low as 50 fW can be measured, with a noise equivalent power of around 8 fW. The output ranges from 0 to around 10 V and is also usually taken both to input of the lock-in amplifier and to an ADC to allow the DC value to be recorded. This photo-diode is used most heavily during alignment of the optical elements but also for differential reflection measurements described later.

Avalanche photo-diode

Lastly, if the intensity of light is low enough it can be measured using an avalanche photo-diode (APD), (Excelitas SPCM-AQRH-14-FC). This module is able to detect single photons with an efficiency of around 20% at a wavelength of 950 nm. The quantum dots used in this thesis fluoresce anywhere from around 900 nm up to around 990 nm. The APD can only be used when the photon rate is under 40 MHz which at 950 nm corresponds to a power of less than 8.4 pW. It generates an electrical pulse whenever it detects a photon. These pulses are carrier by coaxial cable to a time-to-digital-converter (TDC), (IDQ ID800-TDC) which can time-stamp the events with resolution of 81 ps and generate histograms of pulse separation. This can be used to perform photon correlation measurements but in this thesis it is just used to accumulate the total number of photon counts over some time period.

4.2 Operation

4.2.1 Cooling down

The first step in cooling the cryostat is evacuating the OVC. The OVC is pumped out by a turbo-pump backed by a roughing pump for a few days to reach a pressure below 5×10^{-4} mBar. The system is pre-cooled to LN temperature (77 K) before using LH to reach 4 K. This reduces the amount of LH that evaporates during the cooling process.

Pre-cooling involves filling both the main bath and the nitrogen jacket with LN and allowing them sufficient time to cool to 77 K, usually a day. After this the LN and nitrogen gas in the main bath is removed by applying a slight overpressure of clean helium gas. It is important to ensure that all the LN and nitrogen gas has been removed before cooling any further as anything remaining would freeze to the cryostat and remain in place until the system is warmed up. To be sure of this, the main bath is filled with helium gas then evacuated to under 10 mbar. This 'pump and flush' process is repeated 3 times before continuing. Once the main bath contains only helium gas, LH is slowly transferred into it via an insulated transfer tube. The transfer takes on the order of 2 hours to complete. During this whole process the temperature of the main bath can be monitored by the resistance of 3 resistors at different positions on the superconducting magnet. The LN and LH levels in the nitrogen jacket and main bath respectively are read by a level meter (Oxford Instruments ILM 2115). At full capacity the nitrogen jacket can hold 66 L of LN which evaporates at around 9 L a day. The main bath can hold around 70 L of LH which evaporates at around 11 L a day. During operation the system is refilled twice a week.

Before the cryogenic insert is inserted into the cryostat, the air inside it must also be replaced by helium gas to prevent gasses freezing onto the elements inside. The insert is pumped and flushed 3 times with helium gas to a pressure below 5×10^{-4} mbar. It is left containing around $20 - 25$ mbar of helium gas at room temperature to act as a thermal exchange. The insert can then be safely lowered into the cryostat. The temperature of the sample assembly can be monitored by recording the capacitance of the piezo elements in the nano-positioners. The capacitance varies between positioners but generally changes from around 400 pF at room temperature to around 130 pF at 4 K.

The next step is to attach the microscope head to the top of the insert and realign it.

4.2.2 Aligning the microscope

For proper operation of the microscope, it is crucial that all excitation lasers hit the very centre of the microscope lens and follow the same optical path. This ensures that they are focussed onto the same area of the sample. In addition, the collected light

should be coupled into the collection fibre with high efficiency. To align the elements of the microscope head, lasers are sent through the excitation and collection pathways and the camera is used to image the light reflected from the various optical elements along the way. Figures 4.9a and 4.9b show the observed images when a laser is sent via the excitation and collection pathway respectively. The faint spots on the left in each image are reflections from the beam splitter and other optical elements in the microscope head. Figure 4.9b has an additional spot because of an additional reflection from the polariser in the collection path (since the light goes through some elements in the opposite direction compared to the excitation path). The large spot under the blue cross-hair is the reflected light from the sample that passes through the lens. Aligning the excitation and collection pathways such that the corresponding spots are overlapped ensures that both beams follow the same path. This is shown in Figure 4.9c. By visually aligning spots on the camera the coupling efficiency into the collection fibre is typically near maximum. The process can be repeated to align both the excitation paths together. Coupling efficiencies of 60-70% are routinely achievable.

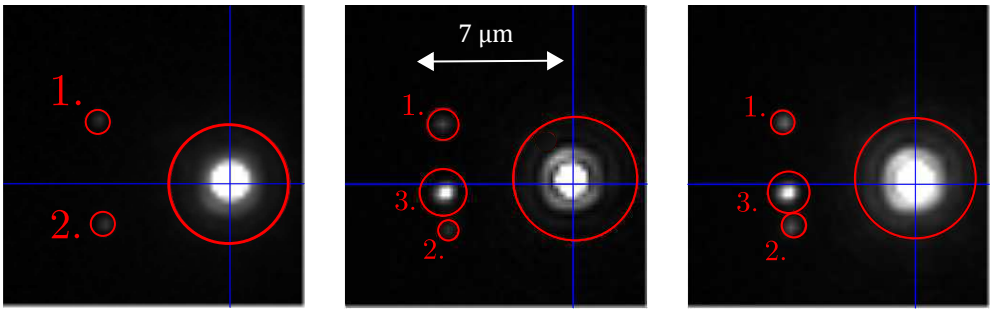

(a) (b) (c)

FIGURE 4.9: Image on the microscope camera during alignment of the excitation and collection pathways of the microscope head. (a) First the laser is sent via the excitation pathway only. The large spot under the blue cross-hair is the reflection the sample through the lens. The smaller spots in the image (1. and 2.) are reflections from the beam splitter. (b) Next the laser is sent though the collection pathway only. The main spot and the two small spots (1. and 2.) are visible in the same position as before. There is an additional spot (3.) which is reflection due to the polariser. (c) To verify the alignment, the lasers are send down both the excitation and collection pathways at once to see that they are overlapped on the camera. Since all the spots are overlapped both lasers must follow the same path. Red circles are auto-detected spot positions.

In addition to making the paths overlap, the optical axis should be aligned with the axis of the lens since this is the path that light emitted from a quantum dot (in the focal volume of the lens) will follow. To do this the beam is aligned to the top of the cryogenic insert using an alignment plate (a metal plate with a hole that can be aligned to exactly

the centre of the insert), and at the bottom by observing the interference pattern formed by the lens and sample when the sample is slightly defocussed. The interference pattern (Newton's rings) formed when the laser the lens exactly in the centre is shown in Figure 4.10. When the laser is slightly off-centre the rings are brighter on one side than the other. The interference pattern thus serves as a sensitive alignment tool.

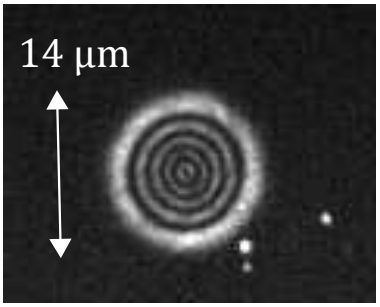

FIGURE 4.10: Interference between light reflected from the lens and sample surface. The pattern is formed when the sample is slightly defocussed away from the lens. When the laser hits the lens exactly in the centre the intensity of the rings is evenly distributed. If the laser hits the lens off-centre then the intensity of the rings is uneven.

4.3 Sample characterisation

4.3.1 Finding quantum dots

With the optics aligned and the sample cooled down to 4 K, the process of locating a suitable quantum dot can begin. The quantum dots can be made to fluoresce either by resonant or non-resonant excitation. Resonant methods described later require tuning a laser to within the linewidth of the quantum dot transitions. This is virtually impossible without knowing something about where the transitions are (the laser wavelength could be scanned across a large range but this would take infeasible amounts of time). The non-resonant method uses the laser at 780 nm to generates free charge carriers in the GaAs and wetting layer which relax via phonon emission into the quantum dots. Once localised there they can recombine radiatively emitting photons whose energy depends on the quantum dot levels. Through this process a region of the sample can be illuminated with a non-resonant laser without needing to know beforehand the exact energetic structure of the quantum dots.

This allows an easy way to physically locate the quantum dots on the sample. Figure 4.11 shows an image from the microscope camera when the sample is illuminated by the 780 nm laser. The laser spot is intentionally defocused to illuminate a larger area of the sample.

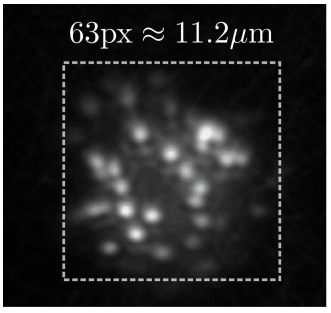

FIGURE 4.11: Quantum dots visible on the microscope camera under non-resonant excitation. The box contains on the order 40 quantum dots to give a density of ~ 4 μm^{-2}

To perform more detailed analysis the light from the dots must be coupled into the collection fibre to be analysed by other instruments. To do this, the position of the resonant laser spot on the camera is recorded during the alignment procedure, and the quantum dot to be analysed is moved underneath it using the nano-positioners. Typically the dots are bright enough and the camera sensitive enough that the quantum dots can be imaged in real time. The sample shown in the image has a reasonably high density of dots so finding the right dot does not need to take long. In other samples such as the one hosting the dot used in Chapter 5 the density is closer to one every 20 μm^{-2} so finding a suitable dot can take anywhere from a few days to a week.

4.3.2 Photoluminescence

The fastest way to characterise the quantum dot uses the non-resonant laser to excite the sample. The light shown on the microscope camera in Figure 4.11 will contain many frequency components which come from different optical transitions in the quantum dots. To discern these components the collection fibre is plugged into the spectrometer where the photo-luminescence (PL) is dispersed and imaged on the CCD. With the sample unbiased (floating) a typical PL spectrum is Figure 4.12.

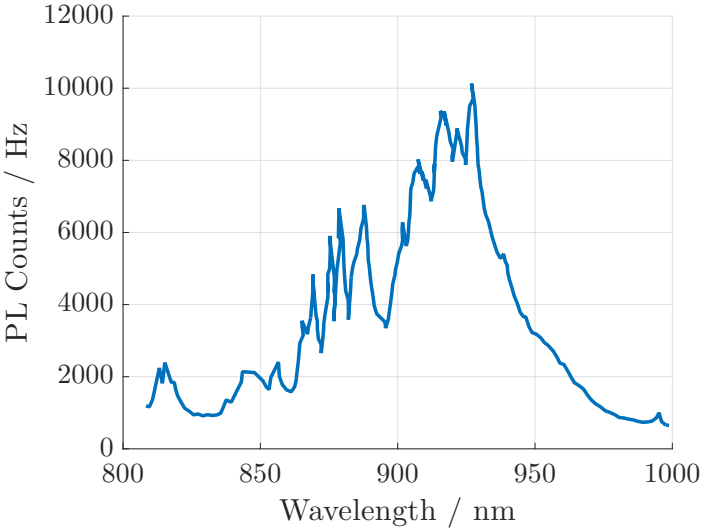

FIGURE 4.12: A photo-luminescence (PL) spectrum taken with no voltage applied to the sample (floating). PL is dispersed on a grating with 1200 grooves per mm.

Some peaks are visible but they are highly broadened. Because the sample is unbiased, the gate voltage can fluctuate and so the quantum dot energy levels fluctuate with respect to the reservoir Fermi level. During the experiment, fluorescence is observed from various different charge states in the device.

When a voltage is applied, the quantum dot energy levels are fixed with respect to the Fermi level and so fluorescence from only one charge state is seen, as shown in Figure 4.13 for a different quantum dot.

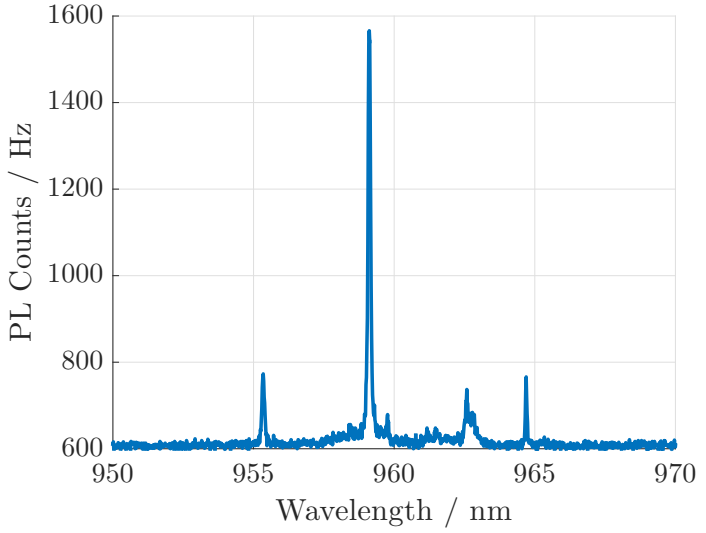

FIGURE 4.13: A photo-luminescence spectrum taken with DC voltage applied to the sample.

The width of the peaks in this image are on the order 100 pm which is cause by local heating of the sample by the non-resonant laser [123]. Not much can be said about the structure from a single spectrum, so multiple spectra are recorded at different DC gate voltages. Figure 4.14 shows a PL gate sweep using a different sample of lower density where only one dot is near the focal region.

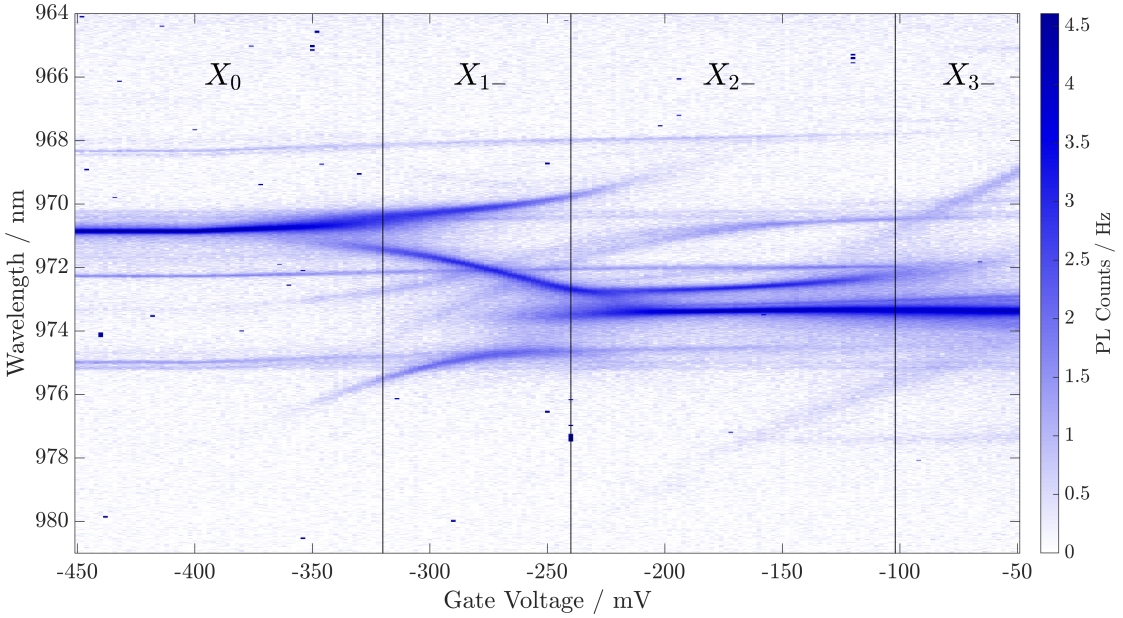

FIGURE 4.14: A photo-luminescence gate sweep plotted using a logarithmic colour scale. One dot is in the focal volume of the lens and the brightest lines come from it. The charging states are labelled. Several other faint lines are seen which come from nearby dots which are also weakly excited.

These gate sweeps are used together with the models developed in Chapter 3 to determine the charging states of the dot at each voltage, and ultimately to decide whether a dot is suitable for a given experiment. The optical power used in Figure 4.14 was around 24.2 μW so the lines are broadened (by phonons generated by local heating) to a width of around 100 pm. As a result of the high power several other faint lines can be seen which originate from other dots even though they are quite far from the focal region. For detailed plots, low optical powers of 10s of nano-watts and exposure times of 10s of seconds are used. Under these conditions, transition lines with widths on the order $50 - 30$ pm can be seen.

Even with a low excitation laser intensity and using a more dispersive grating in the spectrometer, the lines are still broadened by the presence of photo-generated charges around the QD. Resonant methods avoid this problem since excitons are generated

directly inside the quantum dot. In the next sections three resonant, high resolution techniques are discussed

4.3.3 Resonance fluorescence

Resonance fluorescence (RF) is conceptually the simplest technique employed to probe quantum dot transitions. It simply involves tuning the wavelength of the excitation laser so as to resonantly drive the quantum dot transition, and collecting the photons emitted when the system relaxes back to its ground state. In practice it is complicated by the fact that majority of light coming from the sample is reflected laser light, as illustrated in Figure 4.15.

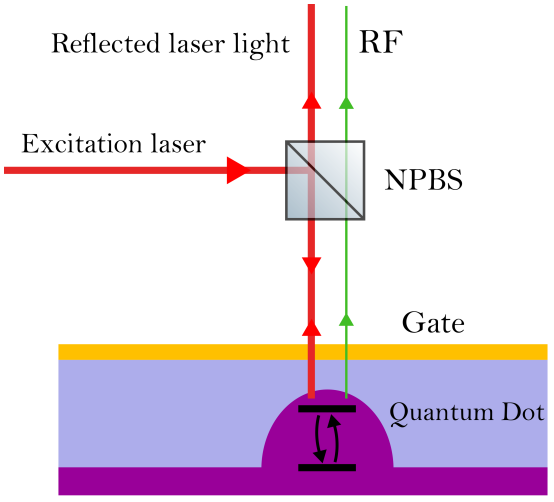

FIGURE 4.15: A schematic illustration of a resonance fluorescence experiment. The red line shows the path of the excitation laser. The green line shows the path of the resonance fluorescence (RF) emitted by the quantum dot. Paths are separated for visual clarity. The laser light reflected from the sample surface dominates over the RF. NPBS: non-polarising beam splitter.

One approach would be to excite from a different direction to the collection axis. This is the approach commonly employed by the atomic physics community. It has been used in quantum dot experiments before as demonstrated by Muller *et al.* [124] but is tricky to do in this setup because the sample optics must operate within the confines of the cryogenic insert. Experiments to investigate whether simply pre-aligning and gluing a fibre next to the sample (which would deliver the excitation light) revealed that this system would not be stable enough. Whilst the fibres survived (at least down to 77 K) the alignment changed considerably. In addition it would not be possible to move the

excitation beam once it was fixed, and as the beam would diverge inside the sample (as it would out of a bare fibre) experiments would be limited to those quantum dots that happened to be in the beam path. Much higher optical powers would be required as the beam would not be focussed. Without additional positioners for the fibre, and perhaps a compact focussing lens, this idea would not work and so was abandoned.

Another approach is to block the reflected laser using crossed polarisers. Using this method the excitation laser is polarised before it hits the sample. An analyser on the collection arm can be adjusted such that the reflected light is extinguished. In practise the extinction coefficient (the ratio of the transmitted laser light when transmission is maximised, to that when it is minimised) can be up to $\sim 10^8$, though is typically closer to $10^6 - 10^7$. This is illustrated in Figure 4.16. An unavoidable consequence of this method is that some fraction, usually half, of the fluorescence from the dot is also lost to the analyser.

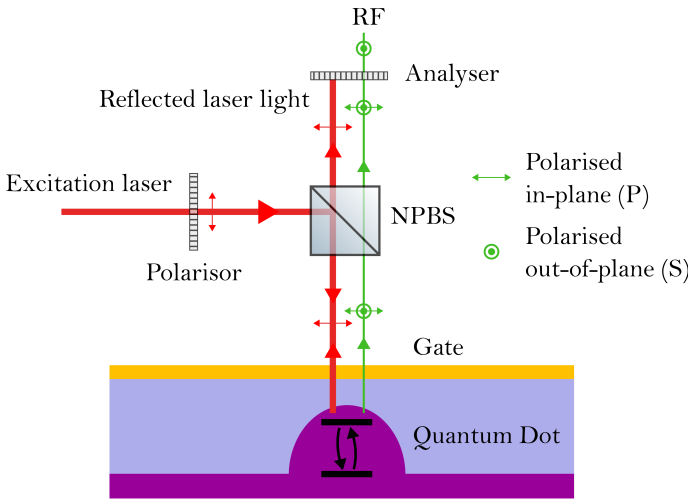

FIGURE 4.16: A schematic illustration of a resonance fluorescence experiment using crossed polarisers to block laser light reflected from the sample surface. The red line shows the path of the excitation laser. The green line shows the path of the resonance fluorescence (RF) emitted by the quantum dot. Paths are separated for visual clarity. Polarisation (S) and (P) are defined relative to the non-polarising beam splitter (NPBS).

The suppression that can be achieved in this way is limited by the polarisers and can be up to $\sim 10^8$. However another limiting factor is that not all of the light reflected from the lens and sample arrangement is of the same polarisation as the incoming light. As described by Novotny [125], the lens introduces additional polarisation components which interact with the sample. The result is that for a linearly polarised incoming beam

the majority of the reflected beam is still linearly polarised in the same direction, but there is a small component polarised orthogonally and with a different intensity profile. The intensity of this orthogonal component is typically around 5 orders of magnitude smaller than the reflected light in the original polarisation. This orthogonal component is shown in Figure 4.17.

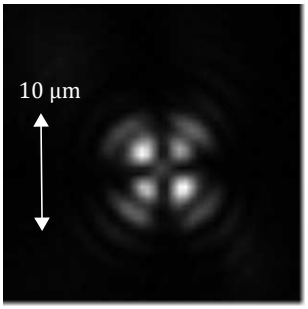

FIGURE 4.17: Intensity distribution of the reflected V component of a strongly focussed H polarised laser. The reflecting medium is a dielectric mirror.

In the configuration shown in Figure 4.16 this light would pass right through the analyser. Thankfully there is a node at the centre and so it does not couple into the collection fibre well. In fact it can be of assistance by acting as a fine alignment tool since small changes in the angle of the beam will cause large changes in signal as the lobes move onto the core of the collection fibre.

With the majority of the laser light blocked by the polariser, the light from the collection fibre is predominantly quantum dot fluorescence. The intensity is low enough that the APD can be used to detect it. To investigate the quantum dot transitions the wavelength of the laser is scanned across the transitions seen in the PL gate sweep. Figure 4.18 shows an RF gate sweep performed by recording the APD count rate whilst scanning the gate voltage and stepping the laser wavelength. Scanning the laser wavelength causes the wavelength and power to jump due to mode-hops, so most gate sweeps are performed by scanning the gate.

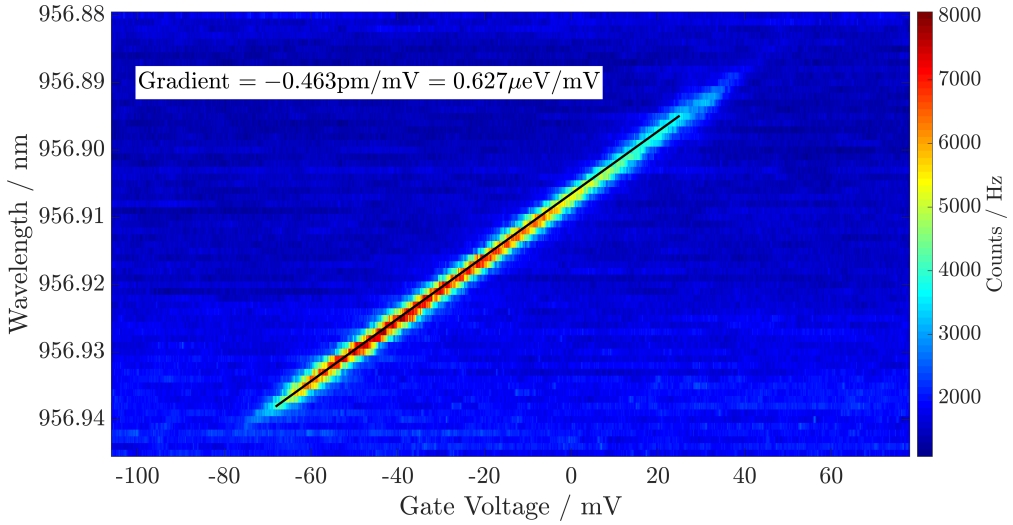

FIGURE 4.18: A gate sweep performed by collecting resonance fluorescence (RF).

The slope of the line can be extracted from this graph to determine the Stark shift, which in this case was 0.627μeV/mV. Each trace (horizontal line) in the RF gate sweep is fitted with a Lorentzian and the FWHM as a function of gate voltage is shown in Figure 4.19.

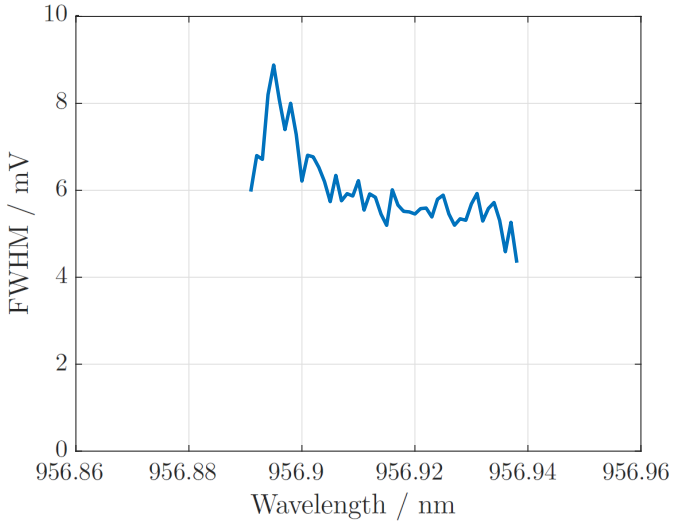

FIGURE 4.19: The full-width-half-maximum of the Lorentzian fits to each wavelength trace in the resonance-fluorescence gate sweep.

Away from the edges of the line where fits become unreliable due to diminishing signal-to-noise, the linewidth is roughly 6 mV, and using the DC Stark shift of 0.627 μeV/mV, this corresponds to a line width of 3.6 μeV. This is several times larger than the radiative linewidth of 0.66 μeV (corresponding to a typical lifetime of 1 ns [126]). The broadening

is caused by charge fluctuations in the sample which shift the transition energy on the time-scale of MHz to GHz [121], much faster than the measurement time-scale of around 1 s. The charge fluctuations are caused by fluctuating occpuation of nearby states [90].

Figure 4.20 shows the expected Lorentzian line-shape measured by fixing the gate voltage at some value and sweeping the laser across the resonance. This more direct measure of the linewidth agrees well. The Lorentzian sits on top of a background of around 2 kHz of unsuppressed laser light which makes it through the crossed polarisers[2].

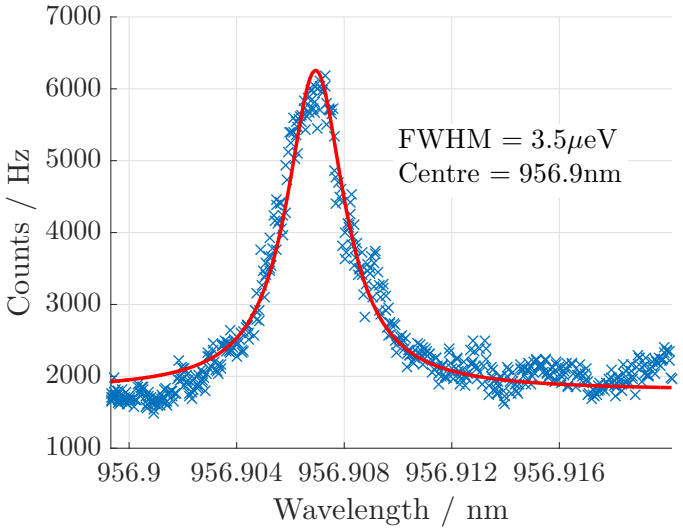

FIGURE 4.20: A resonance-fluorescence scan taken by sweeping the laser wavelength for a fixed gate voltage. Red line is a Lorentzian fit with the given full width half maximum (FWHM) and centre.

Whilst RF is a powerful technique it requires precise alignment of the polarisers to achieve the required extinction ratios of $10^6 - 10^7$. The techniques of differential reflection and transmission, described in the next two sections, are less technically demanding and so are faster to set-up.

4.3.4 Differential reflection

In an RF experiment the quantum dot fluorescence is measured by removing the scattered laser background directly. Differential reflection (dR) directly measures the interference between the fluorescence from the quantum dot and the reflected driving

[2]One could confirm that the background is from the laser rather than the quantum dot by performing a $g^{(2)}$ measurement on the collected light and seeing the change ins bunching behaviour when near resonance.

laser. The light from the collection fibre is sent to the amplified photo-diode. The light intensity on the photo-diode is equal to [126]

$$I \approx |E_L + E_s|^2 = I_L + I_s + 2\mathrm{Re}\left(E_L E_s^*\right) \tag{4.1}$$

where E_L is the electric field of the reflected laser light and E_s is the coherent fraction of the electric field scattered by the quantum dot. The intensity of the laser and quantum dot light are I_L and I_s respectively. The incoherent fraction of scattered light is left out since interference with it average to zero within the bandwidth of the measurement (50 kHz). Without polarisation suppression, $I_L \gg I_s$ and so I_s can be neglected. The interference term is typically on the order of 0.1% of I_L and so is much smaller than the fluctuations in laser intensity which are on the order of 5%. A lock-in amplifier is used to separate the small interference term from the large laser background. The amplitude of the interference term is modulated by applying a square wave to the sample gate, typically of amplitude 100 mV and frequency 300-400 Hz[3], which shifts the quantum dot transition in and out of resonance via the DC stark shift. The lock-in amplifier amplifies components of the photo-diode signal around this frequency whilst attenuating those away from itmea, and thus rejects noise at other frequencies. In this thesis a typical signal-to-noise level achieved using this method is around 20. This technique first demonstrated by Alén *et al.* [53] is commonly employed in the quantum dot community.

To perform a sweep across the resonance, the gate is modulated at the lock-in frequency and the DC offset is scanned. Each quantum dot resonance generates two signatures when it is brought into resonance by the low and high levels of the gate modulation. This is shown in the dR trace shown in Figure 4.21. The laser wavelength is held constant whilst the gate voltage is swept. At each point the system pauses for some time (usually $2-3\times$ the lock-in time constant) to allow the lock-in's filters to settle. As a result, differential reflection and differential transmission (dT, defined next) measurements take some time to perform.

[3]The modulation frequency is chosen to avoid peaks in the laser's noise spectrum. It is kept low to minimise the capacitive coupling of the modulation voltage into the photo-diode wires which are nearby in the sample assembly. Ultimately, quick measurements can be repeated using different frequencies to empirically determine which gives the highest signal-to-noise ratio

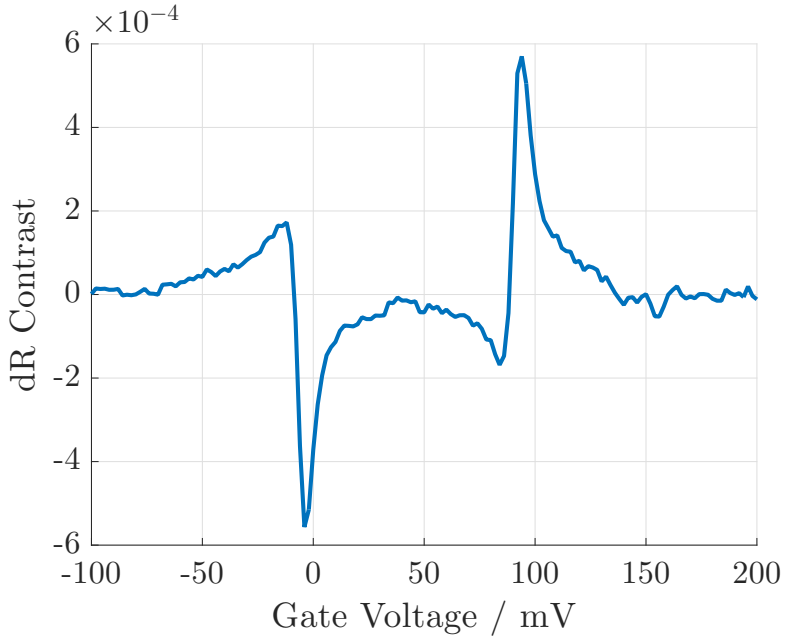

FIGURE 4.21: A differential reflection scan of a quantum dot transition. The left and right-hand lines come from a single transition during the low and high phases of the gate modulation, and thus they are 180° out of phase with each-other. They are separated by the gate modulation amplitude which in this case is 100 mV.

The dR line-shape is clearly asymmetric. The precise mechanism of the asymmetry is unclear, though it can be resolved by realigning the quantum dot position using the nano-positioners so likely is due to an optical interference effect (this is demonstrated in Section 4.3.8). Some of the asymmetry comes about due to the sample thickness [126]: since the dot is only a few 100 nanometres from the sample surface, the light that is back-scattered from the dot adds coherently with the reflected laser light. Since the optical path difference depends on the wavelength and the dot/surface distance, the line-shape is altered from a typical Lorentzian shape. However, this should not change with lateral position so there must be another source. It has been suggested that holes coupling to states in the capping layer could be the cause [68].

Differential reflection measurements don't require precise polariser alignment, however they still require the light to be coupled well into the collection fibre. Greater than 60% is routinely achievable but still takes some time. The last method removes even this requirement.

4.3.5 Differential transmission

The quantum dot dipole radiates in all directions and so there is also a forward scattered component. This interferes with the transmitted laser component on the photo-diode just below the sample as illustrated in Figure 4.22.

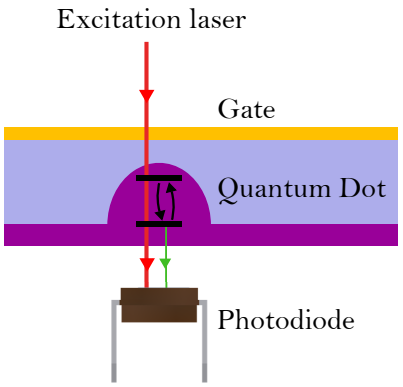

FIGURE 4.22: A schematic illustration of the differential transmission (dT) experiment. The red and green lines show the paths of the excitation laser and forward scattered component of the light from the quantum dot respectively. These two components interfere on the photo-diode.

Gate sweeps are performed in much the same way as for dR measurements except the signal from the photo-diode beneath the sample is used [53]. These measurements are relatively simple in that the only critical alignment is that of the excitation laser to the lens, and the quantum dot to the focal point (as is required for all measurements). Figure 4.23 shows a gate sweep of the upper line in the X_{1-} region seen in Figure 4.14. The laser wavelength is held constant whilst the gate is scanned.

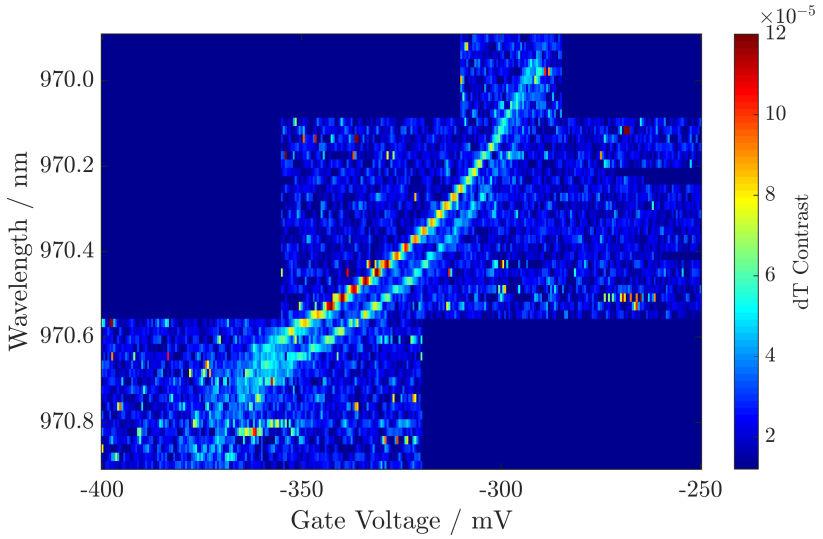

FIGURE 4.23: A gate sweep performed by measuring the differential transmission signal. The image shows three datasets stitched together.

This figure highlights a few important points. Firstly the exchange splitting can be resolved quite easily here whereas PL measurements alone could not resolve this fine structure. Secondly, dT scans can only go as far as the laser wavelength can be scanned. This means longer wavelength scan ranges take a considerable amount of time and cannot be done in one go.

4.3.6 Contrasting the techniques

Four measurement techniques have been described up to now, which each have their own advantages and disadvantages, and are appropriate in different scenarios. In the following, each technique is briefly revisited and advantages and drawbacks of each are mentioned.

PL

PL is a fast technique since a spectra can be collected within a few seconds, given the kHz photon count rate in the current experimental setup. It allows quick interrogation of a sample which is crucial when searching for a quantum dot for a particular experiment.

However, in order to get fast acquisition speeds, powers of 10s of μW are used which broaden the lines due to local heating, and thus limits the detail than can be observed

on plots like Figure 4.14. Using lower, powers reduces the line width but it is still limited by the spectrometer resolution to a few 10s of pm.

Since the dots are bright and the excitation laser is almost 200 nm away from the emission wavelength, reflected laser light can be filtered out and the emission images on a camera. This is again very useful when searching for a dot. Thanks again to the high count rate, alignment of the system can be done in-situ by monitoring the spectrum in real-time.

RF

Since in an RF experiment the laser must be scanned, these measurements take much longer than PL measurements (an RF trace of a single line in Figure 4.14 might take 5 minutes to complete).

The resolution of these measurements is limited only by the laser scan step, and the laser linewidth (which is negligible in comparison to the quantum dot linewidth).

The demands on initial beam alignment for RF experiments are also higher than for PL experiments, since time must be spent optimising the polariser alignment to get the required suppression of the laser. This typically involves switching to higher laser powers and less sensitive detectors (Amplified photo-diode) to optimise the alignment, and then switching back to the desired measurement apparatus (APD).

dR and dT

This is again a scanning technique so these measurements take time comparable and sometimes longer than RF experiments (since time must be allowed at each point for the lock-in filters to settle).

The resolution is limited only by the laser scan step and wavelength, as is the case for RF measurements.

The demands on alignment for dR experiments are similar to PL, since the reflected light must be detected on the amplified photo-diode. For dT the demands are much lower since the photo-diode underneath the sample had a large (accessible) active area

of around 1 mm^2, meaning the only critical alignment that the dot and the excitation laser spot were aligned.

4.3.7 Resonance-fluorescence saturation measurements

Coherent driving of the dot transitions with a laser, generates oscillations between the ground and excited state, at a frequency known as the Rabi frequency. For resonant experiments it must be possible drive the quantum dot transitions with a known Rabi frequency. This requires knowledge of the relationship between the incident optical power and the Rabi frequency which varies from dot to dot and also on the alignment. The response of a driven two level system at low power is a Lorentzian with width limited by the dephasing times of the exciton [62]. The system responds non-linearly to the driving field strength due to power broadening. Figure 4.24 shows several RF traces of a single transition using different incident powers.

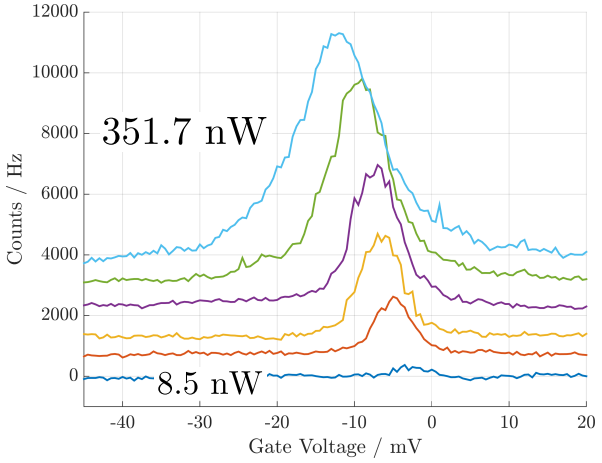

FIGURE 4.24: Broadening of a transition line when the driving power is increased. Plots are offset for clarity.

Both the width and height of the peak increase with power. In addition the peak shifts to a lower gate voltage due to laser induced charging of the sample [121] (which then acts like an applied gate voltage, shifting the transition energies through the DC Stark effect). By fitting each trace with a Lorentzian the power dependence of the linewidth and peak height can be extracted. These fits are shown in Figures 4.25a and 4.25b respectively.

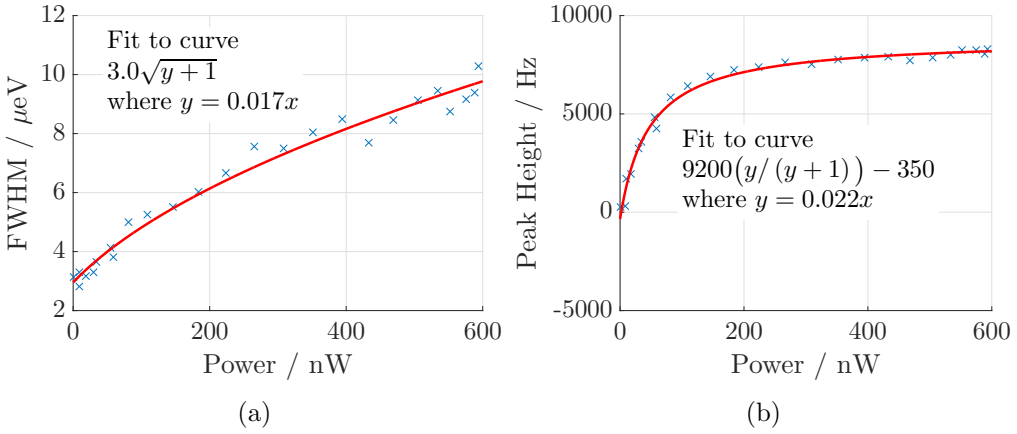

FIGURE 4.25: Change in the (a) full-width-half-maximum (FWHM) and (b) height of the resonance fluorescence peak as the incident power is increased.

The response of a two-level system driven by a coherent radiation field is derived in [62]. The full response of the system at resonance is the Mollow triplet, however a simple model puts the total RF count proportional to the excited state population. Expressions can be derived (see equation (2.8.3) in [62]) for the linewidth

$$\Gamma(P) = 2\gamma\sqrt{1+P} \tag{4.2}$$

and peak height (with fitting parameter h_0)

$$h(P) = h_0 \frac{P}{1+P} \tag{4.3}$$

where γ is the rate of spontaneous emission (ignoring other dephasing mechanisms), P is proportional to the power and squared Rabi frequency Ω through $P = k\Omega^2$. From the fits in Figures 4.25 the low power linewidth 3.0 μeV and fitting constant $k = 0.019 \pm 0.003$ nWμeV^{-2} can be extracted. The constant k encompasses the relation between the incident power on the sample and the power driving the quantum dot and so these saturation measurements can be used to relate the applied optical power to the Rabi frequency.

These saturation measurements can also be performed using dR and dT, the advantage of dT being that less alignment is required.

4.3.8 Peak symmetrisation in differential reflection and transmission

The alignment dependent asymmetry visible in the dR trace of Figure 4.21 is also present in dT traces. The misalignment induced asymmetry is investigated by navigating to a transition and repeatedly taking dT traces such as that shown in Figure 4.26.

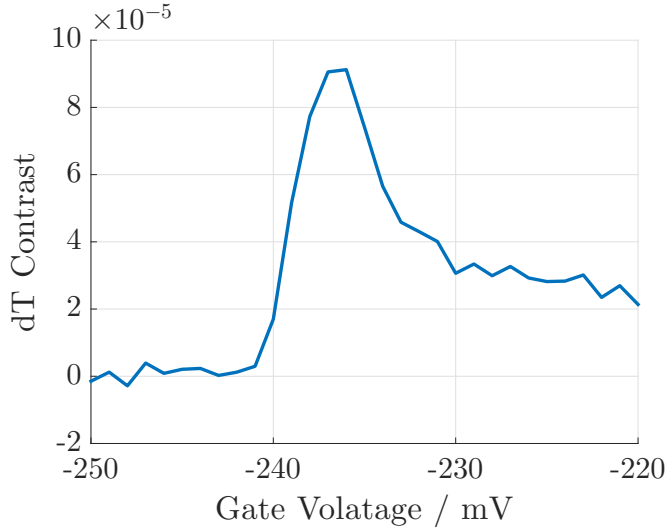

FIGURE 4.26: An asymmetric dT peak.

The asymmetry is quantified by taking the average of a set of points on either side of, and far away from the peak. Only if these two means are the same are the peaks symmetric. Figure 4.27a shows how the asymmetry changes as the quantum dot position in X, Y, and Z is changed as shown in Figure 4.27b. The line can be made more symmetric by fine adjustment of the position.

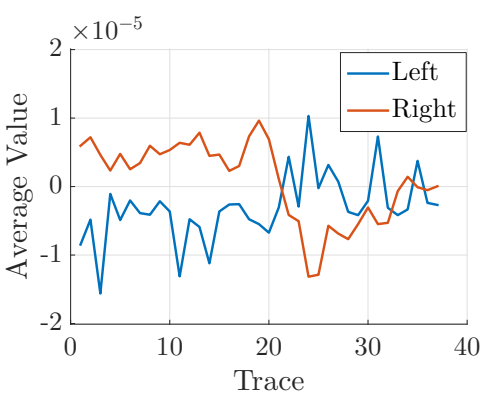

(a) The asymmetry of the line.

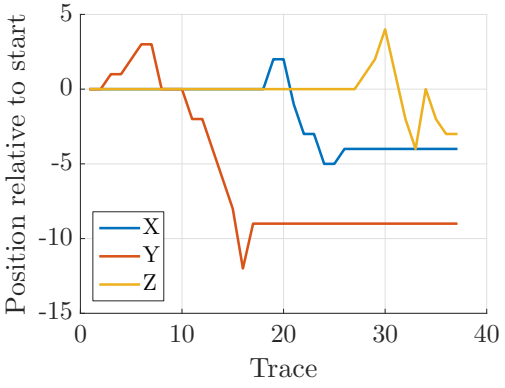

(b) The position of each of the three positioners.

FIGURE 4.27: A demonstration of how the dT line asymmetry can be fixed by changing the dot position.

4.4 Spectral suppression

In the microscope setup described above the reflected resonant laser light is removed from the collection path in RF by polarisation suppression. Any polarisation information in the quantum dot light is therefore lost. In order to generate and keep a photonic state in some polarisation basis the final analyser must be removed, and the reflected light removed in another way. The experiments in Chapter 5 require this capability. If the laser light and the quantum dot emission are spectrally detuned, then they can be separated through the use of a dichroic mirror or diffraction grating [127]. This section describes the setup used to separate laser and quantum dot fluorescence using a transmission diffraction grating.

4.4.1 Experimental setup

Light containing two spectral components (say laser light and detuned quantum dot fluorescence) is sent through a diffraction grating. This introduces an angular separation between the transmitted parts of each spectral component. The separation is used to allow collection of one component and attenuation of the other. The setup is shown in Figure 4.28a. A schematic is shown in Figure 4.28b.

A high efficiency transmission grating with 1600 grooves per mm is used (LightSmyth Technologies T-1500-930). The suppression capabilities of this setup are tested by sending light from a tunable laser through the *In* port and connecting the *Out* port to an amplified photo-detector. The laser is set to a wavelength λ_1 and the system is aligned to maximise coupling into the *Out* port. The laser is then tuned to a different wavelength $\lambda_2 = \lambda_1 + \Delta\lambda$ which causes the beam to become misaligned with the output as shown in Figure 4.29.

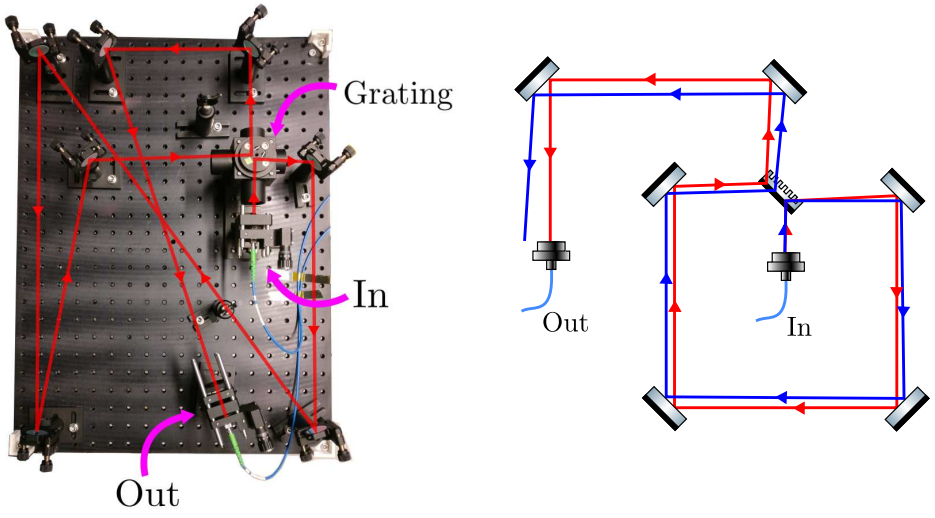

FIGURE 4.28: A photograph (a) and schematic (b) of the experimental setup used for the spectral suppression of laser light reflected from the sample. The element in the middle of the schematic is a transmission diffraction grating. The red and blue lines in the schematic show the path of two spectrally separated beams. Only one path is traced in the photograph.

FIGURE 4.29: Movement of the laser spot on the *Out* port when the wavelength is changed by 1 nm. Before changing the wavelength the laser spot was aligned with the collection lens in the centre of the coupler (red cross).

In this way the system can be aligned to accept light at wavelength λ_1 and reject light at wavelength λ_2. Figure 4.30 shows how the photo-diode signal changes as the laser wavelength is scanned. In this case $\lambda_1 = 940.43$ nm and the laser is scanned to longer wavelengths.

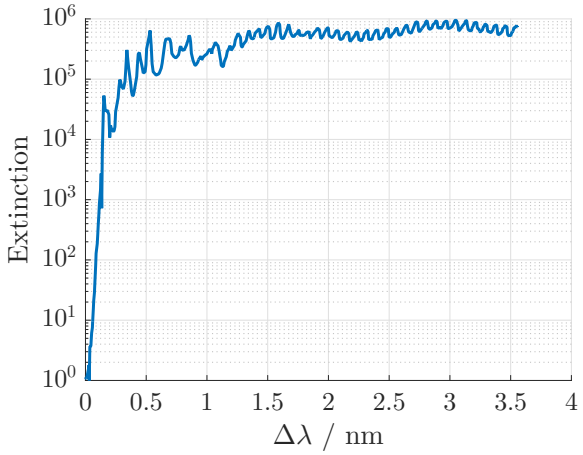

FIGURE 4.30: Laser extinction as the laser is tuned.

The figure shows that this setup can achieve a suppression ratio of at least 10^5 and almost 10^6 by going through the grating twice and having large distances between the mirrors (going twice through the grating increases the suppression by $\sim 2-3$ times). Notice that even at 1 nm when the spot is displaced entirely from the collection lens (as in Figure 4.29) there is still a non-negligible amount of light entering it. Some of the residual signal is caused by large angle scattering off of optical elements upstream (this has been observed in other scenarios and most obviously on the microscope camera), however much of it also comes from broad laser background. Increasing the length of the arm does not help to reject this background since it follows the path aligned with the output port (red path in Figure 4.28a). To improve the suppression the excitation laser line is cleaned by passing it through a monochromator to remove the background. The monochromator used is the same spectrometer described Section 4.1.5 with a flip-mirror set to redirect the light to an exit slit as shown in Figure 4.31.

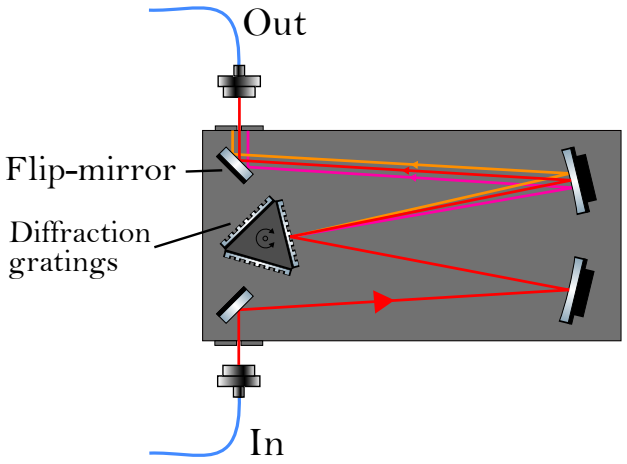

FIGURE 4.31: Schematic to show laser background reduction by passing it through the spectrometer in monochromator mode. Laser background is shown as orange and pink lines and the fundamental laser mode is shown in red. The background is spatially separated from the fundamental mode by the grating and blocked by the exit slit, resulting in a cleaner laser spectrum. The lens/filter assembly on the input is not shown for clarity.

A similar test shows that suppressing the laser background results in an increase of the spectral suppression ratio to $\sim 2.6 \times 10^6$. This is a factor of ~ 10 improvement. Loss in the system is determined by measurements of the optical power along the beam path in Figure 4.28 using a hand-held power meter (Thorlabs PM100D). The power lost in the setup is $13.4\% \pm 1.6\%$ and $21.0\% \pm 1.4\%$ for P and S polarised light respectively. This is power loss due to scattering, absorption, and grating inefficiencies.

4.4.2 Photoluminescent excitation

To demonstrate the use of the setup a photo-luminescence excitation (PLE) type experiment is performed on the X_{2-} singlet-triplet transitions of a quantum dot. The level scheme is shown in Figure 4.32a. A quantum dot is found using the techniques in Section 4.3 that exhibits the characteristics of the X_{2-} charge state. The narrow linewidth laser is tuned so that it is near-resonant with the singlet transition (red arrow). For this experiment the reflected laser is attenuated by crossed polarisers by a factor $\sim 5 \times 10^5$. Light from the collection fibre is sent straight to the spectrometer. Figure 4.33 shows the image captured on the spectrometer CCD when the gate is scanned.

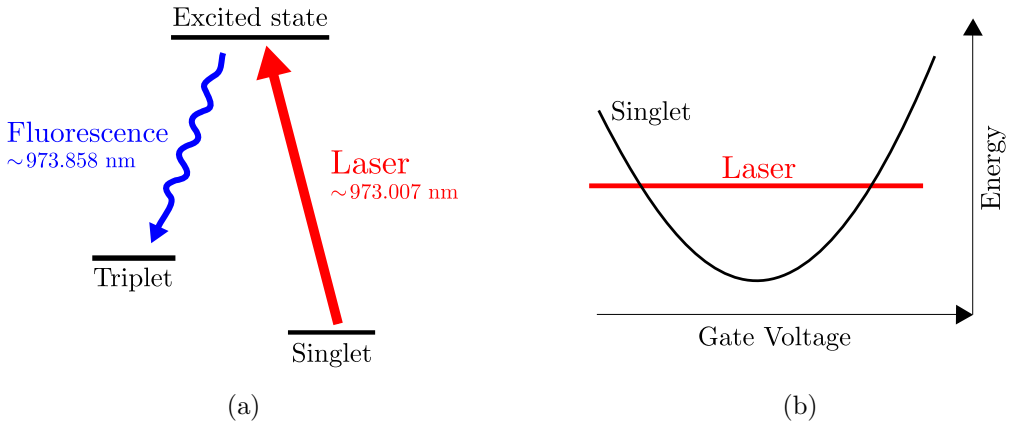

FIGURE 4.32: (a) A simplified picture of the three transitions of the X_{2-} which are used to perform the photo-luminescent excitation experiment. A laser drives population from the singlet to the excited state (red arrow), which can then decay to the triplet (blue arrow). (b) The behaviour of the singlet transition energy with gate voltage. The near parabolic shape comes from tunnel coupling between the different charge distribution states in the system.

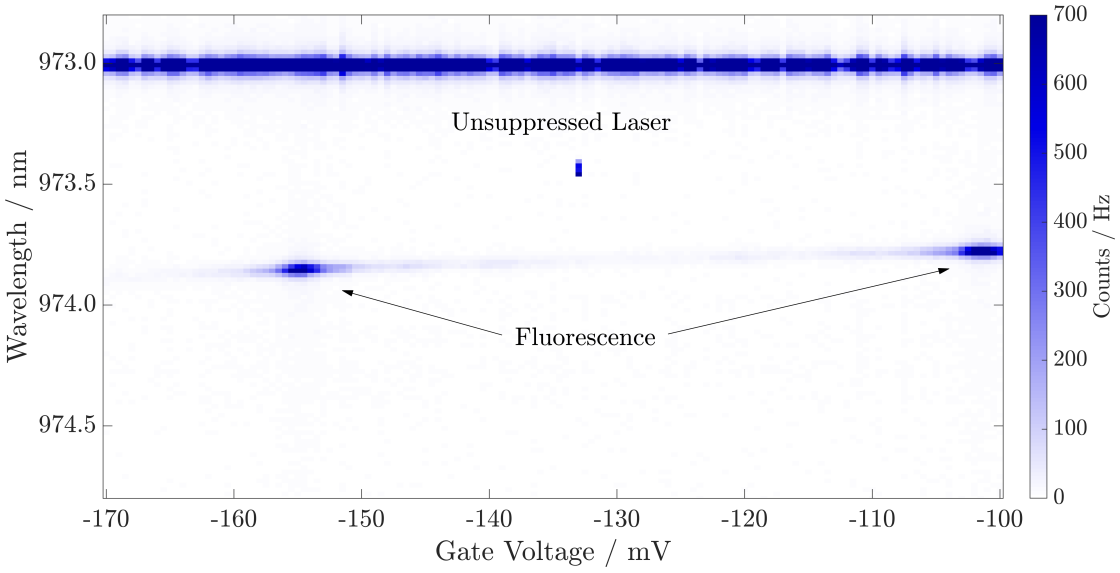

FIGURE 4.33: Photo-luminescent excitation whilst pumping the singlet transition with the excitation laser suppressed by polarisation only. Imaged on the spectrometer CCD.

The strong feature that is independent at a wavelength of 973.007 nm is unsuppressed laser light. The two bright points occur when the singlet transition is tuned into resonance with the laser by the DC Stark shift. There are two bright points because the singlet comes into resonance with the laser twice as shown in Figure 4.32b.

Now the light from the collection fibre is sent through the spectral suppression stage aligned to pass light at a wavelength of 973.858 nm. The output of the spectral suppression stage is sent to the spectrometer. Figure 4.34 shows the image on the spectrometer

CCD demonstrating that laser line is effectively filtered out by the suppression stage.

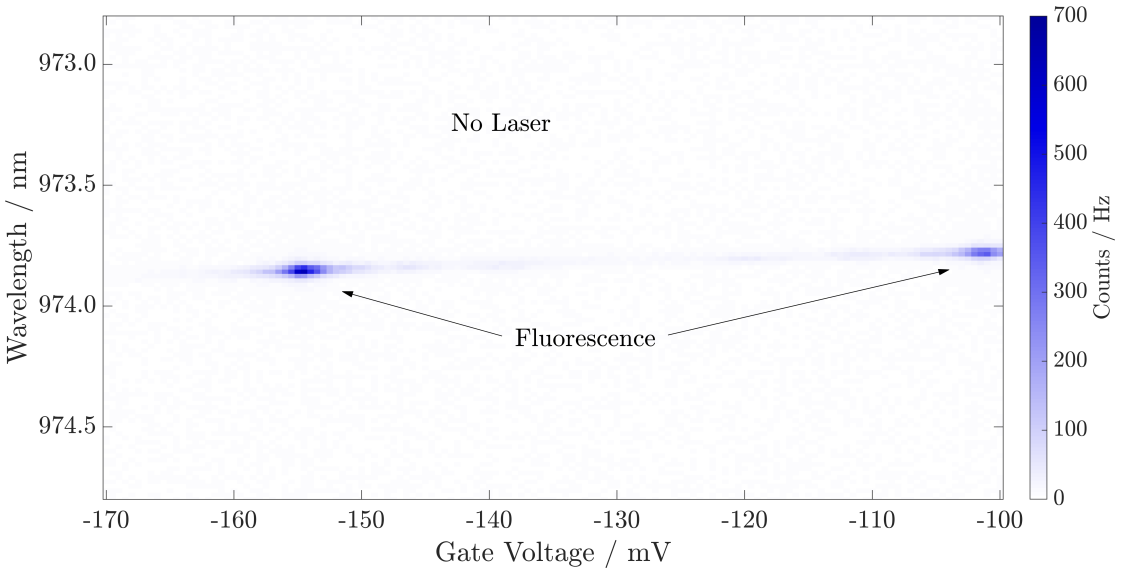

FIGURE 4.34: Photo-luminescent excitation whilst pumping the singlet transition, imaged on the spectrometer. The excitation laser is no-longer visible since it is suppressed by polarisation and the spectral suppression stage.

Figure 4.35 shows the heights of the two fluorescence peaks with (red line) and without(blue line) the spectral suppression stage in-line. When the suppression stage is added, both peak heights reduce due to losses in the setup. In addition the peak at larger voltage is further decreased. The light in this peak is at a different wavelength to that in the other peak (due to the DC Stark shift of the excited state) and so is partially attenuated. The width of the peaks at low and high gate voltage are not strictly the same since the transition at each gate voltage is nearer or further away from the edge of the charge stability region. Closer to the edge, the rate of co-tunnelling induced relaxation increases which can broaden the transitions.

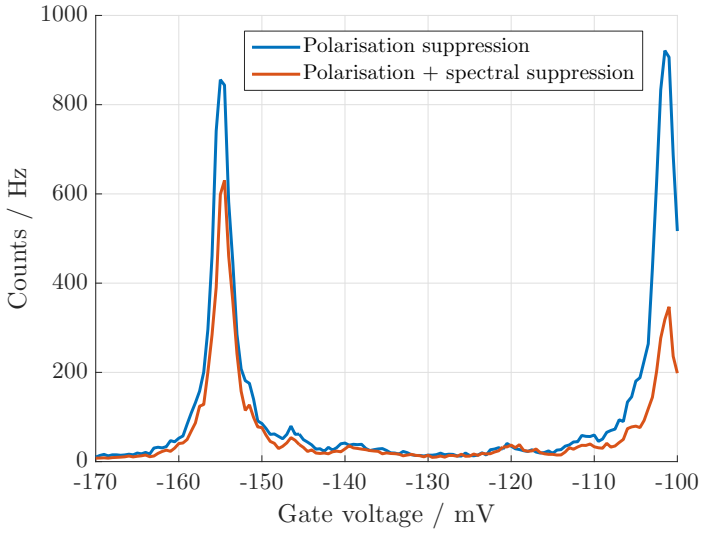

FIGURE 4.35: Comparison of fluorescence peak heights with and without spectral suppression stage.

4.5 Conclusion

In this chapter the construction and operation of the confocal microscope setup has been described. The microscope built here along with the supporting equipment and software was used for all measurements in this thesis.

Chapter 5

Monitoring the nuclear spin environment of a coupled quantum dot

As described in previous chapters, spin qubits in InGaAs quantum dots suffer from decoherence induced by the hyperfine interaction between the electron spin and the spins of the atomic nuclei that make up the quantum dot. This interaction presents itself as an effective magnetic field (known as the Overhauser field), and it is fluctuations of this effective field that lead to dephasing of the electron spin. The theme of this chapter is the development of a scheme to allow fast detection of the Overhauser field in a tunnel coupled quantum dot pair. Ultimately, the goal is to detect the fluctuations of the Overhauser field in real-time, i.e. faster than the dynamics of the field itself. When combined with fast control of the effective magnetic field experienced by the quantum dot, this could allow active stabilisation of the nuclear spins [128, 129], in order to reduce the dephasing rate of electron spin qubits [46, 47].

In this chapter, the concept of the coupled quantum dot field sensing procedure is first described using the simplified system of a neutral single quantum dot. After explaining the fundamental problem with using neutral excitons for this purpose, it is argued that a coupled quantum dot with two-electron singlet-triplet states is much more suitable. To show this, the dynamics of the singlet-triplet states under optical excitation are

simulated, and it is shown that the system would allow fast estimation of both the magnitude and direction of the Overhauser field. This is followed by a proof-of-concept experiment, where a coupled quantum dot is used to sense an externally applied magnetic field. During the experimental investigations, a highly unexpected feature was discovered when resonantly driving the optical transitions from the spin-singlet state at magnetic fields above 500 mT. This feature is studied in detail in Section 5.2.3. The final section 5.3 discusses the prospects for developing schemes to compensate for fluctuations in the Overhauser field.

5.1 Field sensing model

5.1.1 Mechanism

To explain the basic concept of the field-sensing procedure, it is helpful to look at the simplified system of a neutral single dot, which has a ground state that is empty. To start with the electron-hole exchange interaction is ignored, which means the optically excited eigenstates of the dot can be written as $\left|\downarrow\Uparrow\right\rangle$ and $\left|\uparrow\Downarrow\right\rangle$, corresponding to the z-projections of the bright exciton pseudospin [130, 131] with energies E_R and E_L respectively. The ground and excited states form a so-called V level scheme, where the transition to E_R corresponds to a right-circularly polarised photon, and the transition to E_L to a left-circularly polarised one. The empty quantum dot is driven using a resonant laser pulse with polarisation state

$$e \propto \begin{pmatrix} \alpha_0 \\ \beta_0 \end{pmatrix} \tag{5.1}$$

which is written in the R/L basis (i.e. the first component corresponds to R-polarisation and the second to L-polarisation). This laser pulse initialises the neutral exciton in the corresponding normalised state

$$\left|\psi_0\right\rangle = \alpha_0\left|\downarrow\Uparrow\right\rangle + \beta_0\left|\uparrow\Downarrow\right\rangle \tag{5.2}$$

(which requires that the laser pulse is short enough to couple to both levels [132], or alternatively that the laser energy is tuned in the middle of the two excited states). Due

to the neutral quantum dot's V level scheme, the neutral exciton can be initialised in any state on the Bloch sphere by the appropriate choice of laser polarisation. If a magnetic field is present, the exciton created by the laser pulse will start precessing around it with a frequency corresponding to the energy splitting between the eigenstates. Treating the bright exciton as a pseudospin-1/2, it interacts with the field through the Hamiltonian

$$H_B = \mu_B g_X \mathbf{S} \cdot \mathbf{B}_{\text{tot}} \tag{5.3}$$

where g_X is the exciton g-factor and $\mathbf{S}$ is the spin matrix of the exciton. The total field $\mathbf{B}_{\text{tot}} = \mathbf{B}_{\text{ext}} + \mathbf{B}_N$ is the vector sum of the external magnetic field $\mathbf{B}_{\text{ext}}$ and the effective Overhauser field $\mathbf{B}_N$.

This precession will be cut off when the exciton radiatively decays back to the empty quantum dot ground state, which occurs at a stochastic collapse time t_c. Just before the collapse the exciton is in the state

$$\alpha(t_c)\big|\downarrow\Uparrow\big\rangle + \beta(t_c)\big|\uparrow\Downarrow\big\rangle \tag{5.4}$$

The polarisation state of the emitted photon will carry information on the effective magnetic field $\mathbf{B}_{\text{tot}}$ via the coefficients $\alpha(t_c)$ and $\beta(t_c)$. This means that if the cycle of initialisation, precession and emission is repeated many times, and the collected photons are sent to a polarisation analyser projecting them onto one of six polarisations (R,L,H,V,D,A), both the magnitude and direction of $\mathbf{B}_{\text{tot}}$ can be deduced. The initialisation, precession and emission are depicted in Fig. 5.1.

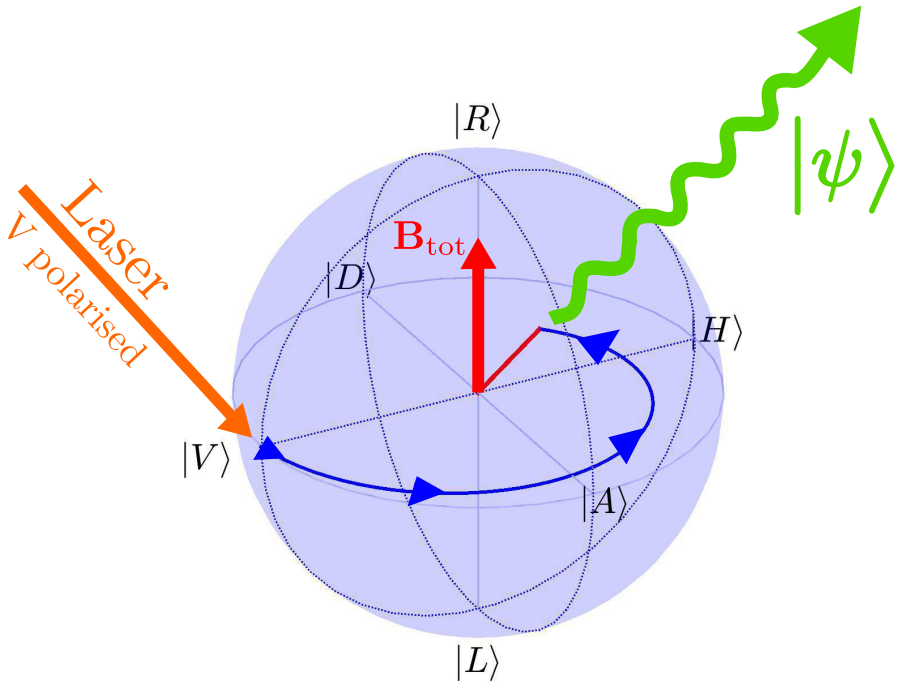

FIGURE 5.1: A cartoon depicting the field sensing mechanism. A vertically polarised laser (orange arrow) initialises the exciton into the state $|V\rangle$ on the Bloch sphere. It precess (blue arrows) under the action of the total field (red arrow) before radiatively decaying into a photon (green arrow) in state $|\psi\rangle$. The state $|\psi\rangle$ depends on where the exciton was on the Bloch sphere when it decayed. This depends on three things; where the exciton was initialised on the Bloch sphere, the strength and direction of the total field, and the time at which the exciton decayed. By repeating this process many times with an appropriate initialisation laser polarisation and by analysing the emitted photons' polarisation state in an appropriate basis, the strength and direction of the total field can be reconstructed. States on the Bloch sphere are the polarisation states that an exciton at that position would decay into, e.g. $|R\rangle = |\downarrow\Uparrow\rangle$ and $|L\rangle = |\uparrow\Downarrow\rangle$. The other states are $|H\rangle = \frac{1}{\sqrt{2}}(|R\rangle + |L\rangle)$, $|V\rangle = \frac{i}{\sqrt{2}}(|L\rangle - |R\rangle)$, $|D\rangle = \frac{1}{\sqrt{2}}(|R\rangle + i|L\rangle)$ and $|A\rangle = \frac{i}{\sqrt{2}}(|R\rangle - i|L\rangle)$.

The reconstruction can be most easily seen for a field along the z-direction, such that $|\downarrow\Uparrow\rangle$ and $|\uparrow\Downarrow\rangle$ are the bright exciton eigenstates. In this case, the polarisation state of the spontaneously emitted photon is

$$\alpha(t_c)|R, E_R\rangle + \beta(t_c)|L, E_L\rangle \tag{5.5}$$

Note that (5.5) contains two different frequency components E_R and E_L. However, measuring the emitted photons is done with single-photon detectors, which are typically broadband. (This issue of detecting a polychromatic state with a broadband detector is addressed in more detail in Section 6.3.4). The single-photon detector projects the

energy component of the state onto

$$\left|E_{\text{det}}\right\rangle = \frac{1}{\sqrt{2}}\left(\left|E_R\right\rangle + \left|E_L\right\rangle\right) \tag{5.6}$$

which leads to a photon polarisation state

$$\frac{1}{\sqrt{2}}\left(\alpha(t_c)\left|R\right\rangle + \beta(t_c)\left|L\right\rangle\right) \tag{5.7}$$

By repeating the cycle many times and analysing the emitted photons in a polarisation analysis setup, the probability that a photon is detected in any of the polarisation states (R,L,H,V,D,A) can be reconstructed. (Note that the mathematical procedure is more involved if the effective field is not along the quantisation axis z; however, the final conclusion is the same, and a full reconstruction of the field using the emitted photons is possible in this case as well.)

Instead of following each trajectory, the statistics of many cycles of the process can be found by integrating a master equation including spontaneous emission at a rate γ_{sp}. The solution gives the 'average' state over many trajectories of the experiment. The probability of observing a photon in a particular state (R,L,H,V,D,A) can be calculated by projecting the density matrix onto the polarisation state. Because the excited population decay is taken into account by the master equation, the total probability of seeing a photon of a particular polarisation $S \in \{H, V, D, A, R, L\}$ is proportional to

$$\text{Pr}_S = k\int_0^{t_{\text{max}}} \text{Tr}\left(\left|S\right\rangle\!\left\langle S\right|\rho(t)\right)\ \text{d}t \tag{5.8}$$

where k is a constant and t_{max} is a time which physically represents the time up until which photon counts are recorded (e.g. only counts in the first 10 ns may be recorded). In practice t_{max} can be truncated since the probability of a detecting a photon after several times the radiative lifetime is exponentially low. The constant k is chosen such that the detection probability for orthogonal bases is normalised e.g. $\text{Pr}_H + \text{Pr}_V = 1$. This will not automatically be the case when the driving laser is added later on.

Statistics with no field

Consider a simple case where the exciton is initialised in the state (5.2), and there is no field. In this case the only dynamics come from the decay of the excited state due to spontaneous emission at rate γ_{sp}, so $\alpha(t) = \alpha_0 \exp(-\gamma_{\text{sp}} t/2)$ and $\beta(t) = \beta_0 \exp(-\gamma_{\text{sp}} t/2)$. In addition, the eigenbasis of the system is not uniquely defined so it can be chosen to be the heavy hole exciton states $\left| \downarrow\Uparrow \right\rangle = \left|R\right\rangle$ and $\left| \uparrow\Downarrow \right\rangle = \left|L\right\rangle$ where the equalities reflect the polarisation of the photon that would be generated by decay of either state. If the photon is measured in the basis $\left|S\right\rangle = \left|R\right\rangle$ and $\left|\overline{S}\right\rangle = \left|L\right\rangle$, then by (5.8) and using the fact that $\Pr_S + \Pr_{\overline{S}} = 1$ the detection probabilities are

$$\Pr_R = |\alpha_0|^2 \qquad\qquad \Pr_L = |\beta_0|^2 \tag{5.9}$$

Hence measuring in the Z basis (R/L polarisation) results in statistics that directly reflect the initial exciton state.

Measuring in the X basis where $\left|S\right\rangle = \left|H\right\rangle = \frac{1}{\sqrt{2}}\left(\left|L\right\rangle + \left|R\right\rangle\right)$ and $\left|\overline{S}\right\rangle = \left|V\right\rangle = \frac{i}{\sqrt{2}}\left(\left|L\right\rangle - \left|R\right\rangle\right)$ gives

$$\Pr_H = \frac{|\alpha_0 + \beta_0|^2}{2} \qquad\qquad \Pr_V = \frac{|\alpha_0 - \beta_0|^2}{2} \tag{5.10}$$

Lastly in the Y (D/A) basis where $\left|S\right\rangle = \left|D\right\rangle = \frac{1}{\sqrt{2}}\left(\left|R\right\rangle + i\left|L\right\rangle\right)$ and $\left|\overline{S}\right\rangle = \left|A\right\rangle = \frac{i}{\sqrt{2}}\left(\left|R\right\rangle - i\left|L\right\rangle\right)$ the statistics are

$$\Pr_D = \frac{|\alpha_0 - i\beta_0|^2}{2} \qquad\qquad \Pr_A = \frac{|\alpha_0 + i\beta_0|^2}{2} \tag{5.11}$$

In this simple case, since the exciton does not precess the statistics from the experiment correspond directly to the polarisation of light used to excite the exciton. For example exciting with R polarised light means

$$e = \begin{pmatrix} 1 \\ 0 \end{pmatrix} \Longrightarrow \qquad \alpha_0 = 1, \;\; \beta_0 = 0 \tag{5.12}$$

and so using equations (5.9), (5.10) and (5.11) the detection probabilities are

$$\Pr_R = 1 \qquad \Pr_L = 0 \qquad \Pr_H = \Pr_V = \Pr_D = \Pr_A = 0.5 \tag{5.13}$$

Similarly, for H polarised excitation

$$\implies \quad e = \frac{1}{\sqrt{2}} \begin{pmatrix} 1 \\ 1 \end{pmatrix} \implies \quad \alpha_0 = \beta_0 = \frac{1}{\sqrt{2}} \tag{5.14}$$

and so

$$\Pr_H = 1 \qquad \Pr_V = 0 \qquad \Pr_R = \Pr_L = \Pr_D = \Pr_A = 0.5 \tag{5.15}$$

These simple examples act as a sanity check to make sure the simulation procedure gives the right results.

Statistics with a field in the z-direction

Now if there is a non-zero total field directed along the $\hat{\mathbf{z}}$ axis the exciton pseudo-spin precesses around the Z axis until it decays. The exciton dynamics when initialised with an H polarised pulse are shown in Figure 5.2. The system is integrated by a master equation and the probabilities are calculated according to (5.8).

The evolution of the excited state plotted on the Bloch sphere in Figure 5.2b shows the exciton starting in the state initialised by the excitation laser and precessing around the field along the Z axis. The excited state population is given by the length of the Bloch vector. Since the precession is in the equatorial plane, the relative excited state population in each state shown in Figure 5.2a stays the same. Spontaneous emission causes the excited state population to decay exponentially. The total probabilities of detection of $\left|R\right\rangle$ and $\left|L\right\rangle$ photons are equal to the normalised areas under the graphs in Figure 5.2a shown in green and red respectively. If the fluorescence is collected and analysed in the $\{\left|R\right\rangle, \left|L\right\rangle\}$ basis, there is an equal number of photon counts on each detector. Changing the strength of the field changes the precession speed but not the projection onto the R/L axis. Thus by observing equal counts in R and L it can be inferred that the field was along $\hat{\mathbf{z}}$.

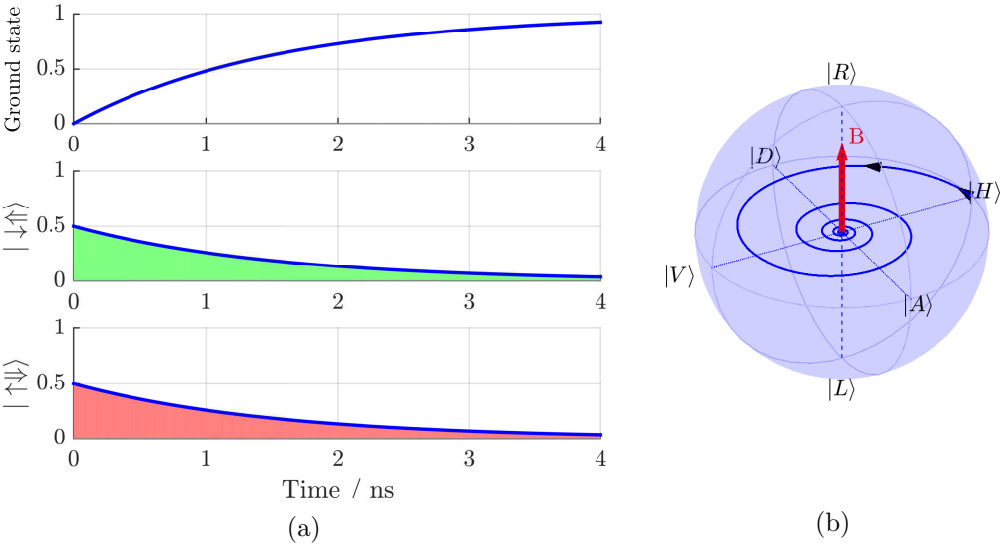

FIGURE 5.2: Dynamics of an exciton initialised along the $\hat{\mathbf{x}}$ axis by an H pulse, in the presence of a magnetic field along $\hat{\mathbf{z}}$. (a) Populations of the vacuum, spin up and spin down exciton states. (b) Blue line shows the evolution of the excited state on the Bloch sphere with population given by the length of the Bloch vector. The red line is the magnetic field vector.

However Figure 5.2b also shows that the projection along the H/V and D/A directions do change in time. The associated detection probabilities are shown in Figure 5.3.

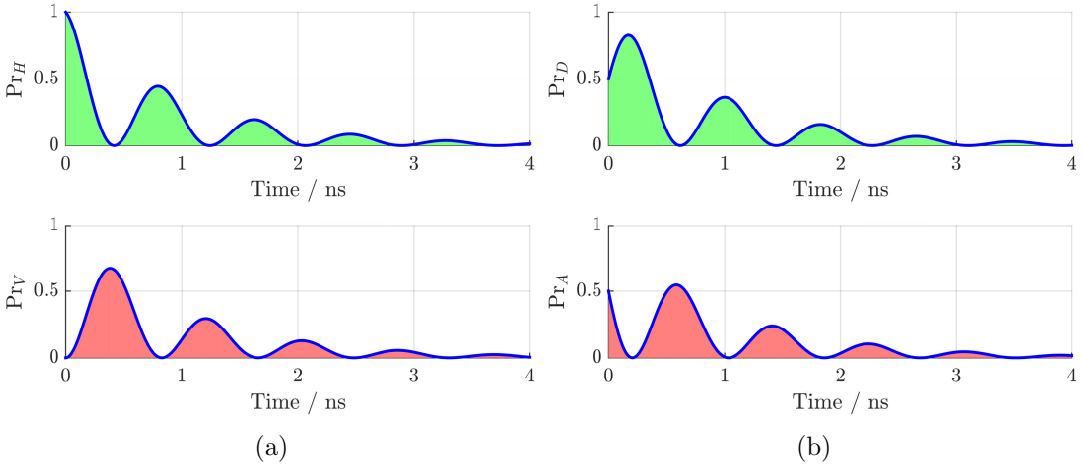

FIGURE 5.3: Changes in the photon detection probability in the (a) H/V and (b) D/A bases when the exciton is initialised along the $\hat{\mathbf{x}}$ axis by an H pulse, in the presence of a magnetic field along $\hat{\mathbf{z}}$.

In this case the strength of the magnetic field *does* have an effect on the probabilities of measuring H, V, D and A. A simple case would be a reasonably weak magnetic field such that the exciton precesses toward $|D\rangle$, but has significantly decayed by the time it reaches $|A\rangle$. Then it would be expected to see far more integrated counts on the

D detector than the A detector. Figure 5.4 shows how all of the detection statistics depend on the field strength. To generalise, the g-factor is set to 1 and the magnetic field is expressed in terms of the exciton Zeeman energy in μeV. In addition, the different lines on each plot correspond to different pump polarisations i.e. different initial exciton states.

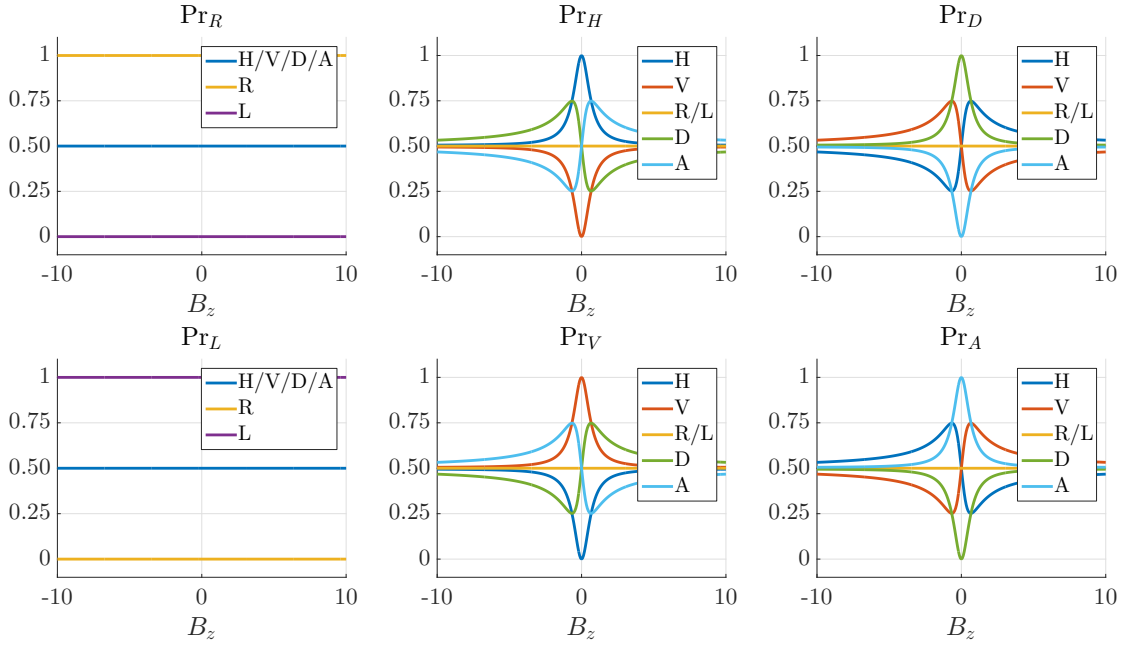

FIGURE 5.4: Detection probabilities for all 6 polarisation channels as a function of the field strength along $\hat{\mathbf{z}}$. The different lines in each plot shown the probabilities for different excitation polarisations.

First of all, note that the two left-hand plots in each row (detection in R and L bases) show no change in field. This is exactly because of the in-plane precession as discussed above, which is true no matter where the exciton is initialised. The top-middle graph shows the probability for detecting in H. When the exciton is initialised in H or V, the distribution is symmetric around zero. When initialised along H, any $\hat{\mathbf{z}}$ field (regardless of its magnitude or sign) will cause the exciton to precess *away* from H and towards V. This results in the monotonic decrease in Pr_H with $|B_z|$. This behaviour is essentially what causes the Hanle effect [133], where spin precession about one axis (due to a magnetic field) causes apparent depolarisation when viewed along a perpendicular axis. The reverse argument applies when initialising along V. When photons are detected along D, on the other hand, the direction of the field becomes important. A field along $+\hat{\mathbf{z}}$ causes the exciton to precess towards D whilst a field along $-\hat{\mathbf{z}}$ causes it to

precess away. Consequently the detection probability increases or decreases from 0.5, respectively. For large fields the precession time is fast compared to the decay time and so all probabilities tend towards 0.5 as the integrand in (5.8) averages out.

5.1.2 Usage and performance

The probability distributions for H, V, D and A detection under H excitation (blue lines in Figure 5.4) taken together hold enough information to infer the field magnitude and direction. This is demonstrated in Figure 5.5 where the probabilities are shown for initialising in H, and detecting in H (blue line) or D (red line). Given a perfect system and a sufficient number of statistics, Pr_H and Pr_D can be estimated, shown on the figure by the blue and red dashed lines. Knowledge of Pr_H constrains the field to be at either of the blue circles (where the dotted line crosses the 'theoretical behaviour' of the blue solid line). Similarly, knowledge of Pr_D constrains the field to be at either of the red circles. Thus by combining the two the field can be constrained to the dark gray line at -2.5 μeV.

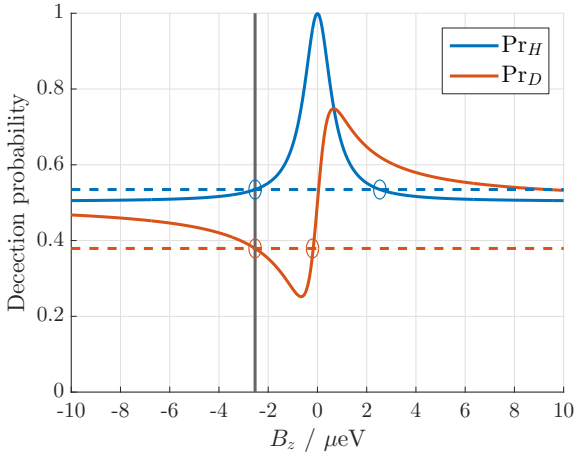

FIGURE 5.5: Detection probabilities for H (blue) and D (red) as a function of field strength along $\hat{\mathbf{z}}$ when initialising in H. Estimates of the probabilities (dashed horizontal line) can be used together to determine the strength of the field (gray vertical line).

Realistically there will be noise in the measurements as well as an error due to the finite number of samples collected. The following takes a Bayesian approach to the estimation problem as done by Bonato *et al.* [128] where the plots in Figure 5.4 are interpreted as likelihood functions $\mathcal{L}(S|T, B_z)$ which give the probability of detecting a photon of polarisation S given that the exciton was initialised in state T and the field strength

was B_z. The initial prior $\mathcal{P}(B_z)$ is uniform for all B_z, meaning to begin with there is no information about B_z. If pumped with polarisation T, the system will evolve according to the above and the photon mode will be measured, resulting in a click in one of the detectors labelled S. The posterior distribution is then calculated according to Bayes' rule. Repeated pump and measurement cycles continue to update the posterior, where the posterior distribution $P(B_z)_{n+1}$ becomes the prior for the next cycle, as shown in (5.16)

$$\mathcal{P}(B_z)_{n+1} = \mathcal{P}(B_z)_n \times \mathcal{L}(S|T, B_z) \tag{5.16}$$

The effect is to narrow the posterior distribution around the most probable value of the field (defined as the position of the maximum of the posterior). This is demonstrated in Figure 5.6 which shows shows the normalised posterior distribution after several detection events, following (5.16). The purple curve (with most events) is strongly peaked around the true value of B_z marked by the black dashed line.

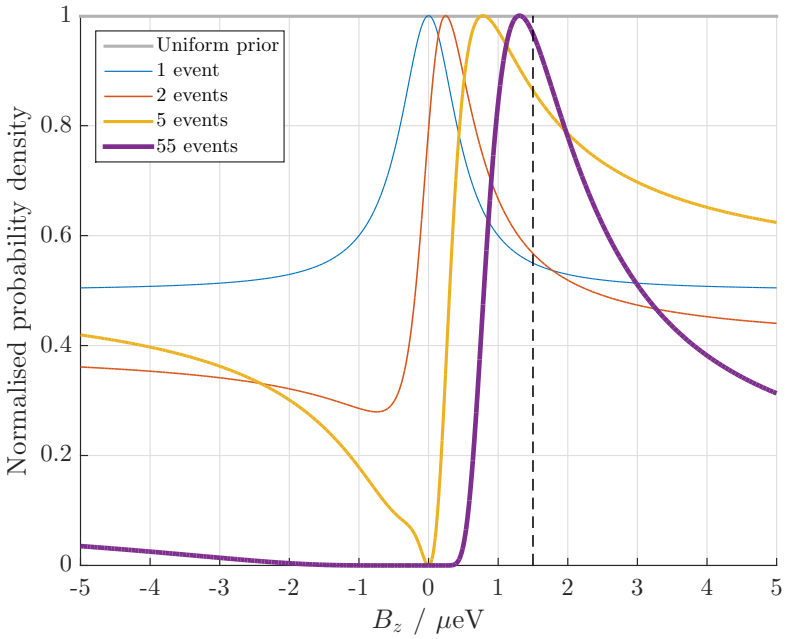

FIGURE 5.6: Demonstration of how the probability distribution changes with increasing numbers of detection events. Starting with the uniform prior, as more detection events occur the posterior distribution peaks around the true field at 1.5 μeV (dashed vertical line).

Increasing the number of trials shrinks the peak in the posterior around the true value.

To estimate the realistic error in this scheme the posterior is evaluated for different values of the field B_z and total counts $N = N_{H/V} + N_{D/A}$. For each event 1 to N, a detection channel is randomly selected from H, V, D or A according to the distribution $\{\frac{1}{2}\mathrm{Pr}_H, \frac{1}{2}\mathrm{Pr}_V, \frac{1}{2}\mathrm{Pr}_D, \frac{1}{2}\mathrm{Pr}_A\}$ which emulates randomly choosing to measure in the H/V or D/A basis. Each time the prior is multiplied by the selected likelihood function. This is repeated for a range of fields. Figure 5.7a shows how the maximum error between the most probable and true values of B_z varies with the total number of events N, for different field ranges. As N increases the probabilities p_S estimated from measurements become better estimates of the true likelihoods Pr_S and so the prediction error decreases (the peak of the posterior gets closer to the true value). Figure 5.7b shows the uncertainty in the prediction, calculated as the standard deviation of the most probable value over several simulations for each B_z and N. For small fields the variance in the p_S decreases as N is increased due to the larger number of statistics. The improvement is slower for larger fields likely because the likelihoods vary more slowly at high fields.

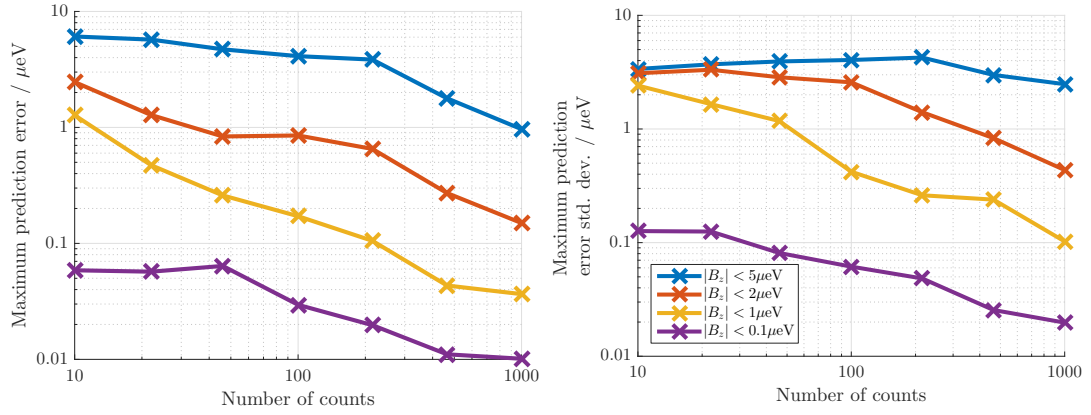

FIGURE 5.7: Detection events are randomly generated according to the likelihood functions. The detection events are then used in the Bayesian update routine to construct the posterior distribution over the field strength. (a) shows the maximum error (across all fields) between the most likely value of the field according to the reconstructed posterior, and the true field. (b) shows the variation in the most likely field value over 30 repeats of statistics generation and reconstruction routine.

A typical exciton g-factor of 1 results in a splitting of ~ 2 μeV for a magnetic field of 35 mT. According to the figures above, to measure this field to within 0.4 μeV $\equiv$ 7 mT would require $\sim$ 1000 measurements. In the quantum dot devices used in this thesis, the

radiative lifetime is typically around 1 ns. The collection efficiency of the experimental setup used described in Chapter 4 is $< 0.1\%$. In micro-pillar devices the collection can be as high as 66% and Purcell enhancement can reduce the radiative lifetime to 84 ps [134]. Given an experimental collection of γ_{c}, photon detection efficiency of γ_{det} and a radiative lifetime of τ_{rad}, detecting N photons will take approximately

$$t_{\mathrm{measure}} = \frac{N\tau_{\mathrm{rad}}}{\gamma_{\mathrm{c}}\gamma_{\mathrm{det}}} \tag{5.17}$$

Using the latter parameters as well as a typical photon detection efficiency of 10%, such a measurement would take $\sim 1000 \times 84\mathrm{ps}/\left(0.66 \times 0.1\right) \approx 1.3\mu\mathrm{s}$.

5.1.3 Exciton state preparation

The analysis so far has assumed that the exciton can instantaneously be initialised anywhere on the Bloch sphere. This is an appropriate assumption when initialised by a very short laser pulse, with a spectral width smaller than the splitting between the exciton eigenstates. For reasonable values of the Overhauser field, this corresponds to sub-nanosecond pulse widths. If the pulse is *not* short compared to the precession period, the model must include not only the exciton precession but also the coupling of the system to a classical laser field. To include this a classical laser interaction Hamiltonian is added to the system

$$H_{\mathrm{int}} = \frac{1}{2}\Omega_u\left(t\right)\left(\left|0\right\rangle\left\langle \downarrow\Uparrow\right| + \left|\downarrow\Uparrow\right\rangle\left\langle 0\right|\right) \tag{5.18}$$

$$+\frac{1}{2}\Omega_d\left(t\right)\left(\left|0\right\rangle\left\langle \uparrow\Downarrow\right| + \left|\uparrow\Downarrow\right\rangle\left\langle 0\right|\right) \tag{5.19}$$

where $\Omega_u\left(t\right) = f\left(t\right)R\alpha_0$ and $\Omega_d\left(t\right) = f\left(t\right)R\beta_0$ are the time dependent Rabi couplings for the right and left-hand circularly polarised components of the laser field. R is a number which controls the power and global phase of the laser, and $f\left(t\right)$ is a pulse envelope function. The laser is assumed to always be tuned to the zero field exciton transition energy. The laser drives population into the exciton state (5.2) whilst spontaneous emission drives the system back to the ground state.

Setting the Rabi frequency R to 1 μeV, the simulation to derive the likelihoods is repeated for different pulse lengths τ_{pump}. For simplicity the pulse envelope used is just a

square pulse with length τ_{pump}. Figure 5.8 shows the results of such a scan when driving the system with an H polarised laser ($\alpha_0 = \beta_0 = 1/\sqrt{2}$).

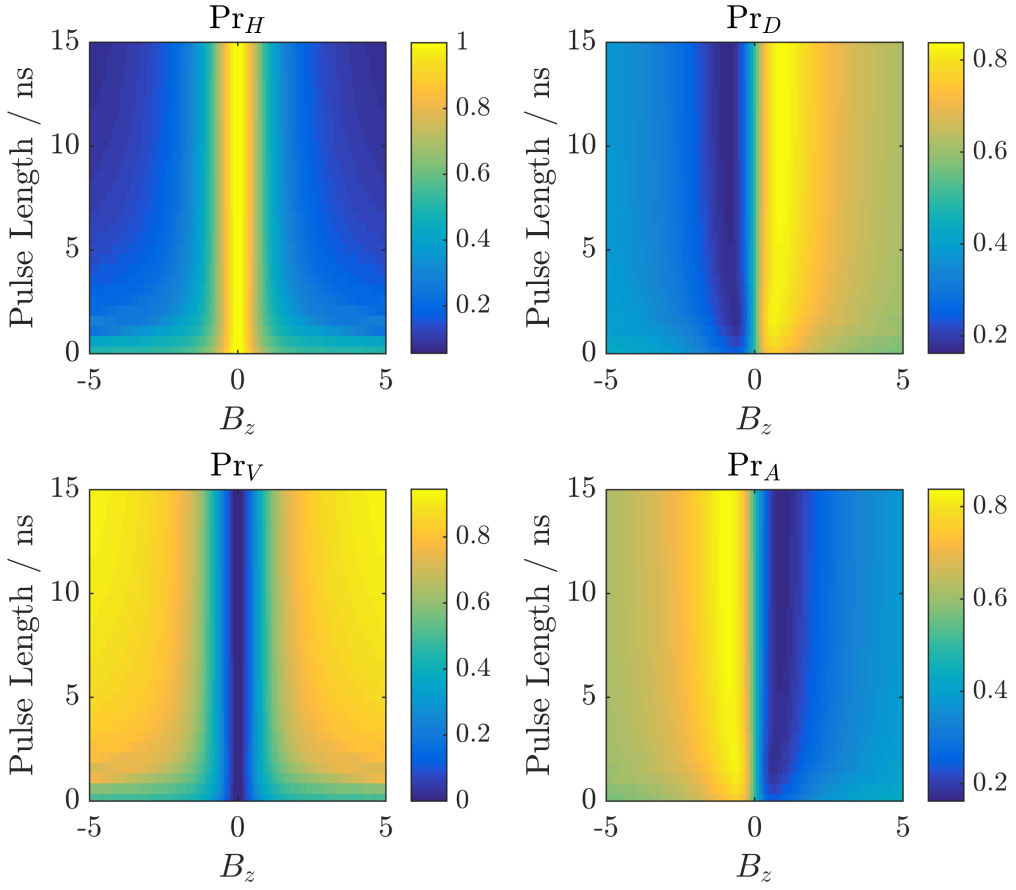

FIGURE 5.8: Probability of detecting a photon in various bases when pumped with an H polarised laser, as a function of the field strength along $\hat{\mathbf{z}}$, and the duration of the pump.

When the pulse is very short (compared to the precession period and radiative lifetime) the situation is very similar to the one above where the exciton is instantaneously initialised. Slices along each of the plots for small τ_{pump} would be similar to the corresponding figures in Figure 5.4. As the pulse length increases, the peak compresses around $B_z = 0$. Since the pump power is kept constant, in the case of small τ_{pump} little exciton population is generated so few counts would be observed. However, for most of the system evolution (until the excited state population decays) only the B_z field is present and so the situation reverts back to the previous case of instantaneous initialisation. The statistics are the same since they are normalised.

5.1.4 Continuous wave experiment

As the results of the previous section suggest, similar results can be obtained by performing a continuous wave experiment, i.e. with the laser constantly on. This simplifies the experimental demonstration considerably since access to a pulse laser is not required. This also means that the steady state of the system can be used to predict the relevant statistics. To confirm this a master equation is solved which includes a constant driving laser and exciton decay via spontaneous emission. The photon detection statistics are found by applying the same photon projectors from the previous section to the steady state solution ρ_{ss}. The statistics are qualitatively the same as before.

5.1.5 Sensing magnetic fields in arbitrary directions

For external field sensing, the 1D results above could be acceptable depending on the particular application. However the Overhauser field fluctuates in all directions. In this section the model is extended to the case of an arbitrary field direction.

Model and likelihoods

To do this, the total field $\mathbf{B}_{\text{tot}}$ is explicitly represented in polar coordinates as

$$\mathbf{B}_{\text{tot}} = \begin{pmatrix} B\sin\theta\cos\phi \\ B\sin\theta\sin\phi \\ B\cos\theta \end{pmatrix} \tag{5.20}$$

where B is the magnitude of the field expressed in energy, θ is the polar angle and ϕ is the azimuthal angle. The likelihoods are calculated as a function of the parameters B, θ and ϕ in the same way as in Section 5.1.1. The one dimensional likelihoods of Figure 5.4 are now replaced by a three dimensional stack shown in Figure 5.9.

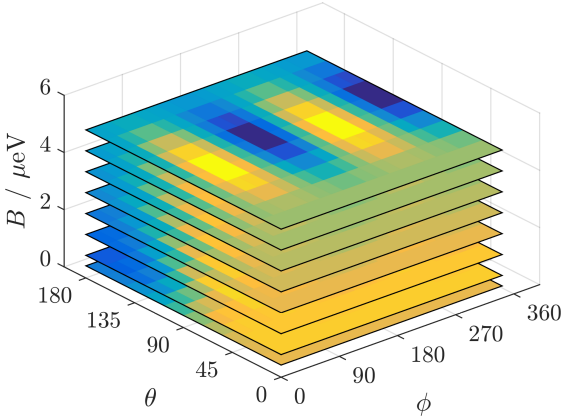

FIGURE 5.9: Likelihoods calculated for B, ϕ and θ.

Figure 5.10 shows some of these likelihoods for H excitation with detection in the H, R and D bases for two different field values. To make sense of them a few select cases can be examined. For example the red crosses in the $\Pr_H$ likelihoods are points where the field lies along the $\hat{\mathbf{x}}$ axis ($\theta = 90°$, $\phi = 0°$ and $180°$). Since the exciton is initialised along this axis by the H excitation, it does not precess under the field and the probability of later detecting an H photon remains 1. The white crosses show positions where the field lies along the $\hat{\mathbf{y}}$ axis ($\theta = 90°$, $\phi = 90°$ and $270°$) so now any field will cause the exciton to precess away from H, lowering the detection probability. Finally at the green cross the field is along the $\hat{\mathbf{z}}$ axis ($\theta = \phi = 0°$) so any field will again lower the detection probability. At first glance there would seem to be a problem since in all the likelihoods several combinations of B, θ and ϕ give the same probability. It is not immediately obvious whether there is enough information in the likelihoods to unambiguously determine the values of the parameters and thus find a reliable prediction for $\mathbf{B}_{\text{tot}}$.

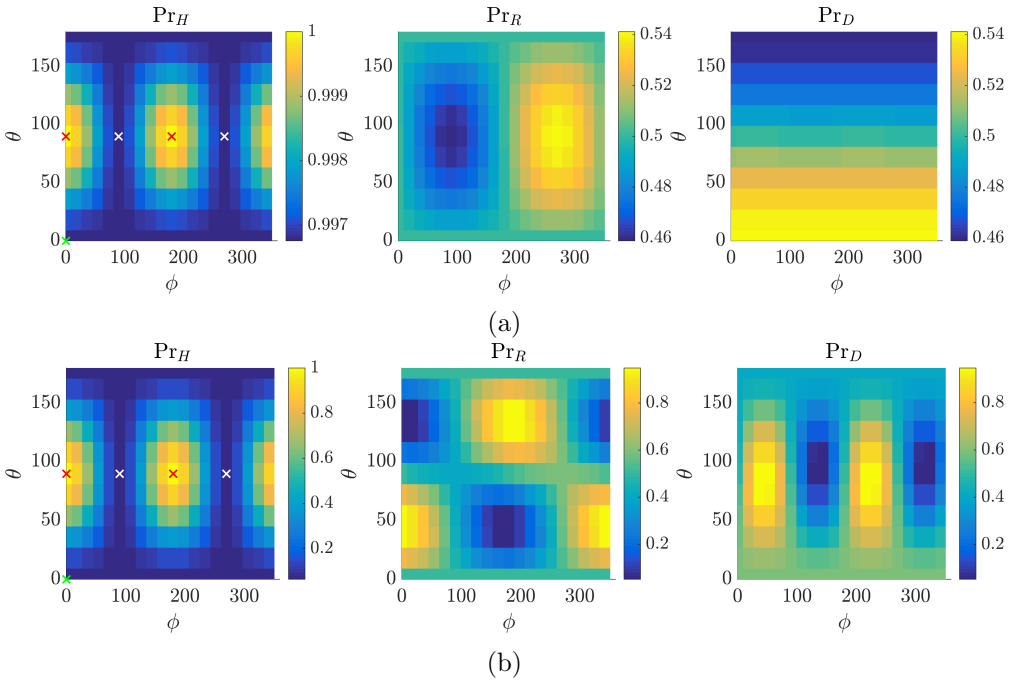

FIGURE 5.10: Likelihoods for photon detection in channels H, R and D when pumping the system with H polarised light in the presence of a field of strength (a) 58 neV and (b) 6.9 μeV. The angles θ and ϕ give the direction of the field vector.

Unambiguous field determination

To tackle this question the problem is approached in the same way as demonstrated in Figure 5.5. For a given parameter combination (B, θ, ϕ) the likelihoods predict values for Pr_{TS}, the probability of detection in basis S when exciting with polarisation T. The task is to estimate Pr_{TS} from experimental data obtained by exciting and detecting in various polarisation bases, and use the estimates to work back to the values of B, θ and ϕ. Having hypothetically performed an experiment similar to the one in Section 5.2 and found estimates for Pr_{TS}, all the likelihoods are searched to find all possible combinations of B, θ and ϕ that give the same values for Pr_{TS} within some margin ϵ_{TS}. The error margin allows for inevitable noise in the estimates for the Pr_{TS}. An example of this searching method is shown in Figure 5.11.

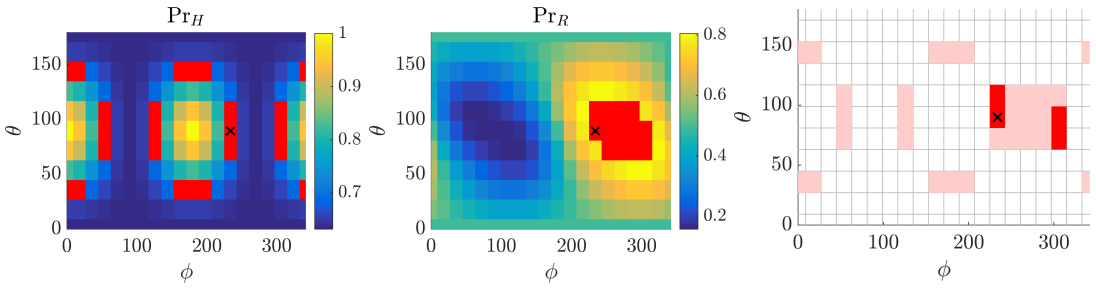

FIGURE 5.11: Likelihoods for photon detection in channels (a) H and (b) R for a field of strength of 0.79 μeV. The credible regions corresponding to a field of 0.79 μeV at angles 90° and 234° are shown in red with the true field location shown by the black cross. (c) the combination of credible regions from (a) and (b).

As an example the likelihoods for a magnetic field described by parameters $(13.6\text{mT}, 90°, 234°)$ give probabilities 0.719 and 0.825, for Pr_{HH} and Pr_{HR} respectively. The location of these parameters is shown by the black cross in Figure 5.11. Figures 5.11a and 5.11b show the likelihoods for 0.79μeV with all the regions where the probabilities are equal to Pr_{HH} and Pr_{HR} shaded in red. These are the credible regions predicted by these likelihoods. Figure 5.11c shows both credible regions combined (pale red) and the overlapping regions (red). Using the same reasoning shown in Figure 5.5, the true values of θ and ϕ must lie somewhere in the red region. The same is done for all the likelihoods in the stack for different values of B and the result is a volume in (B, θ, ϕ) space where all the parameter values within it could give rise to the observed data.

It follows that if more likelihoods are added to the search (which have different structure) then the overlap of the credible regions will get smaller and smaller. It turns out that in order to consistently have a single credible region and thus an unambiguous estimation for B, θ and ϕ, all excitation and measurement combinations from the bases H, R and D are required (the likelihoods for V, L and A give the same information so are not required). All the likelihoods taken together *do* allow unambiguous determination of the parameters.

Usage and performance

To connect this to experiment the search process is evaluated for different combinations of B, θ and ϕ. The experiment is assumed to be shot noise limited with N photon detection events spread over each pair of detectors. The error margins ϵ_{TS} are then

calculated in the same way as (5.23) with the photon counts on channel S equal to $N \times \Pr_{TS}$.

Remarkably, for $N > 1000$ and $B > 0.35$ μeV the angles θ and ϕ are always accurately predicted to within the simulation accuracy of ± 2.25 and ± 9 degrees respectively. This is because of the large variation in the structure of the likelihoods with θ and ϕ as shown for example in Figure 5.10. For smaller fields the likelihoods vary by a very small amount in θ and ϕ (note the small ranges in Figure 5.10a) which causes large spread in the credible values of θ and ϕ. The magnitude B is not so accurately predicted because the likelihoods vary slowly in the B dimension. This is visible by the gradual slope at large field in the one dimensional likelihoods shown in Figure 5.4 which are after all just slices of these more general likelihoods along $\theta = \phi = 0$. Thus the predicted field vectors tend to lie along a line from the origin.

In the spirit of compensating for this field using the upcoming ideas of Section 5.3 the estimated $\hat{\mathbf{z}}$ component of the field is calculated for different parameter combinations. The spread in the credible values of $\tilde{B}_z$ is found by finding the $\hat{\mathbf{z}}$ components of all the fields that lie within the credible region. Figure 5.12a shows the spread in $\tilde{B}_z$ for $N = 10,000$. The behaviour is independent of the angle ϕ which is to be expected given the symmetry of the system. Up until a field strength of around 10 μeV a single credible region exists (only one of the grid squares in Figure 5.11c would be red) and so the uncertainty is limited by the simulation resolution (1.7 mT step size in field strength, 2.25° step size in θ, and 4.5° step size in ϕ). For higher fields the credible region grows in size and uncertainty increases due to this. The steps are caused by the discritization size of the simulation, which could be reduced at the expense of increasing the simulation time.

This process is repeated for several N and the maximum spread across all angles is shown in Figure 5.12b. There is again a minimum linear increase in uncertainty common to all N which is caused by the simulation resolution. Generally, having more detection events lowers the error margins ϵ_{TS} which in turn decreases the size of the credible region and decreases the uncertainty.

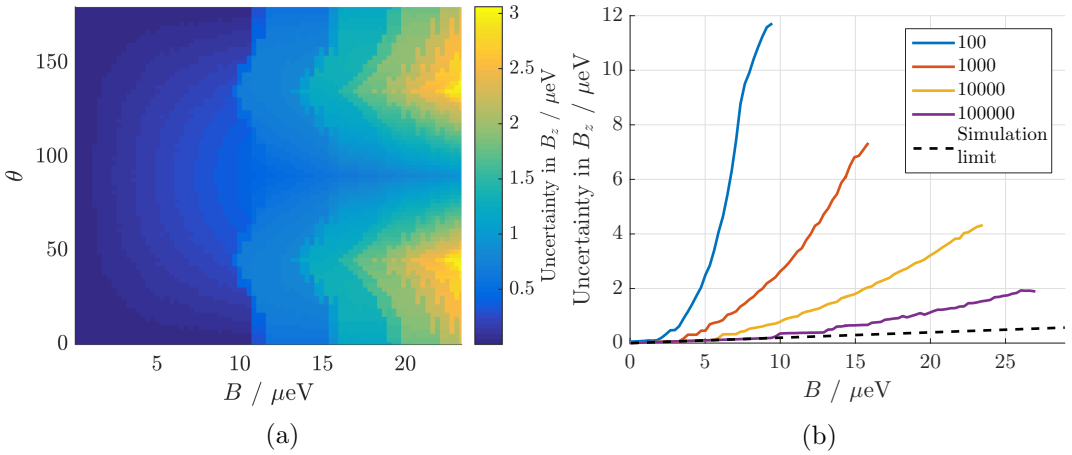

FIGURE 5.12: (a) Spread in the credible values of $\tilde{B}_z$ for $N = 10000$. (b) Maximum spread over all angles θ for different numbers of photon detections N.

To put this into real terms, a g-factor of 1 results in a splitting of $\sim$ 2 μeV for a magnetic field of 35 mT. Figure 5.12b shows that with $N = 1000$ the $\hat{\mathbf{z}}$ component of $\mathbf{B}_{\text{tot}}$ could be estimated to within the simulation accuracy of 0.1 μeV $\equiv$ 1.7 mT. N is the number of photon detection events across detection pairs of detection bases but nine combinations were used in the above simulations, so the actual number of detection events required to obtain this accuracy is 9000. Using again an exciton lifetime of 84 ps and combined collection and detection efficiency of 6.6%, such a measurement would take $\sim$ 9000 $\times$ 84 ps/0.066 $\approx$ 11.5 μs. This is comparable to the numbers found in Section 5.1.2.

5.1.6 Using singlet-triplet states in coupled dots

Using a neutral exciton as the 'probe' brings with it two disadvantages. Most importantly, the bright X_0 states are split and mixed by the anisotropic-exchange interaction. This interaction with a typical energy of around 10 μeV was neglected in the previous discussion, but it acts like a built in in-plane magnetic field for the exciton that can easily overwhelm a small Overhauser field [130]. Another issue is that due to the neutral exciton's very simple level scheme, it is not possible to spectrally separate the resonant excitation laser from the quantum dot emission. Typically, a crossed-polariser scheme is used to suppress the excitation laser by around six orders of magnitude, giving access to the quantum dot resonance fluorescence. However, this is not an option in this case, since field sensing requires access to the *polarisation* state of the quantum dot photons.

Both these issues can be solved by using a two-electron coupled quantum dot featuring singlet-triplet ($S-T$) ground states [115]. To use this system, a dot pair must be found that exhibits the X_{2-} charging region with accessible S and T ground states. At small magnetic field the relevant part of the X_{2-} level scheme simplifies to a Λ scheme as shown in Figure 5.13a.

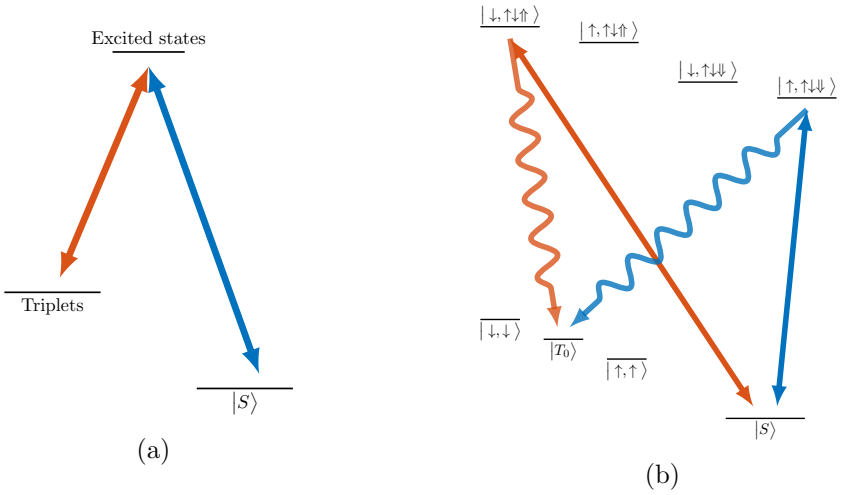

FIGURE 5.13: (a) A simplified level scheme in the X_{2-} system at zero field. Optical transitions between the triplets and the singlet ($|S\rangle$) are efficient. (b) A magnetic field splits the triplet and excited manifold revealing the full 8 levels. The straight arrows represent the possible transitions from the singlet when driving them with a laser. Wavy arrows represent paths of radiative emission from the excited states to the triplet ($|T_0\rangle$).

A magnetic field along $\hat{\mathbf{z}}$ splits the triplet manifold into three and the excited state manifold into four as shown in Figure 5.13b. The $|S\rangle = \frac{1}{\sqrt{2}}\left[|\uparrow,\downarrow\rangle - |\downarrow,\uparrow\rangle\right]$ state plays the role of the ground state in the previous analysis. The role of the excited states is played by $|\downarrow,\uparrow\downarrow\Uparrow\rangle$ and $|\uparrow,\uparrow\downarrow\Downarrow\rangle$. Transitions from $|S\rangle$ to $|\uparrow,\uparrow\downarrow\Uparrow\rangle$ and $|\downarrow,\uparrow\downarrow\Downarrow\rangle$ are forbidden if the magnetic field is along the z-axis.

In this system, the optically excited states consist of a spin singlet plus an unpaired electron and hole *in separate quantum dots*, so that the electron-hole interaction is negligible. This means no built-in effective field is present. Furthermore, if the tunnel barrier between the two dots is sufficiently thin, the S and T ground states can be split by a large energy of ~ 1 meV [82]. Therefore, the dot can be driven with a laser on the singlet transition, spectrally separate from the triplet channel (in which half the dot emission occurs), allowing the two to be separated with a grating without affecting the polarisation of the dot light. It has been shown that a fast effective relaxation

from triplet to singlet states can be engineered in coupled quantum dots by keeping the tunnel barrier between the reservoir and the quantum dot layer less than 50 nm [82], so that after emission in the triplet channel, the system is quickly reset (within a few nanoseconds) to the singlet ground state. This 'reset' time should be fast compared to the radiative lifetime (around 1 ns) in order to increase the measurement rate. Finally, by choosing which of the two quantum dots of a pair to excite, the nuclear field in either the left or right quantum dot can be probed. Due to the advantages mentioned above, it is decided to use this system to experimentally demonstrate the field sensing scheme.

5.2 Field sensing demonstration

With the basic principle understood an experimental demonstration can be attempted. To perform a proof of concept experiment an external magnetic field in the $\hat{\mathbf{z}}$ (growth) direction is used to emulate the Overhauser field. By varying the strength of the external field and recording the photon count in a particular basis for a known driving polarisation, the experiments conducted in silico above can be performed in the lab. To facilitate the experiment, the microscope setup of Chapter 4 is modified slightly as shown in Figure 5.14.

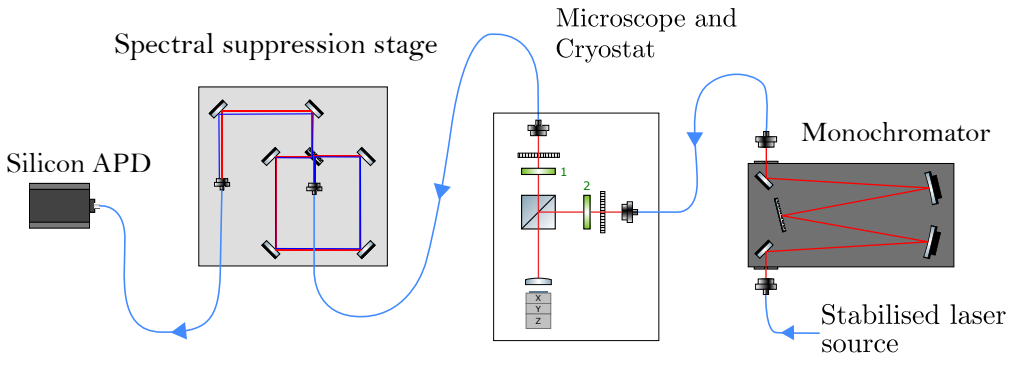

FIGURE 5.14: The experimental setup used for the field sensing experiment. The elements of the spectral suppression stage and microscope are described elsewhere in this thesis. The quarter wave plate in the microscope setup (green rectangle) is moved from position 1 to position 2 depending on the exact experiment at hand.

Wavelength and power stabilised light from the setup detailed in Section 4.1.4 is sent through the spectrometer working in monochromator mode to further suppress the laser side bands (it was demonstrated in Section 4.4 that this gives an additional factor of 10 suppression when using the spectral suppression setup). The light then passes via

fibre to the microscope. One change to the microscope is that the quarter wave plate (green rectangle in the schematic) is moved from the excitation arm to the collection arm, depending on the desired collection and excitation basis. Additionally one of the excitation pathways is removed, which allows the first beam sampler in Figure 4.4 to be removed. This ensures that the polarisation of the excitation light is not altered by the beam sampler's birefringence. The light collected from the microscope is passed to the spectral suppression stage where the excitation light is filtered out. Finally this filtered light is passed to a silicon avalanche photo-diode (APD).

This setup allows a quantum dot to be excited with light of arbitrary polarisation, and the fluorescence analysed in any polarisation so long as it is spectrally detuned from the excitation light.

5.2.1 Dot characterisation

By searching the sample and inspecting the PL, a dot is found which exhibits the required X_{2-} charging region with the singlet triplet states accessible. It is identified by looking for the characteristic shape of the X_{2-} transitions in a PL gate sweep, as determined in Chapter 3. The dot is first characterised using the techniques of Chapter 4.

Mapping out the $S-T$ transitions

The PL gate sweep for this dot is the one shown and fitted in Figure 3.20 of Chapter 3. Figure 5.15 shows the peak positions extracted from the PL gate sweep in the X_{2-} region, and the calculated singlet triplet splitting. The red and blue transitions correspond to the red and blue arrows in Figure 5.13a. There is another set of 4 excited states not shown in Figure 5.13a where the hole is in the left-hand dot, with a corresponding emission that is around 70 meV higher in energy (the energy difference is due to the difference in sizes of the quantum dots in the pair). For this reason, dots R and L are also referred to as the red and blue dots respectively.

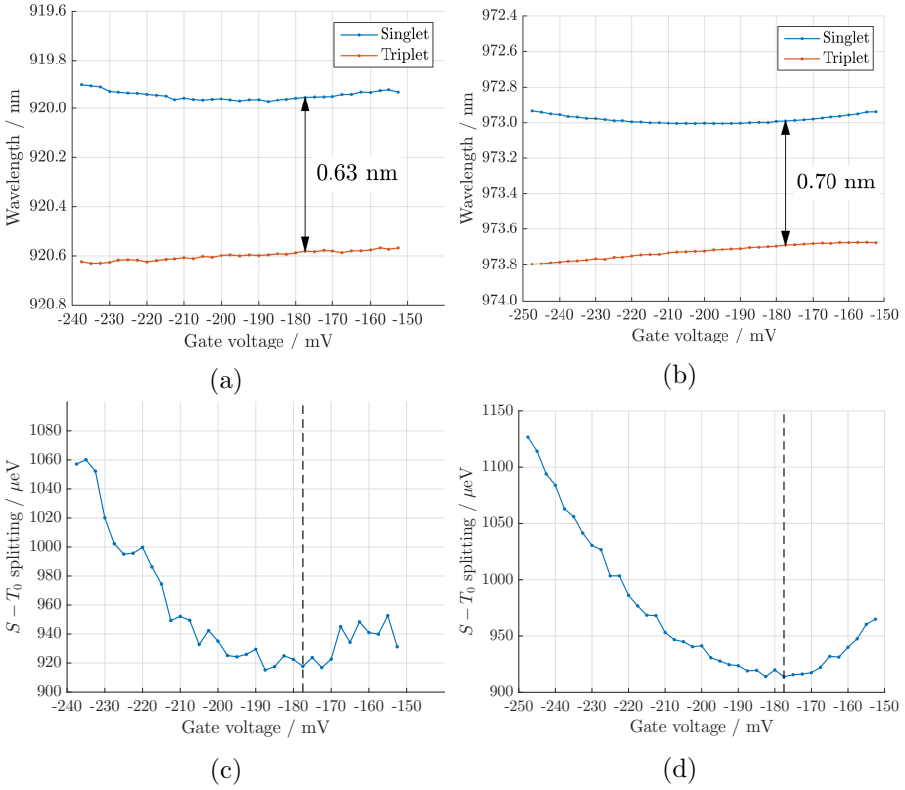

FIGURE 5.15: The energies of the singlet and triplet transitions in the (a) blue and (b) red dot extracted from the photo-luminescence (PL) gate sweep. The difference between the singlet and triplet transition energies has a minimum at the sweet-spot which occurs at the dashed line in the blue (c) and red (d) dots.

The system's 'sweet-spot' is found at the minimum of the $S - T$ splitting, which occurs here around -180 mV. At this voltage the singlet and triplet states are to first order insensitive to the magnetic and electric field fluctuations [115]. The S and T transitions are separated by around 0.7 nm, which would allow a suppression of $\sim 2.6 \times 10^6$ between light at the singlet and triplet wavelengths using the spectral suppression setup described previously.

In non-resonant PL measurements, the generation of charges around the quantum dot causes the dot transitions to shift in energy and gate voltage. To find the unperturbed transition energies, resonant dT gate scans of the singlet and triplet are performed. Gate scans of the red dot are shown in Figures 5.16a and 5.16b.

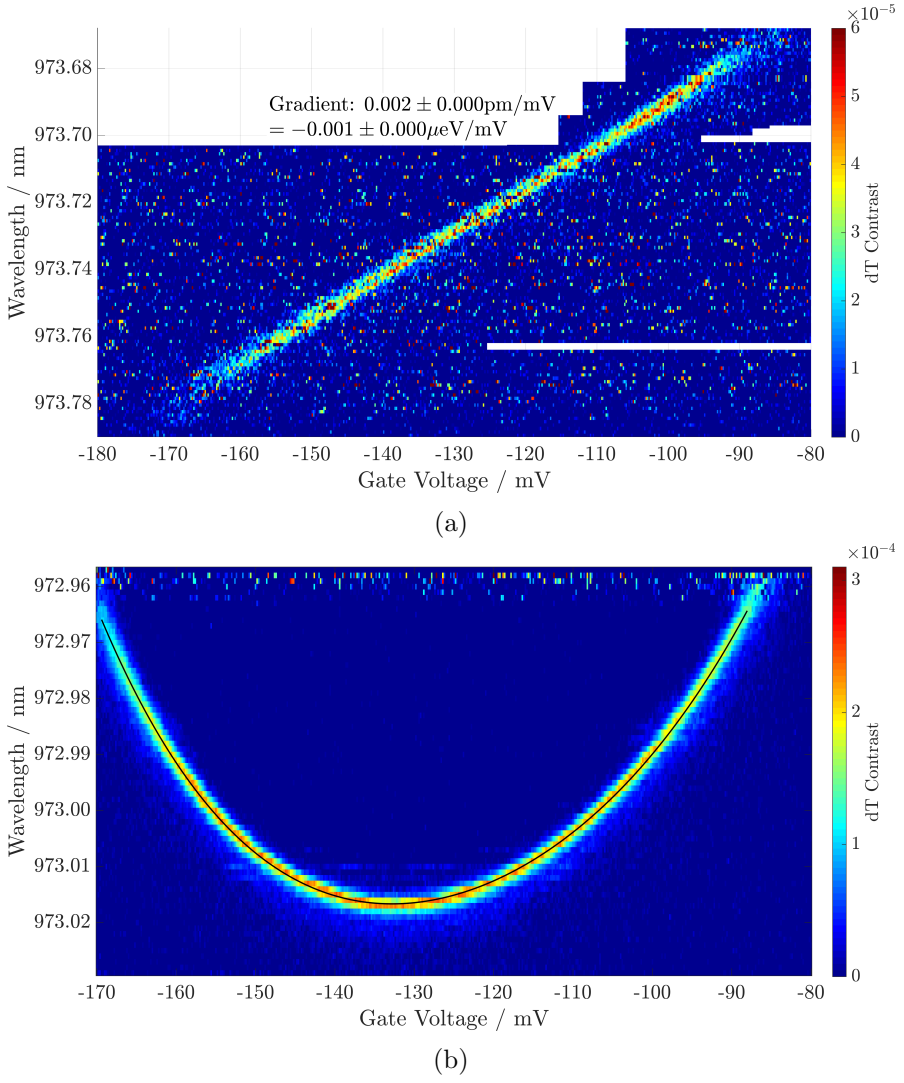

FIGURE 5.16: dT gate scans of the triplet (a) and singlet (b) transitions at 0 T.

Given the Λ level scheme in Figure 5.13 one would expect strong spin pumping when driving the S or T transitions with a single laser. Essentially, driving the singlet transition would quickly result in the system being shelved in the triplet state, where it is no longer resonant with the driving laser. This means that the resonant signal should show negligible contrast; however this is not observed in the measurements here. The reason for the maintained contrast is fast co-tunnelling with the reservoir accross the whole gate voltage range, which acts as a fast relaxation channel from the triplet to the singlet ground states, as has been seen in similar samples previously [82]. The fact that at a temperature of 4 K relaxation from T down to S is much faster than in the opposite direction, means that shelving in the T state is not as efficient as in the S state. This is reflected in the 10 times lower contrast of the T transition (Figure 5.16a) compared to

the contrast of the S transition (Figure 5.16b).

Choosing which transition to pump

Either the singlet transition (blue) can be driven, and fluorescence detected on the triplet transition (red), or the other way around. To decide between the two options, saturation and photoluminescence excitation (PLE) type experiments are performed.

Figure 5.17 shows the data from saturation experiments on the singlet and triplet transitions. Fitting these plots by the expressions in Section 4.3.7 allows extraction of the relation between power and Rabi frequency (as done in Section 4.3.7).

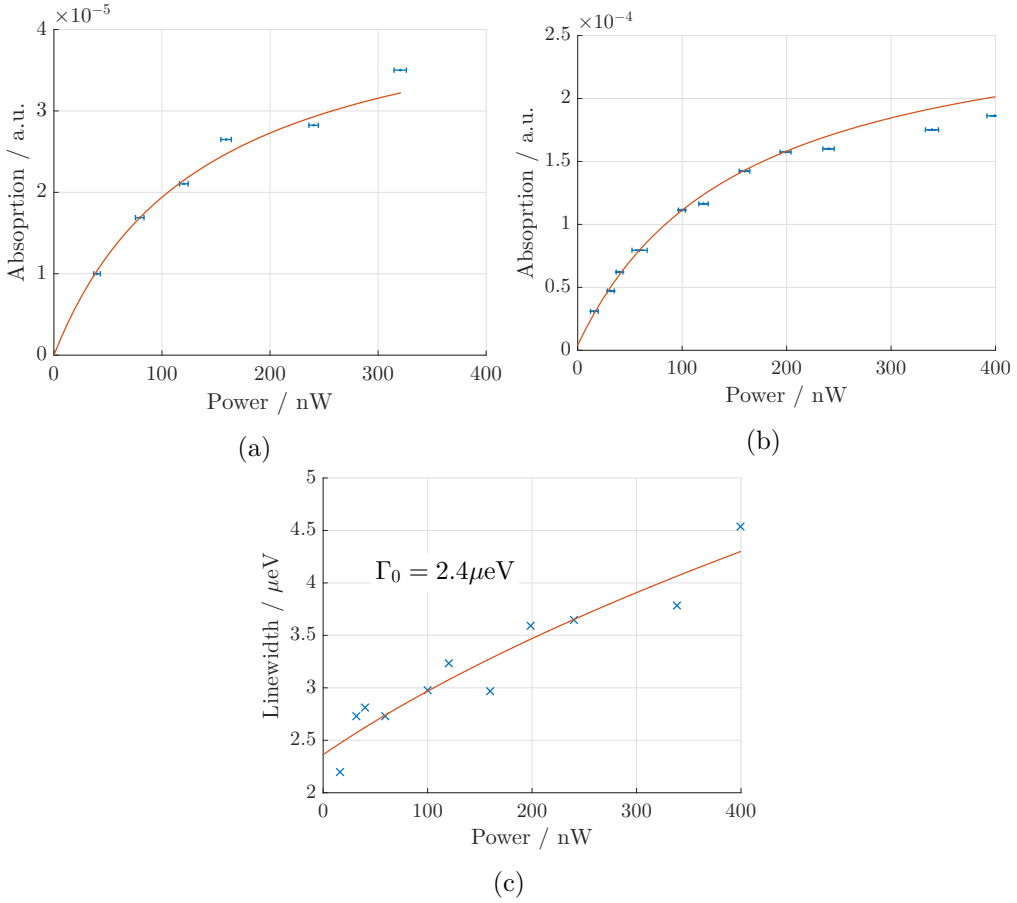

FIGURE 5.17: Saturation measurements of the singlet and triplet transitions performed with differential transmission. The peak heights of the triplet (a) and singlet (b) transitions, and the linewidth of the singlet (c) are extracted from these measurements. The linewidth of the triplet cannot be extracted due to low signal-to-noise.

The singlet linewidth of 2.4 μeV can be extracted from the saturation width but a low signal-to-noise ratio prevents extraction of the triplet width in this way. Instead a triplet

linewidth of 6.7 μeV is extracted from Figure 5.16a. These measurements show that the absorption contrast of the triplet is ~ 10 less than for the singlet.

This can be investigated further by comparing PLE for both the singlet and triplet. In these experiments the excitation laser is linearly polarised and strongly attenuated by an analyser. The experiment in Section 4.4 is repeated by scanning the gate in a small region around where the singlet and triplet are resonant. Figure 5.18 shows two data sets: one where the laser is resonant with the singlet (right), and one where the laser is resonant with the triplet (left). The figure shows the half of each data set containing the PL signal from the dot and not the laser.

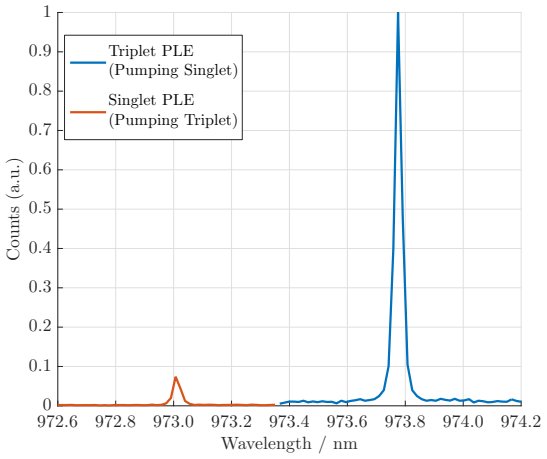

FIGURE 5.18: Comparison of the photoluminescence excitation (PLE) signal when driving either the singlet or triplet transition.

Driving the triplet and observing the singlet gives a count rate of $\sim 100 \pm 20$ Hz compared to $\sim 1000 \pm 100$ Hz the other way round, giving a contrast of around 10. This is consistent with the difference in contrast in the dT scans, and also with previous observations of $S - T$ states in these quantum dots [82]. For the sensing experiment it is advantageous to have bright transitions, and so in the implementation the singlet is driven and fluorescence collected from the triplet.

Characterisation of magnetic response and anomalous transitions

To demonstrate a proof of concept of the field sensing scheme using an external magnetic field, the magnetic properties of the quantum dots should be known in advance. To investigate this, dT gate scans of the singlet are taken at various magnetic fields. From the level scheme in Figure 5.13b, it is clear that the singlet should split into two lines

corresponding to the red and blue straight arrows. In fact, Fig. 5.19 shows that the singlet is split into three lines, the expected red and blue branches plus an unexpected middle branch. Even more surprisingly, at higher fields the middle line is only present in a restricted range of gate voltages. The range of gate voltage in which it appears, depends on the laser wavelength and the direction in which the gate is swept.

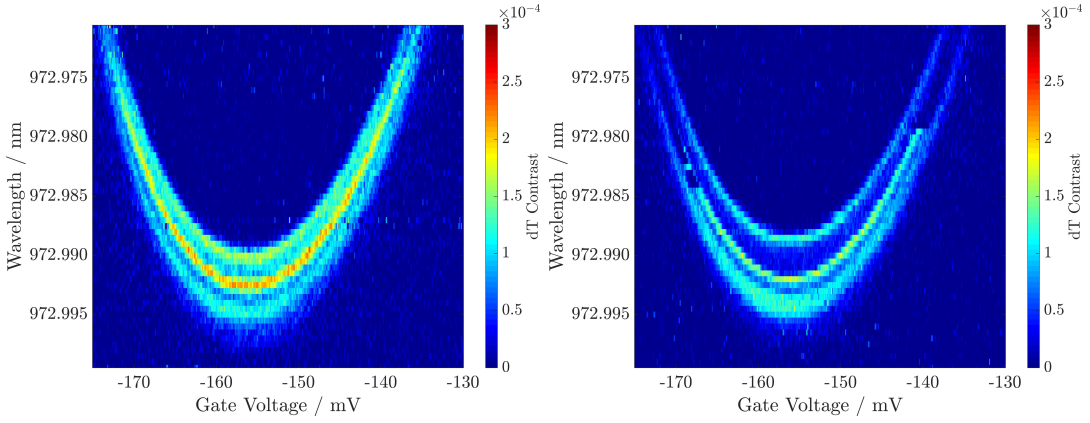

FIGURE 5.19: dT gate sweeps of the singlet transition at (a) 500 mT and (b) 600 mT.

At 500 mT the middle transition is present throughout the entire range of gate voltages. However, from $\sim$ 600 mT upwards it only appears for certain gate voltages and wavelengths. To extract the g-factor and diamagnetic shifts of the transitions, the line position is extracted directly by scanning the laser wavelength across the transitions at a fixed gate voltage for different magnetic fields. The fitted peaks from the dT traces are shown in Figure 5.20.

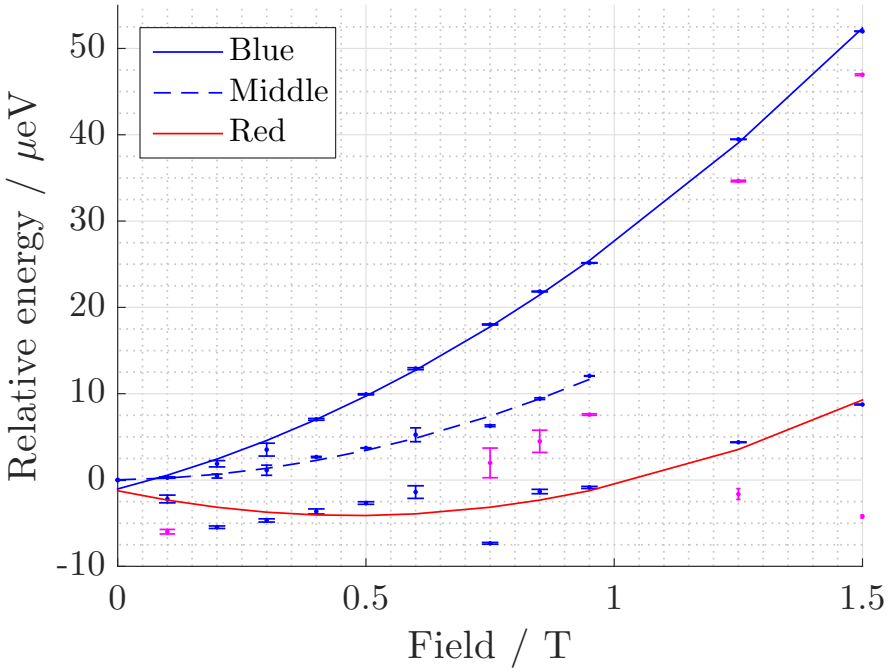

FIGURE 5.20: Transition energies extracted from dT sweeps at different magnetic fields. Peaks are manually assigned to either the red or blue Zeeman transitions, or the middle anomalous transition. Red and blue lines show parabolic fits to red and blue Zeeman transitions respectively. A fit to the middle anomalous transition is shown by the blue dashed line. Magenta points are additional, anomalous peaks seen in the data which are not assigned to any transition.

The peaks are assigned to either the blue, middle or red transition and parabolas are fitted to them to extract the g-factors and diamagnetic shifts. The fitting parameters are shown in Table 5.1.

	linear coefficient	diamagnetic coefficient
Blue line	0.25 ± 0.05	14.11 ± 2.03
Middle line	0.01 ± 0.08	12.27 ± 4.42
Red line	-0.22 ± 0.17	13.08 ± 6.38

TABLE 5.1: The g-factors and diamagnetic coefficients extracted from parabolic fits to the peak positions.

All three lines are consistent with a diamagnetic shift of 14 μeV/T^2. The red and blue lines are consistent with an effective exciton g-factor of around 0.5 and fitting the difference between the red and blue line directly results in an even tighter estimation of 0.49 ± 0.02. In addition to the red, blue and middle lines, some additional peaks are observed which are shown in magenta on Figure 5.20. The origin of the middle transition and its detailed behaviour are explored further in Section 5.2.3.

5.2.2 Field sensing demonstration

Method

To demonstrate the field sensing mechanism the laser is tuned near to the singlet transition. The spectral suppression stage is aligned such that it passes quantum dot light at the wavelength of the triplet transition, whilst suppressing the reflected driving laser light. The output of the suppression stage is sent to the APD. Typically 80% of the signal on the APD comes from the quantum dot and the rest from the remaining unsuppressed laser light. The count rate is recorded whilst the gate voltage is swept over the singlet resonance. This is repeated at magnetic fields from −700 mT to +700 mT.

Figure 5.21a shows a typical dataset generated by this experiment. The color scale gives the count rate on the APD. To understand the pattern in this data, the cartoon in 5.21 shows the singlet transitions (blue lines) as a function of gate voltage, for zero field, −400 mT and −600 mT. For zero field all the excited sates are degenerate and so only one transition is seen. As the gate is swept the singlet moves into resonance at two different voltages (magenta circles) and so two peaks are seen in the count data. When the field strength is increased to −400 mT the singlet splits into three transitions, but they are still sufficiently close that the laser intersects with each of them at two different voltages, leading to six resonances in total. At −600 mT the blue transition has been moved to such high energy that laser never intersects it. The middle and red Zeeman lines still intersect the laser twice, and so a total of four resonances are seen.

This experiment is repeated for different combinations of excitation and collection polarisation, following the simulations in Section 5.1.1. To connect this data to the theoretical predictions of Section 5.1, the height of the peaks is extracted since these are related to the detection probabilities. From the peak height, the likelihood functions in Figure 5.4 can be recreated.

Results

The data for exciting and detecting in the H and V bases are shown in Figures 5.22. The data points in each figure show the extracted count rate of the middle peak. The red lines shows the count rates predicted from a phenomenological steady state model

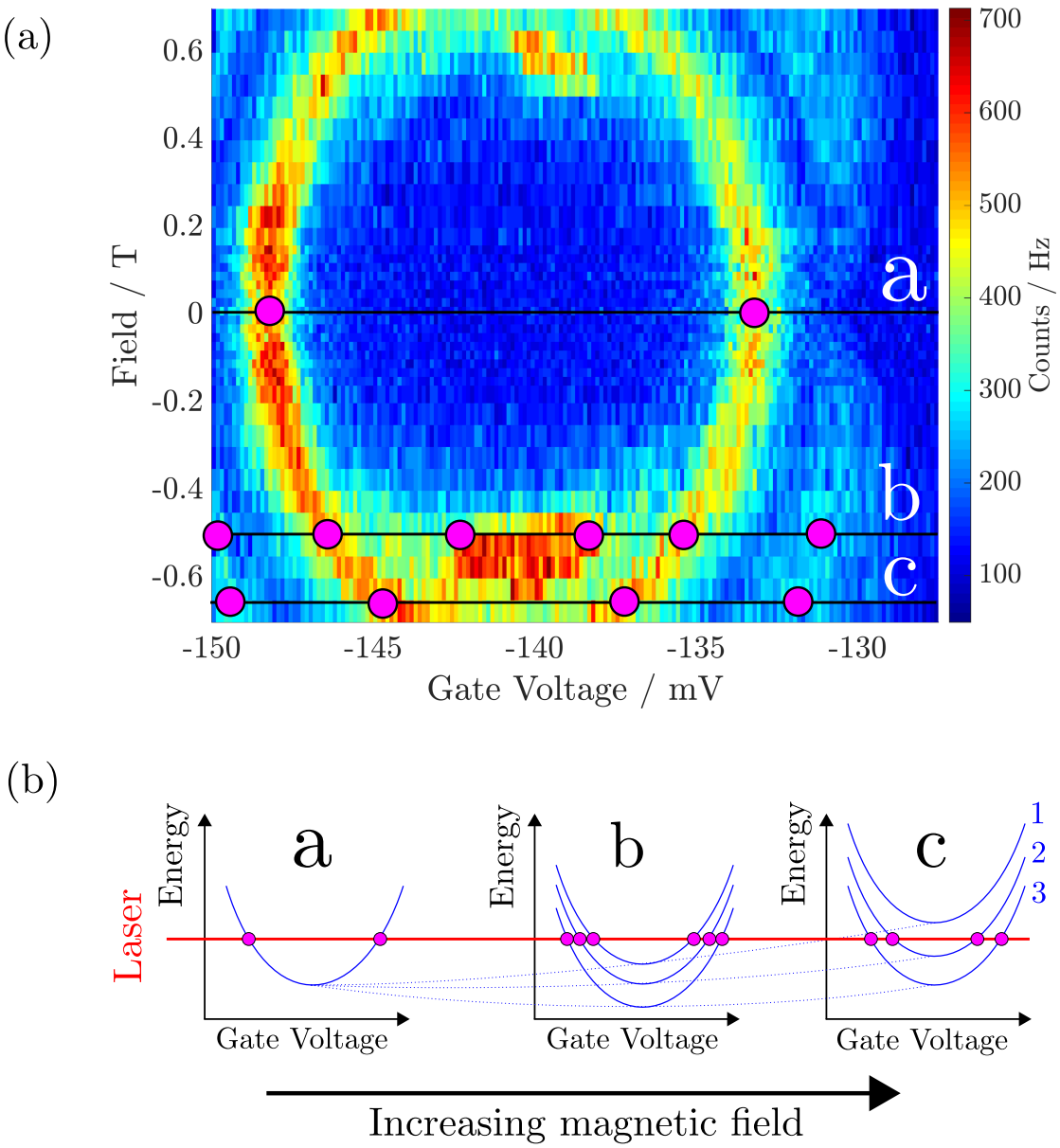

FIGURE 5.21: (a) A typical field-sweep dataset from the field sensing experiment, collected with excitation and collection in the H basis. (b) As the magnetic field increases, the singlet transitions (blue lines) move with respect to the laser (red line) giving rise to several resonance in the data (magenta circles).

described in Section 5.2.3 which uses information extracted from the characterisation steps. To match the data, the simulation results are scaled and an offset is added to account for stray laser counts.

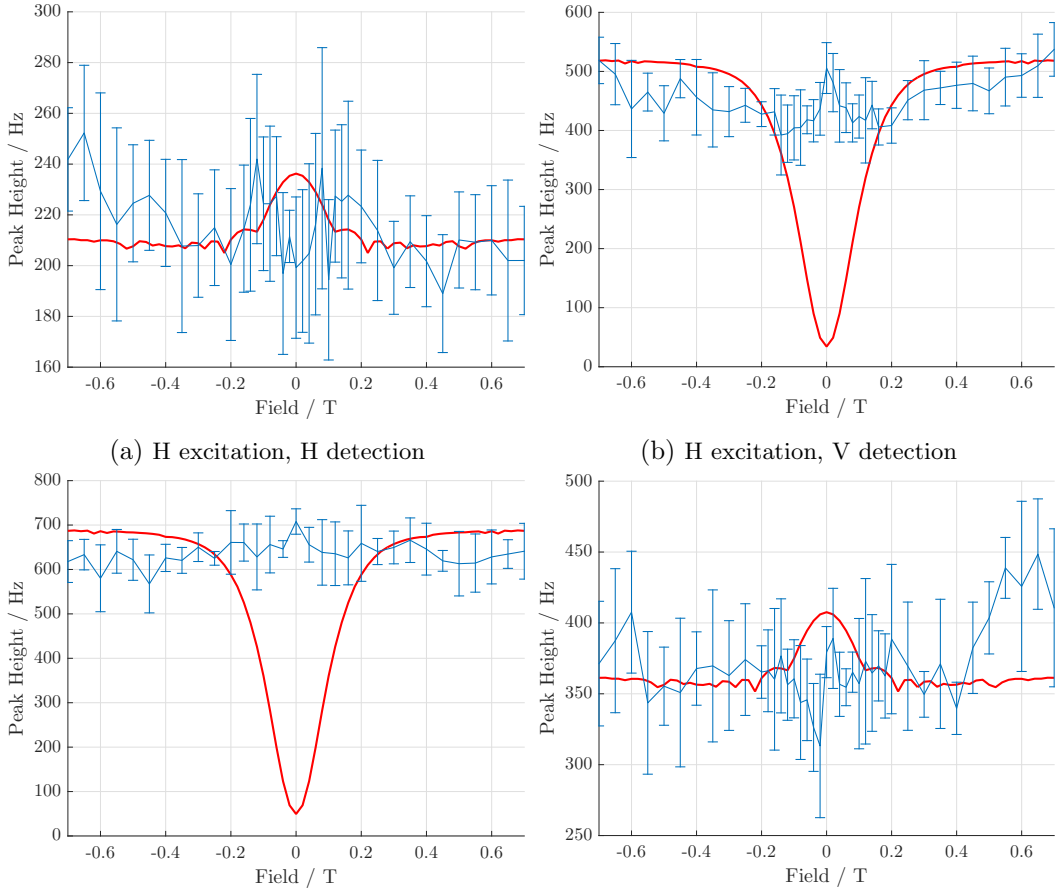

(a) H excitation, H detection

(b) H excitation, V detection

(c) V excitation, H detection

(d) V excitation, V detection

FIGURE 5.22: Data collected when exciting and detecting in the H and V bases. Blue points are the extracted peak heights and the red lines are predictions from the model.

The simulation results are qualitatively similar with those in Section 5.1. The peak height in the case of identical excitation and collection bases, is much reduced and the data fit this, although the contrast is poor due to the remaining unsuppressed laser light. There is significant disagreement between the data and the model for orthogonal excitation and collection bases, even taking measurement error into account.

The data for collection in the D and A bases are shown in Figure 5.23. Here the agreement is much better although the large field data sometimes diverge from the simulation. The data recreate the unambiguous asymmetry in count rate with respect to magnetic field, predicted by both the simple and 8-level model.

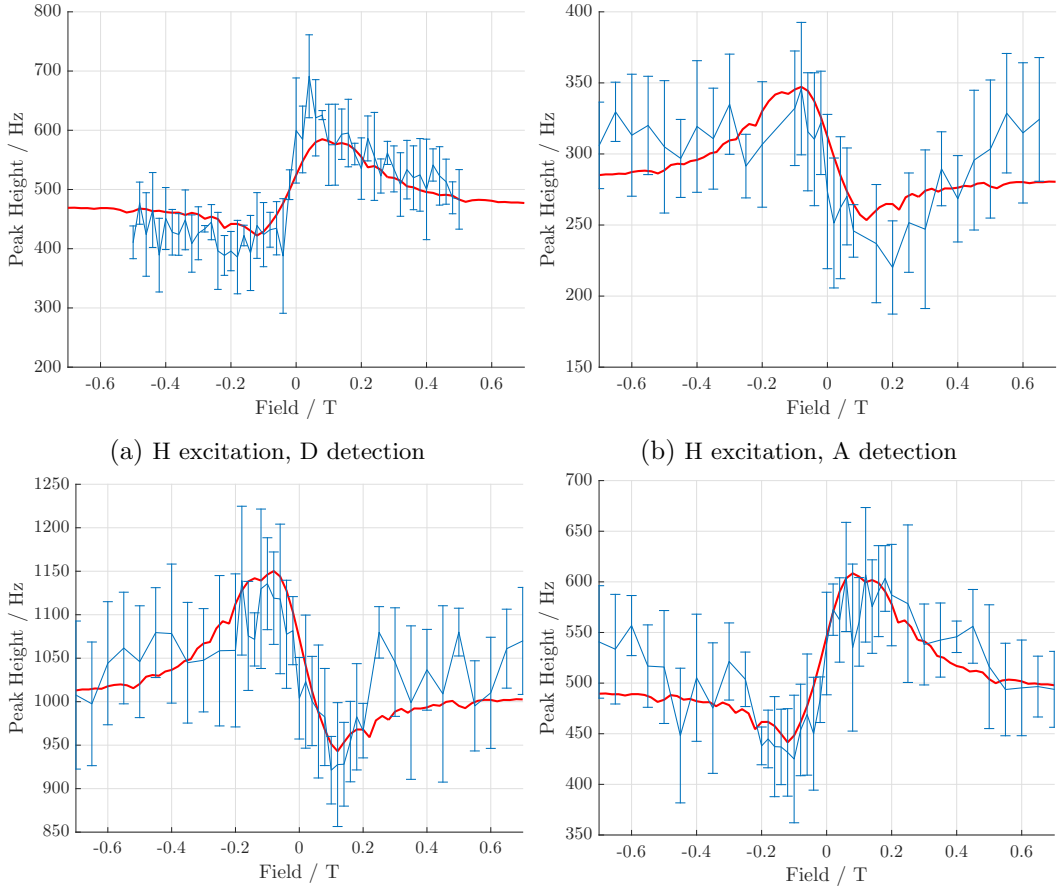

(a) H excitation, D detection

(b) H excitation, A detection

(c) V excitation, D detection

(d) V excitation, A detection

FIGURE 5.23: Data collected when exciting in the H and V bases, and detecting in the D and A bases. Blue points are the extracted peak heights and the red lines are predictions from the model.

The data for R and L detection are shown in Figure 5.24. For these collection bases, only data for excitation in H was recorded. Both the simulation and the data show no change in the detection probability with field.

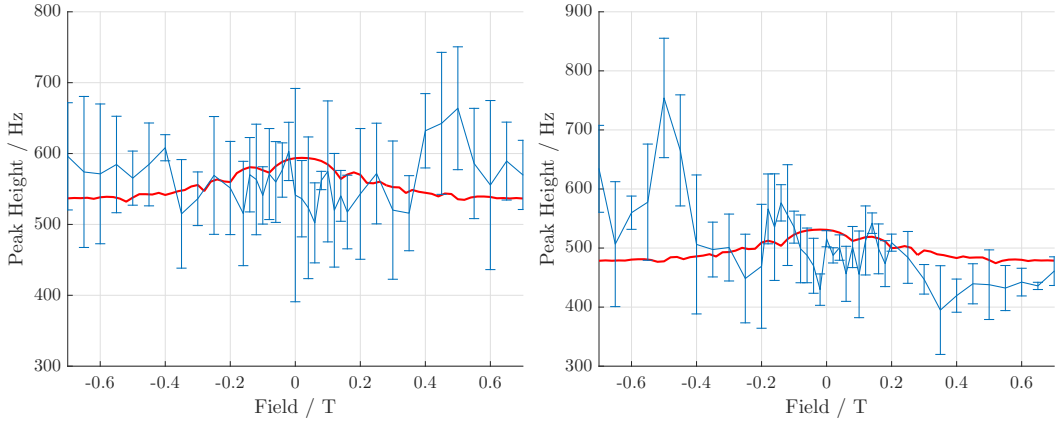

(a) H excitation, L detection

(b) H excitation, R detection

FIGURE 5.24: Data collected when exciting in the H basis and detecting in the R and L bases. Blue points are the extracted peak heights and the red lines are predictions from the model.

Finally, the data (not shown) for exciting in R and L and detecting in any linear basis showed no variation in the count rate with field as predicted by both the simple and 8-level model.

The deviations from theory are most likely related to the appearance of the anomalous middle transition in Figures 5.19a and 5.19b. Whilst the data do not completely follow the predictions, they do so closely enough that the system can still be used as a field sensor. The next section details how this can be done.

Usage and performance as a field sensor

Given the system as characterised above, only the A and D collection statistics under linear excitation show the expected variation for the sensing mechanism. Nevertheless there is still sufficient information to use the system to measure magnetic or Overhauser fields up to $\sim$ 60 mT with an alteration to the sensing procedure. Since only one of the two curve 'types' in Figure 5.5 is known for this system, the Bayesian estimation routine cannot be used. Instead, the detection events on channel H and D together (for normalisation) can be used to directly calculate the estimate of the field.

For illustrative purposes the count rate in detection channels A and D is assumed to follow the modelled curves (red) in Figures 5.23a and 5.23b exactly, referred to in the following as $c_A(B_z)$ and $c_D(B_z)$ respectively. To get the probability that a photon is

detected in either the D or A channel the count rates should be normalised to give

$$\mathrm{Pr}_A = \frac{c_A}{c_A + c_D} \tag{5.21}$$

$$\mathrm{Pr}_D = \frac{c_D}{c_A + c_D} \tag{5.22}$$

where the B_z argument has been suppressed for clarity. These curves could be measured in a known static magnetic field beforehand to calibrate the system, to account for the variation in g-factor between quantum dots for example. Following a measurement run where n_A photons are counted in the A channel, and n_D photons in the D channel, an estimate for the value of Pr_A is given by $p_A = n_A/(n_A + n_D)$. Given this, the predicted value of the field can be read off of the calibration curve, which in Figure 5.25a is labelled $\tilde{B}$.

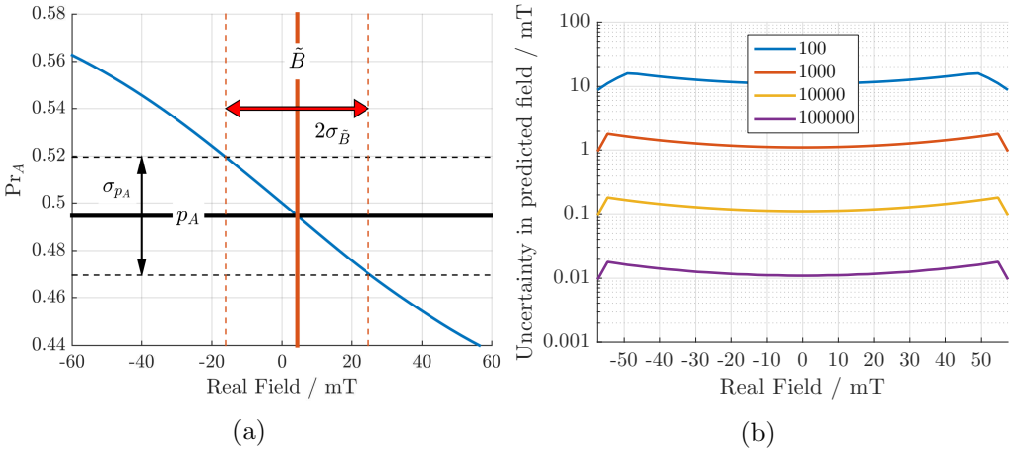

FIGURE 5.25: (a) Mapping from the observed A detection probability Pr_A to a predicted value of the field $\tilde{B}$. Errors in the former (black arrows) map onto errors in the latter (red arrows). (b) How the absolute error in the field $\sigma_{\tilde{B}}$ changes with the applied field and number of observed photons. Each line corresponds to a different number of photon detection events (as shown in the legend).

Note that any error in p_A (σ_{p_A}, black arrows) is mapped straightforwardly onto an error in $\tilde{B}$ ($\sigma_{\tilde{B}}$, red arrows). To quantify this it is assumed that n_A and n_D are shot noise limited and so $\sigma_{n_A} = \sqrt{n_A}$ and $\sigma_{n_D} = \sqrt{n_D}$. Then it can be shown that the error on the estimated probability is

$$\sigma_{p_A} = \frac{1}{N}\sqrt{n_D^2 n_A + n_A^2 n_D} \tag{5.23}$$

where $N = n_A + n_D$ is the total number of photons counted across both channels.

To find the corresponding upper and lower bounds on $\tilde{B}$, the values of the field which correspond to $p_A + \sigma_{p_A}$ and $p_A - \sigma_{p_A}$ are found, as shown in the figure. In general the bounds will not be symmetric as the gradient of the calibration curve Pr_A is not constant. Figure 5.25b shows how the absolute error in the predicted value varies as a function of the real magnetic or Overhauser field present, and crucially on the number of observed detection events across both channels. The error in $\tilde{B}$ is smallest around zero field, because the gradient of Pr_A is highest here. As the field increases, the magnitude of the gradient of Pr_A decreases and so errors in p_A map into larger errors in $\tilde{B}$. The artefacts at large field are cause by the upper (lower) error margin in p_A moving above (below) the maximum (minimum) of c_A. When this happens there is no value of c_A to match the upper error margin of p_A and so the field that maximises c_A is predicted.

Figure 5.25b shows that to achieve a measurement uncertainty of around 0.2 mT for a field of < 50 mT requires $N = 10,000$ photon events. Using again a collection efficiency of 66%, detection efficiency of 10% and radiative lifetime of 84 ps, such a measurement would take $10,000 \times 84$ ps$/\left(0.66 \times 0.1\right) \approx 12.7$ μs.

In the next section the anomalous system behaviour is documented in detail. The 8-level model used to model the field sensing data is built and motivated by observations in the data. Two possible explanations for the observed anomalies are given.

5.2.3 Anomalous behaviour and 8-level model

The anomalies seen in the data all revolve around the appearance of a middle unexpected transition line. Its behaviour is used to inform the model of the system used in Section 5.2.2 which has some success at explaining the features.

Anomalous singlet behaviour

The routine dT gate sweeps performed to characterise the singlet transition showed the appearance of a middle line, deviating from the expected two lines expected from the level diagram in Figure 5.13b. Figure 5.19a showed a dT gate sweep at 500 mT where the middle line was clearly visible. The line is also visible in the magnetic field sweep data set shown in Figure 5.21a, as well as the wavelength sweeps used to extract the g-factors and diamagnetic shifts. The g-factor extracted for this peak both from the

data in Figure 5.20 and from the dT sweeps was consistent with 0. The middle line also had the same diamagnetic shift as the red and blue Zeeman lines.

One of the most striking effects is the sudden disappearance of the middle line during dT gate sweeps at higher magnetic fields. Up to 500 mT (Figure 5.19a) all three lines are consistently present throughout the dT sweep, irrespective of gate sweep direction. At 600 mT (Figure 5.19b) the middle line switches off abruptly when the wavelength is increased. This occurs for both scan directions but the the critical wavelengths are different. From 750 mT upwards (Figures 5.26b and 5.26a) this effect intensifies and the middle line only turns on in one half of the figure, determined by the sweep direction.

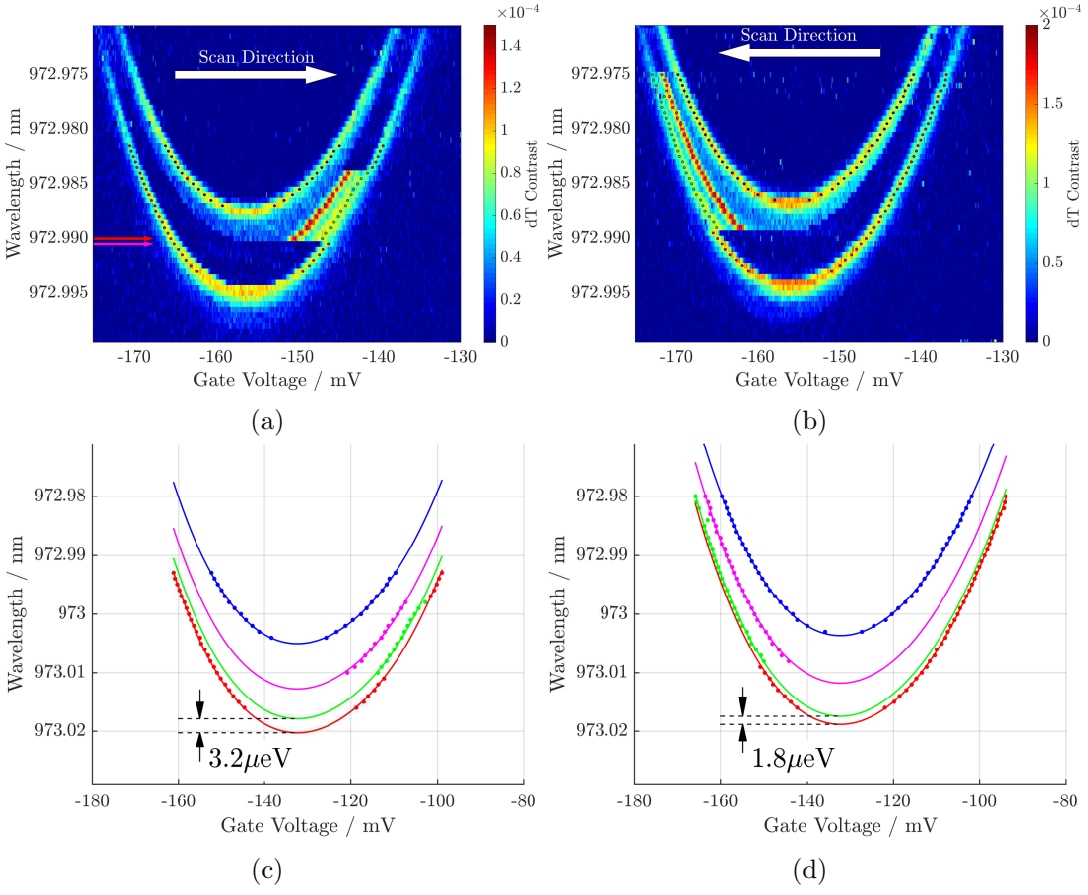

FIGURE 5.26: dT gate sweeps of the singlet transition at 750 mT scanning the gate from (a) low to high voltage, and (b) high to low voltage. Fits to the extracted peaks are shown in (c) and (d). The magenta curve in (c) and (d) is fit to the middle line. The green curve is fit to the points on the low energy line when the middle transition is 'on'. The red and magenta arrows in (a) are referred to in the text.

At 750 mT and 1 T (not shown) the red Zeeman line subtly shifts to slightly higher energy when the middle transition appears. This is shown by the green curves in Figures

5.26c and 5.26d which are fits to the red Zeeman line in the wavelength range where the middle transition is seen. In this region the red Zeeman line shifts up in energy by 3.2 μeV when the gate is scanned from low to high voltage (left to right). The same occurs when scanning from high to low voltage (right to left) but the shift is only 1.8 μeV. The same shift is seen at 1 T, with a low to high shift of 3.5 μeV and high to low shift of 1.8 μeV.

At fields greater than 1.25 T the middle transition doesn't appear at all, regardless of the direction of the gate sweep (left to right). Instead, a new feature appears in the form of 'satellite' transitions (additional transition lines) slightly below the red and blue Zeeman lines. These are shown by the dashed lines in Figures 5.27c and 5.27d for fields 1.25 T and 1.5 T.

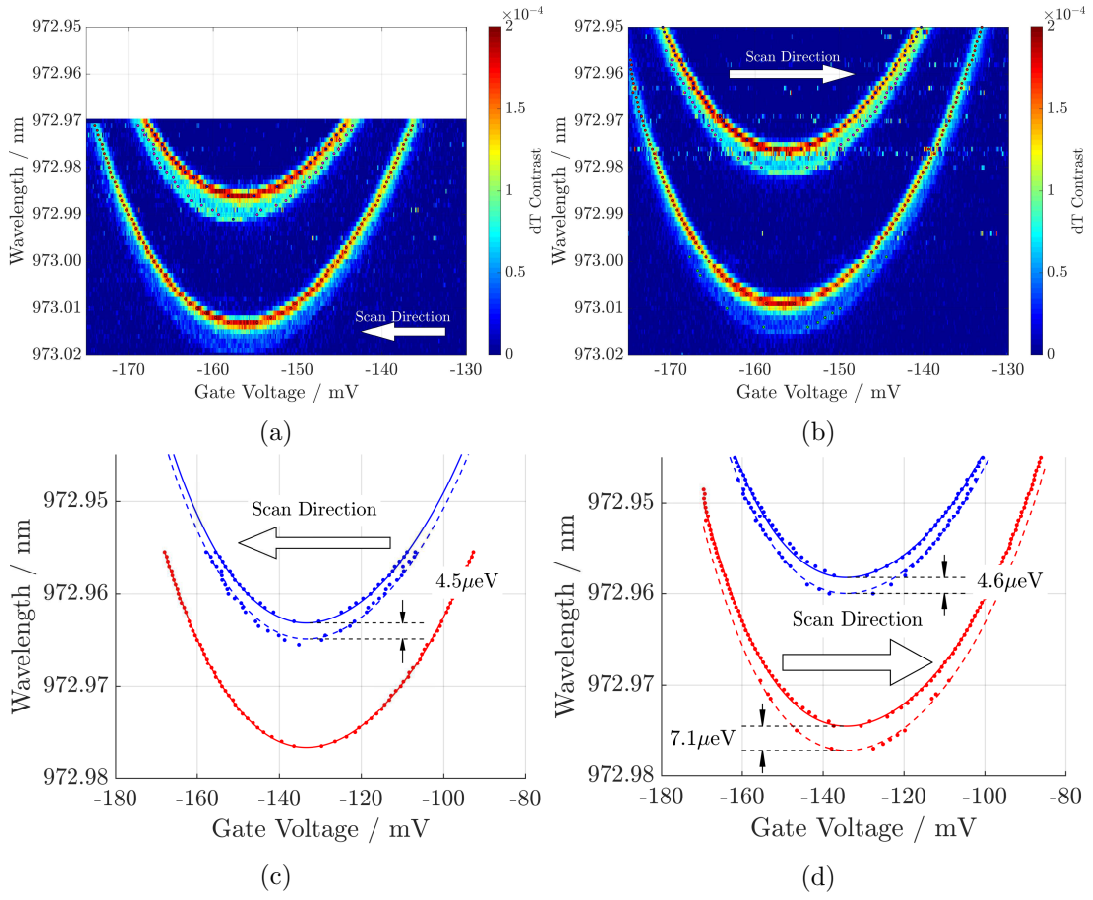

FIGURE 5.27: dT gate sweeps of the singlet transition at (a) 1.25 T and (b) 1.5 T. The data for each field are fitted in (c) and (d) respectively, showing more clearly the smaller satellite peaks (red and blue dashed lines).

For both fields, the satellite spitting in the upper line is $\sim$ 4.55 μeV, and for 1.5 T

the satellite splitting in the red line is ~ 7.1 μeV. (The red satellite splitting at 1.25 T cannot be reliably identified).

The final piece of evidence is provided by the field sweeps taken under circularly polarised excitation. These data sets are shown in Figure 5.28. It is seen that at a critical field magnitude around 300 mT (marked by the dashed black line), the system switches abruptly in one field direction from displaying the middle line only, to displaying the blue line only. When excited with R polarised light the middle transition remains the only transition from -700 mT up to $+300$ mT at which point it turns off and the blue transition turns on. When excited with L polarised light the middle transition is the only transition from $+700$ mT down to around -300 mT at which point it turns off and the blue transition turns on over the space of around 40 mT. In both cases the middle transitions is broadened in the direction of the gate sweep.

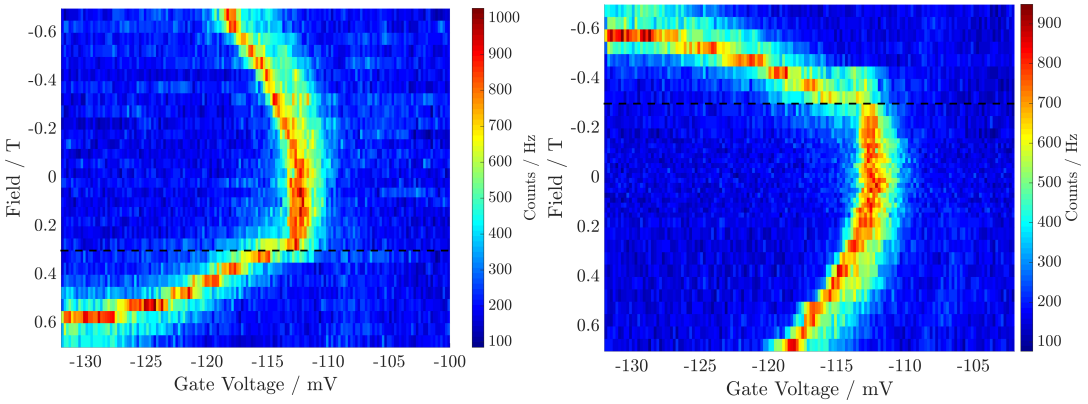

FIGURE 5.28: Data collected when (a) exciting in R and collecting in V, and (b) exciting in L and collecting in D.

The origin and detailed behaviour of the unexpected middle transition is not fully understood at present. Nevertheless, we can shed light on some of the anomalous features by extending the simple model of Section 5.1.1 to include all 8 levels of the single and triplet system shown in Figure 5.13b.

8-level model

A Hamiltonian to describe the relevant levels is built up using the methods in Chapter 3. The singlet energies are set by using a fit to one of the dT traces and other electrostatic energies are derived from them to ensure accurate matching to the data. A laser

interaction Hamiltonian is added to this, which reads (in a rotating frame)

$$H_{\text{int}} = \frac{\Omega_R}{2}\left(\left|S\right\rangle\!\!\left\langle \downarrow,\uparrow\downarrow\Uparrow\right| + f\left|S\right\rangle\!\!\left\langle \uparrow,\uparrow\downarrow\Uparrow\right|\right) + \tag{5.24}$$

$$\frac{\Omega_L}{2}\left(\left|S\right\rangle\!\!\left\langle \uparrow,\uparrow\downarrow\Downarrow\right| + f\left|S\right\rangle\!\!\left\langle \downarrow,\uparrow\downarrow\Downarrow\right|\right) + \text{H.c.} \tag{5.25}$$

where Ω_R and Ω_L are Rabi frequencies of the the right and left-hand circularly polarised components of the laser interaction, and f is a factor which controls the forbidden transition strength relative to the dipole allowed ones (normally f would be very small). The steady state of the system is found using a steady state master equation solver [135] with collapse operators to describe spontaneous emission, mixing between the excited state manifold, and mixing between the singlet and triplet states. The latter is known to be present due to the lack of spin pumping.

The experiments are emulated as closely as possible by stepping the magnetic field and sweeping the gate voltage, and at each point calculating the dT contrast and photon detection probability from the steady state solution ρ_{ss}. The dT contrast is proportional to the imaginary part of the coherences between the ground and excited state of a transition [62]

$$\frac{\mathrm{d}T}{T} \propto \text{Im}[\langle S|\,\rho_{\text{ss}}\,|\uparrow,\uparrow\downarrow\Downarrow\rangle + \langle S|\,\rho_{\text{ss}}\,|\downarrow,\uparrow\downarrow\Uparrow\rangle] + \tag{5.26}$$

$$\text{Im}[\langle S|\,\rho_{\text{ss}}\,|\uparrow,\uparrow\downarrow\Uparrow\rangle + \langle S|\,\rho_{\text{ss}}\,|\downarrow,\uparrow\downarrow\Downarrow\rangle] \tag{5.27}$$

The photon count rate is extracted by applying projectors similar to those in Section 5.1.1. For example the count rate when detecting in the H basis is proportional to

$$\langle H|\,\rho_{\text{ss}}\,|H\rangle + \langle H_{\text{f}}|\,\rho_{\text{ss}}\,|H_{\text{f}}\rangle \tag{5.28}$$

where the projectors are constructed in a similar way to before as

$$\left|H\right\rangle = \frac{1}{\sqrt{2}}\left(\left|\downarrow,\uparrow\downarrow\Uparrow\right\rangle + \left|\uparrow,\uparrow\downarrow\Downarrow\right\rangle\right) \tag{5.29}$$

$$\left|H_{\text{f}}\right\rangle = \frac{1}{\sqrt{2}}\left(\left|\uparrow,\uparrow\downarrow\Uparrow\right\rangle + \left|\downarrow,\uparrow\downarrow\Downarrow\right\rangle\right) \tag{5.30}$$

With f set to 0 this model recreates the 'standard' two Zeeman split transitions.

Two hypotheses are given below to explain first how the forbidden transitions in the

system might be responsible for the observed peak, and secondly how nuclear spin polarisation may be the cause.

Dark state hypothesis

In this first hypothesis the middle line is assumed to arise from the usually forbidden singlet transitions (i.e. the two S transitions marked by arrows in Figure 5.13). It is known from earlier measurements that the red and blue Zeeman lines are split according to a g-factor of 0.5, and the middle line has g-factor of 0. The splitting of the bright excitons is equal to the difference of the electron and hole g-factor so these are constrained to $|g_e^L - g_h^R| = 0.5$. Setting $g_e^L = -0.25$ and $g_h^R = 0.25$ satisfies this constraint and also aligns both forbidden transitions with the middle transition. Putting $f = 1$ turns on the forbidden transitions giving rise to a strong middle transition which is brighter than the individual allowed transitions since it consists of two overlapping resonances. These g-factors are in range of those previously measured in similar systems [80, 136, 137].

The dT simulation using these parameters as well as peak positions extracted from the data in Section 5.2.2 are shown in Figure 5.29a. The peak positions from the dT simulation are then extracted and plotted on top of the data in Figure 5.29b (black crosses). The laser wavelength in the simulation is tuned so that the peaks at zero field match up with the data.

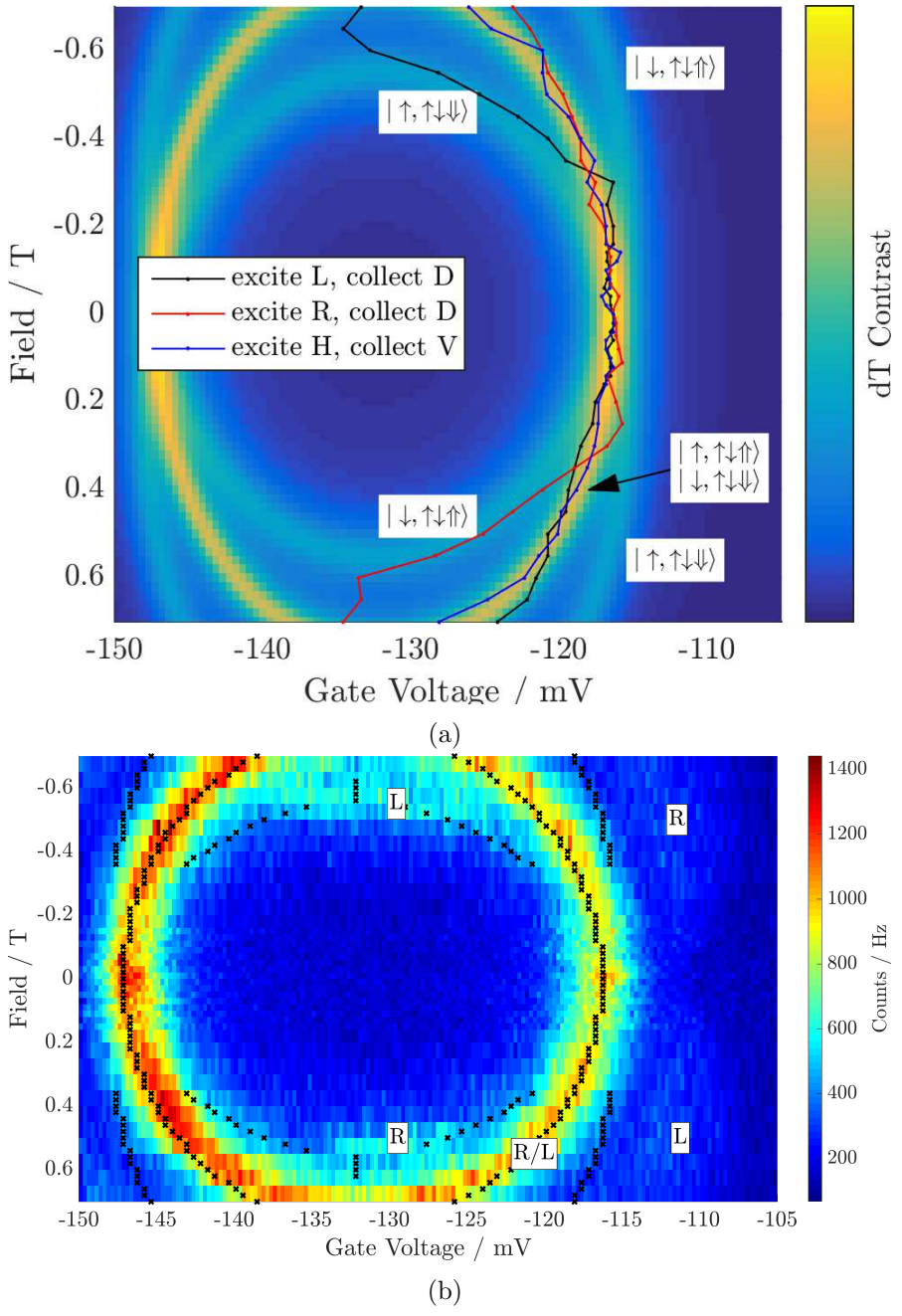

FIGURE 5.29: Comparison between the simulated field-sweep experiments and the experimentally collected data. (a) Experimental data (points and lines) is plotted on the simulated differential transmission gate scan. The simulated peaks are labelled according to what excited state they involve. (b) Peaks extracted from the simulation in (a) (black crosses) are plotted on one of the data sets used for the field sensing demonstration. The peaks in the data are labelled with their polarisation which agrees with the simulation.

There is agreement on the position of the middle and blue peaks as well as the polarisation of all the peaks. However this simulation cannot predict the kink in the behaviour nor the position or broadening of the red Zeeman line (outer transition in Figure 5.29b).

Nevertheless this model has some success in predicting the photon count data in Section 5.2.2. In this model the 'forbidden' transitions contribute to the count rate and dT contrast, though they do not strictly take part in the field sensing mechanism since their effective g-factor is zero.

Since this hypothesis can reproduce some of the behaviour it is worth exploring how it could come about in experiment. In particular; what could be the mechanism that allows the 'forbidden' transitions to become strongly allowed? Figures 5.30 show the effect of a coherent mixing term that couples $\left|\uparrow,\uparrow\downarrow\Downarrow\right\rangle \leftrightarrow \left|\downarrow,\uparrow\downarrow\Downarrow\right\rangle$ and $\left|\uparrow,\uparrow\downarrow\Uparrow\right\rangle \leftrightarrow \left|\downarrow,\uparrow\downarrow\Uparrow\right\rangle$. This causes the excited states to hybridise such that the dark states pick up some light component.

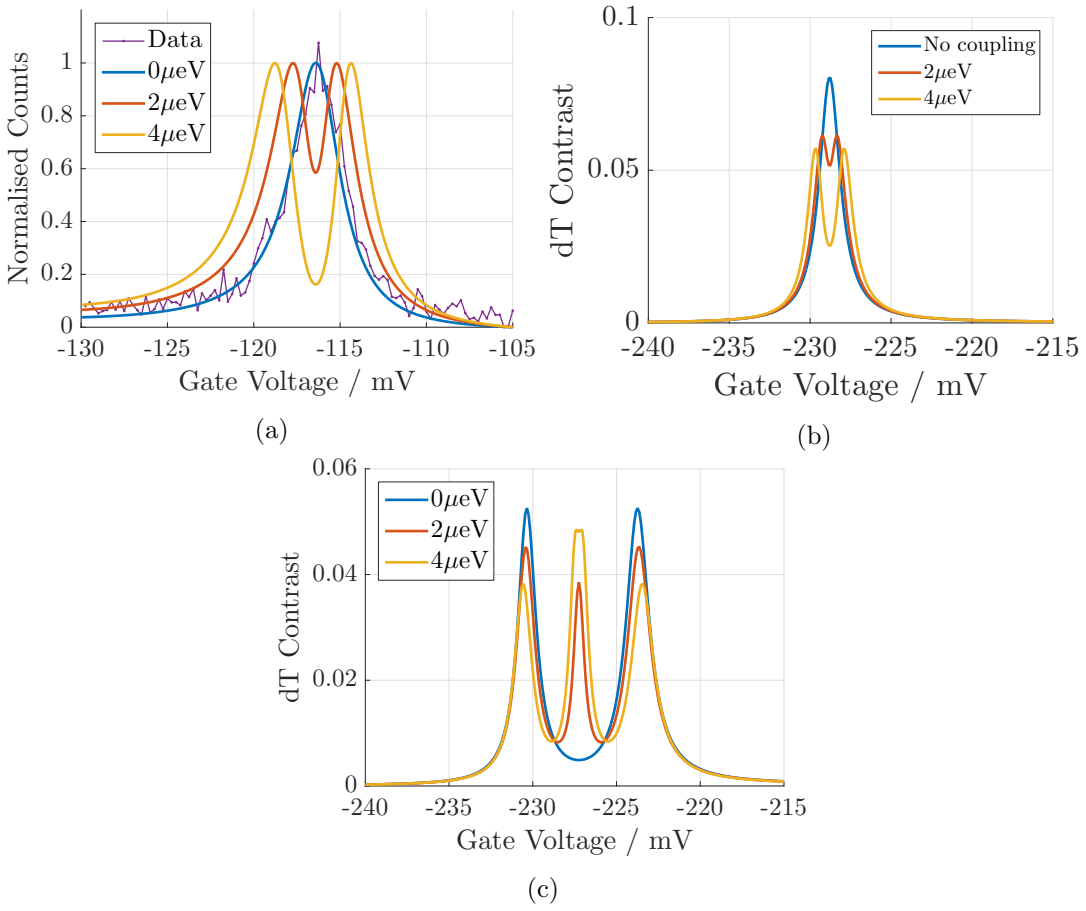

FIGURE 5.30: Photon counts at 0 T (a) and dT gate scan simulations at (b) 0 T and (c) 500mT of one of the singlet transitions for different values of the excited state mixing term. The forbidden transition factor is set to zero.

Figure 5.30a shows the effect on the simulated photon count rate. When the mixing term is zero the simulation fits the data well, however as the coupling is increased the

zero field splitting becomes larger than admissible by the data. This is also the case for the simulated dT line shown in Figure 5.30b at a different wavelength (and hence a difference gate voltage). Figure 5.30c shows that the coupling does indeed brighten the dark states (the middle line lights up when the coupling is increased) however this only occurs for coupling strengths ruled out by the lack of zero field splitting. Even then, the strength of the middle transition is insufficient to explain the data. A constant coupling thus cannot be the cause, but a field dependent coupling that is zero at 0 T is not ruled out, since this would still fit the data at 0 T.

Dragging hypothesis

A second hypothesis is that the middle line consists of the bright transitions which are dragged into the middle by an Overhauser field generated whilst dragging over the blue Zeeman branch. In this hypothesis, when the laser is scanned across the blue Zeeman transition, it generates nuclear polarisation through the dragging mechanism (see Section 2.6.2) which opposes the external field, and thus decreases the Zeeman splitting. Eventually the Overhauser field is sufficiently strong to completely cancel the Zeeman splitting so the red and blue Zeeman transitions lie on top of each other, appearing as a single middle line. Complete cancellation of an external field and switching similar to that seen in Figure 5.28 has been previously observed in InGaAs quantum dots [137]. A dynamic Overhauser field phenomenologically added to the model can reduce the singlet splitting and recreate the peak positions seen in the dT data. This model produces data qualitatively similar to that in Section 5.2.2 but again predicts the large dip for orthogonal excitation and collection bases, which is not seen in the data (for example, in Figure 5.22b).

The involvement of the nuclear spins is strongly hinted at by the abrupt turn on of the middle transition and by the plateaus seen in the dT gate scans, examples of which are shown in Figure 5.31. These plateaus are reminiscent of the line dragging seen in single quantum dots [99, 100]. The traces in Figure 5.31a correspond to the two consecutive traces in Figure 5.26a highlighted by arrows of the same colour.

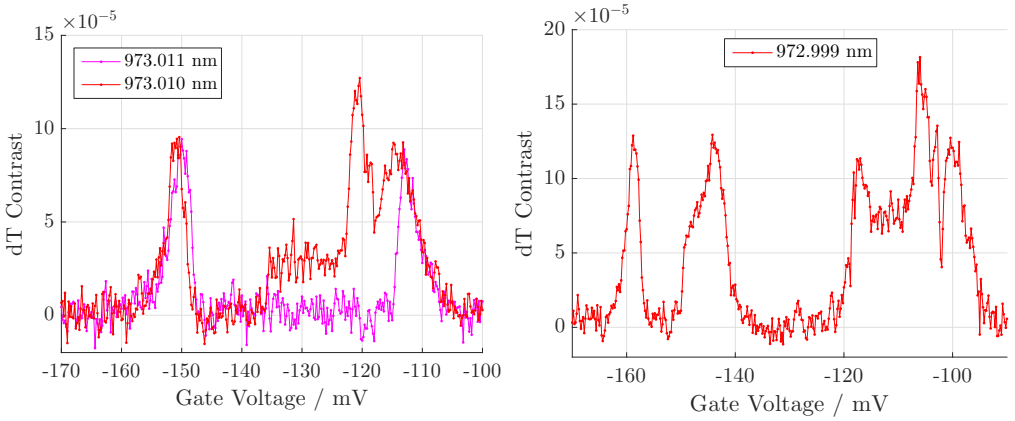

FIGURE 5.31: Selected dT traces from the dT gate sweeps at (a) 750 mT and (b) 1 T, showing the middle transition and unusual line-shapes. In both figures the gate was scanned from low voltage (left) to high voltage (right).

If there is any nuclear polarisation remaining after passing the middle transition this would decrease the Zeeman splitting and so could explain the shift of the red Zeeman line to higher energies. The difference in the magnitude of this shift when scanning the gate voltage to the left or to the right could be related to the fact that the singlet transition minimum is not quite in the centre of the X_{2-} charging region. Because of this, the co-tunnelling rate with the back contact is not equal on either side of the minimum, and it is known that co-tunnelling has a large effect on the presence and magnitude of dynamic nuclear polarisation.

With the middle line and other anomalies potentially related to the nuclear polarisation this leaves the dark states free to explain other features. A dark-bright exciton splitting (δ_2) coupled with fine tuning of the ratio between the electron and hole g-factors can place the forbidden transitions at roughly the locations of the satellite peaks seen in Figure 5.27 (shown through simulations).

So although this hypothesis can qualitatively explain some of the data, a microscopic explanation still remains to be found. A particular failure of this hypothesis is that if dragging is responsible, it is not clear why there is no evidence of this effecting the red Zeeman lines. It is noted that the bright transitions that give rise to the singlet transitions are similar in some ways to those in the X_0 . In both cases the ground state has zero spin and the excited state has a single unpaired but well defined spin state (an

unpaired electron in dot L). This could suggests that the same mechanism for generating polarisation in the X_0 case would work for the X_{2-} .

5.3 Gate controlled effective field

Finally this section develops a compensation scheme complementary to the field sensing already described. This scheme is designed around the singly charged coupled quantum dot. The idea is based on the fact that by operating the device in the region near a tunnelling anti-crossing, the electron wavefunction can be distributed in a controllable way between either of the dots. Starting with a pair of tunnel coupled dots, a strong Overhauser field is generated in the left (L) dot. The gate voltage can be tuned such that the electron wavefunction is mainly in dot L where it would feel the full effect of the Overhauser field. The spin states would then be split by the Overhauser field. Alternatively, the voltage can be tuned the other way such that the electron wavefunction is mainly in the right (R) dot. Far enough away from the anti-crossing it would feel a negligible effect of the Overhauser field, since its wavefunction would only extend minimally into dot L. In between these two cases the electron is distributed between dots L and R and so the effective field strength that it feels can be continuously tuned.

5.3.1 Field cancellation

To quantify this idea the model of Chapter 3 is invoked again. Interaction of the electron with the Overhauser field is modelled by adding an additional term

$$\frac{1}{2}A\Big(\sigma^L \cdot \mathbf{I}^L + \sigma^R \cdot \mathbf{I}^R\Big) \tag{5.31}$$

to the ground state Hamiltonian in (3.8). Term A governs the hyperfine coupling strength and $\mathbf{I}^L$ and $\mathbf{I}^R$ are vectors specifying the nuclear polarisation in each dot. The Pauli matrices are those defined in (3.7). An Overhauser field of strength 3 meV is applied. This splitting is far larger than that obtainable in InGaAs quantum dots, but is used here to make the effects more obvious. Figure 5.32 shows the energies (top) and the two lowest energy ground states in the system (bottom) labelled $\big|\mathrm{G1}\big\rangle$ and $\big|\mathrm{G2}\big\rangle$.

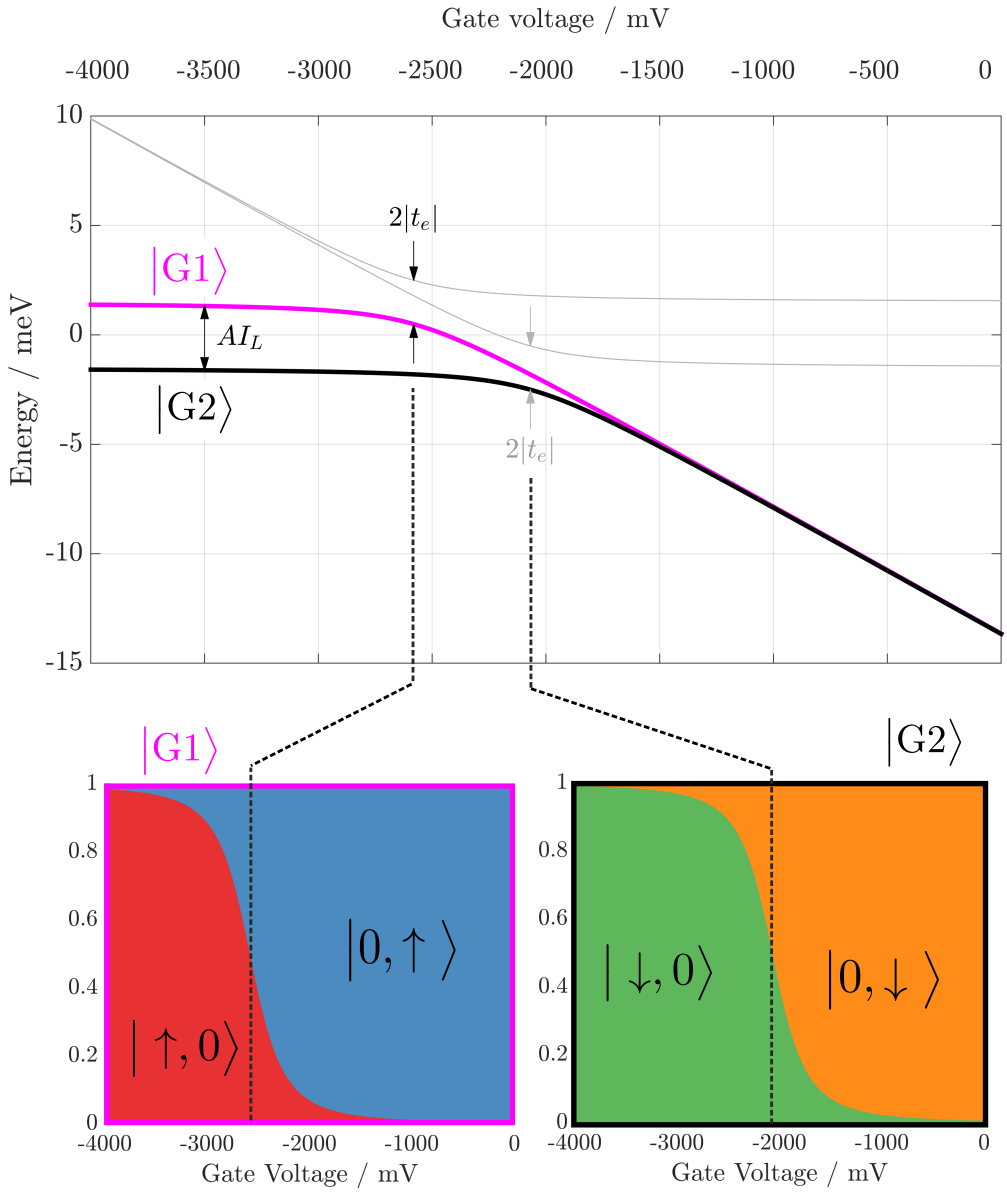

FIGURE 5.32: Sweeping the gate voltage of a coupled double quantum dot charged with a single electron a strong Overhauser field in dot L. The arrows in (a) denote the magnitude and and gate voltage positions of the anti-crossings.

Far to the right the ground state splitting is only 16 μeV since they are almost purely $|0,\uparrow\rangle$ (99.5%) and $|0,\downarrow\rangle$ (99.3%) respectively. The vast majority of the electron wavefunction is in dot R where there is no field and so the splitting is negligible. Far to the left the states change so that the electron wavefunction is mainly in dot L (98.6% $|\uparrow,0\rangle$ and 99.2% $|\downarrow,0\rangle$ respectively). Now the full effect of the field is felt and the two states are split by around 3 meV. Between these limits the electron feels some fraction of the field depending on the gate voltage. Through this mechanism the ground state splitting

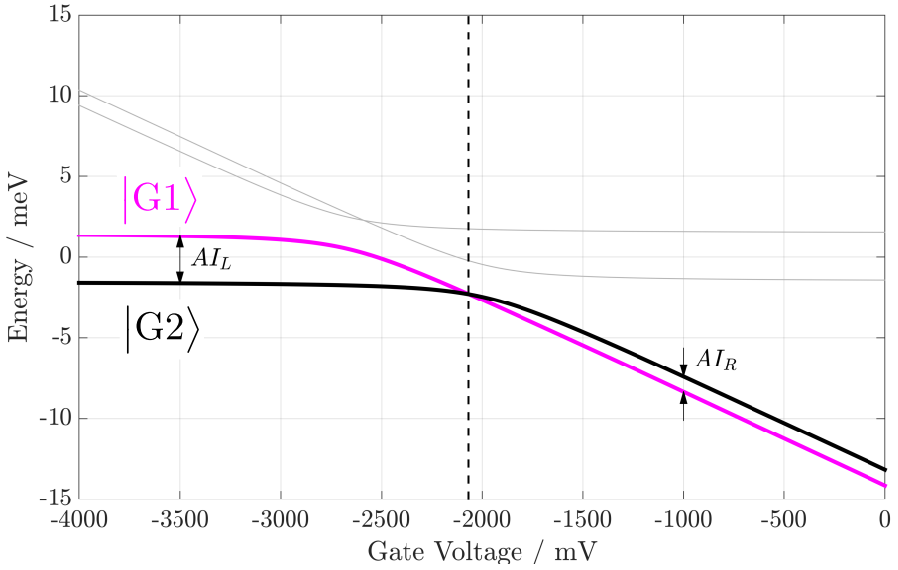

FIGURE 5.33: Demonstration of the field cancellation in a pair of coupled dots.

of a spin qubit in the states$|\mathrm{G2}\rangle$ and $|\mathrm{G1}\rangle$ be continuously varied.

The compensation mechanism is demonstrated by adding a nuclear polarisation in dot R by setting of strength 1 meV in the opposite direction to dot L. This emulates the instantaneous $\hat{\mathbf{z}}$ component of the Overhauser field arising from uncontrolled thermal fluctuations. (This is again around 3 orders of magnitude larger than typical values in order to illustrate the idea better). Figure 5.33 shows the system energy levels in this scenario.

Far on the right the ground states are no-longer degenerate because of the Overhauser field fluctuation. However, it is clear from the figure that a gate voltage exists (shown by the dashed black line) where the splitting of the ground states is zero. At this gate voltage the artificially generated field in dot R has been used to cancel out the field in dot L.

5.3.2 Transitions

The field cancellation mechanism can be monitored by looking at the transition energies of the quantum dot. Figure 5.34 shows the X_{1-} transitions with an Overhauser field in dot L in the $+\hat{\mathbf{z}}$ direction, and an Overhauser field along dot R in the $-\hat{\mathbf{z}}$ direction. (The field strengths are exaggerated as before.)

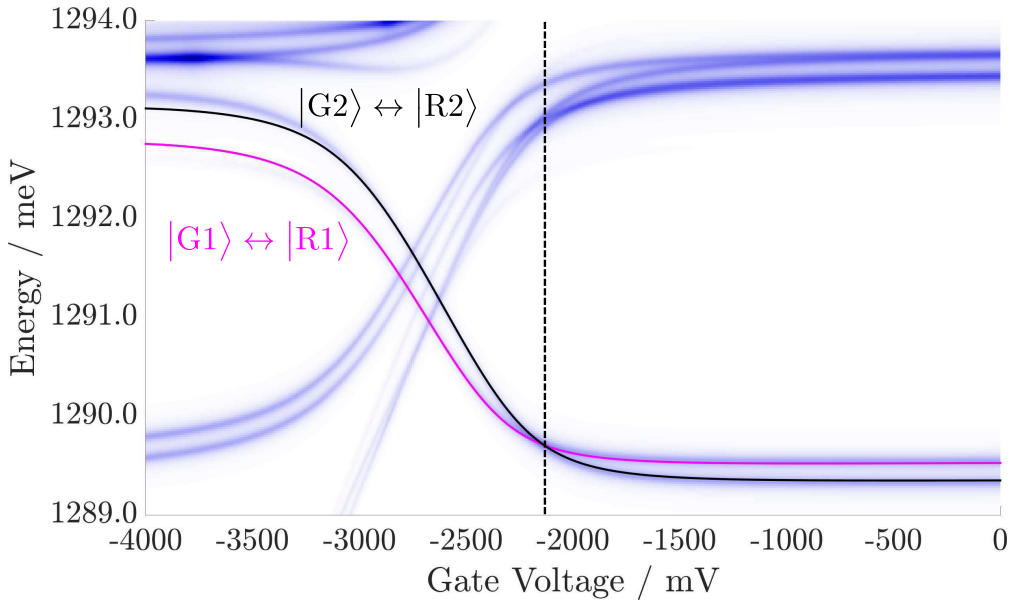

FIGURE 5.34: Transitions in the 1 electron coupled dot system in the presence of an Overhauser field in both dots in opposite directions.

The black and magenta lines show transitions from the ground states $|G1\rangle$ and $|G2\rangle$ to two of the excited states $|G1\rangle$ and $|G2\rangle$. At low and high voltages the transitions are split owing to the Overhauser field. The gate voltage where the fields in dot L and R cancel out is shown by the dashed black line. These transitions provide a means of monitoring the effective ground state splitting (along with a small contribution from the hole hyperfine interaction).

5.3.3 Anti-crossing separation

It is visible in Figure 5.32 that the ground state anti-crossings do not occur at exactly the same gate voltage. This is problematic for a spin qubit stored in states $|G1\rangle$ and $|G2\rangle$ because the coherent tunnelling induced oscillations would not occur at the same frequency for each, thus the qubit would eventually dephase. The separation of the anti-crossings is proportional to the difference in Zeeman splitting between the two uncoupled dots, so as long as the applied fields are low this problem can be alleviated.

5.3.4 Experimental demonstration

With the model built and mechanism understood, an experimental demonstration would use line dragging to generate an Overhauser field in dot L of a coupled dot pair, and then

use the transitions of Section 5.3.2 to determine that the effective splitting could be tuned by varying the gate voltage. Unfortunately no evidence of nuclear spin polarisation could be seen when attempting to drag transitions lines of the dot chosen for the experiment. Therefore the demonstration could not be achieved since the key element (a large enough Overhauser field) could not be generated. It was concluded that fast co-tunnelling with the back contact was responsible for the lack of nuclear polarisation, supported by the lack of any observed spin pumping in dT measurements of the X_{1-} transitions [82].

5.4 Conclusion

The aim of this chapter was to develop procedures for rapidly measuring the Overhauser field, and then actively compensating for it with the aim of improving the coherence time of a spin qubit. In Section 5.1 a procedure was devised to use quantum dot excitons to measure the strength of an Overhauser field along the growth direction, by exciting the system with a polarised laser, and observing the number of photons emitted by the system in different polarisation bases.

By leveraging the additional energy level structure of coupled quantum dots a proof of concept experiment was performed in Section 5.2 that showed some hallmarks of the predicted behaviour. Even though the system did not behave exactly as expected, the sensing scheme was still shown to be possible. In particular, it was shown that fields of up to ~ 60 mT could be unambiguously sensed in time-scales of around 100 μs. Two hypotheses were suggested to explain the departure of the system from the expected behaviour, but no complete understanding of the effect has been reached to date.

Finally in Section 5.3 a system was designed where an effective magnetic field could be rapidly applied to a spin qubit in another dot by changing only the gate voltage. An experiment was performed to demonstrate this effect by finding a dot exhibiting the X_{1-} charging region, and dragging one of the lines in the left hand dot to build up nuclear polarisation. Unfortunately the experiment was not successful since no evidence of nuclear polarisation could be seen.

Chapter 6

Towards generating photonic cluster states using quantum dots

In 2009 Lindner and Rudolph [37] proposed that linear photonic cluster states can be generated by sequential optical excitation and rotation of an electron spin in a single InGaAs quantum dot. In their original proposal, dubbed the 'photonic machine gun', the electron spin is excited using a fast optical pulse and the spin rotation comes from an external in-plane magnetic field. The proposal was picked up by several groups, but the only experimental demonstration so far comes from Schwartz *et al.* [40], who in 2016 used dark exciton states in InGaAs quantum dots to demonstrate the generation of a linear cluster state showing entanglement persisting over a cluster length of five photons. In their implementation, the electron spin of the original proposal was replaced by the spin of a dark exciton [138]. The spin rotation was provided by the dark exciton's electron-hole exchange splitting so no external magnetic field was required.

Although the Schwartz experiment provided a compelling proof-of-principle of the photonic machine gun, the choice of system suffers from several drawbacks that will hinder its use for generating practically useful photonic cluster states. Firstly, the use of the electron-hole exchange as a built-in magnetic field means the spin rotation rate is fixed by properties of the quantum dot and cannot be tuned. In practice, in the experiment the rate was too fast compared to the photon emission rate of 330 ps, which limited the fidelity of the cluster states and the corresponding entanglement length. Secondly,

the dark exciton states have a finite lifetime of around 1 μs (before decaying to the real quantum dot ground state), fundamentally limiting the ultimate length of cluster states that can be created by this method.

Ideally a matter qubit like the electron spin would be used but the dynamics are complicated by interactions with the quantum dot nuclear spins. The Overhauser field influences the precession and causes decoherence. In this chapter, two implementation of the photonic machine are proposed to attempt to overcome these problems. The first proposal makes use of the flexibility and tunability provided by coupled quantum dots. A level scheme is designed that allows all-optical initialisation and manipulation of a spin qubit, and features the necessary transitions to generate spin-photon entanglement required for cluster state generation. The second proposal uses the spin of a defect atom such as Manganese (Mn) in the quantum dot as the qubit from which the photonic cluster state is generated.

In Section 6.1 the Lindner and Rudolph proposal is revisited. Its basic operation is described and it is numerically simulated in order to gather information about how the fidelity of the scheme could be quantified in an experiment. In Section 6.2 a level scheme for generating photonic cluster states in a coupled quantum dot system is proposed and analysed using a theoretical model. Then in Section 6.3 the second proposal of using the spin of a defect atom is designed and simulated to investigate its behaviour.

6.1 The photonic machine gun

6.1.1 The protocol

The machine gun protocol begins with a single electron confined in a quantum dot initialised into a Pauli X eigenstate $\left|+\right\rangle = \left|\uparrow\right\rangle + \left|\downarrow\right\rangle$. Excitation of the quantum dot with a linearly polarised optical pulse and subsequent spontaneous radiative decay generates a photon whose polarisation is entangled with the electron spin. The electron spin is then rotated around the Y axis by an angle of $\pi/2$. This process is depicted in Figure 6.1

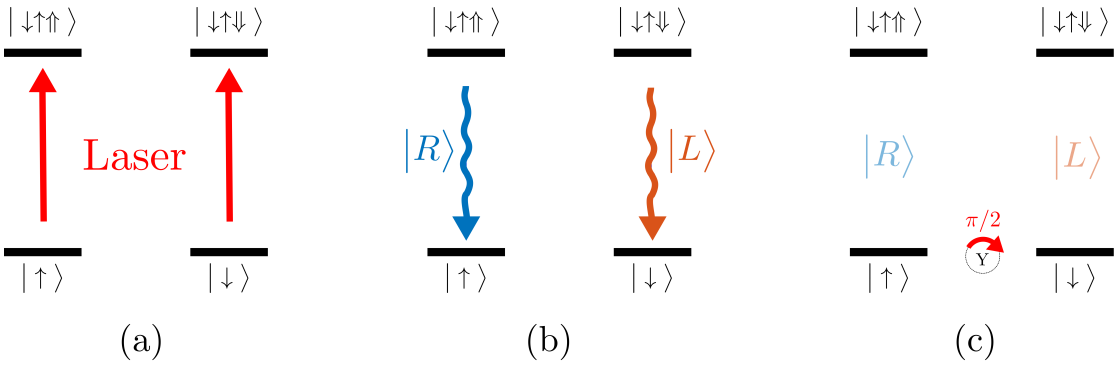

FIGURE 6.1: The electron spin is initialise in the state $|+\rangle = |\uparrow\rangle + |\downarrow\rangle$. (a) A single H polarised laser pulse drives both optical transitions to generate an exciton from each branch of the ground state (red arrows) according to the Faraday geometry selection rules. (b) the exciton recombines (blue and red arrow arrows) emitting a photon whose polarisation is entangled with the electron spin. (c) The electron spin is rotated by an angle of $\pi/2$ around the Y axis.

The state of the system evolves according to

$$\begin{aligned} |\uparrow\rangle + |\downarrow\rangle &\rightarrow |\downarrow\uparrow\Uparrow\rangle + |\uparrow\downarrow\Downarrow\rangle \rightarrow |\uparrow\rangle|R\rangle + |\downarrow\rangle|L\rangle \\ &\rightarrow (|\uparrow\rangle + |\downarrow\rangle)|R\rangle + (-|\uparrow\rangle + |\downarrow\rangle)|L\rangle \end{aligned} \tag{6.1}$$

where $|R\rangle$ and $|L\rangle$ are right and left-hand circularly polarised photons respectively. Normalisation and global phase factors are ignored in the remainder of this chapter. By repeating this process a chain of photons is generated which are in a linear cluster state with the electron. For instance the state after two rounds is

$$\begin{aligned} &|\uparrow\rangle|R\rangle|R\rangle - |\uparrow\rangle|R\rangle|L\rangle - |\uparrow\rangle|L\rangle|R\rangle - |\uparrow\rangle|L\rangle|L\rangle \\ &+|\downarrow\rangle|R\rangle|R\rangle - |\downarrow\rangle|R\rangle|L\rangle + |\downarrow\rangle|L\rangle|R\rangle + |\downarrow\rangle|L\rangle|L\rangle \end{aligned} \tag{6.2}$$

A projective measurement of the electron spin disentangles it leaving the photons in a linear cluster state [7]. To investigate the state of the photons after running the protocol, a method is required to compare the results of the photonic machine with the desired linear cluster state. One metric that can be used is the fidelity [139] between the desired state and the photonic state that is generated by the machine gun. For this, the density matrix that describes the photonic state is required. A way of obtaining this through measurements is quantum state tomography.

6.1.2 Tomography

Quantum state tomography is a way to experimentally determine a quantum state from measurements. Tomography can be performed on an arbitrary state $|\psi\rangle$ of N qubits by measuring it in all combinations of Pauli bases $|M_1\rangle \otimes |M_2\rangle \otimes ... \otimes |M_N\rangle$ where $M_i \in \{|+X\rangle, |-X\rangle, |+Y\rangle, |-Y\rangle, |+Z\rangle, |-Z\rangle\}$ which are the eigenstates of the Pauli operators [140]. These measurements can be used to reconstruct the density matrix either directly or using statistical methods. This can be applied to the photonic state of the machine gun by noting that the photons are generated one by one, and are thus temporally and spatially separated. To perform the measurements required to reconstruct the photonic state, each photon can be sent into the tomography setup shown in Figure 6.2.

By sending many copies of the photonic state into the tomography setup it will be measured along every possible combination of the Pauli bases. The statistics gathered from many such measurements can then be used to perform quantum state tomography to reconstruct the density matrix of the original photonic state. To estimate the number of copies required, a simulation is performed where the photonic state is generated by the machine gun protocol and each photon is sent into the tomography setup. Since only the measurement process is to be evaluated no spin decoherence is included, the selection rules are perfectly obeyed and the rotation direction and angle is exactly as required.

The first part of the simulation involves creating the linear cluster state following the machine gun protocol. The spin starts in the state $|\uparrow\rangle + |\downarrow\rangle$ and the process of optical excitation and decay is effected by applying the rectangular operator $|\uparrow\rangle|R\rangle\langle\uparrow| + |\downarrow\rangle|L\rangle\langle\downarrow|$ which creates a new photon. The spin is then rotated by applying the operator $\exp(-i\sigma_Y\pi/4)$ where σ_Y is the Pauli Y matrix. This is repeated n times and the electron spin is projected out to generate a photonic cluster state of n photons in the state $|\psi_n\rangle$.

The action of the tomography setup is simulated by randomly sending each photon in $|\psi_n\rangle$ down path 1, 2, or 3 in Figure 6.2 and applying the appropriate Jones matrices. The detector that clicks is randomly selected from the probability distribution found by applying each detectors' projectors onto $|\psi_n\rangle$. This process is repeated N times for the

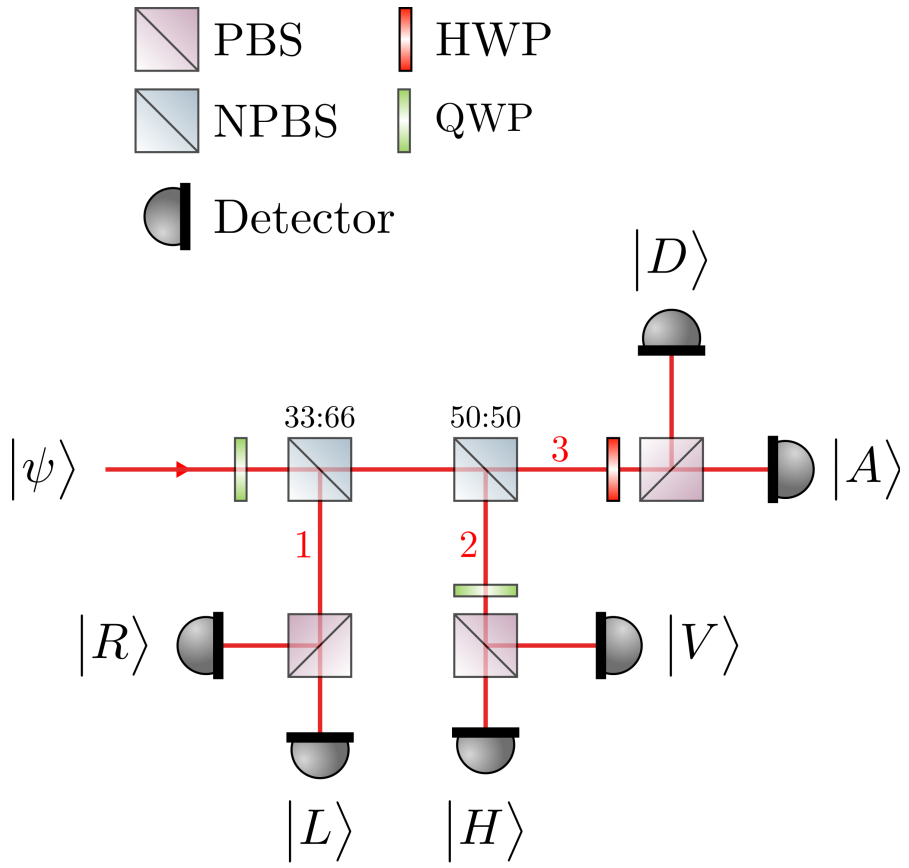

FIGURE 6.2: An optical setup which can probabilistically perform all the measurements required for quantum state tomography of a photonic state $|\psi\rangle$. A click on detector $|S\rangle$ signals that a measurement has been made in the basis $|S\rangle$. A photon entering from the left passes through a quarter-wave-plate (QWP) at $-45°$ to the vertical axis. This rotates the $|R\rangle = \frac{1}{\sqrt{2}}(|H\rangle + i|V\rangle)$ component of the photon to $|V\rangle$ and the $|L\rangle = \frac{1}{\sqrt{2}}(|H\rangle + i|V\rangle)$ component to $|H\rangle$. The combined action of the two non-polarising beam splitters (NPBS) is to send the photon down path 1, 2, or 3 with equal probability. If it goes down path 1 then the polarising beam splitter (PBS) and detectors measure $|\psi\rangle$ in the basis $|R\rangle/|L\rangle$. If it goes down path 2 then a second QWP at an angle of $+45°$ and the PBS measure $|\psi\rangle$ in the basis $|H\rangle/|V\rangle$. If it goes down path 3 then a half-wave-plate (HWP) at an angle of $22.5°$ and the PBS measure $|\psi\rangle$ in the basis $|D\rangle/|A\rangle$ where $|D\rangle = \frac{1}{\sqrt{2}}(|R\rangle + i|L\rangle)$ and $|A\rangle = \frac{1}{\sqrt{2}}(|L\rangle + i|R\rangle)$. Global phases have been discarded.

same $|\psi_n\rangle$ (so N copies of the state are used up). The result is a matrix $\mathcal{M}$ of detection events of size $\overbrace{6 \times 6 \times ... \times 6}^{n}$ where the number at index $(i_1, i_2, ..., i_n)$ in the matrix is the number of times that photon 1 was detected on detector i_1, photon 2 was detected on detector i_2, ... *and* photon n was detected on detector i_n (where i_x is H, V, D, A, R or L). $\mathcal{M}$ is used together with a maximum likelihood estimation (MLE) routine to estimate the density matrix of the system ρ_{MLE}. Finally, the fidelity is calculated between ρ_{MLE} and $|\psi_n\rangle$.

The whole simulation is repeated to get 10 values of the fidelity for each N (each calculated using different statistics $\mathcal{M}$). The average value of the fidelity as a function of N is shown in Figure 6.3a. The errorbars, shown again in Figure 6.3b for clarity, are the standard deviation in the fidelity calculated for each repetition.

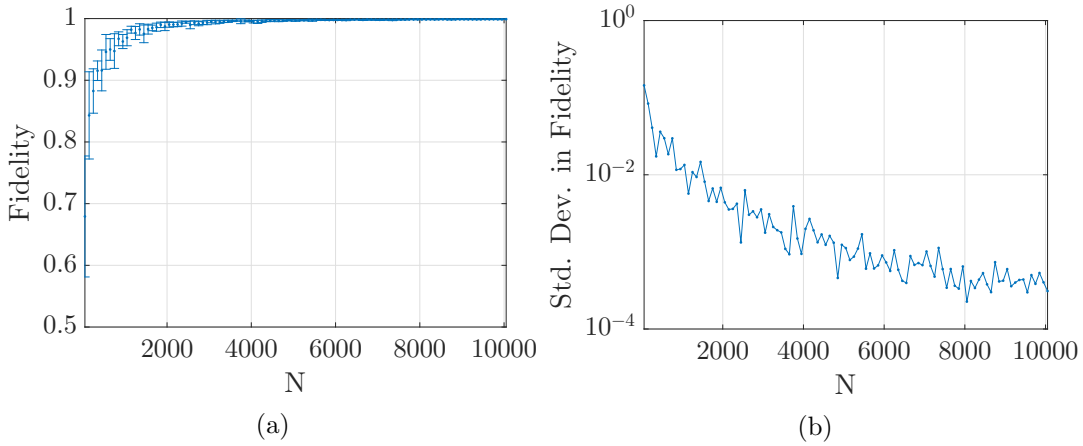

FIGURE 6.3: The fidelity between the real state generated by the photonic machine gun and the state reconstructed via quantum tomography using a maximum likelihood routine. N is the number of copies of the photonic state that were measured. The mean (a) and standard deviation (b) in the fidelity when the simulation is repeated 10 times.

The figures show that for $\sim$ 6000 measured states the fidelity is greater than 0.99 and the standard deviation between runs is below 10^{-3}. The conclusion is that for $N \geq\sim$ 6000 the MLE routine gives a very good estimate of the quantum state and is robust against sampling noise. The time taken for an experimental characterisation run can be estimated, given typical values for InGaAs quantum dots. The time taken to generate a photon and perform the following spin rotation is defined as t_g, and the combined photon collection and detection efficiency is η. The required number of samples for a reliable tomography is n_t. Then for a cluster state of n photons, the time required for a successful tomography is

$$T = \frac{n_t t_g n}{\eta^n} \tag{6.3}$$

Figure 6.4 demonstrates T as a function of η using $n_t = 6,000$ and $t_g \sim 2$ ns to allow for any delays caused by the rotation mechanism.

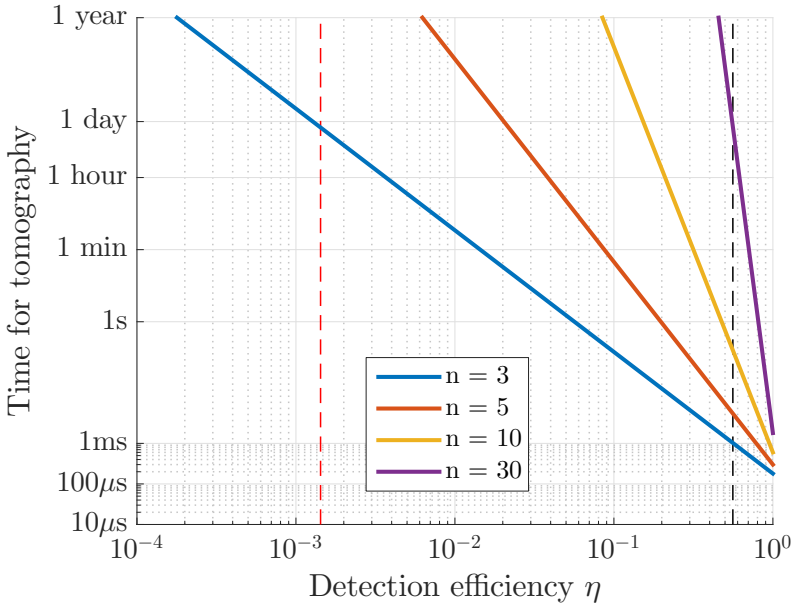

FIGURE 6.4: Time required to collect sufficient statistics to estimate the density matrix as a function of the combined photon collection and detection efficiency η. The black dashed line shows the efficiency possible using the highest values of photon collection and detection available in the literature. The red dashed line shows the efficiency in the experiment by Schwartz *et al.* [40].

Photon collection efficiency for quantum dots embedded in micro-pillars can be up to 66% and photon detection efficiency can be as high as 90% for photons around 900 nm [134]. The combined efficiency of around 59% is shown by the black dashed line in the figure. The overall detection efficiency in the Schwartz experiment was around 0.14% and is shown by the red dashed line. This graph show that a cluster state of up to 30 photons could be characterised by MLE quantum state tomography in a day using highly optimised samples and detectors. For larger states tomography is not a feasible approach due to the exponentially increasing time so other methods must be used, such as the localizable entanglement measure [141] or entanglement witnesses [142] which require fewer measurements to verify entanglement.

The generation step in the simulations above was ideal, in that spin decoherence and Zeeman splitting was not included, nor the effects of random spontaneous emission time. The effects of decoherence can be mitigated if the time-scale of the excitation and rotation steps in the protocol is shorter than the spin decoherence time. This was the case in the Schwartz experiment where the dark exciton had a decoherence time of around 100 ns and spin rotations took place within several nanoseconds [41]. The spin

rotation mechanism (be it a magnetic field or electron-hole exchange) would necessarily split the ground and excited states meaning the two photon polarisations would have a different energy. Each component in the cluster state (6.2) therefore has a different energy and builds up phase at a different rate. These phases can only be taken into account if the photon detection times are tracked to within the Larmour periods of the ground and excited states.

The next section covers work that was done to see if coupled quantum dots could offer a different level scheme that would allow the photonic machine gun to be implemented whilst solving some of these problems.

6.2 Designing a coupled quantum dot qubit with Λ schemes plus recycling transitions

To use spin qubits in quantum dots for generating photonic cluster states three basic process must at least be possible: initialisation, single qubit rotations and readout. In a single quantum dot the Faraday selection rules provide recycling transitions for readout, but no Λ scheme for optical rotation. On the other hand, the Voigt selection rules facilitate rotation but have no recycling transitions. Before embarking on the research in this section some time was spent investigating whether the selection rules in the Voigt geometry would nonetheless allow generation of linear cluster states without modification, but ultimately it became clear that this was not possible.

Kim *et al.* have demonstrated that coupled quantum dots can provide a qubit where optical initialisation, manipulation and readout can all be performed with the same magnetic field orientation [79]. However in their scheme the recycling transitions had the same polarisation and different energies. To generate photonic cluster states using the photonic machine gun the recycling transitions should have orthogonal polarisation. In addition it is desirable to have degenerate ground states and photon transition energies to avoid the build up of phase between terms in the cluster state.

In this section a system using coupled quantum dots is theoretically designed where where spin initialisation, rotation and entanglement generation required by the photonic

machine gun, can all be done optically. The combination of an external magnetic field and a strong prepared Overhauser field generate a double Λ system, whilst keeping the orthogonally polarised recycling transitions of the Faraday geometry. Initially it was though that the level scheme would allow for spin rotations on the picosecond time-scale which would have allowed the generation of hundreds of entangled photons within the homogeneous coherence time of the electron. However it was later realised that picosecond rotations are not possible due to the nature of the exited states of the system. Nevertheless the system provides advantages over the Kim scheme by operating at lower magnetic fields, having orthogonally polarised recycling transitions, and allowing optical rotations within a few tens of nanoseconds [143].

6.2.1 Model

To investigate this system the model of the singly charged coupled quantum dot built in Chapter 3 is used. To take into account the interaction of the electron spin with the Overhauser field, the following term is added to the ground state Hamiltonian

$$H_{oh} = A\Big(\sigma^L \cdot \mathbf{I}^L + \sigma^R \cdot \mathbf{I}^R\Big) \tag{6.4}$$

where A governs the coupling strength and $\mathbf{I}^{(L/R)}$ are vectors specifying the nuclear polarisation in each dot. The Pauli matrices $\sigma^{(L/R)}$ are those defined in (3.7). A similar term is added to the excited state Hamiltonian to describe the interaction of electrons and holes with the Overhauser field

$$H_{oh} = A\Big(\sigma_e^L \cdot \mathbf{I}^L + \sigma_e^R \cdot \mathbf{I}^R\Big) \tag{6.5}$$

$$+ \sum_{j=L,R} \Big(A_{h,p}\left(\sigma_{h,x}^j I_x^j + \sigma_{h,y}^j I_y^j\right) + A_{h,z}\sigma_{h,z}^j I_z^j\Big) \tag{6.6}$$

where the hole also feels an Overhauser field with anisotropic coupling. The in and out of plane hole coupling strengths are given by $A_{h,p}$ and $A_{h,z}$ respectively. The electron coupling term A is set equal to 1 so that the magnitude of the effect is governed only by $\mathbf{I}^{(L/R)}$. $A_{h,z}$ is set to -0.1 to reflect that the Overhauser effect for holes is about one tenth of that for the electrons and dominated by an Ising interaction term [19, 45, 91].

6.2.2 Ground states

The ground states of the system are first investigated by diagonalising the Hamiltonian. An in-plane Overhauser field of strength 35 T is turned on in dot L and an external field of strength -690 mT is applied in both dots along the growth direction (in the Faraday geometry). This Overhauser field is far in excess of the possible field in InGaAs quantum dots (around 5 T) [144–146] but serves to better illustrate the idea. The electron and hole tunnelling strengths are set to $t_e = 0.4$ meV and $t_h = 25$ μeV respectively, corresponding to a quantum dot previously investigated in the literature [115]. Figure 6.5 shows the energy levels of the system (top) and states (bottom) of the two lowest energy ground states of the system, labelled $\big|\mathrm{G1}\big\rangle$ and $\big|\mathrm{G2}\big\rangle$.

At -4 V the electron wavefunction is almost entirely in dot L (the combined populations of the $\big|0,\uparrow\big\rangle$ and $\big|0,\downarrow\big\rangle$ states is less than 1%) so it feels the in-plane Overhauser field as well as the external field. In this case the Overhauser field is much stronger than the external field and so the eigenstates are linear combinations of the Faraday geometry eigenstates. At 0 V the electron wavefunction is almost entirely in dot R. It only feels the external field so the eigenstates remain $\big|0,\uparrow\big\rangle$ and $\big|0,\downarrow\big\rangle$. In between, the tunnelling and in-plane field mix all four states together.

The Overhauser field strength is now reduced to a more realistic 86 mT, and the external field is reduced to -340 mT. This reduces the splitting on either side of the anti-crossing. The electron tunnelling strength is reduced to 0.2 meV which corresponds to a tunnel barrier thickness of around 30 nm [114]. The effect of both is to ensure that from -2 V to 0 V the ground states $\big|\mathrm{G1}\big\rangle$ and $\big|\mathrm{G2}\big\rangle$ are almost purely made up of basis states $\big|0,\uparrow\big\rangle$ and $\big|0,\downarrow\big\rangle$ respectively (the population of other basis states is less than 1%). To store a spin qubit in this system it should be operated above -2 V. In this gate voltage range the ground states can therefore be approximated as $\big|\mathrm{G1}\big\rangle \sim \big|0,\uparrow\big\rangle$ and $\big|\mathrm{G2}\big\rangle \sim \big|0,\downarrow\big\rangle$, and are split by an energy $\Delta_G = 10$ μeV. Next the excited states of the system are calculated that give rise to the necessary transitions. Hole tunnelling in the excited states is not important since the anti-crossings that it generates are over 2 V away from the gate voltage region of interest.

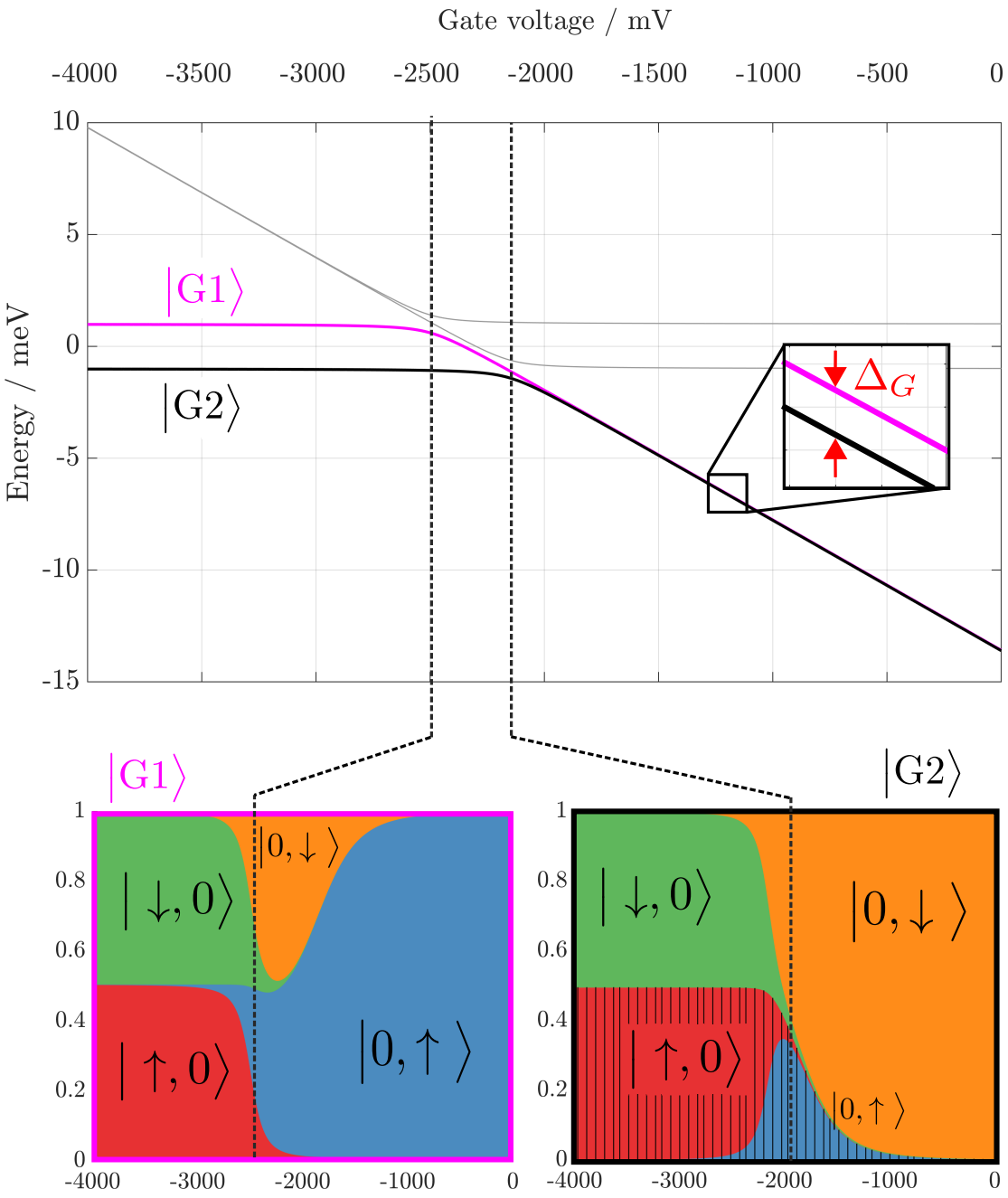

FIGURE 6.5: The energy levels (top) of system ground states with an exaggerated Overhauser field strength of 35 T present in dot L, and an external magnetic field in the Faraday geometry of strength −690 mT. The states of two of the eigenstates $|\mathrm{G1}\rangle$ (bottom left) and $|\mathrm{G2}\rangle$ (bottom right) over the same gate voltage range. Anti-crossing positions are denoted by the dashed black lines. The ground state splitting on the right is Δ_G.

6.2.3 Recycling transitions

Generating entanglement between the polarisation of a spontaneously emitted photon and a spin qubit in states $|\mathrm{G1}\rangle$ and $|\mathrm{G2}\rangle$ requires orthogonally polarised recycling transitions like those of a charged exciton in the Faraday geometry. Two excited states of the

system are labelled $|\mathrm{R1}\rangle$ and $|\mathrm{R2}\rangle$ which are over 95% $|0, s\Uparrow\rangle$ and $|0, s\Downarrow\rangle$ respectively over the whole gate voltage range. They are split by an energy $\Delta_R = 44\ \mu$eV which is just the hole Zeeman splitting in dot R. $|\mathrm{G1}\rangle$ can be excited to $|\mathrm{R1}\rangle$ by a right-hand circularly polarised photon, whilst $|\mathrm{G2}\rangle$ can be excited to $|\mathrm{R2}\rangle$ by a left-hand circularly polarised photon. The orthogonal polarisation of these transitions allows generation of entanglement between the spin and photon polarisation. The energy of these transitions is shown in Figure 6.6.

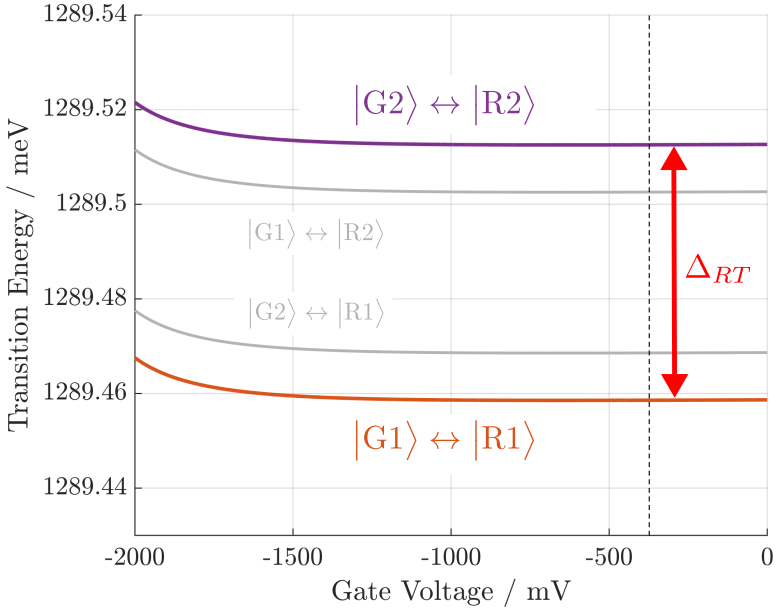

FIGURE 6.6: The energy of the transitions between ground states $|\mathrm{G1}\rangle$ and $|\mathrm{G2}\rangle$, and the excited states $|\mathrm{R1}\rangle$ and $|\mathrm{R2}\rangle$.

The slope towards -2 V is caused by the anti-crossing in the ground state. The difference in transition energies Δ_{RT} is equal to $\mu_B \left| g_e^R - g_{h,z}^R \right| B_z$ which is the sum of the Zeeman splitting due to the hole and electron in dot R (with a negligible correction due to the weak mixing of other basis states). In this case it amounts to 54 μeV however it can be tuned by finding a different coupled quantum dot with a different g-factors.

The gray transitions shown in the figure are not allowed by the selection rules. In this model their strength is over 7 orders of magnitude less than the allowed transitions due to the purity of the ground and excited states. In reality their strength would be only $\sim$3 orders of magnitude lower due to mechanisms that relax the selection rules.

6.2.4 Lambda transitions

The pico-second time-scale electron spin rotations possible in the Voigt geometry are enabled by excited states that can be reached by optical transitions from both ground states. In single quantum dots the Faraday geometry selection rules do not allow such a shared excited state. It is now shown that the combination of the Overhauser and external field mix the excited states to form excited states state which can be reached from $\left|\mathrm{G1}\right\rangle$ and $\left|\mathrm{G2}\right\rangle$ by allowed optical transitions. Figure 6.7 shows the energy (top) and states (bottom) of two of the system's excited states, labelled $\left|\mathrm{L1}\right\rangle$ and $\left|\mathrm{L2}\right\rangle$.

The states $\left|\mathrm{L1}\right\rangle$ and $\left|\mathrm{L2}\right\rangle$ anti-cross at a gate voltage of -381 mV (dotted line). Near the anti-crossing $\left|\mathrm{L1}\right\rangle$ is an equal superposition of $\left|\downarrow\Uparrow,\uparrow\right\rangle$ (purple area) and $\left|\downarrow\Uparrow,\downarrow\right\rangle$ (pink area) with the populations of other basis states less than 1.4% (dark excitons in dot L). $\left|\mathrm{L2}\right\rangle$ is an equal and opposite (shown by the shaded lines) superposition of the same basis states with the population of other basis states totalling to less than 1.1%. Thus $\left|\mathrm{L1}\right\rangle \sim \left|\downarrow\Uparrow,\downarrow\right\rangle + \left|\downarrow\Uparrow,\uparrow\right\rangle$ and $\left|\mathrm{L2}\right\rangle \sim \left|\downarrow\Uparrow,\downarrow\right\rangle - \left|\downarrow\Uparrow,\uparrow\right\rangle$.

The ground state $\left|\mathrm{G1}\right\rangle$ ($\sim \left|0,\uparrow\right\rangle$) can be excited to the state $\left|\downarrow\Uparrow,\uparrow\right\rangle$ by a right-hand circularly (R) polarised photon, and $\left|\mathrm{G2}\right\rangle$ ($\sim \left|0,\downarrow\right\rangle$) can be excited to the state $\left|\downarrow\Uparrow,\downarrow\right\rangle$ by a the same process. Since $\left|\mathrm{L1}\right\rangle$ and $\left|\mathrm{L2}\right\rangle$ both contain $\left|\downarrow\Uparrow,\uparrow\right\rangle$ and $\left|\downarrow\Uparrow,\downarrow\right\rangle$ they can both be reached from both $\left|\mathrm{G1}\right\rangle$ and $\left|\mathrm{G2}\right\rangle$. They are both therefore shared excited states which form a double Λ scheme. The energy of the transitions between the ground states and these two excited states is shown in Figure 6.8.

The transitions between all 4 states are shown by the coloured lines labelled by the ground and excited state that they come from. The other gray lines in the figure are other transitions in the system. These are not relevant since they are all at-least 34 μeV away from the transitions of interest and the closest two have a relative transition strength of less than 0.4%.

Ideally these transitions could be driven by a fast detuned optical pulse to perform picosecond spin rotations [77]. Since the separation between the lambda transitions Δ_{LT} is small compared with the quantum dot linewidth and detuning used in such spin rotation schemes, they would both be driven simultaneously. Since the excited states are symmetric and antisymmetric superpositions, driving both Λ schemes at once with

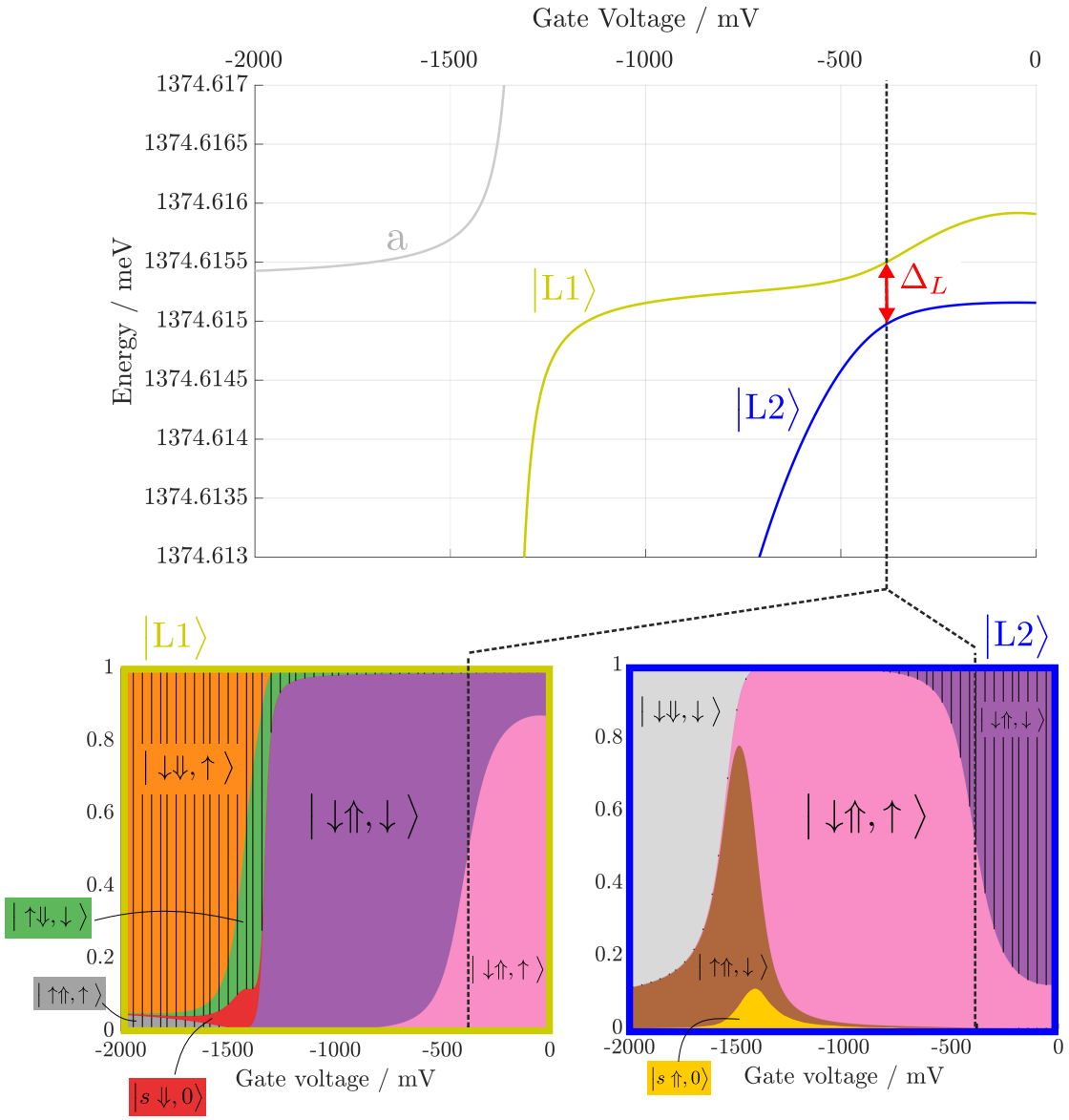

FIGURE 6.7: The energy levels (top) of the shared excited states of the system. The states of two of the eigenstates $|\mathrm{L1}\rangle$ (bottom left) and $|\mathrm{L2}\rangle$ (bottom right) over the same gate voltage range. The position of the anti-crossing caused by the in-plane Overhauser field and electron tunnelling is shown by the black dashed line. At the anti-crossing the levels are separated by Δ_L. The gray line labelled a is another excited state which is irrelevant since it is far detuned from $|\mathrm{L1}\rangle$ and $|\mathrm{L2}\rangle$.

a pulse would result in destructive interference. It is still possible to use this system for spin rotations via stimulated Raman transitions (SRTs) by tuning two phase locked lasers to between the two transitions on each branch [143]. Such a laser is detuned from each excited state, so each Λ scheme generates a SRT (see Section 2.5.2). By tuning the laser between the two excited states, the SRTs interfere constructively. Rotations in this way could be performed within tens of nano-seconds.

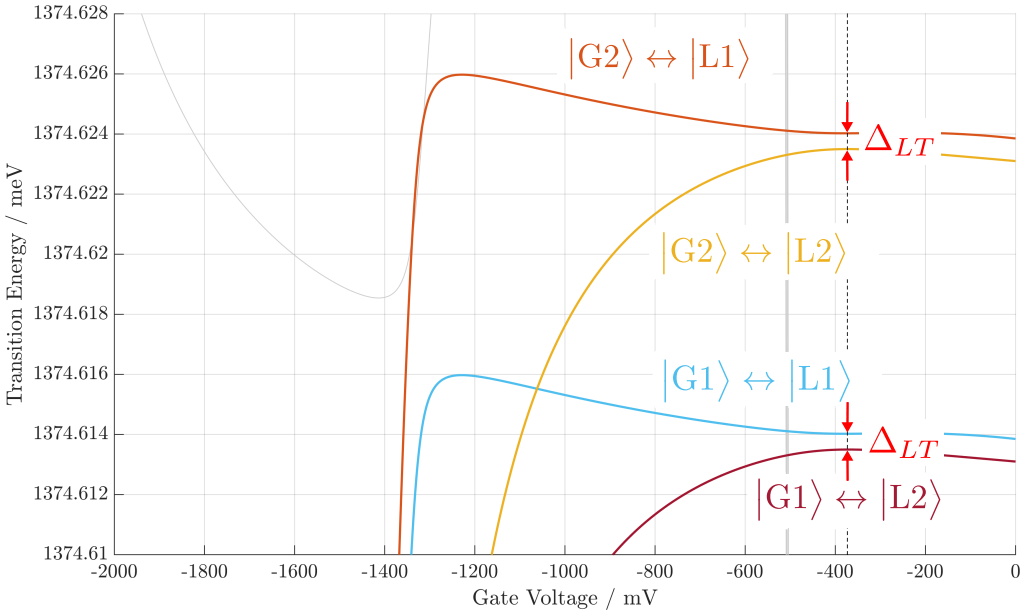

FIGURE 6.8: The energy of the transitions that together form the two Λ schemes. The dashed line is at the anti-crossing gate voltage of −381 mV where these transitions have equal strength. The separation between transitions Δ_{LT} is around 0.5 μeV. Gray lines are other transitions in the system.

6.2.5 Summary

It has been shown that an in-plane Overhauser field of 86 mT and external field of −340 mT in the Faraday geometry lead to system eigenstates in a single electron coupled dot that simultaneously allow all-optical initialisation, rotation and entanglement generation between spin state and photon polarisation. The ground states $|\mathrm{G1}\rangle$ and $|\mathrm{G2}\rangle$ were almost stationary states split by 10 μeV. The recycling transitions were strong and separated by around 54 μeV but this was dependent on the hole and electron g-factors in dot R which could be effectively tuned by moving to a different dot. The energy difference between the two arms of each of the two Λ schemes was $\sim 10\mu eV$ due to the splitting of the ground state. The transition energies of the two Λ schemes were too close to allow individual addressing so destructive interference ruled out the possibility of using a fast optical pulse to drive them. Slower rotations by stimulated Raman transitions were still possible [143].

Figure 6.9 shows the transitions that connect these states along with their polarisation.

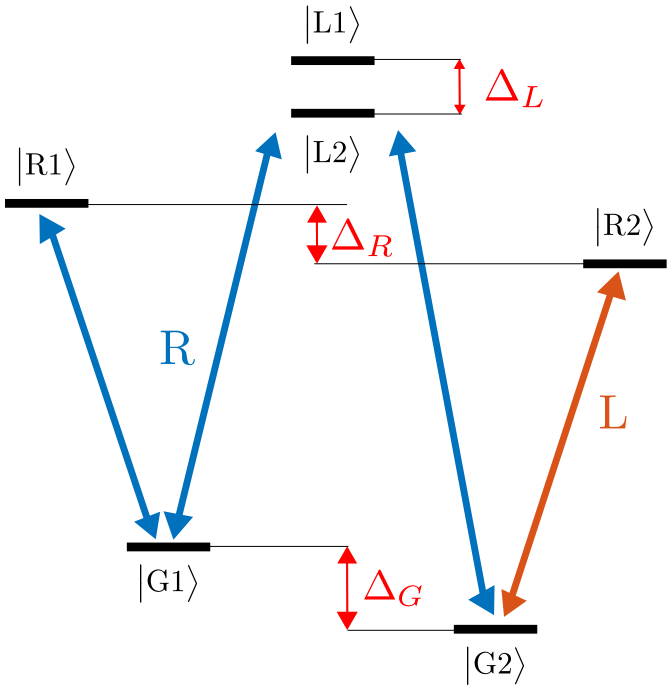

FIGURE 6.9: The relevant transitions in the system which present recycling transitions and two Λ transitions. Blue and red arrows show right (R) and left-hand (L) circularly polarised transitions. The splittings are $\Delta L = 0.5$ μeV, $\Delta G = 10$ μeV, $\Delta R = 44$ μeV.

The approach of this section was to try to design a system where the effects of spin decoherence could be mitigated by manipulating the spin faster than the spin decoherence time. The idea of the next section is to replace the electron spin with a different matter qubit whilst still taking advantage of the optical properties of quantum dots.

6.3 Replacing the electron spin

The original photonic machine gun protocol used the spin of an electron and optical transitions in a quantum dot to generate photonic cluster states. The electron interacts strongly with the nuclear spins in the quantum dot leading to fast decoherence. The Schwartz experiment [40] replaced the electron spin with the spin of a dark exciton which suffers less from decoherence but is metastable with a lifetime of around 1 μs. A solution to both these problems is to find a new replacement for the 'seed' spin in the photonic machine gun.

This section investigates a system where the spin can be replaced by a two level system, referred to throughout as the *host* spin, that interacts with the excitons of the quantum dot through an Ising exchange interaction. A candidate is the total spin of a Mn atom doped in Cadmium telluride/Zinc telluride (CdTe/ZnTe) quantum dots. In these systems the spin of the Mn atom interacts with the electron and hole through Ising interactions to first approximation [147]. Ignoring the dark excitons, the total interaction is an Ising interaction between the pseudo-spin of the exciton and the Mn atom. It has been shown that the Mn spin can be optically manipulated and act as a qubit [148].

To investigate whether the photonic machine gun could be implemented in this system, a model is built and the system is numerically simulated. The simulation is sufficiently general that the results can be applied to other host spins that interact with excitons in the same way. The performance of the scheme is assessed by varying the important system parameters and comparing the final state with the ideal cluster state. The numerical propagation method described in Section 6.3.5 is somewhat different to the one typically employed in the literature. The method used to derive the comparison is also a new development as far as the author is aware.

6.3.1 Ising interaction

In order to create the entanglement in Lindner and Rudolph's cluster state proposal [37], it is necessary to map from the spin states to the photon polarisation states. In the single electron dot in the Faraday geometry it is essentially the Pauli exclusion principle that allows this through the blocking of diagonal transitions. In this section it is shown how the Ising interaction between the host spin and the excitons also allows entanglement generation. The host spin is represented by the states $\left|\uparrow\right\rangle$ and $\left|\downarrow\right\rangle$. The bright neutral excitons with total spin $+1$ and -1 are written as $\left|\downarrow\Uparrow\right\rangle$ and $\left|\uparrow\Downarrow\right\rangle$ respectively, and the empty dot with no exciton is written as $\left|0_X\right\rangle$. Figure 6.10 shows 3 of the 6 spin configurations.

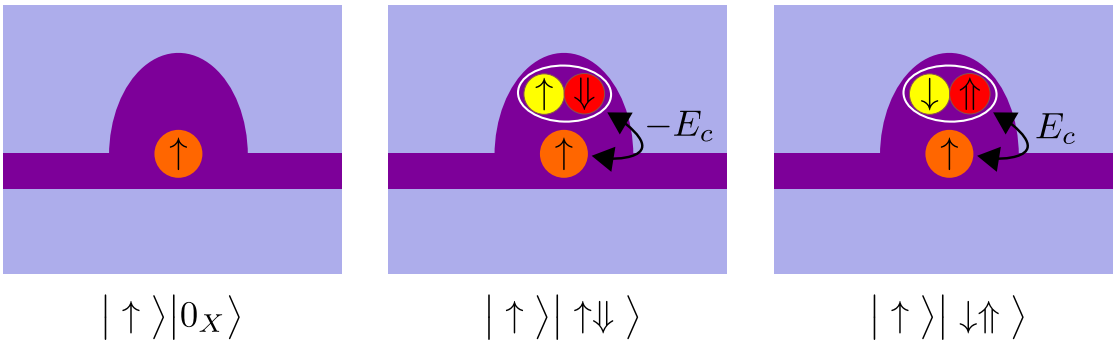

FIGURE 6.10: Three of the possible 6 spin configurations in the system. The spin state is shown beneath each image. The other three states are $|\downarrow\rangle|0_X\rangle$, $|\downarrow\rangle|\uparrow\Downarrow\rangle$ and $|\downarrow\rangle|\downarrow\Uparrow\rangle$.

The host spin is represented by the orange circle, and the electron and hole of the exciton are shown by the yellow and red circles. The arrow inside each circle indicates the spin of the particle. The interaction between the exciton pseudospin and the host spin is shown by the black arrows [147]. Figure 6.11 shows the energy levels in this system where the energy splitting of the excited states due to the Ising interaction is denoted by E_c.

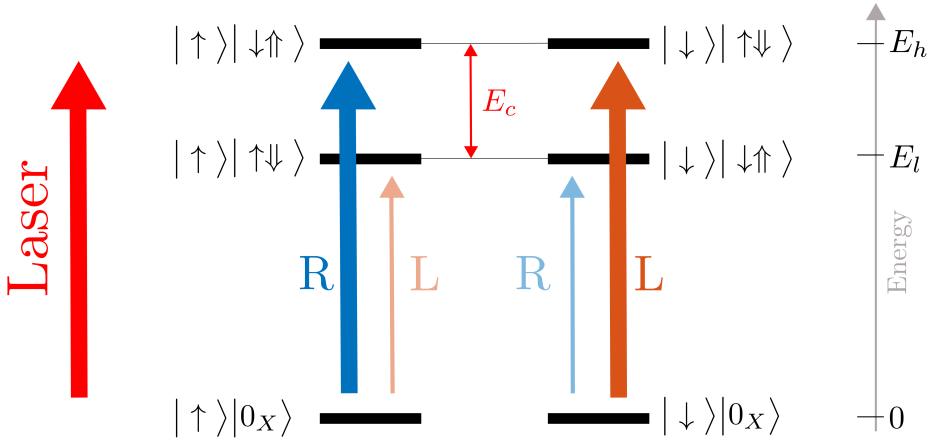

FIGURE 6.11: The energy levels in the system with no magnetic field or electron-hole exchange. A horizontally polarised laser can drive both the right (R) and left-hand (L) circularly polarised transitions allowed by the Faraday geometry selection rules.

In the absence of any magnetic field or electron-hole exchange interaction, $|\uparrow\rangle|\downarrow\Uparrow\rangle$ and $|\downarrow\rangle|\uparrow\Downarrow\rangle$ are degenerate. $|\uparrow\rangle|\uparrow\Downarrow\rangle$ and $|\downarrow\rangle|\downarrow\Uparrow\rangle$ are also degenerate but are lower in energy by E_c. This system is essentially the same as a neutral exciton since the host spin does not occupy the quantum dot levels. As such the system can be optically excited following the red and blue arrows. A laser tuned to energy E_h and

polarisation $|H\rangle = |R\rangle + |L\rangle$ will strongly drive the system into states $|\uparrow\rangle|\downarrow\Uparrow\rangle$ and $|\downarrow\rangle|\uparrow\Downarrow\rangle$ (thicker arrows) and only weakly drive transitions to $|\uparrow\rangle|\uparrow\Downarrow\rangle$ and $|\downarrow,\downarrow\Uparrow\rangle$ (thinner arrows) because of the detuning E_c. After the radiative lifetime of the exciton the excited states will decay back down to the ground states via the arrows in Figure 6.12. Each excited state decays into a different photon mode $|R_h\rangle$, $|L_h\rangle$, $|R_l\rangle$ or $|L_l\rangle$ where the label reflects the polarisation and energy.

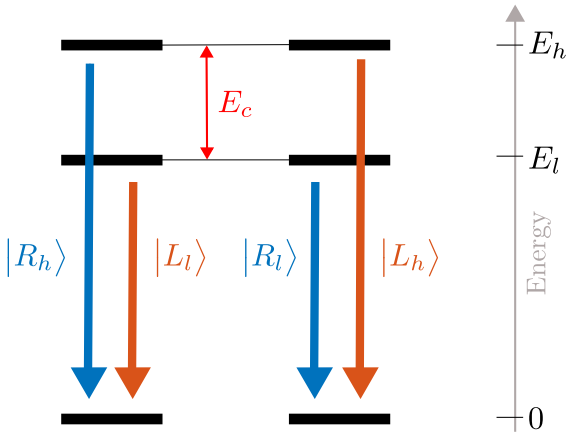

FIGURE 6.12: The possible transitions in the system with no magnetic field or electron-hole exchange. Each exciton/host spin excited state decays into a different photon mode $|R_h\rangle$, $|L_h\rangle$, $|R_l\rangle$ or $|L_l\rangle$ of polarisation R or L, and energy E_h or E_l.

Considering only the strongly driven transitions, a system starting in the state $a|\uparrow\rangle|0_X\rangle + b|\downarrow\rangle|0_X\rangle$ will evolve like

$$a|\uparrow\rangle|0_X\rangle + b|\downarrow\rangle|0_X\rangle \;\rightarrow\; a|\uparrow\rangle|\downarrow\Uparrow\rangle + b|\downarrow\rangle|\uparrow\Downarrow\rangle \;\rightarrow\; a|\uparrow\rangle|R_h\rangle + b|\downarrow\rangle|L_h\rangle \tag{6.7}$$

which has created the entanglement between the host spin and the photon necessary for implementing the photonic machine gun. These transitions are referred to as 'desirable' since they directly map the state from the host spin onto the photon polarisation. The weakly driven transitions will evolve like

$$a|\uparrow\rangle|0_X\rangle + b|\downarrow\rangle|0_X\rangle \;\rightarrow\; a|\uparrow\rangle|\uparrow\Downarrow\rangle + b|\downarrow\rangle|\downarrow\Uparrow\rangle \;\rightarrow\; a|\uparrow\rangle|L_l\rangle + b|\downarrow\rangle|R_l\rangle \tag{6.8}$$

These transitions are referred to as 'undesirable' since they represent the wrong mapping. This system can be used to generate photonic cluster states following the same process of repeated optical excitation and host spin rotation as in the photonic machine gun. The

advantage is that now the electron in the original scheme can be replaced by any two level system which interacts with the exciton spin via an Ising interaction. To investigate further, a model of the system is built and used to simulate the photonic machine gun protocol. The system's performance is then explored as a function of several system parameters.

6.3.2 Model

Including all of the host spin and exciton states the Hilbert space is 6-dimensional, spanned by the basis vectors

$$\left|\uparrow, 0_X\right\rangle \qquad \left|\downarrow, 0_X\right\rangle \tag{6.9}$$

$$\left|\uparrow, \downarrow\Uparrow\right\rangle \qquad \left|\downarrow, \downarrow\Uparrow\right\rangle \tag{6.10}$$

$$\left|\uparrow, \uparrow\Downarrow\right\rangle \qquad \left|\downarrow, \uparrow\Downarrow\right\rangle \tag{6.11}$$

States (6.9) have no exciton, states (6.10) have a spin-up exciton and states (6.11) have a spin-down exciton. Each of the 4 states with an exciton can decay radiatively into a different photon mode according to Figure 6.12. For a single excitation the system will evolve into a general mixture of states (6.10) and (6.11) which can decay into the photon modes $\left|R_h\right\rangle$, $\left|L_h\right\rangle$, $\left|R_l\right\rangle$ and $\left|L_l\right\rangle$. The Ising interaction can be described by the Hamiltonian

$$H_c = \frac{1}{2} E_c S_z^h \cdot S_z^X \tag{6.12}$$

where S_z^h and S_z^X are the host and exciton spins respectively (treating both as pseudo spin-1/2 particles). An external magnetic field in the Z direction can be included via the Hamiltonian

$$H_z = \frac{1}{2} g_h B_z S_z^h + \frac{1}{2} g_X B_z S_z^X \tag{6.13}$$

where g_h and g_X are g-factors of the host spin and exciton respectively, and B_z is the magnetic field strength. The Bohr magneton has been left out so the field is expressed in terms of energy. The horizontally polarised driving laser is included in the rotating

frame through the interaction Hamiltonian

$$H_{\text{int}} = \frac{1}{2}\Omega\left(t\right)\Big(\left|0_X\right\rangle\!\!\left\langle \downarrow\Uparrow\right| + \left|\downarrow\Uparrow\right\rangle\!\!\left\langle 0_X\right| + \left|0_X\right\rangle\!\!\left\langle \uparrow\Downarrow\right| + \left|\uparrow\Downarrow\right\rangle\!\!\left\langle 0_X\right|\Big) \tag{6.14}$$

where $\Omega\left(t\right)$ is the Rabi frequency governing the strength of the interaction along with an envelope function which determines the time behaviour. In this frame the bare exciton energy is described by

$$H_0 = -\delta_\omega\Big(\left|\downarrow\Uparrow\right\rangle\!\!\left\langle \downarrow\Uparrow\right| + \left|\uparrow\Downarrow\right\rangle\!\!\left\langle \uparrow\Downarrow\right|\Big) \tag{6.15}$$

The detuning is $\delta_\omega = \frac{1}{2}E_c$ so that the laser is always resonant with the desirable transitions as in Figure 6.11. The total Hamiltonian is then

$$H_{\text{tot}} = H_c + H_z + H_0 + H_{\text{int}} \tag{6.16}$$

6.3.3 Simulating the system

To estimate the performance of the scheme, the dynamics of the Hamiltonian constructed in the previous section are solved using the quantum Monte Carlo (QMC) solver provided by the QuTip python package [149]. The quantum jump formalism [150] augments the Schrödinger equation with a non-Hermitian term composed of collapse operators for dephasing and relaxation in a system. The system is said to collapse when this non-Hermitian term reduces the norm of the wavefunction to below a random number chosen from a uniform distribution on $[0, 1]$ [151]. The system is initialised into the ground state

$$\Big(\left|\uparrow\right\rangle + \left|\downarrow\right\rangle\Big) \otimes \left|0_X\right\rangle \tag{6.17}$$

where the host spin has been prepared in the state $\left|+\right\rangle$ and the exciton is in the vacuum mode (no excitation). Spontaneous emission is taken into account with collapse operators

$$\begin{aligned} C_1 &= \sqrt{\gamma_{\text{sp}}}\left|\uparrow, 0_X\right\rangle\!\!\left\langle \uparrow, \downarrow\Uparrow\right| & C_3 &= \sqrt{\gamma_{\text{sp}}}\left|\downarrow, 0_X\right\rangle\!\!\left\langle \downarrow, \downarrow\Uparrow\right| \\ C_2 &= \sqrt{\gamma_{\text{sp}}}\left|\uparrow, 0_X\right\rangle\!\!\left\langle \uparrow, \uparrow\Downarrow\right| & C_4 &= \sqrt{\gamma_{\text{sp}}}\left|\downarrow, 0_X\right\rangle\!\!\left\langle \downarrow, \uparrow\Downarrow\right| \end{aligned} \tag{6.18}$$

where γ_{sp} is the spontaneous emission rate set to 1GHz. A collapse matrix is added to include dephasing of the host spin which is written as [152]

$$C_{\text{dp}} = \sqrt{\gamma_{\text{dp}}} \left(|\uparrow\rangle\langle\uparrow| - |\downarrow\rangle\langle\downarrow| \right) \tag{6.19}$$

where $\gamma_{\text{dp}} = 1/T_2$ is the dephasing rate. A typical trajectory of the system is shown in Figure 6.13. Under the action of the laser the populations of the $|\downarrow, 0_X\rangle$ and $|\uparrow, 0_X\rangle$ components decrease and the populations of the $|\downarrow, \downarrow\Uparrow\rangle$ and $|\uparrow, \uparrow\Downarrow\rangle$ components rise. In addition the populations of the $|\uparrow, \uparrow\Downarrow\rangle$ and $|\downarrow, \downarrow\Uparrow\rangle$ states rises since although they are detuned from the laser by E_c they are still very weakly driven. As a result of the detuning the oscillations in their populations are faster and the population never reaches more than around 0.1. At $\tau_{\text{pump}} = 0.2$ ns the pump is turned off and so all driving ceases.

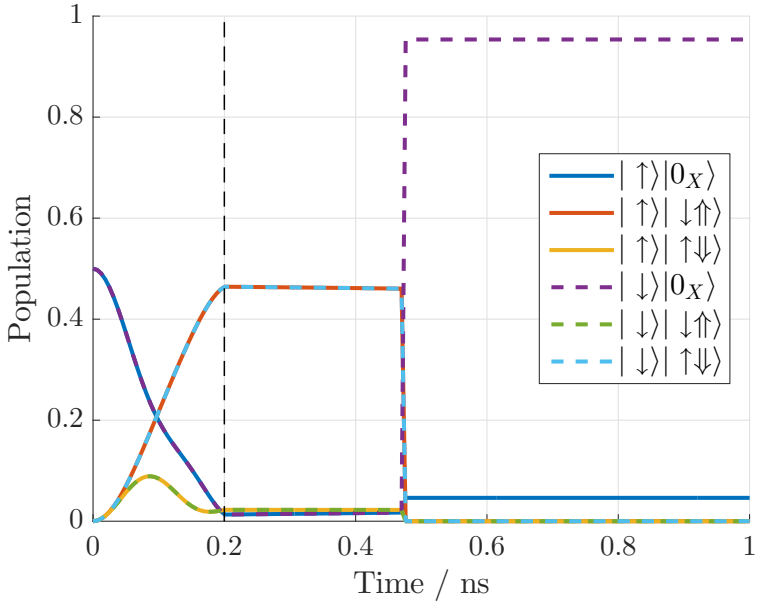

FIGURE 6.13: Populations of the six states during a typical trajectory. The black dashed line shows when the pump laser is switched off. The system decays spontaneously just after 0.47 ns.

The sharp jump in the populations around 0.47 ns indicates that a collapse has occurred and one of the collapse operators has been applied to the wavefunction. In a normal QMC simulation, after a collapse at time t_i *one* of the collapse operators is applied and the wavefunction is renormalised. In the case above a spontaneous emission event has occurred and after the collapse all the excited state population is transferred to

the vacuum state, in this case $\left| \downarrow, 0_X \right\rangle$. This application of a collapse operator destroys coherence in the wavefunction. To investigate the photonic state generated by this system, it could be repeatedly simulated in this way by changing the basis of the collapse operators to gather measurement statistics sufficient for quantum state tomography (with the collapse operators representing photon detection). However it was found in Section 6.1.2 that for a state of 3 photons 6000 measurements were required to obtain a reliable ($> 99\%$ fidelity) estimate of the density matrix. Simulating all these trajectories would take an infeasible amount of time, so instead the full photonic state should be kept which can then be quickly compared with the desired state by calculating the fidelity. To do this the system is integrated up until the point of collapse at time t_i. If the collapse was due to the dephasing operator (6.19), the operator is applied to the system wavefunction and the integration is continued. If the collapse was due to any of the spontaneous emission operators (6.18) then the system is rewound to the time t_i^- just before the collapse. The operator

$$\begin{aligned} U_p = &\left| \uparrow \right\rangle\!\!\left\langle \uparrow \right| \otimes \left|0_X\right\rangle \Big(\left\langle \downarrow\Uparrow \right| \otimes \left|R_h\right\rangle + \left\langle \uparrow\Downarrow \right| \otimes \left|L_l\right\rangle + \left|0_X\right\rangle \otimes \left|0_\gamma\right\rangle \Big) + \\ &\left| \downarrow \right\rangle\!\!\left\langle \downarrow \right| \otimes \left|0_X\right\rangle \Big(\left\langle \downarrow\Uparrow \right| \otimes \left|R_l\right\rangle + \left\langle \uparrow\Downarrow \right| \otimes \left|L_h\right\rangle + \left|0_X\right\rangle \otimes \left|0_\gamma\right\rangle \Big) \end{aligned} \tag{6.20}$$

is applied to the state just before the collapse, $\left|\psi\left(t_i^-\right)\right\rangle$. This rectangular operator U_p enacts the radiative decay paths indicated in Figure 6.12

$$\begin{aligned} \left| \uparrow \right\rangle \left| \downarrow\Uparrow \right\rangle &\rightarrow \left| \uparrow \right\rangle \left|0_X\right\rangle \left|R_h\right\rangle \\ \left| \uparrow \right\rangle \left| \uparrow\Downarrow \right\rangle &\rightarrow \left| \uparrow \right\rangle \left|0_X\right\rangle \left|L_l\right\rangle \\ \left| \downarrow \right\rangle \left| \downarrow\Uparrow \right\rangle &\rightarrow \left| \downarrow \right\rangle \left|0_X\right\rangle \left|R_l\right\rangle \\ \left| \downarrow \right\rangle \left| \uparrow\Downarrow \right\rangle &\rightarrow \left| \downarrow \right\rangle \left|0_X\right\rangle \left|L_h\right\rangle \\ \left| \uparrow \right\rangle \left|0_X\right\rangle &\rightarrow \left| \uparrow \right\rangle \left|0_X\right\rangle \left|0_\gamma\right\rangle \\ \left| \downarrow \right\rangle \left|0_X\right\rangle &\rightarrow \left| \downarrow \right\rangle \left|0_X\right\rangle \left|0_\gamma\right\rangle \end{aligned}$$

where the empty photon mode $\left|0_\gamma\right\rangle$ has been included. Crucially, the application of this operator maintains the coherence of the state. For example, the above operator would

transform

$$a|\uparrow\rangle|\downarrow\Uparrow\rangle + b|\downarrow\rangle|\uparrow\Downarrow\rangle \quad \rightarrow \quad a|\uparrow\rangle|0_X\rangle|R_h\rangle + b|\downarrow\rangle|0_X\rangle|L_h\rangle \tag{6.21}$$

After this, the exciton is reduced to the ground state and the Hilbert space has increased to contain 5 photon modes $|R_h\rangle$, $|L_h\rangle$, $|R_l\rangle$, $|L_l\rangle$ and $|0_\gamma\rangle$. The state

$$|\psi(t_i)\rangle = U_p|\psi(t_i^-)\rangle \tag{6.22}$$

is further integrated until the end of the repetition period τ_{rep} by the QMC routine. The pump laser is turned off during this period, and only the dephasing collapse operator is present. In addition a Hamiltonian is added to describe the different energies of the photon modes

$$\begin{aligned} H_P = \quad & \frac{1}{2}\left(+E^h_{B_z} + E^X_{B_z} + E_c\right)|R_h\rangle \\ & \frac{1}{2}\left(+E^h_{B_z} - E^X_{B_z} - E_c\right)|L_l\rangle \\ & \frac{1}{2}\left(-E^h_{B_z} + E^X_{B_z} - E_c\right)|R_l\rangle \\ & \frac{1}{2}\left(-E^h_{B_z} - E^X_{B_z} + E_c\right)|L_h\rangle \end{aligned} \tag{6.23}$$

where $E^h_{B_z} = g_n B_z$ and $E^X_{B_z} = g_X B_z$ are the Zeeman energies of the host spin and exciton respectively. This free evolution period is important to capture any phase built up between photon components between pumping cycles. At the end of the period τ_{rep} the host spin is rotated around the Y axis by an angle of $\pi/2$.

At this point one of the optical excitation and spin rotation cycles of the photonic machine gun has been performed. To generate more photons and increase the size of the linear cluster state, the above process is repeated with the final state of each round passed on to be the initial state of the next round. After a spontaneous emission collapse event in each round, the size of the Hilbert space increases to include the newly generated photon, and a new photon Hamiltonian is added to the total system Hamiltonian to describe the dynamics of the new photon. Each round the newly generate photon modes form a new node in the linear cluster state.

After N rounds the system is in a linear cluster state with $N+1$ nodes, where the first is

the host spin and the rest are the generated photons. The host spin is more susceptible to decoherence than the photons and should be removed from the cluster state. This can be done by directly measuring it in the Z basis which severs any connections between it and other qubits in the cluster state [37]. However a faster way is to generate $N+1$ photons and not rotate the host spin after the final pumping procedure. A Z measurement of the final photon's polarisation then removes it from the cluster state and leaves the host spin and photon cluster state in a product state. The host spin, exciton and final photon are traced then out of the system (which has no effect on the remaining photonic part since the latter is in a product state with them) leaving just the photonic part

$$\left|\Psi_P\right\rangle = \left|\Psi\left(t_1, t_2, ..., t_N\right)\right\rangle \tag{6.24}$$

6.3.4 Fidelity with cluster state

To quantify the fidelity of the scheme, each photon mode must be transformed from the 4 level system that it is in now (ignoring the vacuum mode), to a 2 level (qubit) system in which the desired cluster state can be expressed. One option is to simply throw away the undesirable photon models ($\left|R_l\right\rangle$ and $\left|L_l\right\rangle$), however this neglects any impact that they might have and may be difficult to do experimentally. Instead the entire photonic state is taken into account by emulating a full photon state tomography. The process, referred to as broadband tomography, is described next.

It is imagined that the whole photonic state (6.24) is sent, photon by photon into the tomography setup in Figure 6.2. The question is, what density matrix would be reconstructed from quantum state tomography given an infinite number of measurements? Note that that each 4-level photon mode impinges on a broad band detector with timing resolution better than $h/\left(2E_c\right)$. To calculate the outcome, projectors onto the $4D$ photon subspace are required which correspond to each of the 6 possible outcomes (for each of the 6 detectors). The problem of a multi-coloured photon mode detected on a colour-blind detector has been previously studied [153–155] and applied to a V system [132]. Extending these ideas, the photon polarisation states that the detectors project

onto are replaced according to

$$\begin{aligned}
\big|R\big\rangle &\to \Big(\big|R_l\big\rangle + \big|R_h\big\rangle\Big) \\
\big|L\big\rangle &\to \Big(\big|L_l\big\rangle + \big|L_h\big\rangle\Big) \\
\big|H\big\rangle &\to \Big(\big|H_l\big\rangle + \big|H_h\big\rangle\Big) \\
\big|V\big\rangle &\to \Big(\big|V_l\big\rangle + \big|V_h\big\rangle\Big) \\
\big|D\big\rangle &\to \Big(\big|D_l\big\rangle + \big|D_h\big\rangle\Big) \\
\big|A\big\rangle &\to \Big(\big|A_l\big\rangle + \big|A_h\big\rangle\Big)
\end{aligned} \tag{6.25}$$

where the photon polarisation components at each energy are related as usual by

$$\begin{aligned}
\big|R_l\big\rangle &= \big|H_l\big\rangle + i\big|V_l\big\rangle & \big|R_h\big\rangle &= \big|H_h\big\rangle + i\big|V_h\big\rangle \\
\big|L_l\big\rangle &= \big|H_l\big\rangle - i\big|V_l\big\rangle & \big|L_h\big\rangle &= \big|H_h\big\rangle - i\big|V_h\big\rangle \\
\big|D_l\big\rangle &= \big|H_l\big\rangle + \big|V_l\big\rangle & \big|D_h\big\rangle &= \big|H_h\big\rangle + \big|V_h\big\rangle \\
\big|A_l\big\rangle &= \big|H_l\big\rangle - \big|V_l\big\rangle & \big|A_h\big\rangle &= \big|H_h\big\rangle - \big|V_h\big\rangle
\end{aligned} \tag{6.26}$$

Photonic state tomography could now be performed by random sampling as it was in Section 6.1.2, using projectors (6.25) in place of the ordinary polarisation projectors. The probability of a click on detector i for photon j of the cluster state is calculated in the same way as $\Pr_{ij} = \langle i|\Psi_P\rangle$ where $\big|i\big\rangle$ is now one of the states in (6.25) (tensored with $j-1$ identities in the appropriate positions). However it was found that using the MLE tomography method, 6000 measurements were required to get an estimate of the true state to fidelity above 0.99. The MLE routine is also computationally expensive. Instead of evaluating discrete detection events and using these to run the MLE routine, the probabilities are used to calculated the Stokes parameters of the photonic state. However there are 6 probabilities for each photon (from the 6 detectors) and so they can be used to calculate the Stokes parameters for a multi-*qubit* state. From these Stokes parameters the density matrix can be directly reconstructed [140]. This multi-qubit density matrix can then be easily compared with the ideal linear cluster state.

6.3.5 Performance

To assess the performance of the scheme, the fidelity [139] of the final state $\left|\Psi_P\right\rangle$ with the desired linear cluster state is calculated. Since $\left|\Psi_P\right\rangle$ depends on the collapse times $t_1, t_2, ..., t_N$ which are random, to truly asses the scheme it must be repeated many times and the fidelities from each run averaged. Due to computational constraints a cluster state of size $N = 3$ is generated and the simulation is repeated 64 times for each setting. The repetition time τ_{rep} and pumping time τ_{pump} are set to 2.5 ns and 0.2 ns, respectively. For each combination of parameters, the optical power Ω is optimised to obtain the highest ratio between the desirable and undesirable exciton components at time τ_{pump}. It is assumed that each pumping step results in a single photon being generated, that is, there are no multi-photon nor photon loss events and the quantum dot doesn't blink (photon loss events can be accounted for by error correction schemes [156]).

Coupling energy

Firstly the most crucial part of the system is inspected, the coupling strength E_c between the host spin and the exciton. No magnetic field is present and spin dephasing is ignored ($\gamma_{\text{dp}} = 0$). The results are shown in Figure 6.14. The line and points show the average of all of the fidelities, and the shaded area gives the standard deviation of the fidelities for each setting.

For E_c greater than around 20 μeV the undesirable transitions are so far detuned from the laser that they are barely populated at all. Thus the generated state is near perfect. The finite standard deviation is caused by the random collapse times. This results in the population of the undesirable states being different for each of the 64 repeats (because the collapse can occur within τ_{pump}). It also means that the phase between the photon components generated by (6.23) is random and different for each of the repeats. Overall this results in a reduction in the fidelity.

At $E_c = 0$ the fidelity is exactly 0.5 and the variance is zero. The photons have the same energy and all 4 exciton transitions are driven equally. As a result the collapse time is not important since the relative population and phase between the excited states

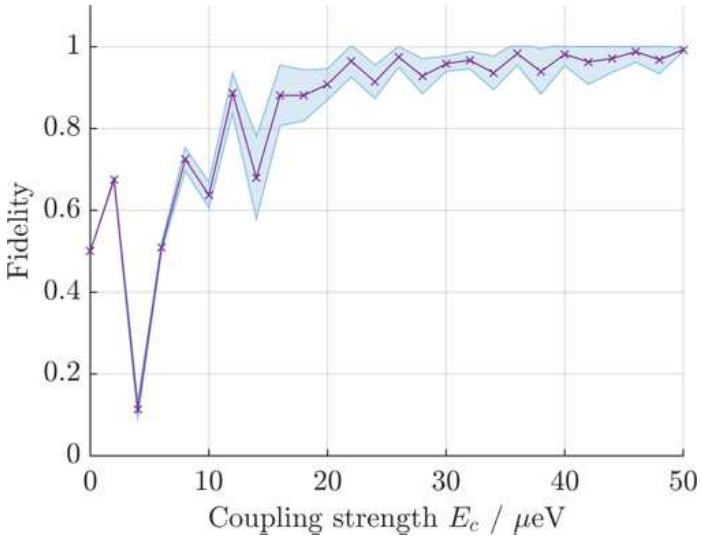

FIGURE 6.14: Variation of the fidelity of the final photonic cluster state with the coupling strength between the host spin and the exciton.

is always identical. Here, the photonic state generated is

$$\left(\left|R_h\right\rangle_1 + \left|R_l\right\rangle_1 + \left|L_h\right\rangle_1 + \left|L_l\right\rangle_1\right) \otimes \left(\left|R_h\right\rangle_2 + \left|R_l\right\rangle_2 + \left|L_h\right\rangle_2 + \left|L_l\right\rangle_2\right) \otimes ... \tag{6.27}$$

which has 0.5 overlap with the desired linear cluster state, and contains no entanglement since the host spin and exciton are not coupled at all.

For E_c between 0 and 20 μeV the behaviour is more complicated and is caused by evolution of the photon modes under H_P. The oscillations are caused by the phase evolution of the undesirable photons with respect to the desirable ones. Increasing τ_{rep} increases the amount of time that H_P has to generate phase between the photons, and this changes the structure of the oscillations. The effects of photon phase evolution are more prominent in this region of E_c because the population of the undesirable photon modes is higher on account of the small detuning between the undesirable transitions and the laser. In CdTe/ZnTe quantum dots doped with Mn atoms the exchange energy between the exciton and Mn spin is around 150 μeV (the strength increases with exciton quantum confinement) [147].

Host spin dephasing

In a real system there will be some dephasing acting on the spin. Figure 6.15 shows the fidelity as a function of the dephasing time $T_2 = 1/\gamma_{\text{dp}}$.

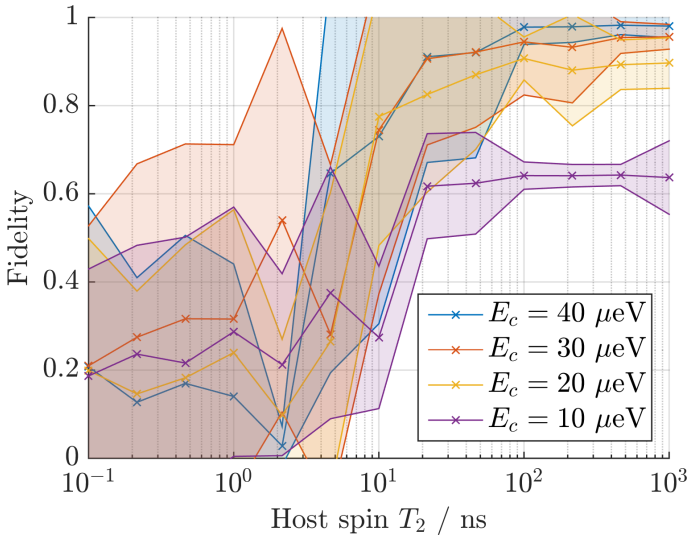

FIGURE 6.15: Variation of the fidelity of the final photonic cluster state with dephasing time of the host spin, for different values of the coupling constant E_c.

For very long dephasing times the system reverts back to the ideal case as in the previous example. The asymptotic values for each E_c are just those in Figure 6.14. As T_2 becomes comparable to the radiative lifetime of the excitons $\tau_{\text{rad}} = \frac{1}{\gamma_{\text{sp}}}$ (in this case set to 1 ns) the fidelity starts to drop. Once T_2 becomes much shorter than the radiative lifetime the generated state is essentially random and so any further decrease in T_2 has no effect.

When E_c becomes larger than around 330 μeV the 'undesired' transition are driven three orders of magnitude less than the desired transitions and so the system behaves like the single electron in the original photonic machine gun. Data for such high E_c (not shown) are quantitatively similar to the data for $E_c = 40$ μeV within the error bars of the simulation. The electron T_2 in InGaAs dots is on the order of several microseconds [77] and so it is expected that in the absence of inhomogeneous dephasing or a magnetic field, the electron based photonic machine gun could reach fidelities close to 1. If inhomogeneous dephasing is included then the effective coherence time drops to around 1 ns in the absence of any preparation of the nuclear spin ensemble [47]. In this case the figure shows that a fidelity of over 70% is achievable.

Magnetic field

A magnetic field is immediately problematic since it splits the two desirable and undesirable transitions and so causes the build-up of phase between the photonic parts of the

cluster state, with some jitter that depends on the collapse time. The Zeeman splitting of the host spin adds to this phase. To investigate this, the exciton g-factor g_X is set to 1 such that the exciton splitting is varied directly. Figure 6.16 shows how the fidelity changes with the splitting for different values of the host spin g-factor g_h. Since $g_X = 1$, $g_h = E^h_{B_z}/E^X_{B_z}$. For these results no spin dephasing was included and E_c was set to 40 μeV.

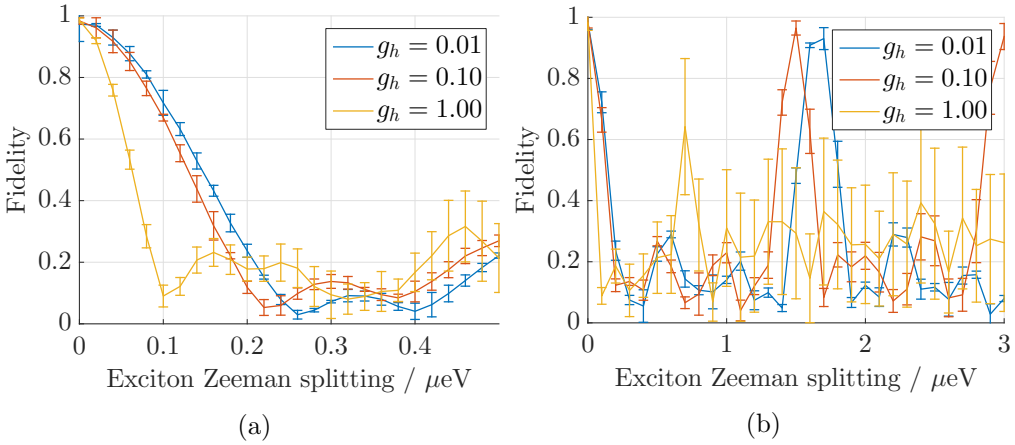

FIGURE 6.16: Variation of the fidelity of the final photonic cluster state with exciton Zeeman splitting. The host spin g-factor g_h is varied from 1 to 0.01, where 1 results in the same splitting as the exciton. (a) shows the results in higher resolution for a splitting of $0 - 0.5$ μeV. (b) shows a larger range of splitting from $0 - 3$ μeV.

Figure 6.16a shows that the fidelity is very sensitive to the magnetic field, especially when both the exciton and host spin states are split. For some larger fields shown in Figure 6.16b the fidelity rises again; these recoveries correspond to fields where the total phase on each component integrates to near zero. These results show that in the worst case considered where $g_h = 1$, a splitting of 0.04 μeV reduces the fidelity to 90%. This splitting is equivalent to a spin rotation time of around 17 ns which together with the radiative lifetime of the exciton would allow on the order 50 photons to be generated within the electron coherence time in InGaAs quantum dots. This rotation time is over two orders of magnitude slower than the jitter of state-of-the-art single photon detectors so the phases built up could be tracked and taken into account, though the state would necessarily be measured and thus used up. In the Mn scenario the results could be improved by using picosecond optical pulses to perform rotations rather than a magnetic field [157].

Electron-hole exchange

Lastly the issue of electron-hole exchange is addressed. It introduces a splitting at zero field (small B_z and E_c) but also changes the system eigenstates from the circularly polarised heavy-hole states to linearly polarised superposition of them. At non-zero field the eigenstates become elliptically polarised. If the scheme is continued regardless then the exchange splitting has a very detrimental effect on the fidelity. However, these effects can be easily taken into account by simply changing the excitation and collection bases from circularly to elliptically polarised. In this case the $\left| \uparrow\Downarrow \right\rangle$ and $\left| \downarrow\Uparrow \right\rangle$ states represent these new elliptically polarised eigenstates (unequal superpositions of the original heavy hole excitons), and the exchange splitting manifests as a constant magnetic field along the quantisation axis. In addition the photonic states $\left|R_h\right\rangle$, $\left|R_l\right\rangle$, $\left|L_h\right\rangle$ and $\left|L_l\right\rangle$ change from being circularly polarised to elliptically polarised.

6.4 Conclusion

The theme of this chapter was to examine ways of implementing Lindner and Rudolph's cluster state proposal in quantum dots, whilst mitigating the effects of electron spin decoherence. This was first investigated by theoretically designing a coupled quantum dot system where, like in the Kim [79] scheme, a spin qubit could exist with both Λ transitions and recycling transitions. It was shown that by using coupled quantum dots with an in-plane Overhauser field a system could be designed which maintained the orthogonally polarised recycling transitions required for the cluster state proposal. Unfortunately the shared excited states meant that picosecond spin rotations [77] could not be performed, however slower rotations on the order of 10s of nanoseconds via SRTs would still be possible [143].

Next the photonic machine gun scheme was theoretically extended to the system of Mn atoms doped in quantum dots. It was shown by numerical investigation that the coupling scheme did indeed allow the generation of photonic cluster states and the performance of the system with respect to various system parameters was determined. Whilst the Mn system was considered in particular, the treatment was sufficiently general that the

results could be applied to any other system with an Ising interaction between the host and exciton spin.

Unfortunately it was not possible to experimentally demonstrate either of these schemes in the lab due to lack of necessary equipment and samples. Nevertheless the simulation results in this chapter have demonstrated the merit in both approaches.

Chapter 7

Conclusions and outlook

This thesis has put forward several new ideas and practical protocols for using coupled quantum dots to sense and ultimately control the fluctuating nuclear spin environment, with the aim of making them suitable as deterministic sources of photonic cluster states.

7.1 Experimental setup

Since the setup was built from scratch, many lessons were learnt and problems solved involving polarisation suppression, mechanical stability and alignment. The configuration of the microscope head in particular underwent many evolutions over the course of the thesis work, starting out as a lightweight cage system and eventually arriving at the form shown in Chapter 4. The move from cage systems to a platform in particular solved many issues with reliability, allowing the microscope to be operated for weeks with little realignment necessary. The addition of the CCD camera after the final analyser also helped since the lobes of described in Section 4.3.3 now made rough polariser alignment very fast.

The spectral suppression stage built in the last part of this chapter performed well and again was stable enough to allow operation over days without realignment. The setup was made as modular as possible by using optical fibres to guide light between different parts of the setup, which meant that misalignment of one section would not affect another. This also helped a great deal in relaxing constraints on the physical

layout of the system, although one has to weigh the benefits of a modular system with the increased loss due to additional fibre couplings. This extra loss is visible in the reduced count rate in the data in Section 5.2.2 compared to the resonance fluorescence characterisation measurement in Section 4.3.7.

The principal limiting factor of the experimental setup was the low collection efficiency in the range of 0.1%, caused mainly by the sample design. The planar sample surface and large refractive index of GaAs limit the amount of light that can escape the sample due to total internal reflection. A solid immersion lens placed on the sample can increase the photon extraction efficiency by around 5 times [158–161]. In modern state-of-the-art devices it has become a standard practice to grow distributed Bragg reflector (DBR) layers below (and possibly above) the quantum dots to form a lossy cavity around them [162]. This can help direct the emission along the collection axis so that the light can more easily make its way out of the sample and be gathered by the lens. Cavities for increased collection efficiency have also been formed between bottom DBR layers in the device and the coated surface of an optical fibre positioned just above the sample surface [163, 164]. More elaborate devices use photonic crystal cavities built around the quantum dot, or etch the region above the dot into structures to again direct the fluorescence along the optical axis [165]. Such modifications have demonstrated photon extraction efficiencies of up to 66% [134]. It is also noteworthy that superconducting photo-detectors have been developed in recent years that allow detection of near-infrared photons with an efficiency of over 93% [166, 167].

7.2 Monitoring the Overhauser field

Chapter 5 described the development of a scheme for fast measurement of the Overhauser field. The modelling in this chapter investigated the proposed protocol and demonstrated that it might be possible to measure both the magnitude and direction of the Overhauser field in real-time, i.e. before it changes substantially. It was then shown how coupled quantum dots could again provide an advantage over single quantum dots by allowing the fluorescence holding the information about the Overhauser field to be spectrally isolated from the reflected laser light used to drive the quantum dot transition. Use of the spectral suppression stage built and characterised in Chapter 4 allowed sufficient suppression of

the laser for the scheme to be experimentally demonstrated. Anomalous behaviour was observed, but nonetheless it was shown that the system could still be used to act as a field sensor to measure a field of < 50 mT to within a value of 0.2 mT. Using idealised device characteristics it was argued that with optimised samples this measurement could be made in around 100 μs. This is faster than the typical Overhauser field fluctuations in a frozen fluctuation model [89]. However recent investigations of the effects of the quadropolar interaction in highly strained self-assembled quantum dots indicate that at small external magnetic fields the nuclear spin bath may vary at shorter time-scales [111]. This is to be contrasted with quantum dots in unstrained systems [168] where the nuclear spin dynamics are expected to be on the time-scale of 100 μs.

Whilst originally developed with the aim of measuring the Overhauser field this method also works for external magnetic fields. Hence the use of this scheme also allows quantum dots to act as sensitive magnetometers.

During the experimental investigation of the sensing protocol, an anomalous feature was discovered in resonant measurements. The intriguing experimental behaviour documented in Section 5.2.3 has not been previously seen in investigations of other systems [115]. Although a model was able to reproduce some of these results, a further investigation of similar quantum dots, likely along with more complex modelling of the nuclear spin ensemble, will be required for a fuller explanation.

Having shown it could be possible to sense the Overhauser field, a complementary method of compensating for it was developed in the end of Chapter 5. The basic mechanism for applying an effective field to a spin qubit in one dot of a coupled pair was demonstrated through modelling of the system. An experiment was attempted to show the proposal in action, but was unsuccessful since the sample did not allow a significant nuclear spin polarisation to be built up due to fast co-tunnelling to the back contact.

7.2.1 Future Work

Changes in the sample structure to afford an increase in detection efficiency might allow real-time estimation of the field. In the proof of concept experiment the integration time was significantly longer than Overhauser field fluctuations so only the effects of total average field were seen. Better collection efficiency would allow shorter integration

times which would then allow real-time fluctuations to be observed. Even with access to shot-by-shot information, the sensing scheme used average statistics of the photon detections to perform its prediction. Using a pulsed laser source would also allow timing information to be extracted which could allow faster predictions by narrowing the probability distribution more quickly. Timing information can be directly incorporated into the scheme, possibly allowing fields to be sensed on a sub-microsecond time-scale. For example, time resolved measurements have been used in gate defined dots and NV centres to perform nuclear and magnetic field sensing by determining the spin precession time [128, 129].

Demonstration of the field compensation mechanism should be fairly straightforward with an appropriate sample, since line dragging is a routinely observed phenomenon in InGaAs quantum dots. Expansion in this direction would just mean moving to a sample with a thicker barrier layer to the back contact, suppressing co-tunnelling.

Further investigation of the anomalous features of Section 5.2.3 should be performed, as well as further microscopic modelling of the nuclear spin ensemble. The involvement of the nuclear spins could be proven by driving them with a nearby coil or micro-strip line to depolarise them during the experiment. This would alter or quench the anomalous features giving additional insight into the system.

Finally, the ultimate extension of this chapter would be to combine the all of the ideas within it to perform real-time sensing and compensation of the Overhauser field. Observation of an increase in coherence time, by enhanced visibility of fringes in a Ramsey experiment for example, would vindicate the work done here. Together it is hoped that these ideas will help to further the field of quantum information processing using quantum dots.

7.3 Cluster state generation

The ultimate goal of this thesis is tackling decoherence of the electron spin due to interaction with the nuclear spins. A first approach to this problem was covered in Chapter 6. That chapter considered the specific case of using quantum dots for generating photonic cluster states using Lindner and Rudolph's photonic machine gun proposal [37]. A brief

investigation of the photonic machine gun showed that a simple passive setup allows the collection of necessary statistics to fully reconstruct the photonic state. The advantage of this characterisation mechanism is that no fast switching or change of measurement settings is necessary so long as the required number of optical elements and detectors are available. It showed that characterisation of cluster states of up to 30 photons was possible within a measurement time of a day. However the time-scales were estimated by assuming rotations could be performed quickly which, as it was mentioned in Chapter 2, can not be done in current systems without sacrificing the ability to generate spin photon entanglement of the kind required for the photonic machine gun.

Instead, motivated by the work of Kim *et al.* [79], a coupled quantum dot system containing one resident electron was investigated for the purpose of providing all of the necessary transitions. Motivated again by observations during the course of developing the models in Chapter 3 and the work of Makhonin *et al.* [103] and Hansom *et al.* [45], it was realised that the generation of an in-plane Overhauser field in one of the quantum dots of a coupled pair was both possible and would enable the transitions required for fast rotation of the electron spin and those required to generate spin-photon polarisation entanglement. Further investigation of this model showed that the transitions were spectrally separated enough to be individually addressed and so could be used for an implementation of the photonic machine gun, but in this case with all optical rotations. This system, together with Overhauser field preparation [47] and dynamic decoupling pulses [169] (now possible thanks to the Λ schemes) could in principle allow the generation of a useful number of entangled photons within the decoherence time of the quantum dot spin.

Leading on from this another interesting avenue was identified, again centred around the photonic machine gun but now with the aim to avoid the spin decoherence by completely replacing the electron with a more coherent spin, such as that provided by a dopant inside the quantum dot [170]. To this end the interaction mechanism that allows the generation of spin photon polarisation entanglement in quantum dots was replaced by a novel mechanism using a spin dependent shift of the exciton energy. A theoretical model of this system was built and numerically simulated in order to assess how well the new system performs at generating photonic cluster states. It was shown that under

suitable conditions near-unity fidelities are achievable. Even with non-unity fidelity it has been shown that errors in the graph state can be probabilistically recovered [10, 37].

The theoretical handling of the simulation in this approach is different in some respects to what has been previously used in the literature. Application of this propagation method allows a simple way of simulating systems where the quantum state of spontaneously emitted photons is of interest. In addition, as far as the author is aware the broadband tomography method is also a new way of treating multi-coloured photonic states.

7.3.1 Future Work

The ideas in this project could be applicable to the case of quantum dots doped with manganese (Mn) atoms. In these systems the Mn atoms couple strongly to the carrier dynamics through an exchange interaction. The interaction allows optical manipulation of the Mn spin state which would allow its use as a qubit [148]. The interaction between the exciton is largely Ising-like in CdTe/ZnTe [147] and CdTe [148, 157] exactly as required to implement the proposal [171, 172]. The ideas in this chapter could be experimentally tested using such samples, in an experimental setup similar to that used by Schwartz et al. [40].

Bibliography

[1] Richard P Feynman. Simulating physics with computers. *International Journal of Theoretical Physics*, 21, 1982.

[2] David P DiVincenzo. Two-bit gates are universal for quantum computation. *Physical Review A*, 51, 1995.

[3] Peter W Shor. Algorithms for quantum computation: discrete logarithms and factoring. *Foundations of Computer Science, 1994 Proceedings., 35th Annual Symposium on*, pages 124–134, 1994.

[4] Don Coppersmith. Modifications to the number field sieve. *Journal of Cryptology*, 6(3):169–180, 1993.

[5] R Barends, J Kelly, A Megrant, A Veitia, D Sank, E Jeffrey, T C White, J Mutus, A G Fowler, B Campbell, Y Chen, Z Chen, B Chiaro, A Dunsworth, C Neill, P O'Malley, P Roushan, A Vainsencher, J Wenner, A N Korotkov, A N Cleland, and John M Martinis. Superconducting quantum circuits at the surface code threshold for fault tolerance. *Nature*, 508:500–503, 2014.

[6] R Raussendorf and H J Briegel. A one-way quantum computer. *Physical Review Letters*, 86(5188), 2001.

[7] H J Briegel and R Raussendorf. Persistent entanglement in arrays of interacting particles. *Physical Review Letters*, 86(910), 2001.

[8] M A Nielsen. Cluster-state quantum computation. *Elsevier*, 57(1):147–161, 2006.

[9] Robert Raussendorf, Daniel E Browne, and Hans J Briegel. Measurement-based quantum computation on cluster states. *American Journal of Physics*, 68(022312), 2003.

[10] Maarten Van den Nest, Akimasa Miyake, Wolfgang Dür, and Hans J Briegel. Universal resources for measurement-based quantum computation. *Physical Review Letters*, 97(150504), 2006.

[11] M Zwerger, H J Briegel, and W Dür. Hybrid architecture for encoded measurement-based quantum computation. *Scientific Reports*, 4(5364), 2014.

[12] D Browne and T Rudolph. Resource-efficient linear optical quantum computation. *Physical Review Letters*, 95(010501), 2005.

[13] C K Hong, Z Y Ou, and L Mandel. Measurement of subpicosecond time intervals between two photons by interference. *Physical Review Letters*, 59(2044), 1987.

[14] P Walther, K J Resch, T Rudolph, E Schenck, H Weinfurter, V Vedral, M Aspelmeyer, and A Zeilinger. Experimental one-way quantum computing. *Nature*, 434:169–176, 2005.

[15] Stefanie Barz, Rui Vasconcelos, Chiara Greganti, Michael Zwerger, Wolfgang Dür, Hans J Briegel, and Philip Walther. Demonstrating elements of measurement-based quantum error correction. *Physical Review A*, 90(042302), 2014.

[16] Jay E Sharping, Kim Fook Lee, Mark A Foster, Amy C Turner, Bradley S Schmidt, Michal Lipson, Alexander L Gaeta, and Prem Kumar. Generation of correlated photons in nanoscale silicon waveguides. *Optics Express*, 14(25):12388–12393, 2006.

[17] Xing-Can Yao, Tian-Xiong Wang, Ping Xu, He Lu, Ge-Sheng Pan, Xiao-Hui Bao, Cheng-Zhi Peng, Chao-Yang Lu, Yu-Ao Chen, and Jian-Wei Pan. Observation of eight-photon entanglement. *Nature Photonics*, 6:225–228, 2012.

[18] David Press, Kristiaan De Greve, Peter L McMahon, Thaddeus D Ladd, Benedikt Friess, Christian Schneider, Martin Kamp, Sven Höfling, Alfred Forchel, and Yoshihisa Yamamoto. Ultrafast optical spin echo in a single quantum dot. *Nature Photonics*, 4:367–370, 2010.

[19] R Warburton. Single spins in self-assembled quantum dots. *Nature Materials*, 12: 483–493, 2013.

[20] Alexander V Khaetskii and Yuli V Nazarov. Spin relaxation in semiconductor quantum dots. *Physical Review B*, 61(19), 1999.

[21] R Hanson, L P Kouwenhoven, J R Petta, S Tarucha, and L M K Vandersypen. Spins in few-electron quantum dots. *Reviews of Modern Physics*, 79(1217), 2007.

[22] R J Warburton, C Schäflein, D Haft, F Bickel, A Lorke, K Karrai, J M Garcia, W Schoenfeld, and P M Petroff. Optical emission from a charge-tunable quantum ring. *Nature*, 405:926–929, 2000.

[23] A N Vamivakas, C-Y Lu, C Matthiesen, Y Zhao, S Fält, A Badolato, and M Atatüre. Observation of spin-dependent quantum jumps via quantum dot resonance fluorescence. *Nature*, 467:297–300, 2010.

[24] Ren-Bao Liu, Wang Yao, and L J Sham. Quantum computing by optical control of electron spins. *Advances in Physics*, 59(5), 2010.

[25] Gert Schedelbeck, Werner Wegscheider, Max Bichler, and Gerhard Abstreiter. Coupled quantum dots fabricated by cleaved edge overgrowth: From artificial atoms to molecules. *Science*, 278(5344):1792–1795, 1997.

[26] M Urdampilleta, A Chatterjee, C C Lo, T Kobayashi, J Mansir, S Barraud, A C Betz, S Rogge, M F Gonzalez-Zalba, and J J L Morton. Charge dynamics and spin blockade in a hybrid double quantum dot in silicon. *Physical Review X*, 5 (031024), 2005.

[27] C W Snyder, B G Orr, D Kessler, and L M Sander. Effect of strain on surface morphology in highly strained ingaas films. *Physical Review Letters*, 66(3032), 1991.

[28] Mete Atatüre, Jan Dreiser, Antonio Badolato, Alexander Högele, Khaled Karrai, and Atac Imamoglu. Quantum-dot spin-state preparation with near-unity fidelity. *Science*, 312(5773), 2006.

[29] Charles Santori, David Fattal, Jelena Vuckovic, Glenn S Solomon, and Yoshihisa Yamamoto. Indistinguishable photons from a single-photon device. *Nature*, 419: 594–597, 2002.

[30] Edward B Flagg, Andreas Muller, Sergey V Polyakov, Alex Ling, Alan Migdall, and Glenn S Solomon. Interference of single photons from two separate semiconductor quantum dots. *Physical Review Letters*, 104(137401), 2010.

[31] Raj B Patel, Anthony J Bennett, Ian Farrer, Christine A Nicoll, David A Ritchie, and Andrew J Shields. Two-photon interference of the emission from electrically tunable remote quantum dots. *Nature Photonics*, 4:632–635, 2010.

[32] C Varnava, R M Stevenson, J Nilsson, J Skiba-Szymanska, B Dzur
vnák, M Lucamarini, R V Penty, I Farrer, DA Ritchie, and A J Shields. An entangled-led-driven quantum relay over 1km. *npj Quantum Information*, 2 (16006), 2016.

[33] Neul Ha, Takaaki Mano, Ying-Lin Chou, Yu-Nien Wu, Shun-Jen Cheng, Juanita Bocquel, Paul M. Koenraad, Akihiro Ohtake, Yoshiki Sakuma, Kazuaki Sakoda, and Takashi Kuroda. Size-dependent line broadening in the emission spectra of single gaas quantum dots: Impact of surface charge on spectral diffusion. *Physical Review B*, 92(075306), 2015.

[34] Mohamed Benyoucef, Verena Zuerbig, Johann Peter Reithmaier, Tim Kroh, Andreas W Schell, Thomas Aichele, and Oliver Benson. Single-photon emission from single ingaas/gaas quantum dots grown by droplet epitaxy at high substrate temperature. *Nanoscale Research Letters*, 7(493), 2012.

[35] Keiji Kuroda, Takashi Kuroda, Katsuyuki Watanabe, Takaaki Mano, Giyuu Kido, Nobuyuki Koguchi, and Kazuaki Sakoda. Distribution of exciton emission linewidth observed for gaas quantum dots grown by droplet epitaxy. *Journal of Applied Physics*, 130(12):2390–2393, 2010.

[36] Aymeric Delteil, Zhe Sun, Wei bo Gao, Emre Togan, Stefan Faelt, and Atac Imamoglu. Generation of heralded entanglement between distant hole spins. *Nature Physics*, 12:218–223, 2015.

[37] N H Lindner and T Rudolph. Proposal for pulsed on-demand sources of photonic cluster state strings. *Physical Review Letters*, 103(113602), 2009.

[38] Yasaman Soudagar, Félix Bussières, Guido Berlín, Suzanne Lacroix, José M Fernandez, and Nicolas Godbout. Cluster-state quantum computing in optical fibers. *Optics InfoBase*, 24, 2007.

[39] S E Economou, N Lindner, and T Rudolph. Optically generated 2-dimensional photonic cluster state from coupled quantum dots. *Physical Review Letters*, 105, 2010.

[40] Ido Schwartz, Dan Cogan, Emma R Schmidgall, Yaroslav Don, Liron Gantz, Oded Kenneth, Netanel H Lindner, and David Gershoni. Deterministic generation of a cluster state of entangled photons. *Science*, 354(6311):434–437, 2016.

[41] Ido Schwartz, Emma Schmidgall, Liron Gantz, Dan Cogan, Eli Bordo, and David Gershoni. Deterministic writing and control of the dark exciton state using short single optical pulses. *Physical Review X*, 5(011009), 2014.

[42] M V Gurudev Dutt, Jun Cheng, Bo Li, Xiaodong Xu, Xiaoqin Li, P R Berman, D G Steel, A S Bracker, D Gammon, Sophia E Economou, Ren-Bao Liu, and L J Sham. Stimulated and spontaneous optical generation of electron spin coherence in charged gaas quantum dots. *Physical Review Letters*, 94(227403), 2005.

[43] A Greilich, D R Yakovlev, A Shabaev, Al L Efros, I A Yugova, R Oulton, V Stavarache, D Reuter, A Wieck, and M Bayer. Mode locking of electron spin coherences in singly charged quantum dots. *Science*, 313(5785):341–345, 2006.

[44] C Langer, R Ozeri, J D Jost, J Chiaverini, B DeMarco, A Ben-Kish, R B Blakestad, J Britton, D B Hume, W M Itano, D Leibfried, R Reichle, T Rosenband, T Schaetz, P O Schmidt, and D J Wineland. Long-lived qubit memory using atomic ions. *Physical Review Letters*, 95(060502), 2005.

[45] Jack Hansom, Carsten H H Schulte, Claire Le Gall, Clemens Matthiesen, Edmund Clarke, Maxime Hugues, Jacob M Taylor, and Mete Atatüre. Environment-assisted quantum control of a solid-state spin via coherent dark states. *Nature Physics*, 10: 725–730, 2014.

[46] Bo Sun, Colin Ming Earn Chow, Duncan G Steel, Allan S Bracker, Daniel Gammon, and L J Sham. Persistent narrowing of nuclear-spin fluctuations in inas quantum dots using laser excitation. *Physical Review Letters*, 108(187401), 2012.

[47] G Éthier Majcher, D Gangloff, R Stockill, E Clarke, M Hugues, C Le Gall, and M Atatüre. Improving a solid-state qubit through an engineered mesoscopic environment. *Physical Review Letters*, 119(130503), 2017.

[48] D Leonard, K Pond, and P M Petroff. Critical layer thickness for self-assembled inas islands on gaas. *Physical Review B*, 50(11687), 1994.

[49] B D Gerardot, G Subramanian, S Minvielle, H Lee, J A Johnson, W V Schoenfeld, D Pine, J S Speck, and P M Petroff. Self-assembling quantum dot lattices through nucleation site engineering. *Elsevier*, 236(4):647–654, 2002.

[50] Hideaki Saito, Kenichi Nishi, and Shigeo Sugou. Influence of gaas capping on the optical properties of ingaas/gaas surface quantum dots with 1.5
mum emission. *Applied Physics Letters*, 73(19), 1998.

[51] Alexander Högele, Stefan Seidl, Martin Kroner, Khaled Karrai, Richard J Warburton, Brian D Gerardot, and Pierre M Petroff. Voltage-controlled optics of a quantum dot. *Physical Review Letters*, 93(217401), 2004.

[52] Susan J Angus, Andrew J Ferguson, Andrew S Dzurak, and Robert G Clark. Gate-defined quantum dots in intrinsic silicon. *Nanoscale Research Letters*, 7(7): 2051–2055, 2007.

[53] Benito Alén, Florian Bickel, Khaled Karrai, Richard J Warburton, and Pierre M Petroff. Stark-shift modulation absorption spectroscopy of single quantum dots. *Applied Physics Letters*, 83(11), 2008.

[54] P W Fry, I E Itskevich, D J Mowbray, M S Skolnick, J J Finley, J A Barker, E P O'Reilly, L R Wilson, I A Larkin, P A Maksym, M Hopkinson, M Al-Khafaji, J P R David, A G Cullis, G Hill, and J C Clark. Inverted electron-hole alignment in inas-gaas self-assembled quantum dots. *Physical Review Letters*, 84(733), 2000.

[55] Shuo Sun, Hyochul Kim, Glenn S Solomon, and Edo Waks. Strain tuning of a quantum dot strongly coupled to a photonic crystal cavity. *Applied Physics Letters*, 103(151102), 2013.

[56] O Gywat. *Spins in Optically Active Quantum Dots*. WILEY-VCH Verlag GmbH and Co. KGaA, 2011.

[57] Rui Q Yang, J M Xu, and Mark Sweeny. Selection rules of intersubband transitions in conduction-band quantum wells. *Physical Review B*, 50(7474), 1994.

[58] Chihiro Hamaguchi. *Basic Semiconductor Physics*. Springer, 2010.

[59] Z M Fang, K Y Ma, D H Jaw, R M Cohen, and G B Stringfellow. Photoluminescence of insb, inas, and inassb grown by organometallic vapor phase epitaxy. *Journal of Applied Physics*, 67(11):7034–7039, 1990.

[60] R J Warburton, C S Dürr, K Karrai, J P Kotthaus, G Medeiros-Ribeiro, and P M Petroff. Charged excitons in self-assembled semiconductor quantum dots. *Physical Review Letters*, 79(5282), 1997.

[61] Marlan O Scully and M Suhail Zubairy. *Quantum Optics*. Cambridge University Press, 2001.

[62] Rodney Loudon. *The Quantum Theory of Light*. Oxford University Press, 2003.

[63] M Bayer, G Ortner, O Stern, A Kuther, A A Gorbunov, A Forchel, P Hawrylak, S Fafard, K Hinzer, T L Reinecke, S N Walck, J P Reithmaier, F Klopf, and F Schäfer. Fine structure of neutral and charged excitons in self-assembled in(ga)as/al(ga)as quantum dots. *Physical Review B*, 65(195315), 2002.

[64] Luca Sapienza, Ralph N E Malein, Christopher E Kuklewicz, Peter E Kremer, Kartik Srinivasan, Andrew Griffiths, Edmund Clarke, Ming Gong, Richard J Warburton, and Brian D Gerardot. Exciton fine-structure splitting of telecom wavelength single quantum dots: statistics and external strain tuning. *Physical Review B*, 88 (155330), 2013.

[65] Alexander Högele, Martin Kroner, Stefan Seidl, Khaled Karrai, Mete Atatüre, Jan Dreiser, Atac Imamoglu, Richard J Warburton, Antonio Badolato, Brian D Gerardot, and Pierre M Petroff. Spin-selective optical absorption of singly charged excitons in a quantum dot. *Applied Physics Letters*, 86(221905), 2005.

[66] D V Regelman, E Dekel, D Gershoni, E Ehrenfreund, A J Williamson, J Shumway, A Zunger, W V Schoenfeld, and P M Petroff. Optical spectroscopy of single quantum dots at tunable positive, neutral, and negative charge states. *Physical Review B*, 64(165301), 2001.

[67] Miro Kroutvar, Yann Ducommun, Dominik Heiss, Max Bichler, Dieter Schuh, Gerhard Abstreiter, and Jonathan J Finley. Optically programmable electron spin memory using semiconductor quantum dots. *Nature*, 432(81-84), 2004.

[68] Xiaodong Xu, Yanwen Wu, Bo Sun, Qiong Huang, Jun Cheng, D G Steel, A S Bracker, D Gammon, C Emary, and L J Sham. Fast spin state initialization in a singly charged inas-gaas quantum dot by optical cooling. *Physical Review Letters*, 99(097401), 2007.

[69] C Emary, Xiaodong Xu, D G Steel, S Saikin, and L J Sham. Fast initialization of the spin state of an electron in a quantum dot in the voigt configuration. *Physical Review Letters*, 98(047401), 2007.

[70] Martin Kroner, Kathrina M Weiss, Benjamin Biedermann, Stefan Seidl, Stephan Manus, Alexander W Holleitner, Antonio Badolato, Pierre M Petroff, Brian D Gerardot, Richard J Warburton, and Khaled Karrai. Optical detection of single-electron spin resonance in a quantum dot. *Physical Review Letters*, 100(156803), 2008.

[71] F Klotz, H Huebl, D Heiss, K Klein, J J Finley, and M S Brandt. Coplanar stripline antenna design for optically detected magnetic resonance on semiconductor quantum dots. *Rev. Sci. Instrum*, 82(074707), 2011.

[72] S Rohr, E Dupont-Ferrier, B Pigeau, P Verlot, V Jacques, and O Arcizet. Synchronizing the dynamics of a single nitrogen vacancy spin qubit on a parametrically coupled radio-frequency field through microwave dressing. *Physical Review Letters*, 112(010502), 2014.

[73] Christopher J Foot. *Atomic Physics*. Oxford University Press, 2005.

[74] Rui Han, Hui Khoon Ng, and Berthold-Georg Englert. Raman transitions without adiabatic elimination: A simple and accurate treatment. *Journal of Modern Optics*, 60(4):255–265, 2013.

[75] J P Marangos. Electromagnetically induced transparency. *Journal of Modern Optics*, 45(3):471–503, 1997.

[76] Sophia E Economou and T L Reinecke. Theory of fast optical spin rotation in a quantum dot based on geometric phases and trapped states. *Physical Review Letters*, 99(217401), 2007.

[77] D Press, T D Ladd, B Zhang, and Y Yamamoto. Complete quantum control of a single quantum dot spin using ultrafast optical pulses. *Nature*, 456:218–221, 2008.

[78] C-Y Lu, Y Zhao, A N Vamivakas, C Matthiesen, S Fält, A Badolato, and M Atatüre. Direct measurement of spin dynamics in inas/gaas quantum dots using time-resolved resonance fluorescence. *Physical Review B*, 81(035332), 2010.

[79] D Kim, S E Economou, S C B
vadescu, M Scheibner, A S Bracker, M Bashkansky, T L Reinecke, and D Gammon. Optical spin initialization and nondestructive measurement in a quantum dot molecule. *Physical Review Letters*, 101(236804), 2008.

[80] D Press. *Quantum Dot Spins And Microcavities For Quantum Information Processing*. PhD thesis, 2010.

[81] J M Smith, P A Dalgarno, R J Warburton, A O Govorov, K Karrai, B D Gerardot, and P M Petroff. Voltage control of the spin dynamics of an exciton in a semiconductor quantum dot. *Physical Review Letters*, 94(197402), 2005.

[82] J M Elzerman, K M Weiss, J Miguel-Sanchez, and A Imamoglu. Optical amplification using raman transitions between spin-singlet and spin-triplet states of a pair of coupled in-gaas quantum dots. *Physical Review Letters*, 107(017401), 2011.

[83] K M Weiss, J Miguel-Sanchez, and J M Elzerman. Magnetically tunable singlet-triplet spin qubit in a four-electron ingaas coupled quantum dot. *Scientific Reports*, 3(3121), 2013.

[84] Jan Dreiser, Mete Atatüre, Christophe Galland, Tina Müller, Antonio Badolato, and Atac Imamoglu. Optical investigations of quantum dot spin dynamics as a function of external electric and magnetic fields. *Physical Review B*, 77(075317), 2008.

[85] S Amasha, K MacLean, Iuliana P Radu, D M Zumbühl, M A Kastner, M P Hanson, and A C Gossard. Electrical control of spin relaxation in a quantum dot. *Physical Review Letters*, 100(046803), 2008.

[86] Alexander V Khaetskii and Yuli V Nazarov. Spin-flip transitions between zeeman sublevels in semiconductor quantum dots. *Physical Review B*, 64(125316), 2001.

[87] Pablo San-Jose, Gergely Zarand, Alexander Shnirman, and Gerd Schön. Geometrical spin dephasing in quantum dots. *Physical Review Letters*, 97(076803), 2006.

[88] Vitaly N Golovach, Alexander Khaetskii, and Daniel Loss. Phonon-induced decay of the electron spin in quantum dots. *Physical Review Letters*, 93(016601), 2004.

[89] I A Merkulov, Al L Efros, and M Rosen. Electron spin relaxation by nuclei in semiconductor quantum dots. *Physical Review B*, 65(205309), 2002.

[90] Andreas V Kuhlmann, Julien Houel, Arne Ludwig, Lukas Greuter, Dirk Reuter, Andreas D Wieck, Martino Poggio, and Richard J Warburton. Charge noise and spin noise in a semiconductor quantum device. *Nature Physics*, 9:570–575, 2013.

[91] B Urbaszek, X Marie, T Amand, O Krebs, P Voisin, P Maletinsky, A Högele, and A Imamoglu. Nuclear spin physics in quantum dots: An optical investigation. *Reviews of Modern Physics*, 85(79), 2013.

[92] M J Stanley, C Matthiesen, J Hansom, C Le Gall, C H H Schulte, E Clarke, and M Atatüre. Dynamics of a mesoscopic nuclear spin ensemble interacting with an optically driven electron spin. *Physical Review B*, 90(195305), 2014.

[93] P-F Braun, X Marie, L Lombez, B Urbaszek, T Amand, P Renucci, V K Kalevich, K V Kavokin, O Krebs, P Voisin, and Y Masumoto. Direct observation of the electron spin relaxation induced by nuclei in quantum dots. *Physical Review Letters*, 94(116601), 2005.

[94] E L Hahn. Spin echoes. *Physical Review*, 80(580), 1950.

[95] A I Tartakovskii, T Wright, A Russell, V I Fal'ko, A B Van'kov, J Skiba-Szymanska, I Drouzas, R S Kolodka, M S Skolnick, P W Fry, A Tahraoui, H-Y Liu,

and M Hopkinson. Nuclear spin switch in semiconductor quantum dots. *Physical Review Letters*, 98(026806), 2007.

[96] Chia-Wei Huang and Xuedong Hu. Theoretical study of nuclear spin polarization and depolarization in self-assembled quantum dots. *Physical Review B*, 81(205304), 2010.

[97] E A Chekhovich, M N Makhonin, K V Kavokin, A B Krysa, M S Skolnick, and A I Tartakovskii. Pumping of nuclear spins by optical excitation of spin-forbidden transitions in a quantum dot. *Physical Review Letters*, 104(066804), 2010.

[98] C Kloeffel, P A Dalgarno, B Urbaszek, B D Gerardot, D Brunner, P M Petroff, D Loss, and R J Warburton. Controlling the interaction of electron and nuclear spins in a tunnel-coupled quantum dot. *Physical Review Letters*, 106(046802), 2011.

[99] A Högele, M Kroner, C Latta, M Claassen, I Carusotto, C Bulutay, and A Imamoglu. Dynamic nuclear spin polarization in the resonant laser excitation of an ingaas quantum dot. *Physical Review Letters*, 108(197403), 2012.

[100] C Latta, A Högele, Y Zhao, A N Vamivakas, P Maletinsky, M Kroner, J Dreiser, I Carusotto, A Badolato, D Schuh, W Wegscheider, M Atature, and A Imamoglu. Confluence of resonant laser excitation and bidirectional quantum-dot nuclear-spin polarization. *Nature Physics*, 5:758–763, 2009.

[101] Andreas V Kuhlmann, Julien Houel, Daniel Brunner, Arne Ludwig1, Dirk Reuter, Andreas D Wieck, and Richard J Warburton. A dark-field microscope for background-free detection of resonance fluorescence from single semiconductor quantum dots operating in set-and-forget mode. *Rev. Sci. Instrum*, 84(073905), 2013.

[102] Patrick Maletinsky. *Polarization and Manipulation of a Mesoscopic Nuclear Spin Ensemble Using a Single Confined Electron Spin*. PhD thesis, 2008.

[103] M N Makhonin, K V Kavokin, P Senellart, A Lemaître, A J Ramsay, M S Skolnick, and A I Tartakovskii. Fast control of nuclear spin polarization in an optically pumped single quantum dot. *Nature Materials*, 10:844–848, 2011.

[104] Alexander Bechtold, Dominik Rauch, Fuxiang Li, Tobias Simmet, Per-Lennart Ardelt, Armin Regler, Kai Müller, Nikolai A Sinitsyn, and Jonathan J Finley. Three-stage decoherence dynamics of an electron spin qubit in an optically active quantum dot. *Nature Physics*, 11:1005–1008, 2015.

[105] A Greilich, A Shabaev, D R Yakovlev, Al L Efros, I A Yugova, D Reuter, A D Wieck, and M Bayer. Nuclei-induced frequency focusing of electron spin coherence. *Science*, 317(5846):1896–1899, 2007.

[106] Mathieu Munsch, Gunter Wüst, Andreas V Kuhlmann, Fei Xue, Arne Ludwig, Dirk Reuter, Andreas D Wieck, Martino Poggio, and Richard J Warburton. Manipulation of the nuclear spin ensemble in a quantum dot with chirped magnetic resonance pulses. *Nature Nanotechnology*, 9:671–675, 2014.

[107] R I Dzhioev and V L Korenev. Stabilization of the electron-nuclear spin orientation in quantum dots by the nuclear quadrupole interaction. *Physical Review Letters*, 99(037401), 2007.

[108] G Sallen, S Kunz, T Amand, L Bouet, T Kuroda, T Mano, D Paget, O Krebs, X Marie, K Sakoda, and B Urbaszek. Nuclear magnetization in gallium arsenide quantum dots at zero magnetic field. *Nature Communications*, 5(3268), 2014.

[109] P Maletinsky, A Badolato, and A Imamoglu. Dynamics of quantum dot nuclear spin polarization controlled by a single electron. *Physical Review Letters*, 99(056804), 2007.

[110] Christian Latta, Ajit Srivastava, and Atac Imamo?lu. Hyperfine interaction-dominated dynamics of nuclear spins in self-assembled ingaas quantum dots. *Physical Review Letters*, 107(167401), 2011.

[111] R Stockill, C Le Gall, C Matthiesen, L Huthmacher, E Clarke, Maxime Hugues, and M Atature. Intrinsic limit to electron spin coherence in ingaas quantum dots featuring strain-induced nuclear dispersion. *arXiv*, 2015.

[112] Qianghua Xie, Anupam Madhukar, Ping Chen, and Nobuhiko P Kobayashi. Vertically self-organized inas quantum box islands on gaas(100). *Physical Review*, 75 (2542), 1995.

[113] D M Bruls, P M Koenraad, H W M Salemink, and J H Wolter. Stacked low-growth-rate inas quantum dots studied at the atomic level by cross-sectional scanning tunneling microscopy. *Applied Physics Letters*, 82(3758), 2003.

[114] A S Bracker, M Scheibner, M F Doty, E A Stinaff, I V Ponomarev, J C Kim, L J Whitman, T L Reinecke, and D Gammon. Engineering electron and hole tunneling with asymmetric inas quantum dot molecules. *Applied Physics Letters*, 89(233110), 2006.

[115] K M Weiss, J M Elzerman, Y L Delley, J Miguel-Sanchez, and A Imamoglu. Coherent two-electron spin qubits in an optically active pair of coupled ingaas quantum dots. *Physical Review Letters*, 109(107401), 2012.

[116] E A Stinaff, M Scheibner, A S Bracker, I V Ponomarev, V L Korenev, M E Ware, M F Doty, T L Reinecke, and D Gammon. Optical signatures of coupled quantum dots. *Science*, 311(5761):636–639, 2006.

[117] M Scheibner, M F Doty, I V Ponomarev, A S Bracker, E A Stinaff, V L Korenev, T L Reinecke, and D Gammon. Spin fine structure of optically excited quantum dot molecules. *Physical Review B*, 75(245318), 2007.

[118] H J Krenner, M Sabathil, E C Clark, A Kress, D Schuh, M Bichler, G Abstreiter, and J J Finley. Direct observation of controlled coupling in an individual quantum dot molecule. *Physical Review Letters*, 94(057402), 2005.

[119] I Toft and R T Phillips. Hole g factors in gaas quantum dots from the angular dependence of the spin fine structure. *Physical Review B*, 76(033301), 2007.

[120] Zhiming M Wang. *Self-Assembled Quantum Dots*. 2008.

[121] Clemens Matthiesen, Megan J Stanley, Maxime Hugues, Edmund Clarke, and Mete Atatüre. Full counting statistics of quantum dot resonance fluorescence. *Scientific Reports*, 4(4911), 2014.

[122] K Liu. Novel geometry for single-mode scanning of tunable lasers. *Optics InfoBase*, 6, 1981.

[123] Andrei Faraon, Dirk Englund, Ilya Fushman, and Jelena Vučković. Local quantum dot tuning on photonic crystal chips. *Applied Physics Letters*, 90(213110), 2007.

[124] A Muller, E B Flagg, P Bianucci, X Y Wang, D G Deppe, W Ma, J Zhang, G J Salamo, M Xiao, and C K Shih. Resonance fluorescence from a coherently driven semiconductor quantum dot in a cavity. *Physical Review Letters*, 99, 2007.

[125] L Novotny and B Hecht. *Principles of Nano-Optics*. Cambridge University Press, 2006.

[126] K Karrai and R J Warburton. Optical transmission and reflection spectroscopy of single quantum dots. *Superlattices and Microstructures*, 33(5-6):311–337, 2003.

[127] Jack Hansom, Carsten H H Schulte, Clemens Matthiesen, Megan J Stanley, and Mete Atatüre. Frequency stabilization of the zero-phonon line of a quantum dot via phonon-assisted active feedback. *Applied Physics Letters*, 105(172107), 2014.

[128] C Bonato, M S Blok, H T Dinani, D W Berry, M L Markham, D J Twitchen, and R Hanson. Optimized quantum sensing with a single electron spin using real-time adaptive measurements. *Nature Nanotechnology*, 11:247–252, 2016.

[129] M D Shulman, S P Harvey, J M Nichol, S D Bartlett, A C Doherty, V Umansky, and A Yacoby. Suppressing qubit dephasing using real-time hamiltonian estimation. *Nature Communications*, 5(5156), 2014.

[130] K Kowalik, O Krebs, A Lemaître, J A Gaj, and P Voisin. Optical alignment and polarization conversion of the neutral-exciton spin in individual inas/gaas quantum dots. *Physical Review B*, 77(161305), 2008.

[131] G V Astakhov, T Kiessling, A V Platonov, T Slobodskyy, S Mahapatra, W Ossau, G Schmidt, K Brunner, and L W Molenkamp. Circular-to-linear and linear-to-circular conversion of optical polarization by semiconductor quantum dots. *Physical Review Letters*, 96(027402), 2006.

[132] Wei bo Gao, P Fallahi, E Togan, A Delteil, Y S Chin, J Miguel-Sanchez, and A Imamoglu. Quantum teleportation from a propagating photon to a solid-state spin qubit. *Nature Communications*, 4(2744), 2013.

[133] Alfred Kastler. The hanle effect and its use for the measurements of very small magnetic fields. *Nuclear Instruments and Methods*, 110:259–265, 1973.

[134] Xing Ding, Yu He, Z-C Duan, Niels Gregersen, M-C Chen, S Unsleber, S Maier, Christian Schneider, Martin Kamp, Sven Höfling, Chao-Yang Lu, and Jian-Wei Pan. On-demand single photons with high extraction efficiency and near-unity indistinguishability from a resonantly driven quantum dot in a micropillar. *Physical Review Letters*, 116(020401), 2016.

[135] Carlos Navarrete-Benlloch. Open systems dynamics: Simulating master equations in the computer. *arXiv*, 2015.

[136] M F Doty, M Scheibner, A S Bracker, I V Ponomarev, T L Reinecke, and D Gammon. Optical spectra of doubly charged quantum dot molecules in electric and magnetic fields. *Physical Review B*, 78(115316), 2008.

[137] O Krebs, P Maletinsky, T Amand, B Urbaszek, A Lemaître, P Voisin, X Marie, and A Imamoglu. Anomalous hanle effect due to optically created transverse overhauser field in single inas/gaas quantum dots. *Physical Review Letters*, 104 (056603), 2010.

[138] I Schwartz, D Cogan, E R Schmidgall, L Gantz, Y Don, M Zieli?ski, and D Gershoni. Deterministic coherent writing of a long-lived semiconductor spin qubit using one ultrafast optical pulse. *Physical Review B*, 92(201201(R)), 2015.

[139] Michael A Nielsen and Isaac L Chuang. *Quantum Computation and Quantum Information*. Cambridge University, 2010.

[140] J B Altepeter, E R Jeffrey, and P G Kwiat. Photonic state tomography. *Advances In Atomic, Molecular, and Optical Physics*, 52:105–59, 2005.

[141] Ilai Schwarz and Terry Rudolph. Efficient entanglement-length measurements for photonic-cluster-state sources. *Physical Review A*, 85(050306(R)), 2012.

[142] O Gühne and G Toth. Entanglement detection. *Physics Reports*, 474(1-6):1–75, 2009.

[143] Christopher G Yale, Bob B Buckley, David J Christle, Guido Burkard, F Joseph Heremans, Lee C Bassett, and David D Awschalom. All-optical control of a solid-state spin using coherent dark states. *The Proceedings of the National Academy of Sciences of the United States of America*, 110(19), 2013.

[144] B Eble, O Krebs, A Lemaître, K Kowalik, A Kudelski, P Voisin, B Urbaszek, X Marie, and T Amand. Dynamic nuclear polarization of a single charge-tunable inas/gaas quantum dot. *Physical Review B*, 74(081306), 2006.

[145] E A Chekhovich, M N Makhonin, A I Tartakovskii, A Yacoby, H Bluhm, K C Nowack, and L M K Vandersypen. Nuclear spin effects in semiconductor quantum dots. *Nature Materials*, 12, 2013.

[146] D Gammon, S W Brown, E S Snow, T A Kennedy, D S Katzer, and D Park. Nuclear spectroscopy in single quantum dots: Nanoscopic raman scattering and nuclear magnetic resonance. *Science*, 277(5322):85–88, 1997.

[147] C Le Gall, R S Kolodka, C L Cao, H Boukari, H Mariette, J Fernández-Rossier, and L Besombes. Optical initialization, readout, and dynamics of a mn spin in a quantum dot. *Physical Review B*, 81(245315), 2010.

[148] Alexander O Govorov and Alexander V Kalameitsev. Optical properties of a semiconductor quantum dot with a single magnetic impurity: photoinduced spin orientation. *Physical Review B*, 71(035338), 2005.

[149] J R Johansson, P D Nation, and F Nori. Qutip: An open-source python framework for the dynamics of open quantum systems. *Computer Physics Communications*, 183(8):1760–1772, 2012.

[150] Klaus Mølmer, Yvan Castin, and Jean Dalibard. Monte carlo wave-function method in quantum optics. *Optics InfoBase*, 10(3):524–538, 1993.

[151] M B Plenio and P L Knight. The quantum-jump approach to dissipative dynamics in quantum optics. *Reviews of Modern Physics*, 70(101), 1998.

[152] David G Tempel and AlÃ¡n Aspuru-Guzik. Relaxation and dephasing in open quantum systems time-dependent density functional theory: Properties of exact functionals from an exactly-solvable model system. *Elsevier*, 391(1):130–142, 2010.

[153] Sophia E Economou, Ren-Bao Liu, L J Sham, and D G Steel. Unified theory of consequences of spontaneous emission in a lambda system. *Physical Review B*, 71 (195327), 2005.

[154] J R Schaibley and P R Berman. The effect of frequency-mismatched spontaneous emission on atom-field entanglement. *Journal of Physics B: Atomic, Molecular and Optical Physics*, 45(12), 2012.

[155] W B Gao, P Fallahi, E Togan, J Miguel-Sanchez, and A Imamoglu. Observation of entanglement between a quantum dot spin and a single photon. *Nature*, 491: 426–430, 2012.

[156] B A Bell, D A Herrera-Martí, M S Tame, D Markham, W J Wadsworth, and J G Rarity. Experimental demonstration of a graph state quantum error-correction code. *Nature Communications*, 5(3658), 2014.

[157] D E Reiter, T Kuhn, and V M Axt. All-optical spin manipulation of a single manganese atom in a quantum dot. *Physical Review Letters*, 102(177403), 2009.

[158] Clemens Matthiesen. *Coherent photons from a solid-state artivcial atom.* PhD thesis, 2013.

[159] B B Goldberg, S B Ippolito, L Novotny, Zhiheng Liu, and M Unlu. Immersion lens microscopy of photonic nanostructures and quantum dots. *IEEE Journal of Selected Topics in Quantum Electronics*, 8(5), 2002.

[160] S Moehl, Hui Zhao, B Dal Don, S Wachter, and H Kalt. Solid immersion lens-enhanced nano-photoluminescence: Principle and applications. *Journal of Applied Physics*, 93(6265), 2003.

[161] Zhiheng Liu, Bennett B Goldberg, Stephen B Ippolito, Anthony N Vamivakas, M Selim Ünlü, and Richard Mirin. High resolution, high collection efficiency in numerical aperture increasing lens microscopy of individual quantum dots. *Applied Physics Letters*, 87(071905), 2005.

[162] Bingyang Zhang, Glenn S Solomon, Matthew Pelton, Jocelyn Plant, Charles Santori, Jelena Vuckovic, and Yoshihisa Yamamoto. Fabrication of inas quantum dots in alas/gaas dbr pillar microcavities for single photon sources. *Journal of Applied Physics*, 97(7, 073507), 2005.

[163] D Hunger, T Steinmetz, 4 Y Colombe1, C Deutsch, T W Hänsch, and J Reichel. A fiber fabry-perot cavity with high finesse. *New Journal of Physics*, 12(065038), 2010.

[164] Javier Miguel-Sánchez, Andreas Reinhard, Emre Togan, Thomas Volz, Atac Imamoglu, Benjamin Besga, Jakob Reichel, and Jérôme Estève. Cavity quantum electrodynamics with charge-controlled quantum dots coupled to a fiber fabry-perot cavity. *New Journal of Physics*, 15(045002), 2013.

[165] A J Bennett, J P Lee, D J P Ellis, T Meany, E Murray, F Floether, J P Griffths, I Farrer, D A Ritchie, and A J Shields. Cavity-enhanced coherent light scattering from a quantum dot. *Science Advances*, 2(4, e1501256), 2016.

[166] Luca Redaelli, Gabriele Bulgarini, Sergiy Dobrovolskiy, Sander N. Dorenbos, Val Zwiller, Eva Monroy, and Jean-Michel Gérard. Design of broadband high-efficiency superconducting-nanowire single photon detectors. *Superconductor Science and Technology*, 29(6):065016, 2016.

[167] F Marsili, V B Verma, J A Stern, S Harrington, A E Lita, T Gerrits, I Vayshenker, B Baek, M D Shaw, R P Mirin, and S W Nam. Detecting single infrared photons with 93 *Nature Photonics*, 7:210–214, 2013.

[168] Y H Huo, B J Witek, S Kumar, J R Cardenas, J X Zhang, N Akopian, R Singh, E Zallo, R Grifone, D Kriegner, R Trotta, F Ding, J Stangl, V Zwiller, G Bester, A Rastelli, and O G Schmidt. A light-hole exciton in a quantum dot. *Nature Physics*, 10:46–51, 2014.

[169] G de Lange, Z H Wang, D Ristè, V V Dobrovitski, and R Hanson. Universal dynamical decoupling of a single solid-state spin from a spin bath. *Science*, 330 (6000):60–63, 2010.

[170] L J Hu, Y H Chen, X L Ye, Y H Jiao, L W Shi, and Z G Wang. Mn-including inas quantum dots fabricated by mn implantation. *Physica E: Low-dimensional Systems and Nanostructures*, 40(9):2869–2873, 2008.

[171] E Baudin, E Benjamin, A Lemaître, and O Krebs. Optical pumping and a nondestructive readout of a single magnetic impurity spin in an inas/gaas quantum dot. *Physical Review Letters*, 107(197402), 2011.

[172] A Kudelski, A Lemaître, A Miard, P Voisin, T C M Graham, R J Warburton, and O Krebs. Optically probing the fine structure of a single mn atom in an inas quantum dot. *Physical Review Letters*, 99(247209), 2007.